A VERTEX BASED DISCRETISATION SCHEME APPLIED TO MATERIAL NON-LINEARITY WITHIN A MULTI-PHYSICS FINITE VOLUME FRAMEWORK

GARETH ANTHONY TAYLOR [1]

A thesis submitted in partial fulfilment of the
requirements of the University of Greenwich
for the degree of Doctor of Philosophy

November 1996

---

[1] Centre for Numerical Modelling and Process Analysis, School of Computing and Mathematical Sciences, University of Greenwich, London, UK

Dedications

For my grandmother,
Florence Taylor,
3rd September 1911 – 18th November 1985,

and my grandfather,
George David Taylor,
17th June 1911 – 4th September 1986.

Acknowledgements

Firstly, I acknowledge the people directly associated with this research project. This group includes, primarily, Prof. Mark Cross and Dr. Chris Bailey, who have both provided careful supervision and displayed significant amounts of patience.

This group also includes a considerable number of acedemic, research and technical staff associated with the School of Computing and Mathematical Sciences at the University of Greenwich. This collection of people have all provided invaluable support to varying degrees, but two people deserve a particular acknowledgement, Nick Croft for his academic contribution and Frank for his technical support.

Secondly, I acknowledge both my parents and my brother for their complete support and also my friends for their entertaining distractions and polite interest.

Finally and maybe most importantly, I acknowledge the Engineering and Physical Sciences Research Council without whose financial support this research may not have been possible.

Abstract

The objective of this research is the development of novel three dimensional Finite Volume (FV) algorithms for the solution of small strain, quasi-static, Computational Solid Mechanics (CSM) problems involving non-linear material behavior, specifically materials described by an elasto-visco-plastic constitutive relationship and a von-Mises yield criterion. The motivation is to contribute the non-linear CSM capability to an integrated FV framework for the comprehensive solution of the thermo-mechanical behaviour exhibited by the shape casting of metals.

A study of novel two and three dimensional FV algorithms associated with CSM is presented. The algorithms employ a variety of two and three dimensional elements and are compared with the standard Bubnov-Galerkin Finite Element Method, with regard to algorithmic procedure, linear solvers, accuracy and computational cost. A variety of benchmark solid mechanics problems involving elasto-plastic and elasto-visco-plastic material behaviour are studied. These include the plane stress analysis of a perforated tensile strip of aluminium, the plane strain analysis of a hollow metal cylinder and the three dimensional analysis of a hollow metal sphere.

The control volume-unstructured mesh, vertex based, FV algorithm for CSM problems is integrated within a multi-physics FV framework PHYSICA, which includes cell-centred FV procedures for the solution of problems involving simultaneous heat transfer, solidification and fluid flow. The thermo-mechanical coupling is described in detail. A variety of thermo-mechanical benchmark problems involving thermo-elasto-plastic and thermo-elasto-visco-plastic behaviour are studied, these include the quenching and the solidification of an infinite steel plate. Finally, the completely coupled capability of the FV framework PHYSICA is validated against experimental observations obtained from the gravity die casting of a hollow aluminium cylinder.

Contents

List of Figures

List of Tables

Chapter 1

Introduction

The goal of the research project is to extend novel two and three dimensional implementations of linear elastic, small strain deformation algorithms using Finite Volume (FV) discretisation techniques [43, 42, 4], in order to model non-linear material behaviour, such as elasto-plastic and elasto-visco-plastic deformation. The novelty of the original deformation algorithms is their ease of coupling with Computational Fluid Dynamics (CFD) procedures based upon FV discretisation techniques [42, 3]. This was achieved using generically similar discretisation, formulation and solution techniques for both Computational Solid Mechanics (CSM) and CFD procedures [42, 3]. The ultimate aim of this research is the modelling of multi-physics problems, such as the shape-casting of metals, within a completely integrated numerical framework [26, 25].

A review of numerical discretisation methods for CSM problems involving material non-linearity is presented, with passing reference to the applicability of the methods discussed to CFD problems. Specifically, the various classes of Finite Volume Methods (FVM) are then described in more detail, with particular reference to the methods employed in this research project. Finally, a brief outline of the remaining chapters of the thesis is included.

1.1 Review of numerical discretisation methods

Historically, it is accepted that the broad field of continuum physics is conventionally limited by the extreme behaviour of either solid or fluid continua.

Over the last three decades the Finite Element Method (FEM) has firmly established itself as the pioneering approach for CSM, especially with regard to solid body stress analysis [107, 108, 72, 86]. Contemporarily, the FVM, which originated from Finite Difference Methods (FDM) associated with a control volume [101, 74, 52], has similarly established itself within the CFD community.

The following section describes these trends in more detail by studying the above mentioned numerical techniques separately, with particular regard to CSM problems involving material non-linearity. Additionally, the Boundary Element Method (BEM) is described as, potentially, a further alternative.

1.1.1 Finite Difference Methods (FDM)

The FDM was widely used in continuum physics well before the advent of computers, particularly in such fields as solid mechanics where applications date back to the turn of the century. Indeed Timoshenko and Goodier [94] credit the first application of the FDM to the solution of elastic problems by Runge in 1908, who applied the method to torsional problems.

Conversely, the FDM has had limited use in CSM since the advent of computers, especially with regard to problems involving non-linear materials. This was mostly attributable to the early domination of the extremely efficient FEM in this field as developed from the early 1960's onwards. At that time some interest was directed at the FDM, but for mainly linear elastic analysis of two and three dimensional continua, beam, plate and shell problems [94, 38, 45].

As described by Fenner [38], two distinct types of governing equations dominate in quasi-static CSM problems, namely, second-order harmonic and fourth-order biharmonic types, where the unknown, which is usually a displacement or stress function, is defined in terms of the relevant coordinates. With regard to stress functions, for planar and axisymmetric problems a single Airy stress function can be introduced, while for three dimensional problems the three Clerk Maxwell stress functions can be introduced [38].

The problems are discretised by the classical FDM in conjunction with a Taylor series approximation. The diagonally dominant system of algebraic equations thus formed, are solved either, directly, by suitable elimination techniques such as the tri-diagonal matrix solver or, iteratively, by techniques such as Successive Over Relaxation (SOR) schemes [38, 10, 45]. These early techniques had limited success with CSM problems compared with other methods such as the FEM. There were a number of reasons for this, the most important being the difficulty of applying these techniques to irregular geometries in a simple fashion [42, 38].

The FDM received a renewed interest when associated with a control volume. This was a major influence in the field of CFD [74, 52, 75]. The approach allowed the numerical analyst a simple interpretation of the method when applied to a physical situation. The method enforces conservation of the dependent variable over the designated control volume as described by Patankar et al [74, 52]. This was a ground breaking step in discretisation methods, as the method originally had the appearance of a FDM but employed some of the typical conventions of a FEM.

This was the initial step in the creation of a new concept of discretisation under the heading Finite Volume Methods (FVM) and early credit for the naming convention, Finite Volume Method, in the context of CFD can be attributed to Jameson [57], though the origin of the discretisation approach can be traced much earlier. McDonald [66] proposed a novel Finite Area Method, applicable to two dimensional CFD applications and even earlier, in 1967, Winslow [101] applied a novel FDM, using a nonuniform triangular mesh, to the numerical solution of magnetostatic problems. The nonuniform mesh consisted of linear triangular elements with regular topology. Winslow illustrated the equivalence of this novel FDM, which was associated with a vertex based control volume, and a standard Rayleigh-Ritz variational approach [101]. Indeed, as the Rayleigh-Ritz variational approach is equivalent to the Bubnov-Galerkin weighted residual approach, by virtue of Green's theorem [30], this is an early indication of the direct equivalence of a FVM and a FEM with regard to linear elements. This equivalence will be commented upon in more detail in the following sections.

The success of the control volume – finite difference methods in CFD is widely reported [74, 52, 75], particularly with regard to the leading commercial CFD software packages [19, 18, 41]. The inherent satisfaction of the principle of conservation and the extremely high efficiency with respect to non-linear iterative procedures on a structured mesh [74, 75] has caused the FVM to be the dominant method employed in CFD applications.

As the original development of a discretisation technique using a FDM associated with a control volume was restricted to a structured mesh, additional discretisation methods were developed associating a control volume with an unstructured mesh for the solution of CFD problems [74]. A number of researchers developed such methods initially described as control-volume-based finite-element methods [7, 6, 8, 57]. Standard CFD problems were modelled on unstructured meshes using this discretisation technique, such as conduction, convection-diffusion, laminar fluid flow and laminar forced and natural convection [83, 5]. This technique is now well established for the modelling of CFD problems and has been analysed quite extensively by Morton et al with regard to accuracy when compared to the traditional FEM for a variety of CFD problems [69, 54].

This vertex based approach to numerical discretisation as described by Patankar and Schneider for CFD applications [5, 83], provides the unstructured discretisation method as implemented by Fryer et al [43, 42, 4] for the solid body stress analysis of linear elastic materials, upon which the present research is based. The discretisation technique has also been described generally and analytically compared against the standard FEM with regard to linear elastic, structural mechanics problems [71]. The method will be fully described in the context of a FVM in the following section.

More recently, the control volume FDM has been extended to unstructured meshes for CFD problems [20] and the above mentioned CFD problems have been successfully modelled on unstructured meshes [20, 22], particularly in connection with solidification processes [20]. This cell centred technique is currently being applied to more complex fluid flow situations involving such phenomena as swirl with highly irregular mesh geometries [24].

A similar research trend has developed in the field of CSM. Initially, with Hattel et al investigating the applicability of the control volume FDM for thermo-elastic and thermo-elasto-plastic problems on structured meshes [48, 31] and lately Demirdzic et al have had some success extending these discretisation methods to unstructured meshes, though this work has so far been limited to linear elastic materials [32]

A summary of the most recent discretisation techniques associated with the FVM is presented in section 1.2.

1.1.2 Finite Element Methods (FEM)

The FEM has been applied extensively to the field of solid mechanics, since the advent of numerical computation in the early 1960's. This is historically illustrated if we focus on the modelling of small strain, non-linear material behaviour, particularly elasto-plastic and elasto-visco-plastic deformation.

Some of the earliest applications of the FEM to an elasto-plastic constitutive relationship were performed in the 1960's by Marcal and King, 1967 [65], Yamada et al, 1968 [103] and Zienkiewicz et al, 1969 [109]. During the 1970's Zienkiewicz et al applied the FEM to an elasto-visco-plastic constitutive relationship [105, 23]. This work utilised the well known Perzyna model to describe the visco-plastic strain rate [76, 77]. The Perzyna model is also adopted in this research and a detailed description is provided in the next chapter, though it should be noted that the FVM described in this work can be generally applied to other non-linear material models.

The introduction of the Finite Element (FE) discretisation technique to problems involving material non-linearity was a natural extension of the FE discretisation approach as previously applied to a linear elastic constitutive relationship. Solid mechanics problems often involve irregular geometries and the FE discretisation approach is well suited to unstructured meshes, for such reasons the FEM is well established as the ruling discretisation technique for solid mechanics problems. Detailed accounts are available in standard texts [107, 30, 38].

A great deal of study has been completed into a variety of weighted residual criteria associated with FE discretisation techniques [107, 30]. This work has compared many such criteria, the most salient being collocation, least squares and Bubnov-Galerkin. It is well known that the Bubnov-Galerkin weighted residual approach is accepted as the optimum weighted residual method within the FE community [107, 71]. The fundamental reason being the self-adjoint nature of linear elastic, small strain problems, which is inherently satisfied by the Bubnov-Galerkin residual method.

For small strain problems involving associative, non-linear material behaviour, such as the elasto-plastic or elasto-visco-plastic deformation of metals with a von-Mises or Tresca yield criteria the problem can remain self-adjoint [70]. For this reason the Bubnov-Galerkin weighted residual FEM has generally been applied to these problems [65, 103, 109, 70].

At this point it is also interesting to note the equivalence of the sub-domain collocation, weighted residual, approach and the FVM from a mathematical description of the weighting functions. However, from a conceptual view point the FVM differs as it is developed directly from the principle of conservation over an elemental volume as opposed to an abstract mathematical technique [52, 107, 71]. This point will be described in detail in the following section, but it is immediately obvious from this equivalence of the FVM and the sub-domain collocation method that symmetry is no longer enforced with regard to the choice of weighting functions, thus providing an argument for the inferiority of the FVM when applied to self-adjoint problems [106, 71]. As the self-adjoint nature of the problem depends upon the type of material non-linearity encountered with a specific problem, part of the research described here, was to establish the effect of this possible asymmetry with reference to the FVM when applied to problems involving material non-linearity.

1.1.3 Boundary Element Methods (BEM)

The Boundary Element (BE) discretisation technique, in addition to the FEM, has also been employed in a wide variety of problems in CSM [11]. However, it is generally accepted that the BEM is more suitable to specific types of problems as described below, when compared to other discretisation techniques such as the FEM or the FVM.

The BEM is generally suitable for problems involving homogeneous and linear elastic materials, requiring a high accuracy of boundary stresses and a low ratio of boundary surface to volume with regard to problem geometry [11]. Alternatively, the FEM or potentially the FVM are more suitable for problems where the material is non-homogeneous and exhibits non-linear material behaviour, where boundary stresses are not of primary importance and where geometrically there exists a high ratio of boundary surface to volume [11]. As the object of this research is to model problems such as the shape-casting and quenching of metals, which exhibit material non-linearity and where, geometrically, there exists a high ratio of boundary surface to volume, the FVM presents itself, potentially, as a more suitable discretisation technique when compared to the BEM, for the applications studied in this research.

Though it is generally accepted that the BEM is not directly suitable for problems involving material non-linearity, Heinlein et al have successfully applied the BEM to the complete analysis of temperature fields and stresses during solidification processes [49]. Initially, this implementation was restricted to a one dimensional approach, but further work was suggested to extend the techniques to a two dimensional model.

Difficulties will arise in applying the BEM generally, as the method essentially involves the application of the analytically obtained fundamental solution as a weighting function in the formulation of the overall system of equations [104, 49]. Obviously, for non-linear problems involving two and three dimensions, the practicality of this method is severely limited.

In this research, it was not possible to compare and analyse the BEM in detail with other discretisation techniques, but in closure it should be noted that a number of researchers have investigated the coupling of the BEM with the FEM at an iterative level for problems involving material non-linearity [11]. Additionally, with particular regard to extrusion or forming processes, it is possible to adopt a staggered or stepped coupling approach where in this instance the momentum and constitutive equations are solved by different discretisation techniques, while the velocity field may be computed using the BEM, the stress field may be computed by the FEM or any other potentially suitable discretisation technique [78].

1.2 Finite Volume Methods

As originally stated by Hirsch [52], the FVM is the name given to the technique by which the integral formulation of the conservation laws are discretised directly in physical space. This definition illustrates the conceptual approach to a physical problem which is particular to the FV discretisation technique.

In the previous section, though the FVM was not explicitly described passing reference was made when necessary. From these references it should be noted that the FVM can be viewed in two ways, it may be considered a FDM associated with the conservation principle applied over a control volume or as the sub-domain collocation technique as developed from the standard FEM discretisation approach. As the importance and the application of the FVM has increased it has emerged as a discretisation technique in its own right, this emergence has been formally described by a number of authors Hirsch [52], Oñate et al [71, 54, 106] and Selim [84] to mention but a few.

In the following section the FV discretisation technique is examined in detail. The FVM has been developed recently, with regard to other discretisation techniques, and for some applications it is still under development as indicated by the research presented here. For these reasons the FVM is not yet as rigorously or formally defined as say the FEM. In this section a current overview of the FVM is provided, which attempts to expand on the naming conventions as used by many authors. The classification is independent of which particular field of continuum physics the FVM discretisation technique is applied to, though specific reference will be made to how the techniques have been applied within the fields of CSM or CFD when appropriate.

The FVM is generally divided under two headings, the cell-centred and the cell-vertex. It is possible to describe all cases of the FVM within either of these two categories. Firstly this section describes the cell-centred FVM, then secondly the cell-vertex FVM and finally concentrates specifically on the Control Volume – Unstructured Mesh (CV-UM) vertex based FVM [43, 42, 4], where comparisons are made with the Bubnov-Galerkin FEM.

1.2.1 Cell-centred FVM

The cell-centred FVM is traditionally associated with CFD discretisation techniques. In these cases suitable values of the dependent variable are stored at the cell centres, the control volume over which the conservation principle is applied is usually over the mesh cell and no overlapping of the control volumes can occur. A definition of the cell-centred FVM has been described by Hirsch [52], which simply states:

> When, for instance, the average value of the variable over the cell is associated with the central point of the cell, a *cell-centred* FVM is defined.

The implementation of a cell-centred FV discretisation technique on a two dimensional structured mesh is illustrated in Figure 1.1, where the control volume over a mesh cell $\overline{ABCD}$ is designated by $\Omega_{i,j}$. In this case a simple structure is illustrated by the orientation of the neighbouring control volumes, which for a simple two dimensional case involve the subscripts i and j for the rows and columns, respectively. The concept may be simply extended to three dimensions. Additionally, more complex structured meshes are possible employing variable cell sizes and, alternatively, curvilinear coordinate systems. However, the topology remains consistent throughout the mesh and generally structured meshes are employed.

Over the last few years a considerable amount of research has been performed by Hattel et al [48, 47, 46] to model thermo-mechanical effects in casting processes using the cell-

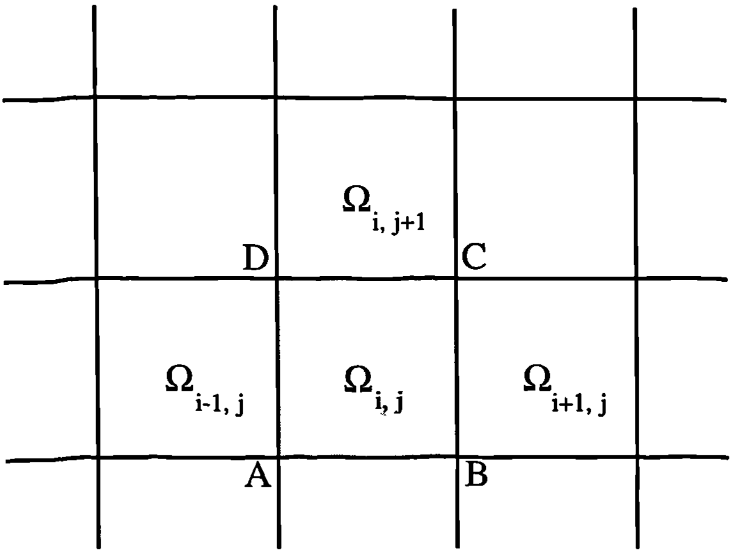

Figure 1.1: Cell-centred FVM applied to a structured mesh

centred FVM. When employing a cell-centred technique a decoupling phenomenum can occur between the displacement and stress fields. A more detailed discussion of this phenomenum is provided in Chapter 3. However, a brief outline of the techniques employed to address this problem is included here. In this particular cell-centred approach a novel technique is utilised to overcome this problem, where a collection of staggered grids, and hence control volumes over which the conservation principle is applied, are associated with each dependent variable, in this case displacement components [48, 47, 46]. Though this technique is commonly incorporated in the field of CFD [74, 19] it is new to the field of CSM. This research has had initial success in stress analysis involving thermal and mechanical loading conditions, but is so far limited to linear elastic material behaviour on structured meshes [48, 47, 46].

Additionally, Ivankovic et al have modelled the thermo-mechanical effects associated with the Rapid Crack Propagation (RCP) in polymer pipes using a cell-centred FVM. This implementation does not utilise a staggered approach as described above and stores all variables at the cell centres. A higher order term is included in the displacement gradient approximation, which requires next nearest neighbour information [31, 55, 35]. However, this higher order scheme will suffer from the usual difficulties when applied to an unstructured mesh. The implementation has included non-linear material effects, but is again restricted to a structured mesh [31, 55, 35].

A further difficulty which arises when using a cell-centred scheme is obtaining the required accuracy of the variables, such as displacement or stress, at the boundary of the problem domain. This requires suitably accurate interpolation and extrapolation of the variable from the cell faces to the cell centres and vice versa [46, 31]. A more detailed discussion of these problems is provided in Chapter 3.

At present, the cell-centred FV technique as described above has been mainly applied to a structured mesh, but recently the technique has been extended to unstructured meshes for CFD applications. These applications include thermally convective and conductive solidification processes by Chow et al [20, 22] and complex swirling flows by Croft et al [24]. The technique has also been extended to unstructured meshes for CSM applications, these include linear elastic thermo-mechanical behaviour by Demirdzic et al [32].

An example of the cell-centred FVM applied to a two dimensional unstructured mesh is illustrated in Figure 1.2(a). The control volume Ω_1 is described over the mesh cell $\overline{ABC}$ and similarly the control volume Ω_2 is described over the mesh cell $\overline{ACDE}$. The concept may again be simply extended to three dimensions, but is described here in two dimensions for simplicity. From the numbering of the surrounding control volumes it is self evident that there is no orientation or structure to the mesh as previously described.

1.2.2 Cell-vertex FVM

The cell-vertex FVM describes techniques as originally applied to unstructured meshes, where variables are typically stored at the vertices of the mesh cell and the control volume over which the principle of conservation is applied is vertex based and may include a variety of contributions from surrounding mesh elements. A variety of cell-vertex techniques as described by Hirsch [52] may be utilised so long as they meet the defined criterion:

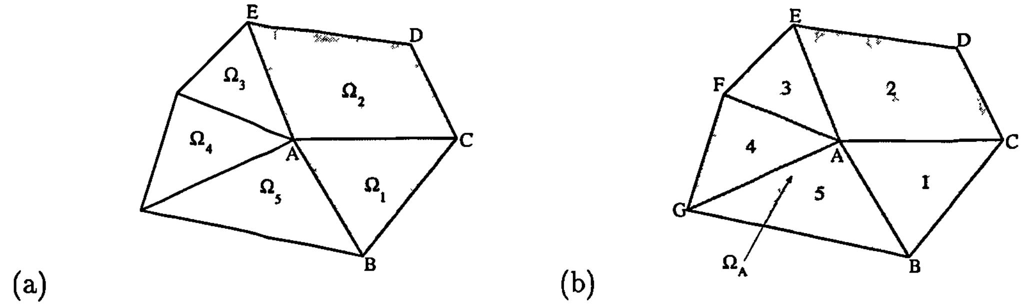

Figure 1.2: FVM applied to an unstructured mesh. (a) Cell-centred and (b) Cell-vertex.

> When the variables are attached to the mesh points, that is, to the cell vertices, a *cell-vertex* FVM is defined.

An illustrative example of the cell-vertex FVM applied to a two dimensional unstructured mesh is given by Figure 1.2(b). The control volume Ω_A is based around the vertex at point A and includes contributions from the five surrounding mesh cells. The complete control volume over which the conservation principle is applied is described by the polygon $\overline{BCDEFG}$.

This method has been extensively applied in the field of CFD for a variety of problems as described earlier *in the previous section under the heading of control-volume finite-element* methods, and has been rigorously compared with traditional FEM discretisation techniques with regard to order of accuracy for standard CFD problems [69]. Additionally, Chow et al have compared a cell-vertex and a cell-centred FVM when applied to thermally conductive solidification processes [20, 22].

In closure of this sub-section it should be noted that a number of researchers have described various implementations of the cell-vertex FVM on a structured mesh for CFD applications. These include a general overview of current techniques by Hirsch [52], and specific techniques described by Denton [33] and McDonald [66].

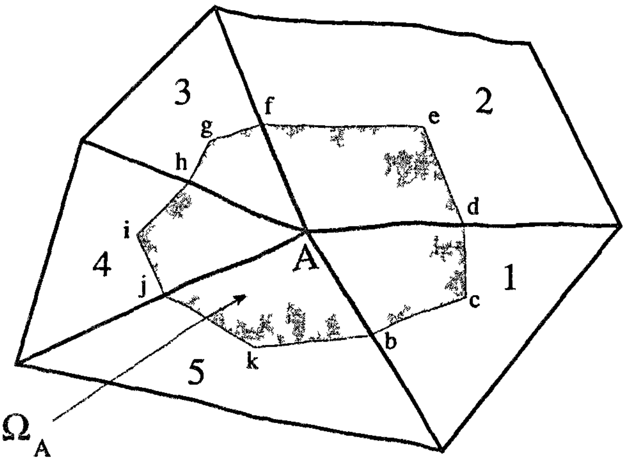

Figure 1.3: CV-UM vertex based FVM applied to an unstructured mesh

More recently, the cell-vertex method has been applied to problems concerning CSM. The previous work upon which the present research is based involved a CV-UM vertex based FVM in the analysis of two and three dimensional linear elastic problems [43, 42, 4]. Also, Oñate et al have broadly investigated the accuracy of the cell-vertex FVM when compared against the Bubnov-Galerkin FEM for standard CSM problems in one and two dimensions, again involving linear elastic material behaviour [71, 106]. The conclusions of these comparisons are discussed in the following section.

1.2.3 Control Volume-Unstructured Mesh vertex based FVM

At this point, the CV-UM vertex based FVM is introduced, with reference to the specific characteristics of the method within the cell-vertex category. Then the method is compared with the standard Bubnov-Galerkin FEM to identify the fundamental differences of the two discretisation techniques.

A comprehensive definition of the above two categories of the FVM has been compiled by Hirsch [52]. In this definition, the CV-UM vertex based FVM is described as being a particular case of the cell-vertex FVM. Other authors such as Oñate et al [71, 106] and Selim [84] describe this particular FVM separately from the general cell-vertex method, thus proposing a third category where the dependent variable is located at the vertices and the control volumes are centred around the vertices, but the control volumes do not overlap.

This suggests that the CV-UM vertex based FVM is unique from cell-vertex methods as it does not allow overlapping control volumes, where as cell-vertex methods always have overlapping control volumes over which the conservation principle is applied. Examples of overlapping control volumes with regard to cell-vertex schemes have been described by Oñate et al [71, 106] in the context of CSM and Hirsch [52] in the context of CFD.

In this research, the CV-UM vertex based scheme is regarded as a particular case of the cell-vertex FVM. This may be justified by the fact that all the key attributes of the scheme satisfy the above description, as originally defined by Hirsch [52], for the cell-vertex FVM.

The CV-UM vertex based FVM is illustrated in Figure 1.3 with regard to a two dimensional mesh for simplicity, though the concept will apply generally to a three dimensional unstructured mesh. The complete control volume over which the conservation principle is applied is circumscribed by the polygon $\overline{bcdefghijk}$. The polygon is defined by the midpoints of the mesh cell sides b, d, f, h, j and the centres of the mesh cells c, e, g, i, k. The control volume is based around a vertex or node, in this case A, and has contributions from the five surrounding elements.

When comparing the FV discretisation technique with the Bubnov-Galerkin FE technique, it is possible to illustrate the fundamental differences between the two techniques by describing each technique with regard to the associated weighting function W.

The weighting functions for a cell-vertex FVM, a Bubnov-Galerkin FEM and a CV-UM vertex based FVM are illustrated in Figure 1.4. The two dimensional mesh in the $x - y$ plane is drawn inclined to the plane of the page to illustrate in three dimensions the variation

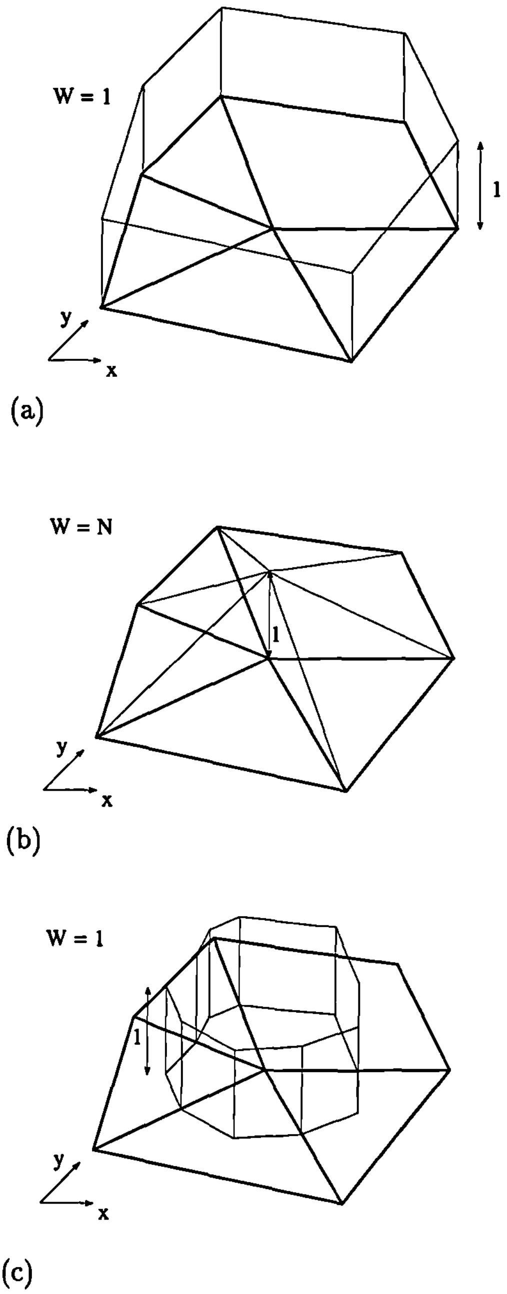

Figure 1.4: Weighting function W. (a) Cell-vertex FVM and (b) Bubnov-Galerkin FEM and (c) CV-UM vertex based FVM.

of the weighting functions over the mesh.

From the description of the weighting functions as utilised in the FV techniques illustrated in Figure 1.4(a) and Figure 1.4(c), the essential equivalence of the sub-domain collocation technique as derived from FE theory and the FV technique is now clearly apparent. This equivalence was initially mentioned in the previous section and has been noted by a number of authors [52, 71]. It should be noted that the existence of a number of possible alternatives for the FVM as described in this section, warrants an independent analysis of the FVM as a discretisation technique in its own right.

Oñate et al have originally analysed the techniques described in Figure 1.4 for one and two dimensional linear elastic problems. In the results they presented, the CV-UM vertex based FVM was described as a 'cell-centred' FVM, this description can be misleading as the term cell-centred FVM generally refers to the other category of the FVM, where variables are stored at the centre of the mesh cells, as defined above by Hirsch [52]. To avoid confusion, the 'cell-centred' FVM technique as described by Oñate et al will be referred to as a CV-UM vertex based scheme in this discussion, as the two techniques are exactly the same [71, 106].

The results presented by Oñate et al [71] indicate the superiority of the CV-UM vertex based FVM described in Figure 1.4(c) to the cell-vertex FVM as described in Figure 1.4(a). Also, the complete equivalence of the CV-UM vertex based FVM and the Bubnov-Galerkin FEM for one dimensional problems and two dimensional problems involving linear Constant Strain Triangular (CST) elements, in static elastic analysis is indicated. For higher order elements in two dimensions such as Bilinear Quadrilateral (BLQ) elements, the CV-UM vertex based FVM and the Bubnov-Galerkin FEM are not exactly equivalent, but this inequality is within an acceptable numerical tolerance and does not immediately indicate the superiority or inferiority of one method compared to the other [71].

For the cell-vertex FVM and the Bubnov-Galerkin FEM techniques as described in Figure 1.4(a) and Figure 1.4(b), respectively, the overlapping of the control volumes based around the vertices of the mesh is indicated. There are no overlapping control volumes in the CV-UM vertex based FVM and the prescribed control volumes obviously enforce conservation at a more local level than the other two methods, as illustrated in Figure 1.4(c). From this conceptual viewpoint it is possible to interpret the greater accuracy of the CV-UM vertex based FVM when compared against alternative cell-vertex FVM.

Fryer et al [43, 42] have compared the two methods for a number of standard two dimensional linear elastic problems with a variety of thermal and mechanical loading conditions on meshes consisting of BLQ elements. From these results the equivalence of the CV-UM vertex based FVM and the Bubnov-Galerkin FEM with regard to solution accuracy is indicated.

Bailey and Cross [4] have extended this work to three dimensions and have compared the two methods when applied to linear elastic problems involving thermal and mechanical load conditions on meshes consisting of Trilinear Hexahedral (TLH) elements. Again, the equivalence of the two techniques with regard to solution accuracy is indicated.

1.3 Overview of the thesis

In this section a brief overview of the remaining thesis is given. From this outline a general understanding of the direction and content of the research undertaken in this project is available.

In Chapter two, material non-linearity is described generally within the context of solid mechanics. The background theory to an elasto-visco-plastic constitutive relationship is presented, followed by a specific description of the Perzyna model as utilised in the research presented here.

In Chapter three, the governing and constitutive equations associated with material non-linearity are described, with specific regard to the elasto-visco-plastic constitutive relationship as described by the Perzyna model. The equations will then be discretised using the CV-UM vertex based FVM, and compared to a standard Bubnov-Galerkin FEM. Additionally, the possible iterative techniques available for the solution of the non-linear problem are discussed. The techniques are described as possible algorithms within a FORTRAN 77 software framework.

In Chapter four, the CV-UM vertex based FVM is theoretically analysed and compared with the Bubnov-Galerkin FEM. The direct equivalences and the basic differences of the two techniques are described and discussed at an elemental level, in two and three dimensions.

In Chapter five, the discretisation and solution techniques described in chapter three are applied to a variety of non-linear material problems in the field of CSM. These applications include a simple uniaxial problem involving strain hardening, for which an analytical solution is available. Then a pressurized thick cylinder exhibiting an ideal plastic behaviour is modelled with a plane strain approximation assumed, a reference solution is available. A perforated tensile strip with strain hardening is also modelled with a plane stress approximation, for which experimental results are available. Finally, a fully three dimensional analysis of a hollow spherical vessel undergoing internal pressure is performed, an analytical solution is available.

In Chapter six, a general discussion of the coupling of heat transfer and non-linear solid mechanical problems is presented, with reference to the merits of a variety of coupling techniques. A specific treatment of coupled problems within a FV framework will be described, as implemented and utilised in the modelling of an infinite steel plate in two and three dimensions. The implementation of constraint boundary conditions as required for this problem is also described. Finally an infinite steel slab undergoing solidification by heat conduction only is modelled. Classical analytical solutions to these thermo-mechanical problems are available from Weiner and Boley [98], who used the well known thermal analysis of Carlsaw and Jaeger [17].

In Chapter seven, the main physical processes associated with the shape-casting of metals are described. A complete description of the modelling approach will be given. Including a discussion of the required internal and external boundary conditions. Realistic, complex geometries will be modelled in three dimensions, including a 3D test bar problem.

In Chapter eight, the conclusions and suggestions for future work relating to the research presented in this thesis will be given.

Chapter 2

Material Non-linearity

In this chapter an overview of material non-linearity with regard to solid mechanics is presented. Initially, a general description of the constitutive relationships associated with material non-linearity in solid mechanics is presented. Then a brief description of the most common cases of material non-linearity is given, with specific material examples included where appropriate. This description will involve a comparison of rate dependent and rate independent material non-linearity. The concept of a yield surface will be introduced and a number of examples will be described with regard to their applicability to particular classes of material. Finally, a detailed description of the well known Perzyna model as utilised in this research to describe an elasto-visco-plastic constitutive relationship is presented.

2.1 Classification of Material Non-linearity

Material non-linearities occur in solid mechanics when the relationship between stress and strain, otherwise known as the constitutive relationship of the material, is no longer linear. The direct proportionality of stress and strain can no longer be assumed, as it is in the simple linear elastic case.

The constitutive relationship may now be a function of the combined or individual stress, strain or strain rate and may also be path dependent with regard to the load history. The variation of the constitutive relationship also causes the stiffness of the structure or component consisting of the non-linear material to vary also. Thus the stiffness of the structure or component may vary as a function of the combined or individual load level and load history [51].

To describe a particular case of non-linear material behaviour in solid mechanics a suitable model must be adopted. Non-linear material models describe the macroscopic behaviour of the material, hence they are approximations to the real behaviour of the material as the real behaviour is also related to micro-mechanical effects within the material. For example, the plastic behaviour of metals is related to dislocations and slip planes within the crystal lattice [50, 59, 34]. These defects are assumed to be randomly distributed throughout the material such that a degree of homogeneity can be assumed by the model at a macroscopic level. This allows a uniform macroscopic approximation of the discrete microscopic behaviour of the material over a suitably large volume [50].

It is possible to classify non-linear material behaviour in solid mechanics into two categories, rate independent and rate dependent [51]. Some of the most important cases are described for each category in the following sub-sections.

2.1.1 Rate Independent Material Non-linearity

The cases of material non-linearity described under this category are assumed to be independent of time. This is an immediate approximation as all materials are dependent to some degree upon the rate at which the load is applied [105]. The rate dependence for some materials under specific loading conditions is such that it can be neglected, without reasonable loss of accuracy.

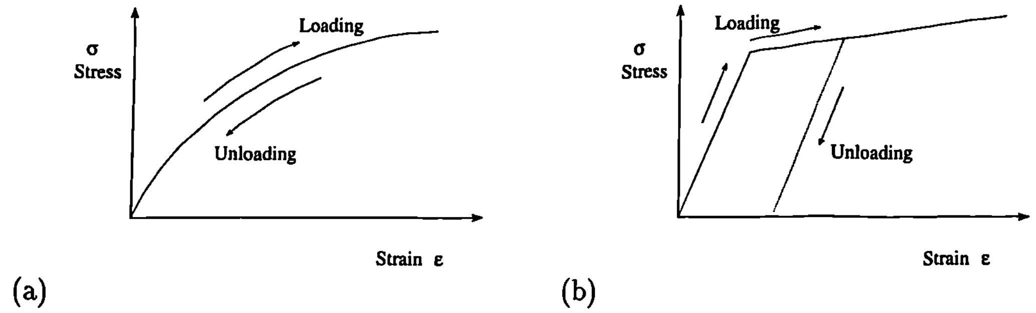

Figure 2.1: Non-linear stress-strain relationships. (a) Non-linear elasticity and (b) elasto-plasticity.

2.1.1.1 Non-linear Elasticity

A case of material non-linearity in solid mechanics for which rate independence is assumed is non-linear elastic behaviour, where the stress is not linearly related to the strain. In this case the deformation is recoverable and no energy is lost from the system. A particular case is the hyper-elastic behaviour of materials such as rubber, where the stresses are a function of a strain dependent constitutive relationship [108, 72]. A simple non-linear elastic relationship is illustrated in Figure 2.1(a), which indicates the conservative nature of the non-linear stress-strain relationship, as it follows the same path through loading and unloading.

2.1.1.2 Plasticity

Another case of material non-linearity which can be assumed to be rate independent for particular materials under specific conditions is plasticity. Plasticity describes non-linear material behaviour where the material deforms permanently due to the application of a loading condition. Some materials exhibit rigid-plastic or to be more specific almost rigid-plastic behaviour when large deformations occur, where the elastic strains are negligible when compared to the plastic strains [56]. Most engineering materials in solid mechanics exhibit elasto-plastic behaviour, in either case a transition to plastic behaviour must occur at some point. This transition occurs when the stress level in the loaded structure or

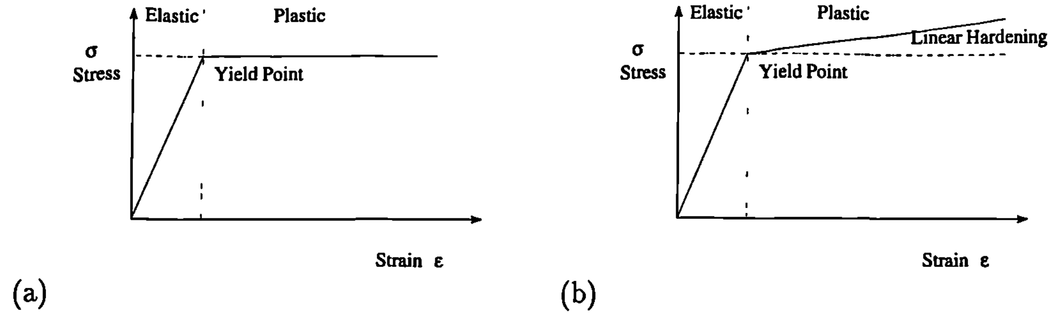

Figure 2.2: Plastic material behaviour. (a) Elastic, perfectly plastic and (b) elastic, linear work-hardening.

component exceeds the yield point stress level [72, 51]. A detailed description of yield criteria for particular classes of material will be presented in the next section.

For an elasto-plastic case the material behaves elastically below the yield point and any straining which occurs is recoverable. Typical elasto-plastic stress-strain relationships are illustrated in Figure 2.2(a) for an elastic, perfectly plastic material and in Figure 2.2(b) for an elastic, linear work-hardening material [59, 34]. Work-hardening or equivalently strain-hardening will be described in more detail in the following section.

As plastic strains are not recoverable and a problem exhibiting plastic strains is non-conservative, the problem is path dependent and the solution relies upon the load history of the problem. This is analogous to the laws governing reversible processes in classical thermodynamics, where a process is irreversible if it exhibits hysteresis [2]. This is the case for an elasto-plastic problem. When a load is applied which raises the stress level beyond the yield condition, and causes plastic deformation an initial path is followed, but when the load condition is reversed an alternative path is followed. This behaviour is illustrated in Figure 2.1(b) for an elastic, linear work-hardening material. The problem is initially loaded elastically until the yield point is reached and then deforms plastically. When the problem is unloaded it returns elastically to a permanently deformed state [108]. The problem is non-conservative as the plastic strains are associated with heat generation, for a complete thermo-mechanical analysis the heat loss must be included as a source term in the thermal analysis, which will satisfy conservation of energy. However, in many cases the total strains are small, much less than 1%, so the heat loss can be neglected in the thermal analysis without any significant loss of accuracy [27, 49].

2.1.2 Rate Dependent Material Non-linearity

The cases of material non-linearity described in this category are time-dependent. This is true for a large number of materials under specific conditions, where the rate dependency of the material can no longer be neglected. An example is the behaviour of metals at elevated temperatures [34].

2.1.2.1 Visco-elasticity

An example of material non-linearity in continuum mechanics for which rate dependence is evident is visco-elastic behaviour. This behaviour is evident in materials undergoing forming processes, where the material has a tendency to recoil over time after a deformation has been imposed. The material is associated with a shape memory, which consists of the full history of the viscous strain development. Some materials exhibit what is described as a fading shape memory when the deformation is imposed over longer periods of time. This causes the tendency to recoil to diminish resulting in permanent deformation [78].

There are a variety of forming or processing situations in which visco-elastic effects have to be modelled. Examples are flowing material processes which include polymer extrusion and melt fibre drawing [78], in these examples only the viscous terms are modelled. The inertial effects have been neglected, as a very low Reynolds number ($Re << 1$) is associated with the flowing material. When modelling material flows with a higher Reynolds number inertial terms can no longer be neglected and are included in the governing equations. Darwish et al have applied a cell-centred FVM discretization technique on staggered grids to problems involving such flows [28]. A full discussion of visco-elastic behaviour and the associated constitutive relationships is not presented in this thesis, only a brief reference is made in the context of rate dependent, elastic, material behaviour and the finite volume method. However, complete descriptions are available in the following references [108, 72].

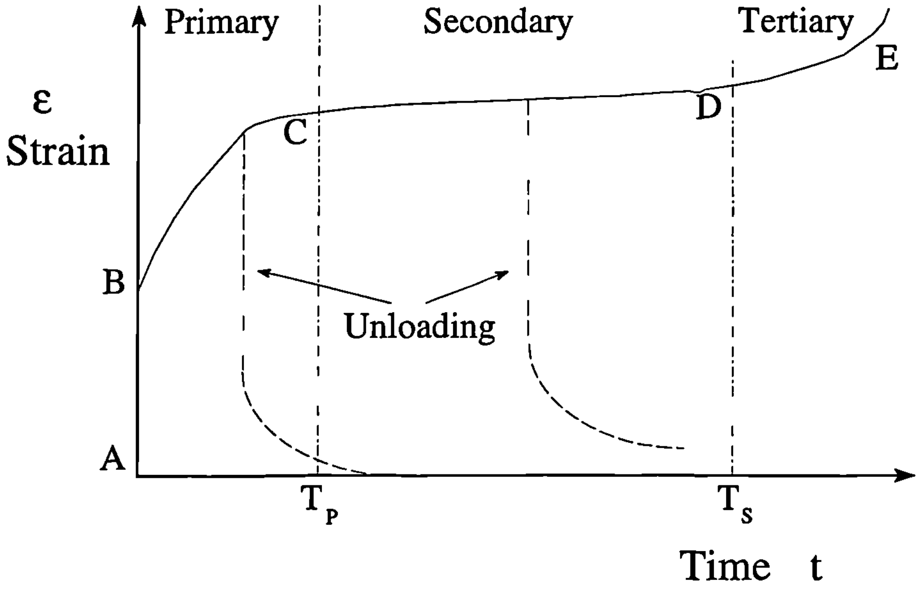

Figure 2.3: Uniaxial strain–time curve at constant stress.

2.1.2.2 Visco-plasticity

Another example of material non-linearity which includes rate dependence is visco-plastic behaviour. This behaviour always results in a permanent deformation of the material and possesses the yield criterion as described for rate independent plasticity [72, 108]. Materials exhibiting visco-plastic behaviour are assumed to be rate independent below the yield point and rate dependent when the yield point is exceeded [72, 108, 51]. In the research presented here visco-plastic behaviour is described using the Perzyna model, which will be discussed in detail in the final section of this chapter.

2.1.2.3 Creep and Stress Relaxation

Another example of material non-linearity which includes rate dependence is the phenomenon of creep. This is simply described by the strain–time relationship at constant stress as illustrated in Figure 2.3 [72, 73]. The creep strain develops after an instantaneous elastic deformation along the line $\overline{AB}$. Initially, a primary creep condition occurs during which time the strain rate is decelerating. This is a relatively short lived condition and is described by the curve $\overline{BC}$. If during this period of time the material is unloaded complete recovery will occur via an instantaneous elastic recovery, followed by a visco-elastic recovery. As indicated by the dashed unloading curve in the primary region. When the load is applied beyond the primary creep region ie. longer than time T_p, then a secondary creep condition occurs which has a constant strain rate associated with it as indicated by the line $\overline{CD}$. If the material is unloaded in this region a permanent deformation or visco-plastic effect is also included as illustrated by the dashed unloading curve in the secondary region. Finally, a tertiary creep condition occurs after time T_S, this is again a relatively short lived condition during which time the strain rate accelerates as indicated by the curve $\overline{DE}$. This condition eventually results in the failure of the material at point E on the curve. For these reasons the tertiary creep condition is usually of less interest than the primary or secondary conditions in the modelling of deformation. Nearly all materials exhibit creep to some degree, a particular case when creep phenomena cannot be neglected is metals at high temperatures, typically over 50% of their melting temperature [34].

Another rate dependent phenomenon that is associated with creep is stress relaxation. This occurs when a constant stress is applied to a material over a period of time during which the material can no longer deform and the internal stresses decrease [34].

From this description of rate dependent material non-linearity, the equivalence of secondary creep when permanent deformation occurs and visco-plasticity is indicated. This is further illustrated by reference to the theory behind the models governing creep in metals. Where the equivalence of an associated form of visco-plasticity using the von-Mises yield criterion and the widely used Norton-Soderberg creep law for metals can be derived analytically [108, 72]. From the illustrated equivalence of the two phenomena on a macroscopic scale, the similarity of the micro-mechanical behaviour governing rate dependent plasticity and creep is indicated. This is generally accepted, as experimentally it is very difficult to distinguish between the two phenomena and this has instigated the development of unified models which offer smooth transitions between different material behaviour [105, 51]. The unified modelling approach will be discussed in more detail at the end of this chapter.

2.2 Mathematical Theory of Plasticity

In this section a brief theoretical description of materials which exhibit plasticity is presented, with particular regard to metals. The nature of yield criteria will be discussed with attention focused on the von-Mises yield criterion. Finally the phenomenon of work-hardening will be described. This section provides the basic rate independent plasticity theory required for a description of the elasto-visco-plastic constitutive relationship as described using the Perzyna model in the final section of this chapter.

2.2.1 Overview of Yield Criteria

When considering the phenomena of plasticity and the associated yield criterion, the nature of the material under consideration is very important. For example, experimental tests in tension, compression and torsion on a number of metals including copper and steel have indicated that hydrostatic pressure has negligible effect on the yield point and flow stress level [59]. This is not the case when considering other classes of materials such as ceramics. For these classes of materials the yield point and flow stress level are generally dependent upon the hydrostatic pressure. For example, experimental tests in compression and tension on sandstone and marble under hydrostatic pressure indicated that materials which are brittle at atmospheric pressures deformed in a manner typical of ductile materials at high pressures [59]. Thus, when considering metals which are ductile independently of the hydrostatic pressure and hence the volumetric component of stress the yield criterion should be a function of the stress component associated with a change of shape only [50, 72, 34].

Another important consideration of the material with regard to the yield criterion is isotropy. If the material is isotropic then the yield criterion should be independent of the orientation of the coordinate system employed. Thus, the yield criterion should be an invariant function of the components of stress in the coordinate system [50, 72, 34].

There is no theoretical method of deriving a relationship between the stress components in order to correlate yielding for a three dimensional state of stress with yielding in a uniaxial test. At present yielding criteria are essentially empirical relationships. However, a yield criterion must agree with the material behaviour as observed experimentally [50, 34].

At present there are two established yield criteria for isotropic ductile metals. These are the von-Mises and Tresca yield criteria [50, 34]. These two criteria have been widely applied to problems involving metals. For most metals the von-Mises criterion is in better agreement with experimental data than the Tresca criterion [50, 72]. For this reason the von-Mises yield criterion is utilised in this research, though the techniques will apply generally to any suitable yield criterion. The von-Mises yield criterion is described in detail in the following section.

2.2.2 The von-Mises Yield Criterion

Initially, some basic concepts from the mathematical theory of plasticity as required for the definition of the yield criterion will be defined and finally the yield criterion will be defined with regard to these concepts. When describing the von-Mises yield criterion it is useful to consider a general three dimensional stress state σ_{ij} at a point in static equilibrium as described using the following Cartesian tensor notation:

$$\sigma_{ij} = \begin{pmatrix} \sigma_{xx} & \sigma_{xy} & \sigma_{xz} \\ \sigma_{yx} & \sigma_{yy} & \sigma_{yz} \\ \sigma_{zx} & \sigma_{zy} & \sigma_{zz} \end{pmatrix}. \tag{2.1}$$

In the mathematical theory of plasticity it is meaningful to consider direct stress relative to the mean direct stress

$$\overline{\sigma} = \frac{\sigma_{xx} + \sigma_{yy} + \sigma_{zz}}{3} = \frac{\sigma ii}{3}. \tag{2.2}$$

The mean direct stress can be regarded as a hydrostatic stress which acts equally in all directions and is therefore related to volumetric changes only [34, 38].

This allows the stress to be decomposed into a deviatoric stress s_{ij} and a volumetric stress $\delta_{ij}\overline{\sigma}$, utilizing the standard Kronecker delta δ_{ij} as defined in Appendix A, such that

$$\sigma_{ij} = s_{ij} + \delta_{ij}\overline{\sigma}. \tag{2.3}$$

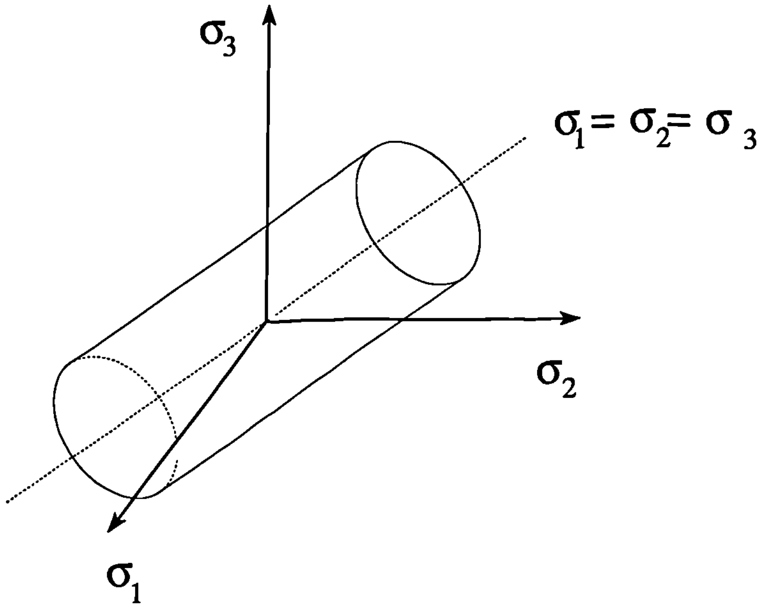

Figure 2.4: Yield surface in principal stress space.

The normal stress relative to the mean normal stress is then described by the deviatoric stress

$$\begin{aligned} s_{ij} &= \sigma_{ij} - \delta_{ij}\overline{\sigma}, \\ s_{ij} &= \begin{pmatrix} \sigma_{xx} - \overline{\sigma} & \sigma_{xy} & \sigma_{xz} \\ \sigma_{yx} & \sigma_{yy} - \overline{\sigma} & \sigma_{yz} \\ \sigma_{zx} & \sigma_{zy} & \sigma_{zz} - \overline{\sigma} \end{pmatrix}, \end{aligned} \tag{2.4}$$

which is associated with a change of shape only. As described earlier, most metals can be considered to be independent of hydrostatic pressure with regard to the yield point. Thus the yield criterion can be assumed to be dependent on the deviatoric stress only [50, 72, 34].

Any three dimensional stress state as described by the symmetrical tensors in equations (2.1) or (2.4) can be resolved quite simply to three principal stresses acting at a point [34, 38]. The principal stresses are the three roots of the cubic characteristic polynomial obtained during the resolution. The coefficients of the characteristic polynomial are invariant functions and may be expressed in terms of the stress state [38].

Thus it is possible to define the von-Mises yield criterion for isotropic metals as follows. When the second invariant of the deviatoric stress tensor J_2 reaches a critical value yielding occurs. From the considerations of this theory for uniaxial tension it is possible to define the von-Mises yield criterion in terms of the effective stress [72, 34]

$$\begin{aligned} \sigma_{eff} &= \sqrt{3}\{J_2\}^{\frac{1}{2}}, \\ \sigma_{eff} &= \sqrt{3}\{\frac{1}{2}s_{ij}s_{ij}\}^{\frac{1}{2}}. \end{aligned} \tag{2.5}$$

The yield criterion can now be defined as the point when the effective stress reaches a critical value Y. The critical value is obtained by experimental tests in uniaxial tension on the specific material. Hence, a yield function F can now be defined for the von-Mises yield criterion as follows:

$$F = \sigma_{eff} - Y. \tag{2.6}$$

The von-Mises yield criterion can be illustrated graphically when equation (2.5) is plotted in relation to the three dimensional space defined by the principal stresses. This results in a cylindrical surface of radius $Y\sqrt{2/3}$ aligned along the axis as illustrated in Figure 2.4. The axis of the cylinder is the hydrostatic component of the stress and any stress state that exists inside the cylinder remains elastic [34, 72, 50].

A number of physical interpretations have been suggested for the criterion, which was originally proposed by von-Mises in 1913 because of its mathematical simplicity. The earliest is that proposed by Hencky in 1924 which implies that yielding begins when the recoverable elastic energy of distortion reaches a critical value. The distortion energy is that part of total strain energy per unit volume which is associated with a change of shape as opposed to a change in volume [34]. A complete description of the physical interpretations available for the von-Mises criterion is available in the standard texts [50, 34, 72].

2.2.3 Strain-hardening of Materials

An important factor governing the plastic behaviour of a material is the phenomenon of strain-hardening. Also referred to as work-hardening in the associated literature [59]. In simple terms, the phenomenon occurs during the plastic deformation of metals at a micro-mechanical level due to the generation and the changing interaction between dislocations as the degree of deformation increases. Basically, the larger the number of dislocations produced, the larger their interaction and hence the larger the stresses required for the yielding of the metal [50]. Temperature is an important consideration when describing strain-hardening.

Conventionally, materials which become permanently harder during a tensile test at room temperature are said to be cold-worked. This is true for most metals though a few metals such as lead, tin and cadmium only strain-harden permanently below room temperature. If the latter metals are left at room temperature they soften over a period of time, or in other words they self-anneal [59].

When a tensile test has been performed on metals at elevated temperatures, which is conventionally referred to as hot-working, it is experimentally shown that at critical temperatures the hardening phenomenon ceases[59]. This can be attributed to the softening or strain-hardening removal processes such as recrystallization which are thermally activated and cancel out the strain-hardening process [59].

Strain-hardening will be considered in a number of solid mechanics problems in the following chapters. The simplest case is linear strain-hardening, which is actually a reasonable approximation for the cold-working of a number of metals such as the Aluminium alloy 57S [91].

Considering the uniaxial case of linear strain-hardening as described in Figure 2.2(b). It is possible to associate the gradient in the elastic region with the standard Youngs modulus E and the gradient in the plastic region with the elastic/plastic modulus H. From these moduli and the initial yield stress Y_0, it is possible to derive a linear relationship between the yield stress $Y(\epsilon_p)$ and the plastic strain ϵ_p of the form

$$Y(\epsilon_p) = Y_0 + \beta\epsilon_p \tag{2.7}$$

where the hardening function β can be algebraically derived [72, 59] as a function of the elastic and elastic/plastic moduli as follows:

$$\beta = \frac{H}{1 - H/E}. \tag{2.8}$$

It should be noted that the same relationships for the effective stress and effective strains can be obtained directly from the uniaxial experimental data [91, 72], hence enabling the relationships to be applied generally in two and three dimensions.

2.3 Elasto-visco-plasticity

In this section an elasto-visco-plastic constitutive relationship is described using the standard theory of elasticity and the Perzyna model. First, the basic linear elastic constitutive relationship is stated and the associated material properties are described. Then the Perzyna model is described and the constitutive relationship is extended to include visco-plastic and thermal effects. The description will be limited to an associated case with a von-Mises yield criterion. The applicability of the constitutive relationship to a variety of problems involving metals will be indicated.

2.3.1 Linear Elasticity

In this section the linear elastic constitutive relationship is described for a three dimensional cartesian coordinate system. The relationships for the two dimensional plane stress, plane strain and axisymmetric approximations are described as required in the remaining thesis, but the theoretical approach applies generally.

The stress state at a point was defined in equation (2.1). The strain state associated with a stress state at a point is now defined. The strain state at a point is dependent upon the variation of the displacement with regards to the x, y and z coordinates. The displacement at a point can be defined by the three displacement components u, v and w in the x, y and z coordinates, respectively. For infinitesimal strain problems, with strains typically less than 1%, the displacement variation can be assumed to be linear [38].

For metals exhibiting non-linear material behaviour with a limited amount of deformation an infinitesimal strain approximation is possible [103, 105]. In a number of metal forming processes such as rolling and stamping large deformations can occur and a small strain approximation is not suitable. Problems involving large deformations are not considered in this research, though it should be noted that the numerical approach can apply generally to such cases.

2.3.1.1 Tensor Definition

When defining the state of strain at a point it is meaningful to define the strain tensor in terms of the deformation (or displacement) tensor [59, 34]

$$e_{ij} = \begin{pmatrix} e_{xx} & e_{xy} & e_{xz} \\ e_{yx} & e_{yy} & e_{yz} \\ e_{zx} & e_{zy} & e_{zz} \end{pmatrix} = \begin{pmatrix} \frac{\partial u}{\partial x} & \frac{\partial u}{\partial y} & \frac{\partial u}{\partial z} \\ \frac{\partial v}{\partial x} & \frac{\partial v}{\partial y} & \frac{\partial v}{\partial z} \\ \frac{\partial w}{\partial x} & \frac{\partial w}{\partial y} & \frac{\partial w}{\partial z} \end{pmatrix}. \tag{2.9}$$

In general the deformation tensor is composed of a strain tensor and a rotation tensor as follows [59, 34]:

$$\begin{aligned} e_{ij} &= \epsilon_{ij} + w_{ij}, \\ e_{ij} &= \frac{1}{2}(e_{ij} + e_{ij}) + \frac{1}{2}(e_{ij} - e_{ij}). \end{aligned} \tag{2.10}$$

Thus from the tensor description the strain is a symmetric second rank tensor of the following form:

$$\epsilon_{ij} = \begin{pmatrix} \epsilon_{xx} & \epsilon_{xy} & \epsilon_{xz} \\ \epsilon_{yx} & \epsilon_{yy} & \epsilon_{yz} \\ \epsilon_{zx} & \epsilon_{zy} & \epsilon_{zz} \end{pmatrix} = \begin{pmatrix} \frac{\partial u}{\partial x} & \frac{1}{2}\left(\frac{\partial u}{\partial y} + \frac{\partial v}{\partial x}\right) & \frac{1}{2}\left(\frac{\partial u}{\partial z} + \frac{\partial w}{\partial x}\right) \\ \frac{1}{2}\left(\frac{\partial v}{\partial x} + \frac{\partial u}{\partial y}\right) & \frac{\partial v}{\partial y} & \frac{1}{2}\left(\frac{\partial v}{\partial z} + \frac{\partial w}{\partial y}\right) \\ \frac{1}{2}\left(\frac{\partial w}{\partial x} + \frac{\partial u}{\partial z}\right) & \frac{1}{2}\left(\frac{\partial w}{\partial y} + \frac{\partial v}{\partial z}\right) & \frac{\partial w}{\partial z} \end{pmatrix}. \tag{2.11}$$

The strain tensor defined in equation (2.11) is of the same form as the stress tensor defined in equation (2.1). Therefore, as described by equations (2.2), (2.3) and (2.4) for stress the strain tensor can also be decomposed into a volumetric component, dilation, and a component associated with a change of shape. Also a similar triaxial state of strain can be described in terms of the principal strains, thus allowing allowing an effective strain to be defined. This is particularly useful in strain hardening as described in the previous section, when an effective plastic strain ϵ^p_{eff} is often required and can be defined in terms of the invariant of the strain tensor as follows [72, 34]:

$$\epsilon^p_{eff} = \sqrt{\frac{2}{3}}\{\epsilon^p_{ij}\epsilon^p_{ij}\}^{\frac{1}{2}}. \tag{2.12}$$

The strain tensor component of the deformation tensor is associated constitutively with the stress tensor as follows:

$$\sigma_{ij} = C_{ijkl}\epsilon_{kl} \tag{2.13}$$

where C_{ijkl} is the fourth rank tensor of elastic constants [72, 34]. As the stress and strain tensors are symmetric and the material can be assumed to be isotropic and homogenous, the independent components of the tensor of elastic constants can be reduced significantly. This allows equation (2.13) to be simplified to [34]

$$\sigma_{ij} = 2\mu\epsilon_{ij} + \lambda\epsilon_{kk}\delta_{ij} \tag{2.14}$$

where μ and λ are the Lamé constants, which can be defined in terms of the Youngs modulus E and the Poisson ratio ν as

$$\begin{aligned} \mu &= \frac{E}{2(1+\nu)}, \\ \lambda &= \frac{\nu E}{(1+\nu)(1-2\nu)}. \end{aligned}$$

The Lamé constant μ is equivalent to the shear modulus G, there is no direct physical equivalent for the Lamé constant λ. The constitutive relationship can be decomposed into deviatoric and hydrostatic components, respectively, [34]

$$\begin{aligned} s_{ij} &= \frac{E}{1+\nu}\epsilon_{ij}{}' = 2G\epsilon_{ij}{}', \\ \sigma_{ii} &= \frac{E}{1-2\nu}\epsilon_{kk} = 3K\epsilon_{kk}. \end{aligned}$$

where $\epsilon_{ij}{}'$ is the deviatoric strain and K is the bulk modulus.

2.3.1.2 Engineering Definition

When describing the constitutive relationship as employed in engineering problems it is common practice to dispense with tensor notation [38, 107]. The following matrix form of notation is meaningful when describing computational algorithms and will be adopted in the thesis when necessary. It is defined here as a comparison to the succinct and more mathematical tensor notation.

In this case, for an isotropic homogenous material undergoing small strains the linear elastic constitutive relationship is generally defined in a matrix form as follows:

$$\sigma = \mathbf{D}\epsilon \tag{2.15}$$

where the stress σ and strain ϵ are represented by vectors of six components for a three dimensional isotropic approximation.

$$\begin{aligned} \sigma^T &= \begin{bmatrix} \sigma_x & \sigma_y & \sigma_z & \tau_{xy} & \tau_{yz} & \tau_{zx} \end{bmatrix}, \\ \epsilon^T &= \begin{bmatrix} \epsilon_x & \epsilon_y & \epsilon_z & \gamma_{xy} & \gamma_{yz} & \gamma_{zx} \end{bmatrix}, \end{aligned} \tag{2.16}$$

and the elasticity matrix $\mathbf{D}$ is defined in terms of the material properties E and ν as

$$\mathbf{D} = \frac{E(1-\nu)}{(1+\nu)(1-2\nu)} \begin{pmatrix} 1 & \frac{\nu}{1-\nu} & \frac{\nu}{1-\nu} & 0 & 0 & 0 \\ \frac{\nu}{1-\nu} & 1 & \frac{\nu}{1-\nu} & 0 & 0 & 0 \\ \frac{\nu}{1-\nu} & \frac{\nu}{1-\nu} & 1 & 0 & 0 & 0 \\ 0 & 0 & 0 & \frac{1-2\nu}{2(1-\nu)} & 0 & 0 \\ 0 & 0 & 0 & 0 & \frac{1-2\nu}{2(1-\nu)} & 0 \\ 0 & 0 & 0 & 0 & 0 & \frac{1-2\nu}{2(1-\nu)} \end{pmatrix} \tag{2.17}$$

This is the standard matrix form of the constitutive relationship for a linear elastic material as described in the standard texts [38, 107].

At this point it should be noted that the shear strain components in the strain vector in equation (2.16) are not equivalent to the shear strains described in the tensor definition of strain in equation (2.11). The former are generally referred to as the engineering shear strains and can be defined as follows using the linear differential operator $\mathbf{L}$ and the displacement vector $\mathbf{u}$ as

$$\epsilon = \mathbf{L}\mathbf{u} = \begin{pmatrix} \frac{\partial}{\partial x} & 0 & 0 \\ 0 & \frac{\partial}{\partial y} & 0 \\ 0 & 0 & \frac{\partial}{\partial z} \\ \frac{\partial}{\partial y} & \frac{\partial}{\partial x} & 0 \\ 0 & \frac{\partial}{\partial z} & \frac{\partial}{\partial y} \\ \frac{\partial}{\partial z} & 0 & \frac{\partial}{\partial x} \end{pmatrix} \begin{pmatrix} u \\ v \\ w \end{pmatrix} = \begin{pmatrix} \frac{\partial u}{\partial x} \\ \frac{\partial v}{\partial y} \\ \frac{\partial w}{\partial z} \\ \frac{\partial u}{\partial y} + \frac{\partial v}{\partial x} \\ \frac{\partial v}{\partial z} + \frac{\partial w}{\partial y} \\ \frac{\partial u}{\partial z} + \frac{\partial w}{\partial x} \end{pmatrix} = \begin{pmatrix} \epsilon_x \\ \epsilon_y \\ \epsilon_z \\ \gamma_{xy} \\ \gamma_{yz} \\ \gamma_{zx} \end{pmatrix}. \tag{2.18}$$

The engineering shear strains are often described as the total shear deformation as opposed to the average shear deformation as described in the strain tensor in equation (2.11) [38, 59, 34].

2.3.2 Perzyna Model

The elasto-visco-plastic constitutive relationship adopted in this research is based on the original description of the Perzyna model for an associated material as proposed by Perzyna in 1963 [76, 77]. It is also equivalent to the constitutive relationship described by Zienkiewicz and Cormeau [105] which uses a modified Perzyna model to describe associative and non-associative material behaviour.

The visco-plastic strain rate tensor can be defined as follows:

$$\dot{\epsilon}_{ij}^{vp} = \gamma \left\langle \frac{F}{Y} \right\rangle^{N} \frac{\partial Q}{\partial \sigma_{ij}}, \tag{2.19}$$

where γ is the material property fluidity, the yield function F is rendered non-dimensional by the uniaxial yield value Y, the power law is obeyed by raising the dimensionless yield function to a power N and Q is the plastic potential [105]. The operator $\langle . \rangle$ is defined as follows [76]:

$$\langle . \rangle = \begin{cases} 0 & \text{when } . \leq 0 \\ . & \text{when } . > 0 \end{cases}.$$

In this research the Perzyna model is restricted to associated material behaviour where the yield function is directly equivalent to the plastic potential:

$$F \equiv Q.$$

Thus, the visco-plastic strain rate is simplified as follows:

$$\dot{\epsilon}_{ij}^{vp} = \gamma \left\langle \frac{F}{Y} \right\rangle^{N} \frac{\partial F}{\partial \sigma_{ij}}, \tag{2.20}$$

When the von-Mises yield function as defined in equation (2.6) is substituted in equation (2.20) and is differentiated with regard to the stress tensor the visco-plastic strain rate can be defined in terms of the deviatoric stress tensor as

$$\dot{\epsilon}_{ij}^{vp} = \gamma \left\langle \frac{\sigma_{\mathit{eff}}}{Y} - 1 \right\rangle^{N} \frac{3}{2\sigma_{\mathit{eff}}} s_{ij}. \tag{2.21}$$

Considering a thermo-elasto-visco-plastic constitutive relationship, the total strain rate tensor is comprised of three parts

$$\dot{\epsilon}_{ij} = \dot{\epsilon}_{ij}^{el} + \dot{\epsilon}_{ij}^{vp} + \dot{\epsilon}_{ij}^{th}, \tag{2.22}$$

which also includes the elastic strain rate $\dot{\epsilon}_{ij}^{el}$ and the thermal strain rate

$$\dot{\epsilon}_{ij}^{th} = \alpha \dot{T} \delta_{ij}, \tag{2.23}$$

where α is the linear Coefficient of Thermal Expansion and $\dot{T}$ is the rate of change of temperature. It should be noted that additional to thermal strain rates it is also possible to consider other self produced strain rates such as those associated with a material transformation, but they are neglected here for simplification.

From equation (2.22) the elastic strain rate can be defined as follows:

$$\dot{\epsilon}_{ij}^{el} = \dot{\epsilon}_{ij} - \dot{\epsilon}_{ij}^{vp} - \dot{\epsilon}_{ij}^{th} \tag{2.24}$$

and if the elastic constitutive relationship described by equation (2.14) is modified to rate form

$$\dot{\sigma}_{ij} = 2\mu \dot{\epsilon}_{ij}^{el} + \lambda \dot{\epsilon}_{kk}^{el} \delta_{ij} \tag{2.25}$$

the non-linear nature of the constitutive relationship with regard to stress is apparent.

In addition to their rate forms, it is also possible to state equations 2.24 and 2.25 in their incremental forms as follows:

$$\begin{aligned} \Delta\epsilon_{ij}^{el} &= \Delta\epsilon_{ij} - \Delta\epsilon_{ij}^{vp} - \Delta\epsilon_{ij}^{th}, \\ \Delta\sigma_{ij} &= 2\mu\Delta\epsilon_{ij}^{el} + \lambda\Delta\epsilon_{kk}^{el}\delta_{ij}. \end{aligned} \tag{2.26}$$

2.3.3 Closure

The Perzyna model, in conjunction with the von-Mises yield criterion, has provided the basis for the constitutive relationship in many applications of the Bubnov-Galerkin FEM to non-linear material problems involving metals [105, 23, 72, 86, 108].

A comprehensive description of the FE implementation is given by Zienkiewicz and Cormeau [105, 108], where a unified approach is described and adopted. This unified approach allows a variety of non-linear material phenomema to be modelled, such as elasto-plasticity, elasto-visco-plasticity and pure creep, by varying the material properties and the model parameters. As discussed in section 2.1.2.3, the Norton-Soderberg creep law for metals can be derived from the associated form of visco-plasticity described here [108, 72]. Numerically, this is achieved by assigning the uniaxial yield stress with a conveniently small value to reflect zero and N to a value in the range $4 - 7$ which is typical of most metals exhibiting creep behaviour [105]. Thus, the behaviour of metals over an extreme range of temperatures can be modelled.

For these reasons, the Perzyna model and the von-Mises yield criterion have been adopted in a number of FE applications to complex problems such as the shape-casting of metals, where extreme temperature conditions occur causing a variety of non-linear material behaviour [93, 13, 92].

Thus, the Perzyna model is a suitable candidate to introduce non-linear material behaviour into a FV framework to solve multi-physics problems [26, 25]. The 'node-centred' FVM and the Bubnov-Galerkin FE discretization and solution procedures to material non-linearity are theoretically compared with regard to this specific case in the following chapter.

Chapter 3

Numerical Computation

In this chapter the numerical computation of the thermo-elasto-visco-plastic material behaviour as described in the previous chapter is developed. Initially, a detailed description of numerical discretisation approaches with regard to solid mechanical behaviour is presented. Then a theoretical analysis and comparison of the CV-UM vertex based FVM and the Bubnov-Galerkin FEM discretisation techniques is presented. The potential algorithmic approaches are discussed and available time stepping schemes are described. Finally, the linear solvers employed in this research are described and a brief discussion of axisymmetric problems is provided.

3.1 Numerical Discretisation

In this section the necessary numerical discretisation techniques are described from first principles, with particular emphasis on control volume definition. Initially, the governing equations are described in the context of the conservation equations required for a control volume method. Then a general discretisation technique is applied which can lead to either a cell-vertex FVM or a Bubnov-Galerkin FEM. Finally, the FVM control volume technique is applied directly in a standard fashion.

3.1.1 Governing Equations

In the previous chapter, the stress state at a point was described. When considering the complete analysis of stress within a continuum, whether it is a solid or a fluid in motion, the governing equation concerning the conservation of momentum is

$$\nabla.\sigma_{ij} + b_i = \rho a_i, \tag{3.1}$$

which is Cauchy's equation of motion [61], also referred to as the stress equation of small motion [38]. Where b_i is the body force per unit volume, due to gravity for example, a_i is the local acceleration and ρ is the density of the material.

In the research presented here only quasi-static problems are of interest and the acceleration will be considered to be equal to zero. Hence, only the static equilibrium equation will be considered, which is then obtained as

$$\nabla.\sigma_{ij} + b_i = 0. \tag{3.2}$$

Though it should be noted that Demirdžić and Martinović have applied a cell-centred FVM to thermo-mechanical problems on structured meshes involving non-zero accelerations using the conservation equation (3.1) [31]. Hence, indicating that the CV-UM vertex based FVM described in this research will apply generally to such problems.

3.1.2 General Discretisation

In a generalized FEM discretisation treatment an integral formulation is obtained using the method of weighted residuals [107, 52]. This method is also known as the weak formulation of the problem [107, 52].

The method of weighted residuals will be applied to the displacement formulation of the governing equations [108]. In developing the displacement formulation the equations will be described in matrix form. Hence, the governing equilibrium equation (3.2) in matrix form is

$$\mathbf{L^T}\sigma + \mathbf{b} = \mathbf{0} \qquad \text{in } \Omega, \tag{3.3}$$

where $\mathbf{L}$ and σ are the linear differential operator and the stress vector, respectively, and are defined in equations (2.16) and (2.18),

$$\mathbf{b}^{\mathbf{T}} = \begin{bmatrix} b_x & b_y & b_z \end{bmatrix}$$

is the body force vector and Ω is the domain volume (or area as the theory applies generally for the two dimensional case with suitably defined matrices and vectors).

To develop the standard displacement formulation, the elastic strain rate defined in equation (2.24) is redefined in vector form as the elastic strain at any instant in time,

$$\epsilon^{el} = \epsilon - \epsilon^{th} - \epsilon^{vp} \tag{3.4}$$

where each strain vector contains six components of the form described in equation (2.16). The constitutive relationship as described in matrix form in equation (2.15) now becomes

$$\sigma = \mathbf{D}\left(\epsilon - \epsilon^{th} - \epsilon^{vp}\right). \tag{3.5}$$

The boundary conditions on the surface $\Gamma = \Gamma_t \cup \Gamma_u$ of the domain Ω can be defined as [107, 71]

$$\mathbf{R}^{\mathbf{T}}\sigma = \mathbf{t_p} \quad \text{on } \Gamma_t, \tag{3.6}$$

$$\mathbf{u} = \mathbf{u_p} \quad \text{on } \Gamma_u, \tag{3.7}$$

where $\mathbf{t_p}$ are the prescribed tractions on the boundary Γ_t, $\mathbf{u_p}$ are the prescribed displacements on the boundary Γ_u and

$$\mathbf{R} = \begin{bmatrix} n_x & 0 & 0 \\ 0 & n_y & 0 \\ 0 & 0 & n_z \\ n_y & n_x & 0 \\ 0 & n_z & n_y \\ n_z & 0 & n_x \end{bmatrix} \tag{3.8}$$

is the outward normal operator.

Applying the strain-displacement relationship of equation (2.18) to equation (3.5) and substituting the resulting equation in the traction boundary condition as defined in equation (3.6),

$$\mathbf{R}^{\mathbf{T}}\left(\mathbf{DLu} - \mathbf{D}\epsilon^{th} - \mathbf{D}\epsilon^{vp}\right) - \mathbf{t_p} = \mathbf{0} \quad \text{on } \Gamma_t, \tag{3.9}$$

and also performing the same substitution on the governing equilibrium equation (3.3):

$$\mathbf{L}^{\mathbf{T}}\left(\mathbf{DLu} - \mathbf{D}\epsilon^{th} - \mathbf{D}\epsilon^{vp}\right) + \mathbf{b} = \mathbf{0} \qquad \text{in } \Omega. \tag{3.10}$$

Applying the method of weighted residuals to equations (3.9) and (3.10), and assuming the displacement boundary conditions as described by equation (3.7) are directly satisfied by the displacement vector **u** [107],

$$\begin{aligned} &\int_{\Omega} \mathbf{W}^{\mathbf{T}}\left[\mathbf{L}^{\mathbf{T}}(\mathbf{DLu} - \mathbf{D}\epsilon^{th} - \mathbf{D}\epsilon^{vp})\right] d\Omega + \int_{\Omega} \mathbf{W}^{\mathbf{T}}\mathbf{b}\, d\Omega \\ &\qquad + \int_{\Gamma_t} \overline{\mathbf{W}}^{\mathbf{T}}\left[\mathbf{R}^{\mathbf{T}}(\mathbf{DLu} - \mathbf{D}\epsilon^{th} - \mathbf{D}\epsilon^{vp})\right] d\Gamma - \int_{\Gamma_t} \overline{\mathbf{W}}^{\mathbf{T}}\mathbf{t}_{\mathbf{p}}\, d\Gamma = \mathbf{0}, \end{aligned} \tag{3.11}$$

where **W** and $\overline{\mathbf{W}}$ are arbitrary weighting functions. Applying Green's first theorem as defined in Appendix A.2 to the first volume integral term in equation (3.11) and assigning $\mathbf{W} = -\overline{\mathbf{W}}$ without any loss of generality as the weighting functions are completely arbitrary at this point,

$$\begin{aligned} &- \int_{\Omega} [\mathbf{LW}]^{\mathbf{T}}[\mathbf{DLu} - \mathbf{D}\epsilon^{th} - \mathbf{D}\epsilon^{vp}]\, d\Omega + \int_{\Omega} \mathbf{W}^{\mathbf{T}}\mathbf{b}\, d\Omega \\ &\qquad + \int_{\Gamma_u} [\mathbf{RW}]^{\mathbf{T}}[\mathbf{DLu} - \mathbf{D}\epsilon^{th} - \mathbf{D}\epsilon^{vp}]\, d\Gamma + \int_{\Gamma_t} \mathbf{W}^{\mathbf{T}}\mathbf{t}_{\mathbf{p}}\, d\Gamma = \mathbf{0}. \end{aligned} \tag{3.12}$$

It should be noted that the displacement **u** has disappeared from the integrals taken along the boundary Γ_t and that the boundary condition as described by equation (3.6) is automatically satisfied. Also, restricting the displacement **u** to satisfy the boundary condition as described by equation (3.7) is equivalent to restricting the choice of the weighting function associated with the integral along the boundary Γ_u to be zero [107].

The form of equation (3.12) is the weak form of the equilibrium condition, this is indicated as it permits discontinuous first derivatives of the displacement, which was not permitted in equation (3.11) [52, 107].

At this point the unknown displacement is approximated as [107]

$$\mathbf{u} \simeq \hat{\mathbf{u}} = \sum_{j=1}^{n} \mathbf{N}_j \bar{\mathbf{u}}_j = \sum_{j=1}^{n} \mathbf{I} N_j \bar{\mathbf{u}}_j, \tag{3.13}$$

where $\bar{\mathbf{u}}_j$ is the unknown variable, in this case displacement. N_j is the shape or basis function associated with the unknown displacement, which can be a function of local or global coordinates. The shape functions utilised in this research are described in Appendix B.9. **I** is the third order identity matrix for the three dimensional case.

The displacement approximation can be introduced into equation (3.12) if the arbitrary weighting function **W** is replaced by a finite set of prescribed functions [107, 71]

$$\mathbf{W} = \sum_{i=1}^{n} \mathbf{W}_i, \tag{3.14}$$

where $\mathbf{W}_i$ is the weighting function associated with an unknown displacement. Introduction of the displacement approximation into equation (3.12) yields a set of algebraic equations of the following form:

$$\begin{aligned} - \int_{\Omega} [\mathbf{L}\mathbf{W}_i]^{\mathbf{T}} [\mathbf{D}\mathbf{L}\hat{\mathbf{u}} - \mathbf{D}\epsilon^{th} - \mathbf{D}\epsilon^{vp}]\, d\Omega + \int_{\Omega} \mathbf{W}_i^{\mathbf{T}} \mathbf{b}\, d\Omega & \\ + \int_{\Gamma_u} \{\mathbf{R}\mathbf{W}]_i^{\mathbf{T}} \{\mathbf{D}\mathbf{L}\hat{\mathbf{u}} - \mathbf{D}\epsilon^{th} - \mathbf{D}\epsilon^{vp}\}\, d\Gamma + \int_{\Gamma_t} \mathbf{W}_i^{T} \mathbf{t}_{\mathbf{p}}\, d\Gamma = \mathbf{0} & \\ \text{for} \qquad i = 1, n. & \end{aligned} \tag{3.15}$$

It should be noted that the introduction of the displacement approximation introduces the residuals or errors into equation (3.12) and the weighting functions are associated with these residuals or errors. This is the essence of the method of weighted residuals.

The method of weighted residuals outdates the FEM and the latter generally uses local shape or basis functions. As described, the method of weighted residuals always leads to equations of integral form. This integral property is important as the overall system of algebraic equations can be obtained by the summation of contributions from various subdomains. For these reasons, all weighted residual approximations have often been described under the heading of the generalized finite element method [107, 71].

Equation (3.15) can be expressed as a linear system of equations of the form

$$\mathbf{K}\bar{\mathbf{u}} - \mathbf{f} = \mathbf{0}, \tag{3.16}$$

where **K** is the global stiffness matrix, $\bar{\mathbf{u}}$ is the global displacement approximation and **f** is the global equivalent nodal force vector. **K** and **f** can be formed from the summation of the following contributions:

$$\mathbf{K}_{ij} = \int_{\Omega_i} [\mathbf{L}\mathbf{W}_i]^{\mathbf{T}} \mathbf{D}\mathbf{L}\mathbf{N}_j\, d\Omega - \int_{\Gamma_{u_i}} [\mathbf{R}\mathbf{W}_i]^{\mathbf{T}} \mathbf{D}\mathbf{L}\mathbf{N}_j\, d\Gamma, \tag{3.17}$$

$$\begin{aligned}\mathbf{f}_i &= \int_{\Omega_i} \mathbf{W}_i^{\mathrm{T}}\mathbf{b}\,d\Omega - \int_{\Omega_i}[\mathbf{L}\mathbf{W}_i]^{\mathrm{T}}\mathbf{D}\epsilon^{th}d\Omega - \int_{\Omega_i}[\mathbf{L}\mathbf{W}_i]^{\mathrm{T}}\mathbf{D}\epsilon^{vp}\,d\Omega \\ &+ \int_{\Gamma_{t_i}} \mathbf{W}_i^{\mathrm{T}}\mathbf{t}_{\mathrm{p}}\,d\Gamma + \int_{\Gamma_{u_i}}[\mathbf{R}\mathbf{W}_{\mathrm{i}}]^{\mathrm{T}}\mathbf{D}\epsilon^{th}d\Gamma + \int_{\Gamma_{u_i}}[\mathbf{R}\mathbf{W}_{\mathrm{i}}]^{\mathrm{T}}\mathbf{D}\epsilon^{vp}\,d\Gamma, \qquad (3.18)\end{aligned}$$

where Ω_i is the control volume associated with the node i and $\Gamma_i = \Gamma_{u_i} \cup \Gamma_{t_i}$ is the boundary of the control volume.

At this stage, the finite weighting functions have not been specified and the discretisation has been performed in a general fashion. It should be noted that equations (3.17) and (3.18) defining integral control volume contributions to the overall system of equations is significantly different to the standard elemental contributions in the usual FEM discretisation approach.

An important consideration is the possibility that control volumes over which the integral contribution is taken may overlap. Thus, this is not a straight forward integral summation. The assumption is that each finite weighting function removes the residual or error for that individual control volume, thus allowing the summation, as the residual or error over the complete domain must also be removed.

The general discretisation approach described here is vertex based with regard to the control volume. This is a consequence of the application of the boundary conditions to unknowns on the boundary of the domain and associating the unknown with a node as opposed to a cell or element [52]. The specific weighting functions associated with the cell-vertex FVM or the Bubnov-Galerkin FEM can now be applied to equations (3.17) and (3.18).

3.1.2.1 Bubnov-Galerkin FEM

In the Bubnov-Galerkin FEM the weighting function associated with a node is equal to the shape function of the unknown associated with that node [107, 52, 71],

$$\mathbf{W}_i = \mathbf{N}_i.$$

The shape function describes the variation of an unknown over an element and there can be a number of elements associated with each node. Hence, it is apparent that control volumes

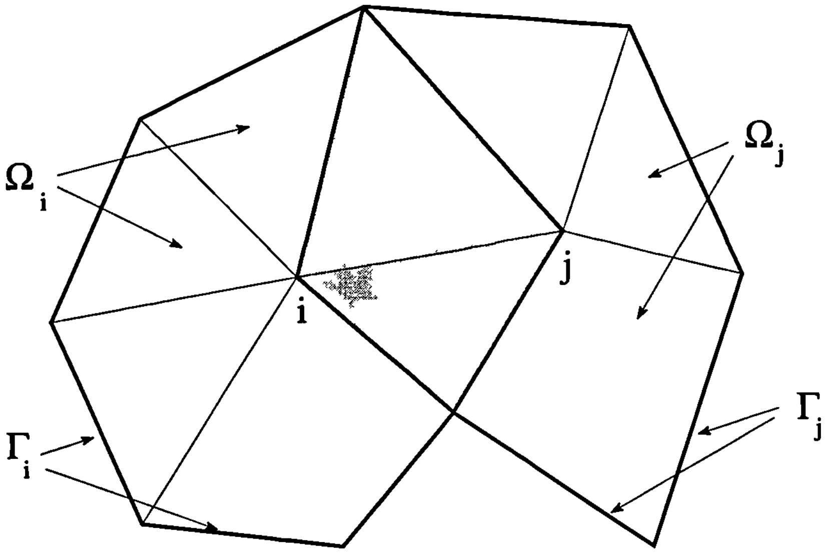

Figure 3.1: Overlapping control volumes in two dimensions.

described by weighting functions of this form will always overlap. This is illustrated in Figure 3.1 for a simple two dimensional case of two adjacent nodes i and j, where the control volumes Ω_i and Ω_j have contributions from all the elements associated with their respective nodes i and j.

Hence, with regard to the Bubnov-Galerkin FEM the contributions to the overall system of equations as described by equations (3.17) and (3.18) are

$$\mathbf{K}_{ij} = \int_{\Omega_i} \mathbf{B}_i^{\mathrm{T}}\mathbf{D}\mathbf{B}_j \, d\Omega, \tag{3.19}$$

$$\mathbf{f}_i = \int_{\Omega_i} \mathbf{N}_i^{\mathrm{T}}\mathbf{b} \, d\Omega - \int_{\Omega_i} \mathbf{B}_i^{\mathrm{T}}\mathbf{D}\epsilon^{th} d\Omega - \int_{\Omega_i} \mathbf{B}_i^{\mathrm{T}}\mathbf{D}\epsilon^{vp} \, d\Omega + \int_{\Gamma_{t_i}} \mathbf{N}_i^{\mathrm{T}}\mathbf{t}_{\mathrm{p}} \, d\Gamma, \tag{3.20}$$

where

$$\mathbf{B}_i = \mathbf{L}\mathbf{N}_i. \tag{3.21}$$

It should be noted that if the boundary of the control volume, such as that described by Γ_i in Figure 3.1, coincides with the external boundary of the domain, the shape functions are not necessarily zero along that part of the boundary. Thus, if a flux is prescribed such as a traction this will not disappear and is included in the contribution to the equivalent nodal load vector as described in equation (3.20). If the boundary of the control volume does not coincide with the external boundary of the domain, then by definition the weighting function will be zero at these boundaries and the surface integrals will disappear.

It should also be noted that the symmetrical nature of the overall stiffness matrix $\mathbf{K}$ is indicated by equation (3.19). The Bubnov-Galerkin weighting approach is accepted as the optimum technique for treating physical situations described by elliptic or self-adjoint differential equations, as the inherent symmetrical nature is preserved by the choice of weighting functions [107, 71].

3.1.2.2 Cell-vertex FVM

In the cell-vertex FVM the weighting functions associated with a node are equal to unity within the control volume,

$$\mathbf{W}_i = \mathbf{I},$$

and zero elsewhere. In the three dimensional case $\mathbf{I}$ is again the third order identity matrix. This definition is equivalent to that for the subdomain collocation method as defined in the standard texts [52, 107].

However, it should be noted that weighting functions defined in this manner permit a variety of possibilities with regard to the control volume definition. This is because the weighting functions are not restricted to a direct association with the cell or element as in the standard Bubnov-Galerkin case. This is an important consideration and requires the recognition of the cell-vertex FVM as a discretisation technique in its own right [52].

For the cell-vertex FVM the contributions to the overall system of equations as described by equation (3.17) and (3.18) are

$$\begin{aligned} \mathbf{K}_{ij} &= -\int_{\Gamma_{u_i}} \mathbf{R}^{\mathrm{T}}\mathbf{D}\mathbf{L}\mathbf{N}_j \, d\Gamma, && (3.22) \\ \mathbf{f}_i &= \int_{\Omega_i} \mathbf{b} \, d\Omega + \int_{\Gamma_{u_i}} \mathbf{R}^{\mathrm{T}}\mathbf{D}\epsilon^{th} d\Gamma + \int_{\Gamma_{u_i}} \mathbf{R}^{\mathrm{T}}\mathbf{D}\epsilon^{vp} \, d\Gamma + \int_{\Gamma_{t_i}} \mathbf{t}_{\mathrm{p}} \, d\Gamma. && (3.23) \end{aligned}$$

It should be noted that the traction boundary conditions can be applied directly as another

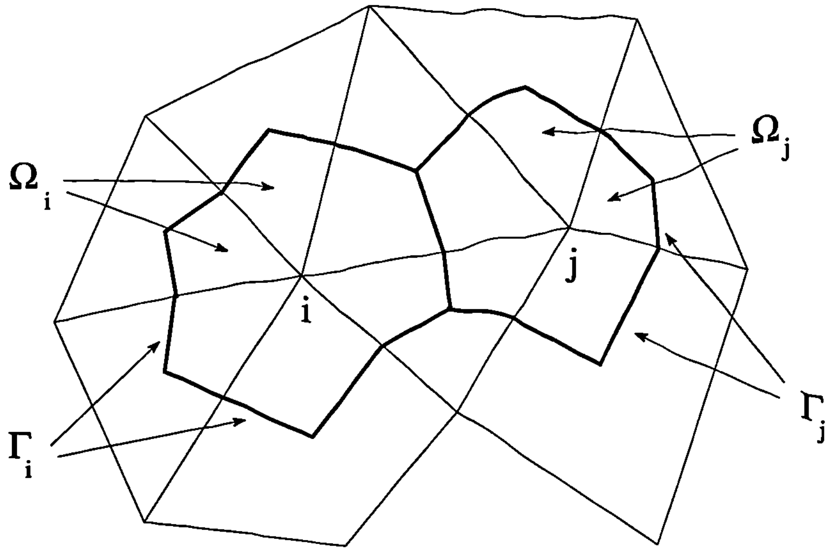

Figure 3.2: Non-overlapping control volumes in two dimensions.

surface integral, but in the previous Bubnov-Galerkin FEM an extra surface element is generally included on the domain boundary. However for lower order elements involving linear shape functions this distinction is a minor issue.

An overlapping control volume definition suitable for a cell-vertex FVM in two dimensions is illustrated in Figure 3.1. Alternatively, a non-overlapping cell-vertex FVM in two dimensions is indicated in Figure 3.2. These two techniques have been compared in the numerical solution of one and two dimensional solid mechanics problems involving linear elastic materials [71]. The non-overlapping or CV-UM vertex based FVM proved superior with regard to accuracy and agrees in essence with the standard requirements of conservative control volume methods as given by Patankar [74].

It should be noted from the asymmetric contributions to the overall stiffness matrix as described by equation (3.22) that unlike the Bubnov-Galerkin case the symmetry of the problem cannot be preserved. As mentioned earlier, this is an important issue in solid mechanics problems, where the differential equations are often elliptical in nature [107, 71].

The accuracy of the Bubnov-Galerkin and the subdomain collocation approach has been reported in many cases and the Bubnov-Galerkin approach is shown to be more accurate [107, 106]. Subdomain collocation techniques equivalent to the cell-vertex FVM and the CV-UM vertex based FVM have been considered [107]. However, in the comparisons of the two methods global shape functions were employed as opposed to local, piecewise, shape functions [107]. The combination of a global shape function and a locally conservative weighting function is not consistent with conservative control volume techniques as described by Patankar [74].

For this reason the cell-vertex FVM was initially argued as being inferior, due to it's theoretical equivalence to the subdomain collocation method, but in the light of further research where different control volume definitions have been proposed such as the CV-UM vertex based FVM, the extent of this inferiority has come into question [71].

3.1.3 Conservative Discretisation

When applying the FV discretisation technique directly, the integral formulation of the conservation equation is discretised directly in physical space [74, 52]. Thus, the integral formulation of the conservation equation (3.2) over a control volume Ω_{cv} is

$$\int_{\Omega_{cv}} (\nabla.\sigma_{ij} + b_i)\, d\Omega = 0 \tag{3.24}$$

and if the divergence theorem as defined in Appendix A.1 is applied to the first integral term on the left then

$$\oint_{\Gamma_{cv}} \sigma_{ij}.n_j d\Gamma + \int_{\Omega_{cv}} b_i d\Omega = 0 \tag{3.25}$$

where n_j is the outward normal and the integration is now applied over the closed surface Γ_{cv}. At this point the conservative nature of the FVM is established as the flux, stress, is integrated over the closed surface Γ_{cv} [43, 42, 4, 31, 48].

From a theoretical mechanics viewpoint, this approach is equivalent to applying the virtual work concept, which is traditionally viewed as the starting point of a Bubnov-Galerkin FEM [105]. Though in the FVM unit virtual displacements are prescribed, as opposed to arbitrary virtual displacements in the Bubnov-Galerkin FEM [71].

It is now possible to define a collection of discrete control volumes which form the complete solution domain, each of which is independently conservative. These can be cell-centred or cell-vertex control volumes [43, 42, 4, 31, 48]. The CV-UM vertex based FVM will be described in full in the following sections.

It should be noted that in the cell-centred FVM, where in the case of CSM problems the stress, strains and displacements are all stored at the cell centres, a decoupling phenomenon can occur between stress and displacement. This phenomenon is analogous to that which occurs in CFD when the pressure field is decoupled from the velocity field. This similarity allows the solutions to this problem in CSM to be compared with those in CFD. Demirdžić and Martinović [31] have used an approach which is very similar to that of Rhie and Chow [80]. This approach includes a higher order term in the displacement gradient approximation. Whilst, Hattel and Hansen [48] have adopted a staggered grid approach, where a staggered grid is associated with each displacement component and displacements are stored at the cell faces. This is very similar to methods employed in a number of CFD software packages, such as the commercial software package PHEONICS [19].

On the other hand, the cell-vertex FVM stores the displacements at the vertices and stress and strains at the integration points, which can be within the cell or element. The required derivatives are approximated at integration points using the shape function derivatives, this technique will be described in further detail in the following sections. This method inherently avoids the problem of decoupling in the same fashion as the standard Bubnov-Galerkin FEM and is often referred to as partial staggering.

It should also be noted that no distinction has been made between the deformed and undeformed configurations in describing the FVM. This is permissible as an infinitesimal strain approximation is adopted and small displacements are assumed [31].

3.2 Algorithmic techniques

Non-linear problems require special solution techniques. These techniques can be simply viewed as iterative methods, which involve the repeated solution of a linear system of equations, in order to approximate the behaviour of a non-linear relationship.

In the specific case of non-linear material problems a large number of solution techniques are currently available. In the description of the algorithms developed in this research the origin and development of the non-linear solution techniques will be described.

It should be noted that in this research the simpler non-linear solution techniques have initially been implemented, though the approach should apply generally to most non-linear solution techniques.

In this research two algorithmic approaches were initially developed. The first approach follows the more traditional FEM algorithmic approach for non-linear problems, where the displacement variable is solved in a linear whole field fashion for each non-linear iteration. In the second approach the displacement is solved in a non-linear segregated fashion, for each non-linear iteration. This segregated approach was originally applied to two dimensional linear elastic problems by Fryer et al [43]. These two algorithmic approaches are described and compared in the following sections.

3.2.1 Standard non-linear approach

The algorithmic technique adopted in this approach is based upon that of Zienkiewicz and Cormeau [105]. The method can be classified as an initial strain method, which is accepted as being the suitable algorithmic approach for problems involving visco-plastic strains. The implementation of this algorithm in a FVM context for elasto-visco-plastic problems is now described.

The numerical procedure in matrix form is as follows:

(1) Assume known values of the variables σ_n, $\overline{\mathbf{u}}$, ϵ_n^{vp} and $\mathbf{f_n}$ at the time instant t_n. Calculate the visco-plastic strain rate using the following relationship obtained from equation 2.21:

$$\dot{\epsilon}_n^{vp} = g\{\sigma_n\}.$$

(2) Approximate the visco-plastic strain increment $\Delta\epsilon_n^{vp}$ and update t_n as follows:

$$\Delta\epsilon_n^{vp} = \dot{\epsilon}_n^{vp}\Delta t_n, \quad t_{n+1} = t_n + \Delta t_n.$$

(3) Update the total visco-plastic strain at the current instant in time as follows:

$$\epsilon_{n+1}^{vp} = \epsilon_n^{vp} + \Delta\epsilon_n^{vp}.$$

(4) Update the load vector with regard to the latest visco-plastic strains using a FVM contribution as described in equation 3.23:

$$\mathbf{f_{n+1}} = \mathbf{p_0} + \int_\Gamma \mathbf{R}^\mathrm{T}\mathbf{D}\epsilon_{n+1}^{vp}\mathrm{d}\Gamma,$$

where $\mathbf{p_0}$ represents the time independent applied loads.

(5) Calculate the associated displacement and stress as follows:

$$\begin{aligned} \overline{\mathbf{u}}_{\mathbf{n+1}} &= \mathbf{K}_0^{-1}\mathbf{f}_{\mathbf{n+1}}, \\ \sigma_{n+1} &= \mathbf{D}\left(\epsilon_{n+1} - \epsilon_0^{th} - \epsilon_{n+1}^{vp}\right), \\ &= \mathbf{D}\mathbf{B}\overline{\mathbf{u}}_{\mathbf{n+1}} - \mathbf{D}\epsilon_{n+1}^{vp}. \end{aligned} \tag{3.26}$$

(6) Return to step (1) and repeat for the next time step with the updated values. The solution has converged if the Euclidian norm ratio of the effective visco-plastic strain rate is within tolerance, i.e.

$$\frac{\|\dot{\epsilon}_n^{eff}\|}{\|\dot{\epsilon}_0^{eff}\|} \times 100 < \text{Tolerance}.$$

The technique utilises an explicit method with regard to time stepping, and this issue will be discussed in detail in the following sections. It is important to note that the FVM only differs from the FEM algorithm in the calculation of the external force vector $\mathbf{f_{n+1}}$ in step (4) and the formulation of the initial stiffness matrix $\mathbf{K_0}$ utilised in step (5). Hence, allowing an accurate comparison of the two methods.

3.2.2 Segregated approach

Initially in this section, the FV formulation as outlined in the previous section will be described in further detail.

Consider equation 3.22 for an arbitrary three dimensional element. It is possible to obtain the complete stiffness matrix $\mathbf{K}_{ij}$ associated with the contributions from the nodes $j = 1, n$ at node i of the element. In three dimensions, this is achieved using the elasticity matrix as described in equation 2.17, the normal operator $\mathbf{R}$ as described in equation 3.8 and the differential operator $\mathbf{L}$ as described in equation 2.18. The shape functions N are dependent upon the element and are described in Appendix B.

The complete stiffness matrix is then multiplied by the unknown displacement vector $\overline{\mathbf{u}}$ for the element to obtain the following equations:

$$\begin{aligned}
&\frac{E}{2(1+\nu)}\left[\frac{2}{1-2\nu}\left((1-\nu)\sum_{i=1}^{n}\frac{\partial N_i}{\partial x}\overline{u}_i+\nu\sum_{i=1}^{n}\left(\frac{\partial N_i}{\partial y}\overline{v}_i+\frac{\partial N_i}{\partial z}\overline{w}_i\right)\right)n_x\right.\\
&\qquad\left.+\sum_{i=1}^{n}\left(\frac{\partial N_i}{\partial y}\overline{u}_i+\frac{\partial N_i}{\partial x}\overline{v}_i\right)n_y+\sum_{i=1}^{n}\left(\frac{\partial N_i}{\partial z}\overline{u}_i+\frac{\partial N_i}{\partial x}\overline{w}_i\right)n_z\right]\Delta s \;=\; f_{x_i},\\
&\frac{E}{2(1+\nu)}\left[\sum_{i=1}^{n}\left(\frac{\partial N_i}{\partial x}\overline{v}_i+\frac{\partial N_i}{\partial y}\overline{u}_i\right)n_x+\frac{2}{1-2\nu}\left((1-\nu)\sum_{i=1}^{n}\frac{\partial N_i}{\partial y}\overline{v}_i\right.\right.\\
&\qquad\left.\left.+\nu\sum_{i=1}^{n}\left(\frac{\partial N_i}{\partial x}\overline{u}_i+\frac{\partial N_i}{\partial z}\overline{w}_i\right)\right)n_y+\sum_{i=1}^{n}\left(\frac{\partial N_i}{\partial z}\overline{v}_i+\frac{\partial N_i}{\partial y}\overline{w}_i\right)n_z\right]\Delta s \;=\; f_{y_i},\\
&\frac{E}{2(1+\nu)}\left[\sum_{i=1}^{n}\left(\frac{\partial N_i}{\partial x}\overline{w}_i+\frac{\partial N_i}{\partial z}\overline{u}_i\right)n_x+\sum_{i=1}^{n}\left(\frac{\partial N_i}{\partial y}\overline{w}_i+\frac{\partial N_i}{\partial z}\overline{v}_i\right)n_y\right.\\
&\qquad\left.+\frac{2}{1-2\nu}\left((1-\nu)\sum_{i=1}^{n}\frac{\partial N_i}{\partial y}\overline{v}_i+\nu\sum_{i=1}^{n}\left(\frac{\partial N_i}{\partial x}\overline{u}_i+\frac{\partial N_i}{\partial z}\overline{w}_i\right)\right)n_z\right]\Delta s \;=\; f_{z_i}. \qquad (3.27)
\end{aligned}$$

The integral contributions defined on the LHS of equation 3.27 are performed over each sub-control volume surface, of area Δs, associated with a node.

Similarly, considering equation 3.23 for the three dimensional elasticity matrix, the following contributions to the load vector at node i can be obtained:

$$f_{x_i} \;=\; b_x\Delta v+\left[\frac{E}{1-2\nu}\epsilon_{xx}^{th}n_x+\frac{E}{1+\nu}\left[\epsilon_{xx}^{vp}n_x+\frac{1}{2}\epsilon_{xy}^{vp}n_y+\frac{1}{2}\epsilon_{xz}^{vp}n_z\right]+t_{p_x}\right]\Delta s,$$

$$\begin{aligned} f_{y_i} &= b_y\Delta v + \left[\frac{E}{1-2\nu}\epsilon^{th}_{yy}n_x + \frac{E}{1+\nu}\left[\frac{1}{2}\epsilon^{vp}_{yx}n_x + \epsilon^{vp}_{yy}n_y + \frac{1}{2}\epsilon^{vp}_{yz}n_z\right] + t_{p_y}\right]\Delta s, \\ f_{z_i} &= b_z\Delta v + \left[\frac{E}{1-2\nu}\epsilon^{th}_{zz}n_x + \frac{E}{1+\nu}\left[\frac{1}{2}\epsilon^{vp}_{zx}n_x + \frac{1}{2}\epsilon^{vp}_{zy}n_y + \epsilon^{vp}_{zz}n_z\right] + t_{p_z}\right]\Delta s. \end{aligned} \tag{3.28}$$

Here the thermal strains are defined by the linear coefficient of thermal expansion α and the temperature change ΔT as

$$\epsilon^{th}_{xx} = \epsilon^{th}_{yy} = \epsilon^{th}_{zz} = \alpha\Delta T$$

and the following relationship is utilised:

$$\epsilon^{vp}_{xx} + \epsilon^{vp}_{yy} + \epsilon^{vp}_{zz} = 0,$$

which stems from the incompressible nature of the visco-plastic strains. Again the integrations are performed over each sub-control volume surface associated with a node. The body force vector **b** contributions are assembled from sub-control volumes associated with a node.

Equations 3.27 and 3.28 represent the complete formulation of the FVM for a three dimensional elasto-visco-plastic analysis including thermal and mechanical loads and are an extension to the three dimensional elastic formulation of the FVM by Bailey and Cross [4]. With regard to the algorithm described in the previous section the initial stiffness matrix is constructed by contributions from equations 3.27 and the load vector is updated by contributions from equations 3.27. In the two dimensional case similar equations can be obtained using the appropriate matrices associated with a plane stress or strain approximation, which are described in Appendix D. Indeed, a complete two dimensional implementation of the FVM for an elasto-visco-plastic analysis involving a plane stress approximation has been described by Taylor et al [89].

Alternatively, equations 3.27 and 3.28 can be rearranged in a segregated fashion with regard to displacement components. Considering the x component of equations 3.27, it can be rearranged as follows:

$$\frac{E}{2(1+\nu)}\left[\frac{2}{1-2\nu}(1-\nu)\sum_{i=1}^{n}\frac{\partial N_i}{\partial x}\overline{u}_i + \sum_{i=1}^{n}\frac{\partial N_i}{\partial y}\overline{u}_i n_y + \sum_{i=1}^{n}\frac{\partial N_i}{\partial z}\overline{u}_i n_z\right]\Delta s = f'_{x_i}. \tag{3.29}$$

Additionally, the x component of equations 3.27 can be rearranged as

$$f'_{x_i} = b_x\Delta v + \left[\frac{E}{1-2\nu}\epsilon^{th}_{xx}n_x + \frac{E}{1+\nu}\left[\epsilon^{vp}_{xx}n_x + \frac{1}{2}\epsilon^{vp}_{xy}n_y + \frac{1}{2}\epsilon^{vp}_{xz}n_z\right] + t_{p_x}\right]\Delta s$$

$$+\frac{E}{2(1+\nu)}\left[\frac{2}{1-2\nu}\left(\nu\sum_{i=1}^{n}\left(\frac{\partial N_i}{\partial y}\overline{v}_i+\frac{\partial N_i}{\partial z}\overline{w}_i\right)\right)n_x\right.$$
$$\left.+\sum_{i=1}^{n}\frac{\partial N_i}{\partial x}\overline{v}_i n_y+\sum_{i=1}^{n}\frac{\partial N_i}{\partial x}\overline{w}_i n_z\right]\Delta s. \quad (3.30)$$

The y and z components of equations 3.27 and 3.28 can be also be arranged in similar forms to that of equations 3.29 and 3.30. Thus permitting the solution of the x, y and z components of the displacement vector in a segregated fashion. The segregated solution approach is an extension of the two dimensional approach described by Fryer et al for elastic problems [43, 42]. A two dimensional implementation of the FVM utilizing a segregated solution approach for an elasto-visco-plastic analysis with a plane strain approximation has been described by Taylor et al [90].

In this approach the algorithm described in the previous section is extended within each time step to include a segregated solution approach for the displacement variable. The segregated solution approach for the displacement is based upon the iterative algorithm originally described by Fryer et al for the solution of linear elastic problems [43, 42]. The complete algorithm is defined as follows:

(1) Assume known values of the variables σ_n, $\overline{\mathrm{u}}$, ϵ_n^{vp} and $\mathbf{f}_n$ at the time instant t_n. Calculate the visco-plastic strain rate using the following relationship obtained from equation 2.21:

$$\dot{\epsilon}_n^{vp} = g\{\sigma_n\}.$$

(2) Approximate the visco-plastic strain increment $\Delta\epsilon_n^{vp}$ and update t_n as follows:

$$\Delta\epsilon_n^{vp} = \dot{\epsilon}_n^{vp}\Delta t_n, \quad t_{n+1} = t_n + \Delta t_n.$$

(3) Update the total visco-plastic strain at the current instant in time as follows:

$$\epsilon_{n+1}^{vp} = \epsilon_n^{vp} + \Delta\epsilon_n^{vp}.$$

(4) Construct the associated coefficient matrix $\mathbf{A}$ for the displacement component ϕ and the load vector $\mathbf{b}$ using equations 3.29 and 3.30 respectively, and solve using the correction format

$$\mathbf{A}\phi^c = \mathbf{b} - \mathbf{A}\phi^{old},$$

where $\phi^{new} = \phi^{old} + \phi^{c}$.

(5) Return to step (4) and repeat for each displacement component.

(6) Return to step (4) and repeat for the next global iteration. The displacement solution has converged if the error norms and the residual norms for all the displacement components are within the convergence criterion.

$$Max\,(ENORM,\ RNORM) \leq Tolerance.$$

(7) Calculate the stress associated with the whole displacement vector $\overline{\mathbf{u}}$ assembled from each displacement component ϕ

$$\begin{aligned} \sigma_{n+1} &= \mathbf{D}\left(\epsilon_{n+1} - \epsilon_0^{th} - \epsilon_{n+1}^{vp}\right), \\ &= \mathbf{D}\mathbf{B}\overline{\mathbf{u}}_{n+1} - \mathbf{D}\epsilon_{n+1}^{vp}. \end{aligned} \tag{3.31}$$

(8) Return to step (1) and repeat for the next time step with the updated values. The solution has converged if the Euclidian norm ratio of the effective visco-plastic strain rate is within tolerance, i.e.

$$\frac{||\dot{\epsilon}_n^{eff}||}{||\dot{\epsilon}_0^{eff}||} \times 100 < \text{Tolerance}.$$

3.2.3 Time stepping schemes

The algorithms described in this section have employed an explicit time stepping scheme. This is consistent with the original FE algorithm as originally described and employed by Zienkiewicz and Cormeau [105], upon which the previously described FV algorithms are based. Alternatively, the methods employed in developing the FV algorithms will apply generally to the implicit methods employed in the FE algorithms for the solution of elasto-visco-plastic problems as described by Owen and Hinton [72]

3.2.3.1 Estimation of time step length

The estimation of the time step length is an important consideration with regard to the performance of the algorithms. The time step limit must be limited in order to both preserve numerical stability of the time integration process and to ensure solution accuracy. The methods associated with the original FE algorithm of Zienkiewicz and Cormeau [105] have been adopted in the FV algorithms and are described in the following sections.

3.2.3.2 Analytical estimation

A theoretical restriction on a fixed time step length can be derived for an elasto-visco-plastic formulation. The derivation involves the analysis of the formulation as a non-linear system of first order differential equations and was originally performed by Cormeau [23] with regard to a FE algorithm.

The derived limit ensures the stability of the solution and is dependent upon the material properties as follows:

$$\Delta t \leq \frac{4(1+\nu)}{3\gamma E}. \tag{3.32}$$

3.2.3.3 Empirical estimation

A variable time step can be obtained empirically for each interval of integration [105, 81]. The time step limit must be limited in order to both preserve numerical stability of the time integration process and to ensure solution accuracy. The magnitude of the time step is controlled by a factor τ which limits the maximum effective visco-plastic strain increment $\Delta\epsilon_n^{evp}$ as a fraction of the total effective strain ϵ_n^{eff} which implies

$$\Delta t \leq \tau \left[\frac{\epsilon_n^{eff}}{\dot{\epsilon}_n^{evp}} \right]_{min} . \tag{3.33}$$

The minimum is found over all integration points associated with an element in the structure or component. The value τ is empirically defined and for explicit time stepping schemes experience suggests values in the range $0.01 < \tau < 0.1$. Additionally, experience suggests that the change in time step length between any two integration intervals is limited to

$$\Delta t_{n+1} \leq 1.5\Delta t_n.$$

For many problems the choice of time step calculation is not a major issue. In general the empirical scheme is more robust and handles problems involving a number of materials without any extra consideration and is generally employed throughout this research.

3.3 Linear solvers

At this point it is important to note that the two algorithmic approaches described in this Chapter furnish differently conditioned matrices as associated with the linear system of equations to be solved.

For the segregated algorithmic approach the matrices are always diagonally dominant and fully iterative linear solvers, such as the Gauss-Seidel (GS) and Successive Over Relaxation (SOR) solution procedures [9], can be employed. Alternatively, semi-direct solvers can be employed. Hence, the Conjugate Gradient Method (CGM) and the BiConjugate Gradient Method (BiCGM) [9] can be employed when the matrices are symmetric and asymmetric, respectively. In both cases it is possible to precondition the matrices to improve the efficiency of the particular solver employed [42, 43].

For the whole field algorithm the matrices are not generally diagonally dominant and fully iterative procedures are not practical [9]. For this reason the above described semi-direct solvers are employed. It is also important to note that the FEM employed in this research will always furnish a symmetric matrix and a CGM solver can always be employed.

It is also important to note that a compacted storage technique is employed for the sparse matrices encountered in this research and the linear solvers are modified accordingly [9].

3.4 Axisymmetric problems

For a number of CSM problems involving cylindrical polar (r, θ, z) coordinates it is possible to assume the solution is invariant in the hoop or θ direction, which leads to axial symmetry about the z axis.

Considering the axisymmetric stress equilibrium equations [38]

$$\begin{aligned}\frac{\partial \sigma_{rr}}{\partial r}+\frac{\partial \sigma_{rz}}{\partial z}-\frac{\sigma_{rr}-\sigma_{\theta\theta}}{r} &= 0,\\ \frac{\partial \sigma_{zr}}{\partial r}+\frac{\partial \sigma_{zz}}{\partial z}-\frac{\sigma_{zr}}{r} &= 0.\end{aligned}$$

Where body forces are neglected.

It is possible, using the following expressions:

$$\begin{aligned}\frac{1}{r}\frac{\partial\left(r\sigma_{rr}\right)}{\partial r} &= \frac{1}{r}\frac{r\partial\sigma_{rr}}{\partial r}+\frac{\sigma_{rr}}{r},\\ \frac{1}{r}\frac{\partial\left(r\sigma_{rz}\right)}{\partial r} &= \frac{1}{r}\frac{r\partial\sigma_{rz}}{\partial r}+\frac{\sigma_{rz}}{r},\end{aligned}$$

to rearrange the equilibrium equations as

$$\begin{aligned}\frac{1}{r}\frac{\partial\left(r\sigma_{rr}\right)}{\partial r}+\frac{\partial \sigma_{rz}}{\partial z}-\frac{\sigma_{\theta\theta}}{r} &= 0,\\ \frac{1}{r}\frac{\partial\left(r\sigma_{zr}\right)}{\partial r}+\frac{\partial \sigma_{zz}}{\partial z} &= 0.\end{aligned}$$

Integrating the above equations over a control volume bounded by the closed curve c and then applying Stokes's theorem (in the plane) as described in Appendix A.3, to the first two terms in both the above equations furnishes,

$$\begin{aligned}\oint_c \left(r\sigma_{rr}dz - r\sigma_{rz}dr\right)-\iint \sigma_{\theta\theta}drdz &= 0,\\ \oint_c \left(r\sigma_{zr}dz - r\sigma_{zz}dr\right) &= 0.\end{aligned}$$

It is now apparent that a considerable disadvantage of the FVM should be noted, when compared to the standard FEM, for axisymmetric problems. The disadvantage arises as it is not possible to transform all the integral terms in the above equations from surface integrals to line integrals, hence complicating the FVM.

This point is further illustrated when comparing the FVM and the FEM with regard to matrix formulations. In Appendices D.2 and D.5 the elasticity matrix and the differential operator associated with the standard FEM, when applied to axisymmetric problems are described, respectively, but it is not possible when applying standard control volume techniques to derive a corresponding normal operator matrix as required by the FVM described here.

This complication was discussed by Fryer [42] with regard to a segregated algorithmic approach and a hybrid numerical scheme involving line and surface integrals was employed, with the surface integrals appearing as additional source terms [42]. This was feasible as the originally linear elastic problem was solved in a non-linear fashion, when the segregated algorithmic approach was employed [42].

Conversely, when the whole field algorithmic approach is employed the same technique was not possible as the whole displacement field is solved in one linear iteration. For this reason it was not possible to include the axisymmetric approximation in the general description and formulation of the FVM with regard to the whole field algorithm.

3.5 Closure

In this chapter, the essential differences of the FVM and the FEM have been highlighted with regard to numerical algorithms for the solution of mechanical problems involving material non-linearity. Additionally, two FV algorithmic approaches have been described, a whole field displacement and a segregated displacement technique.

The algorithms described in this chapter will be applied to a variety of mechanical problems in the following chapters in order to compare their suitability.

Chapter 4

Numerical Analysis

In this chapter the numerical techniques as described in the previous chapter are compared and analysed in detail. Initially, the CV-UM vertex based FVM and the Bubnov-Galerkin FEM are shown to be equivalent for an academic one dimensional comparison. Next, the two techniques are compared and analysed for the two dimensional case with a full description of the computational elements in both cases. Finally, the three dimensional implementations are also compared and analysed again in both cases. In the remaining chapter, the Bubnov-Galerkin FEM will be simply referred to as the FEM and the CV-UM vertex based FVM will be simply referred to as the FVM.

4.1 Theoretical analysis of discretisation

In this section, the FVM and the FEM will be analysed and compared in detail. The analysis and comparison is performed in a one, two and three dimensional context. In each case, the similarities and differences of the two methods are described.

As visco-plasticity is time dependent, a time stepping scheme must be introduced in order to describe the situation numerically. A time stepping scheme allows the solution to march through the instances in time t_n and t_{n+1} using the time step Δt_n as follows:

$$t_{n+1} = t_n + \Delta t_n,$$

where the subscripts denote successive time steps. A number of time stepping schemes are available as described in the previous chapter, the simple Euler method is adopted for this analysis. Using the Euler method it is possible to integrate the visco-plastic strain rate vector over a time step and obtain the following visco-plastic strain increment vector;

$$\Delta\epsilon_n^{vp} = \dot{\epsilon}_n^{vp}\Delta t_n.$$

From this integration the total visco-plastic strain vector

$$\epsilon_{n+1}^{vp} = \epsilon_n^{vp} + \Delta\epsilon_n^{vp},$$

occurring at the time instant t_{n+1}, is obtained. Having obtained the total visco-plastic strain vector, it is now possible to perform a numerical analysis of a visco-plastic problem.

4.1.1 One Dimensional Analysis

The one dimensional analysis is presented in order to compare the two approaches in their simplest forms. A one dimensional approach is not practical for the numerical applications in this research, but it is useful from a theoretical viewpoint.

The problem illustrated in Figure 4.1 consists of a one dimensional, two noded element with linear displacement variation. The problem was analyzed for the FEM by Owen and Hinton [72]. Assuming that the total visco-plastic strain is constant over the element, the change of length of this element due to the total visco-plastic strain at time t_{n+1} is

$$u_{n+1} = \epsilon_{n+1}^{vp} L,$$

where ϵ_{n+1}^{vp} is the one dimensional total visco-plastic strain. Including the additional change in length due to the applied load at a node p_{n+1}, occurring at the time instant t_{n+1}, gives

$$u_{n+1} = \epsilon_{n+1}^{vp} L + \frac{L}{AE} p_{n+1}, \tag{4.1}$$

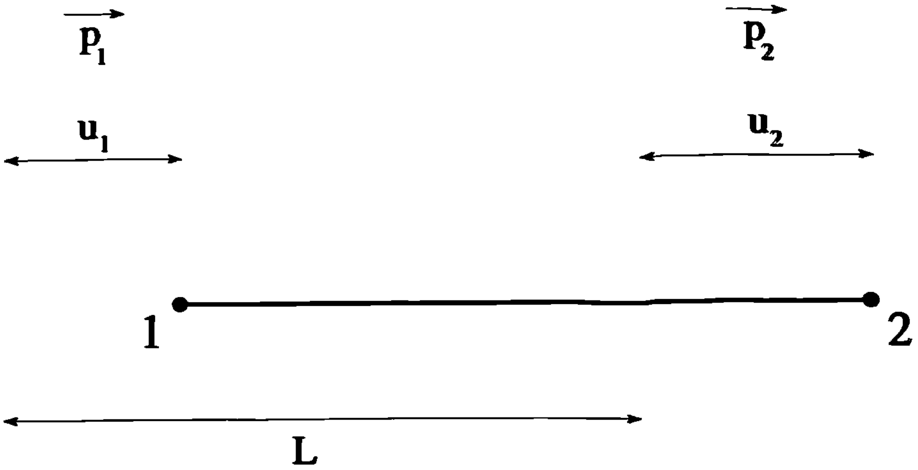

Figure 4.1: One dimensional, two noded element.

where E is Young's modulus, A is the cross-sectional area and L is the element length. Equation (4.1) can be expressed in matrix form,

$$\mathbf{u}_{n+1} = \mathbf{K}^{-1}\mathbf{f}_{n+1},$$

where the displacements and nodal forces are

$$\begin{aligned} \mathbf{u}_{n+1} &= \begin{bmatrix} u_1 \\ u_2 \end{bmatrix}_{n+1}, \\ \mathbf{f}_{n+1} &= AE\epsilon^{vp}_{n+1}\begin{bmatrix} 1 \\ -1 \end{bmatrix} + \begin{bmatrix} p_1 \\ p_2 \end{bmatrix}_{n+1} \end{aligned} \tag{4.2}$$

and the elemental stiffness matrix is

$$\mathbf{K}^e = \frac{EA}{L}\begin{bmatrix} 1 & -1 \\ -1 & 1 \end{bmatrix}. \tag{4.3}$$

It should be noted that $\mathbf{K}^e$ cannot be inverted directly in the present form, but if a fixed displacement is applied to the single element or element assembly form then inversion is possible as the matrix then becomes non-singular.

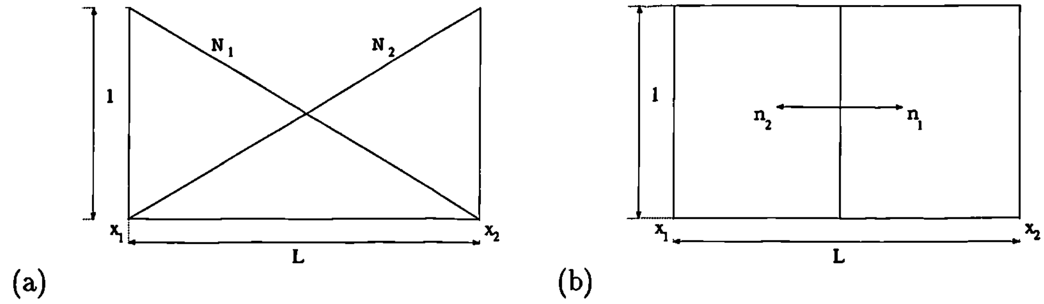

Figure 4.2: 1D (a) shape functions and FEM weighting functions, (b) FVM weighting functions.

The expressions obtained by the previous one dimensional analysis can be obtained directly from the FEM and the FVM. This can be achieved using the simplified elemental versions of the general FEM equations (3.19) and (3.20),

$$\begin{aligned} \mathbf{K}_e^{\mathrm{fe}} &= \int_v \mathbf{B}^{\mathrm{T}}\mathbf{D}\mathbf{B}\,dv, \\ \mathbf{f}_{n+1}^{\mathrm{fe}} &= -\int_v \mathbf{B}^{\mathrm{T}}\mathbf{D}\epsilon_{n+1}^{vp}\,dv + \mathbf{p}_{n+1} \end{aligned} \tag{4.4}$$

and the simplified elemental versions of the general FVM equations (3.22) and (3.23)

$$\begin{aligned} \mathbf{K}_e^{\mathrm{fv}} &= -\int_s \mathbf{R}^{\mathrm{T}}\mathbf{D}\mathbf{B}\,ds, \\ \mathbf{f}_{n+1}^{\mathrm{fv}} &= \int_s \mathbf{R}^{\mathrm{T}}\mathbf{D}\epsilon_{n+1}^{vp}\,ds + \mathbf{p}_{n+1}. \end{aligned} \tag{4.5}$$

Surface tractions, thermal strains and body forces are neglected in equations (4.4) and (4.5) for simplicity.

For the one dimensional case described in Figure 4.1

$$\begin{aligned} \int_v dv &= AL, \\ \int_s ds &= A, \\ \mathbf{D} &= E. \end{aligned}$$

The displacement variation is assumed linear and can be described by shape functions of the following form:

$$\mathbf{N} = \begin{bmatrix} N_1 \\ N_2 \end{bmatrix} = \begin{bmatrix} \frac{x_2 - x}{L} \\ \frac{x - x_1}{L} \end{bmatrix}.$$

The shape functions are illustrated in Figure 4.2(a) and are used to approximate the displacement derivative in both the FEM and the FVM. They are also equivalent to the weighting functions in the FEM. For the one dimensional case $\mathbf{L} = d/dx$ and using equation (3.21)

$$\mathbf{B} = \mathbf{L}\mathbf{N} = \begin{bmatrix} -1/L \\ 1/L \end{bmatrix}. \tag{4.6}$$

Also, the normal operator

$$\mathbf{R} = \begin{bmatrix} n_1 \\ n_2 \end{bmatrix} = \begin{bmatrix} \cos\alpha_1 \\ \cos\alpha_2 \end{bmatrix} = \begin{bmatrix} 1 \\ -1 \end{bmatrix}, \tag{4.7}$$

where α is the angle of the outward normal with respect to the one dimensional coordinate, in this case x. The normals and the weighting functions for the FVM are illustrated in Figure 4.2(b).

It is now possible to substitute $\mathbf{B}$ and $\mathbf{R}$ as defined by equations (4.6) and (4.7), respectively, into equations (4.4) and (4.5) relating to the FEM and the FVM, respectively.

Hence,

$$\mathbf{K}_e^{\text{fe}} = \int_v \mathbf{B}^{\mathrm{T}}\mathbf{D}\mathbf{B}dv = \begin{bmatrix} -1/L & 1/L \end{bmatrix} E \begin{bmatrix} -1/L \\ 1/L \end{bmatrix} AL = \frac{EA}{L}\begin{bmatrix} 1 & -1 \\ -1 & 1 \end{bmatrix}$$

and

$$\mathbf{K}_e^{\text{fv}} = -\int_s \mathbf{R}^{\mathrm{T}}\mathbf{D}\mathbf{B}ds = -\begin{bmatrix} 1 & -1 \end{bmatrix} E \begin{bmatrix} -1/L \\ 1/L \end{bmatrix} A = \frac{EA}{L}\begin{bmatrix} 1 & -1 \\ -1 & 1 \end{bmatrix}.$$

Similarly, as the total visco-plastic strain is constant over the element

$$\begin{aligned} \mathbf{f}_{n+1}^{\text{fe}} &= -\int_v \mathbf{B}^{\mathrm{T}}\mathbf{D}\epsilon_{n+1}^{vp}dv + \mathbf{p}_{n+1} = -\begin{bmatrix} -1/L & 1/L \end{bmatrix} E\epsilon_{n+1}^{vp}AL + \begin{bmatrix} p_1 \\ p_2 \end{bmatrix}_{n+1} \\ &= AE\epsilon_{n+1}^{vp}\begin{bmatrix} 1 \\ -1 \end{bmatrix} + \begin{bmatrix} p_1 \\ p_2 \end{bmatrix}_{n+1} \end{aligned}$$

and

$$\begin{aligned} \mathbf{f}_{n+1}^{\text{fv}} &= \int_s \mathbf{R}^{\mathrm{T}}\mathbf{D}\epsilon_{n+1}^{vp}ds + \mathbf{p}_{n+1} = \begin{bmatrix} 1 & -1 \end{bmatrix} E\epsilon_{n+1}^{vp}A + \begin{bmatrix} p_1 \\ p_2 \end{bmatrix}_{n+1} \\ &= AE\epsilon_{n+1}^{vp}\begin{bmatrix} 1 \\ -1 \end{bmatrix} + \begin{bmatrix} p_1 \\ p_2 \end{bmatrix}_{n+1}. \end{aligned}$$

In both cases the resulting equations are directly equivalent to those described by equations (4.2) and (4.3). Hence, the numerical equivalence of the two methods is illustrated with regard to a one dimensional analysis.

4.1.2 Two Dimensional Analysis

Directly equivalent meshes can be handled by the FEM and the FVM, though the stiffness or system matrix contributions are computed differently. The differing elemental contributions per element are illustrated in Figure 4.3 for a general cluster of two dimensional elements surrounding an arbitrary mesh vertex. Figure 4.3(a) illustrates the integration points associated with the elemental contributions for the FVM and Figure 4.3(b) illustrates the Gauss points associated with the elemental contributions for the FEM.

As in the traditional FEM context it is computationally convenient to work in local coordinates so that all elements can be treated identically regardless of how distorted any element may be in terms of global coordinates. The local coordinate systems for triangular and quadrilateral elements are illustrated in Figures 4.4 and Figures 4.7 respectively.

The mapping from local coordinates to global coordinates is performed via shape functions using the standard FEM techniques. The elements described here are isoparametric, thus allowing the shape functions to be utilised for both coordinate transformation and variable approximation. The standard processes of local-global coordinate and derivative transformations as associated with the FEM are described generally in Appendix C, regardless of element type or dimension.

4.1.2.1 Constant strain triangular elements

Directly equivalent shape functions are utilised in the application of both the FEM and the FVM to describe the variation of the displacement (or any other variable) over an element. The shape functions for constant strain triangular (CST) elements are described in Appendix B.

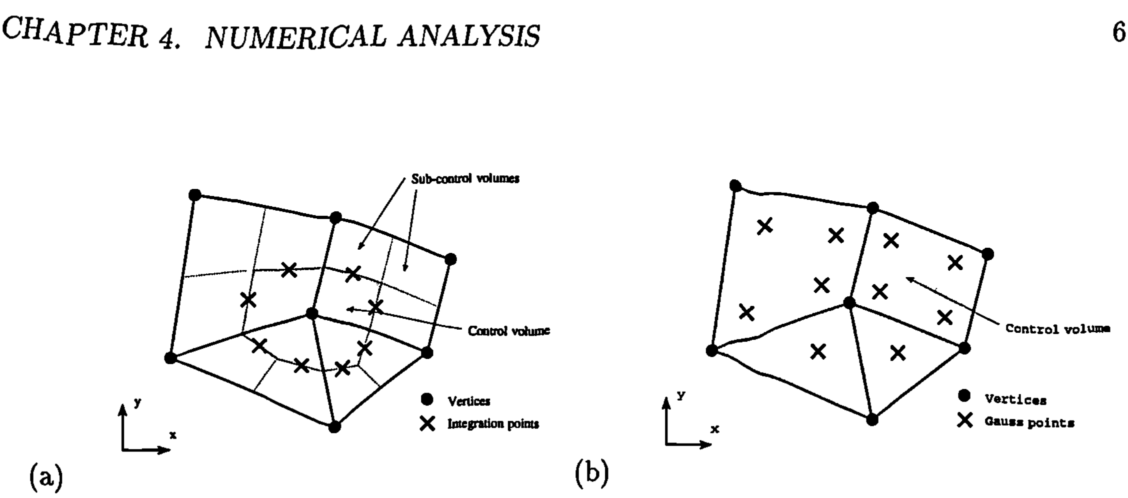

Figure 4.3: Two dimensional integration points (a) FVM and (b) FEM.

The representation of CST elements in local coordinates is illustrated for the FEM and the FVM in Figures 4.4b and 4.4c respectively, both are representations of an arbitrarily deformed CST element in global coordinates as illustrated in Figure 4.4a. In the FEM case the CST element involves one Gauss point, where as in the FVM three integration points are required to construct the associated sub-control volumes.

It is important to note that it is possible to analyse and compare the FVM and the FEM for the CST element due to its simple linear nature. Indeed, it has been shown by Oñate et al [71] that, for elastic problems involving CST elements, the internal force terms contributing to the element stiffness matrix coincide exactly for the FVM and the FEM. Hence, the two methods produce identical stiffness (or coefficient) matrices for two dimensional problems involving CST elements. It should also be noted at this point, that this indicates the general agreement in accuracy between the different integration processes involved in the two methods.

Extending the linear elastic analysis of Oñate et al [71] to problems involving material non-linearity, it can be further shown that the external force terms generated by the visco-plastic strains are also identical for the two methods in the case of two dimensional problem involving CST elements. The visco-plastic terms are described in general for the FEM and FVM in equations 3.20 and 3.23 respectively.

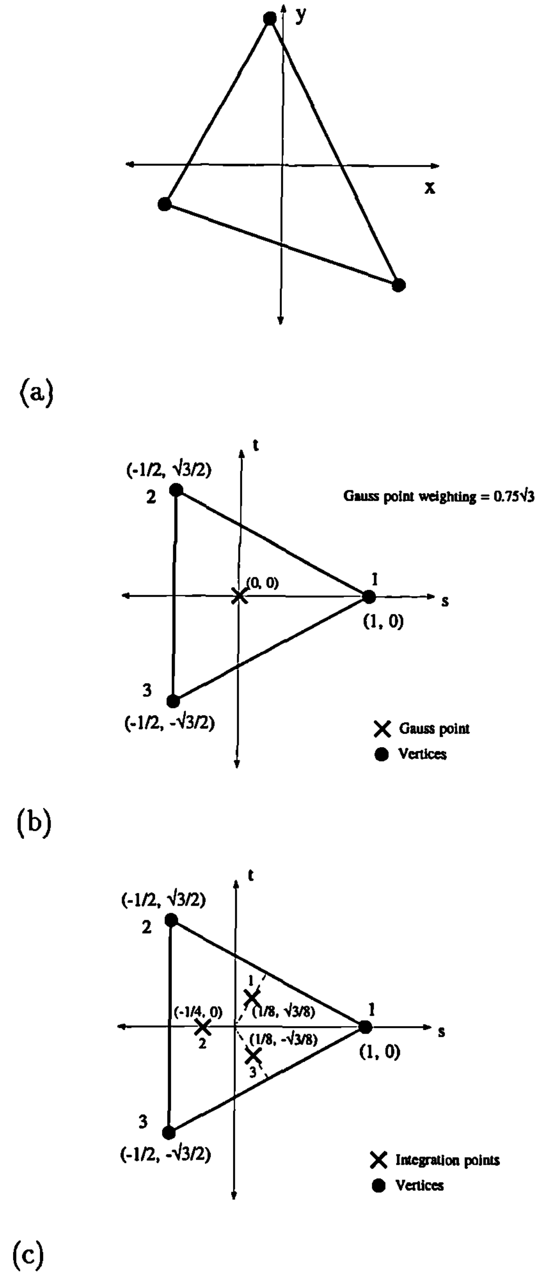

Figure 4.4: CST element. (a) Global, (b) FEM local and (c) FVM local coordinates.

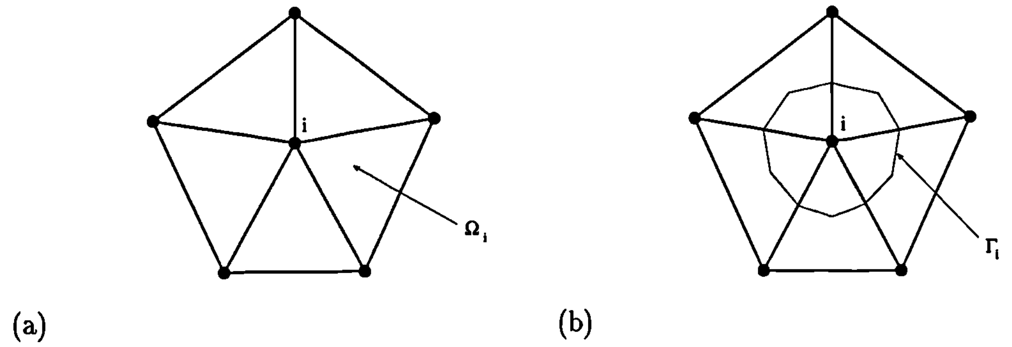

Figure 4.5: Elemental contributions to the control volume at node i (a) FEM and (b) FVM.

Concentrating on the visco-plastic terms the external force contributions at a node i are

$$\begin{aligned} \mathbf{f}_i^{fe} &= -\int_{\Omega_i} \mathbf{B}_i^{\mathrm{T}} \mathbf{D} \epsilon^{vp}\, d\Omega, \\ \mathbf{f}_i^{fv} &= +\int_{\Gamma_i} \mathbf{R}_i^{\mathrm{T}} \mathbf{D} \epsilon^{vp}\, d\Gamma. \end{aligned} \tag{4.8}$$

for the FEM and the FVM respectively. Where, for the general case $\mathbf{B} = \mathbf{LN}$ and the general two dimensional differential operator $\mathbf{L}$ is described in Appendix D. The shape functions for CST elements are described in Appendix B and the plane stress or strain elasticity matrices and the general two dimensional normal operator $\mathbf{R}$ are also described in Appendix D.

Consider a collection of CST elements surrounding a node i, as illustrated in Figures 4.5a and 4.5b for the FEM and the FVM respectively. The kth component of the external force vector due to visco-plastic strains for the FEM with contributions from n_{el} elements is

$$f_{ik}^{fe} = -\sum_{e=1}^{n_{el}} \int_{\Omega_i^e} \frac{\partial N_i^e}{\partial x_j} D^e \epsilon^e_{vp_{jk}} \mathrm{d}\Omega = \sum_{e=1}^{n_{el}} D^e \epsilon^e_{vp_{jk}} \left(-\int_{\Omega_i^e} \frac{\partial N_i^e}{\partial x_j} \mathrm{d}\Omega \right) \tag{4.9}$$

at node i.

Alternatively, for the FVM it is

$$f_{ik}^{fv} = \sum_{e=1}^{n_{el}} \int_{\Gamma_i^e} n_j D^e \epsilon^e_{vp_{jk}} \mathrm{d}\Gamma = \sum_{e=1}^{n_{el}} D^e \epsilon^e_{vp_{jk}} \left(\int_{\Gamma_i^e} n_j \mathrm{d}\Gamma \right). \tag{4.10}$$

In both cases the visco-plastic strain tensor is constant over the element, thus allowing the visco-plastic strain factor to be taken outside of the integral. This is a consequence of

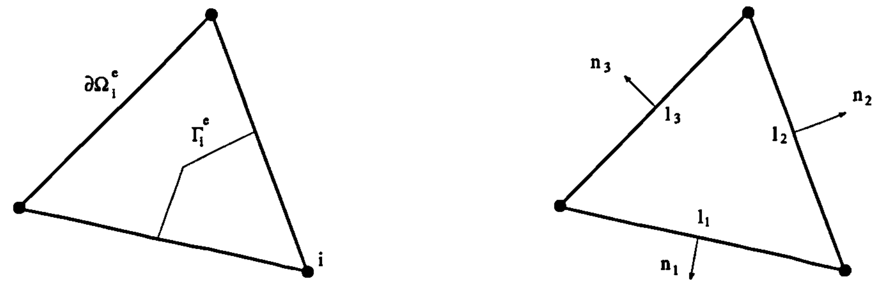

Figure 4.6: Single CST (a) elemental contributions and (b) sides and lengths.

the linear nature of the element which furnishes strain and other associated constitutive variables as constants over the element.

Hence, the contributions for the two methods are identical if the bracketed integrals in equations 4.9 and 4.10 are equivalent. The equivalence of these two integrals has been comprehensively described by Oñate et al [71] in the analysis of elastic problems. The proof is also described here in order to provide a complete analysis of CST elements.

Concentrating on a single element, taken from the collection described in Figure 4.5a, it is possible to analyse the elemental contributions for the FEM and the FVM as illustrated in Figure 4.6a. The element is assumed to consist of sides of lengths l_1, l_2, l_3 and unit outward normals $\mathbf{n_1}, \mathbf{n_2}, \mathbf{n_3}$ as illustrated in Figure 4.6b. The boundary of the element is $\partial\Omega_i^e$ and the elemental contribution to the FVM control volume boundary is Γ_i^e.

Hence, the following derivation is possible:

$$\int_{\Omega_i^e} \frac{\partial N_i^e}{\partial x_j} \mathrm{d}\Omega = \int_{\partial\Omega_i^e} n_j N_i \mathrm{d}\Gamma = n_{1j}\frac{1}{2}l_1 + n_{2j}\frac{1}{2}l_2 = -\int_{\Gamma_i^e} n_j \mathrm{d}\Gamma \qquad (4.11)$$

which is in essence obtained by application of the divergence theorem as described in Appendix A.

The direct equivalence of the two methods for problems involving material non-linearity is an important consideration and is further illustrated by the results obtained when modelling two dimensional applications with CST elements. This equivalence will also be highlighted in the following chapter for a variety of numerical applications.

4.1.2.2 Bilinear quadrilateral elements

As for the previous CST elements, directly equivalent shape functions are utilised in the application of both the FEM and the FVM to describe the variation of the displacement over an element. The shape functions for bilinear quadrilateral (BLQ) elements are described in Appendix B.

The representation of BLQ elements in local coordinates is illustrated for the FEM and the FVM in Figures 4.7b and 4.7c respectively, both are representations of an arbitrarily deformed BLQ element in global coordinates as illustrated in Figure 4.7a. In the FEM case the BLQ element involves four Gauss points, similarly in the FVM four integration points are required to construct the associated sub-control volumes.

At present there is no accurate method available to analyse and compare the implementation of higher order two dimensional elements, such as BLQ elements. The previous method for CST elements relies on the fact that the strain and associated constitutive variables are constant over the element. This is not the case for BLQ elements, which by definition are bilinear as opposed to linear, and hence the strain and associated constitutive values vary linearly over the element. Though it is possible to assume that BLQ elements will approach a condition where there is limited variation of the constitutive variables over an element for a suitably refined mesh. Hence, indicating the equivalence of the two methods in that limit. Indeed, as indicated by the numerical results in the following chapter, this is apparently the case, but it does not provide a method of determining which method is superior or inferior with regard to accuracy.

It should be noted that for BLQ elements the FVM and the FEM will always provide distinctive elemental contributions.

Finally, the issue of asymmetric elemental stiffness contributions arises for non-orthogonal

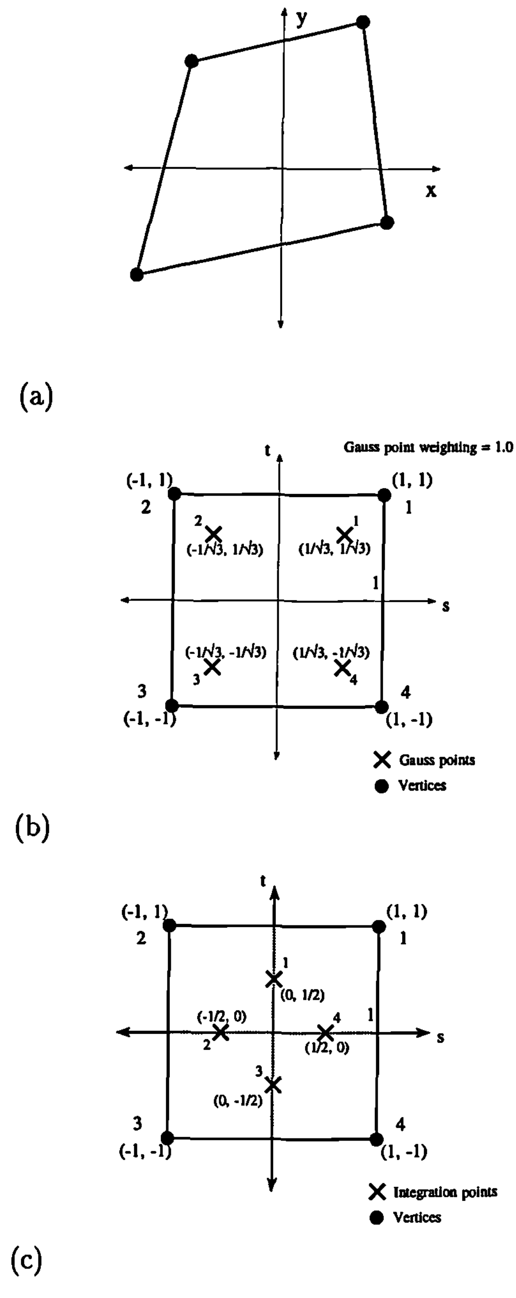

Figure 4.7: BLQ element. (a) Global, (b) FEM local and (c) FVM local coordinates.

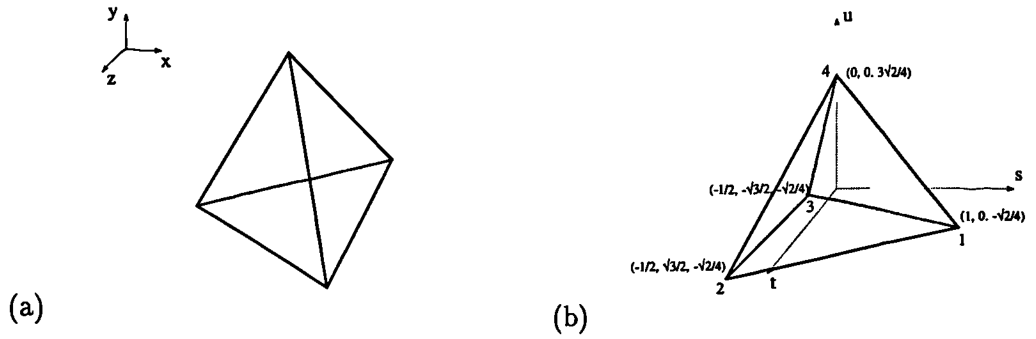

Figure 4.8: Linear tetrahedral element in (a) global coordinates and (b) local coordinates.

BLQ elements. This leads to an asymmetric coefficient matrix, which requires specialised linear solvers. This is opposite to the FEM which will always produces a symmetric elemental stiffness contribution, regardless of the orthogonality of the element concerned. This issue will be further highlighted in the following chapter for a variety of numerical applications.

4.1.3 Three Dimensional Analysis

In this section the implementation of three dimensional elements in the FEM and the FVM will be described and compared. As in the case of the CST element, it is possible to analyse and compare the FVM and the FEM for the linear tetrahedral element. Unfortunately, as with BLQ elements in the two dimensional case no simple analytical comparison is available with regard to the higher order bilinear or trilinear elements in three dimensions, though the same arguments apply with regard to closer agreement of the two methods in the limit of a suitably refined mesh.

The three dimensional elements discussed in this section are illustrated in both global and local coordinates in Figures 4.8, 4.9 and 4.10 respectively. The element described in Figures 4.8a and 4.8b is the linear tetrahedral (LT) element, while the element described in Figures 4.9a and 4.9b is the bilinear pentahedral (BLP) or wedge element and the element described in Figures 4.10a and 4.10b is the trilinear hexahedral (TLH) or brick element.

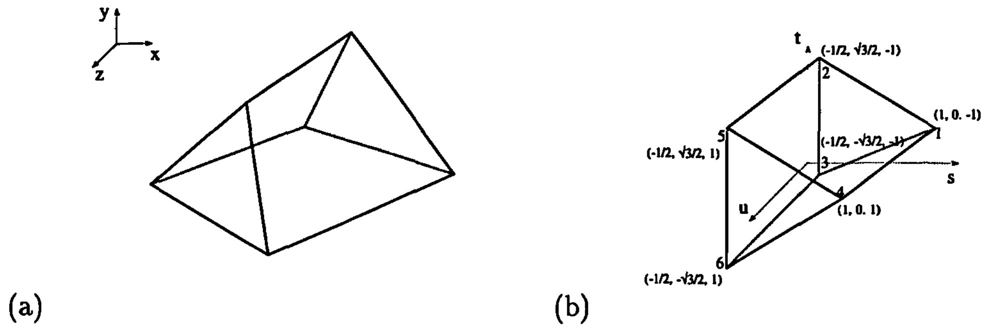

Figure 4.9: Bilinear pentahedral element in (a) global coordinates and (b) local coordinates.

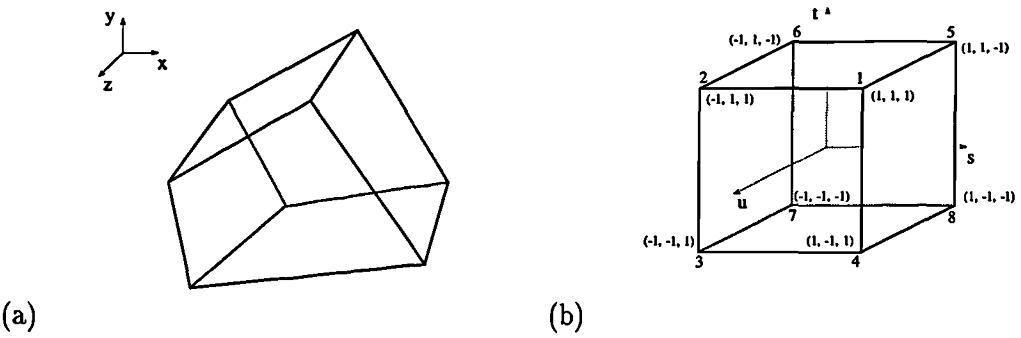

Figure 4.10: Trilinear hexahedral element in (a) global coordinates and (b) local coordinates.

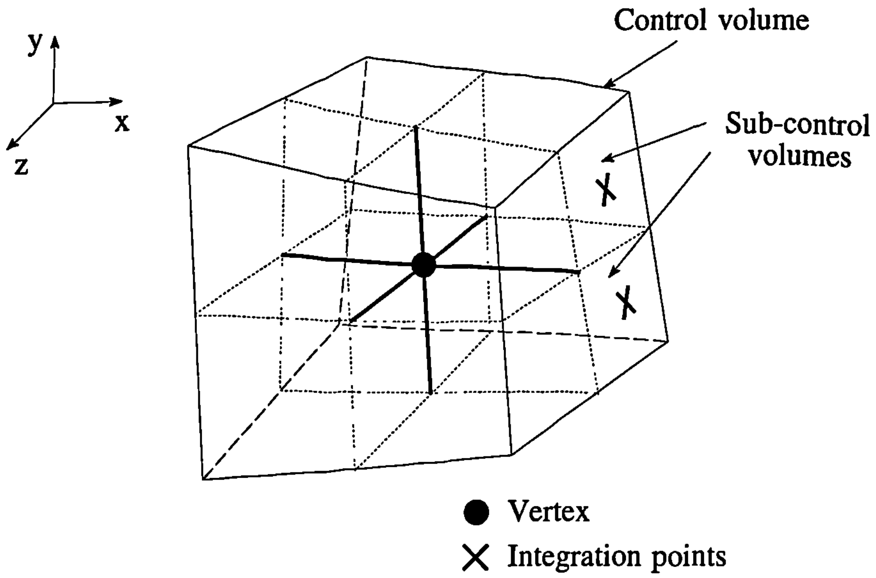

Figure 4.11: Three dimensional vertex based control volume.

As for the two dimensional case, directly equivalent meshes can be handled by the FEM and the FVM, though the stiffness matrix contributions are computed differently. Additionally, the global to local mapping of the elements again allows an arbitrarily deformed three dimensional element to be treated identically in computational terms.

For the FVM the construction of the sub-control volumes is a relatively straight forward extension of the two dimensional approach, except that in the three dimensional approach the control volumes are defined by internal surfaces of the mesh element. In this way it is possible to construct a control volume consisting of cubic sub-control volume contributions from associated elements.

This approach is illustrated in Figure 4.11 for the simple case of eight arbitrary elements contributing to a vertex based control volume. The control volume consists of the eight surrounding cubic sub-control volumes. Each sub-control volume has three integration points associated with it, which are situated at the face centres. It should be noted that it is possible to utilise a numerical integration scheme involving a greater number of weighted integration points. Though this approach is relatively straight forward it has not been investigated in the research presented here, as it essentially involves the further comparison of the two methods for higher order numerical integration point schemes. This research is restricted to comparing equivalent lower order integration schemes for the two methods.

Finally, it should be noted that the case works equally well for a vertex with n associated elements, where n may consist of a variety of element types, such as tetrahedra, wedges or bricks.

4.1.3.1 Linear Tetrahedral elements

The shape functions associated with both the FVM and the FEM for linear tetrahedral (LT) elements are described in Appendix B. Naturally, as in the two dimensional case, the nodal points are equivalently defined in the local coordinate system for the FEM and the FVM. This is necessary in order to be consistent with the shape functions. The LT element is described in local coordinates in Figure 4.8b.

Obviously, the coordinates for the FEM Gauss points and the FVM integration points are different. To illustrate this difference the Gauss point for the FEM and the integration points for the FVM are described in Figure 4.12 and Figures 4.13 respectively. The six integration points for the FVM are illustrated in Figure 4.13a and Figure 4.13b, where as the single Gauss point is illustrated in Figure 4.12. The weighting associated with the Gauss point is equivalent to the volume the tetrahedron occupies in the local coordinate system.

For the FVM the six integration points coincide with the six internal surfaces required to construct the four cubic sub-control volumes associated with a LT element.

It is important to note that it is possible to analyse and compare the FVM and the FEM for the LT element due to its simple linear nature. It is possible to extend the previous two dimensional analysis of CST elements to the three dimensional analysis of LT elements.

The previous analysis was dimensionless upto the consideration of the equivalence of the

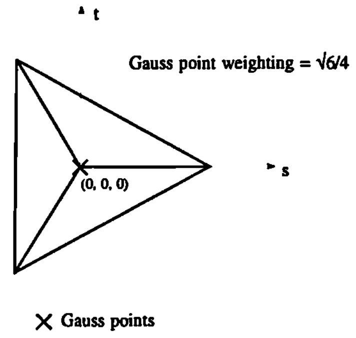

Figure 4.12: LT element Gauss point in local coordinates and associated weighting.

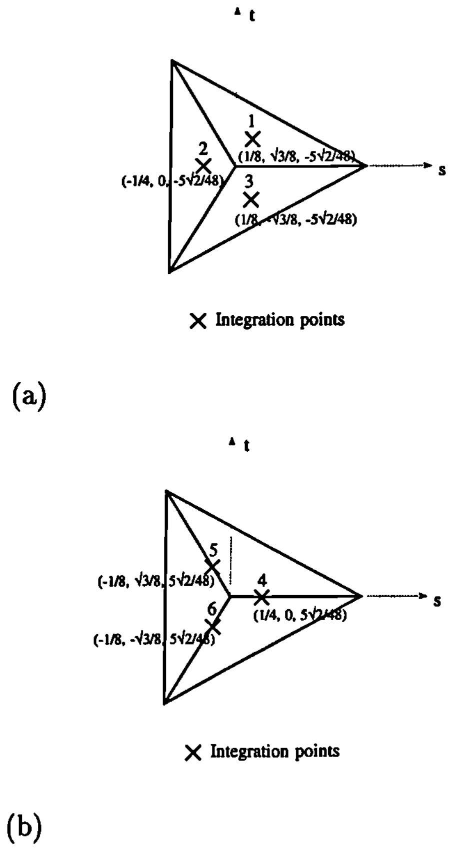

Figure 4.13: LT element integration points in local coordinates (a) vertical and (b) horizontally inclined.

two integrals as described in equations 4.9 and 4.10. It is further possible to prove the equivalence of these two integrals with regard to LT elements. Consider a cluster of LT elements surrounding the vertex i in a similar fashion to that described for CST elements in Figure 4.6(a).

In this three dimensional case it is possible to consider a single LT element from the cluster with surfaces of area s_1, s_2, s_3 and s_4 and unit outward normals $\mathbf{n_1}, \mathbf{n_2}, \mathbf{n_3}$ and $\mathbf{n_4}$.

Hence, extending the derivation described in equation 4.11 for CST elements to the case of LT elements it follows that

$$\int_{\Omega_i^e} \frac{\partial N_i^e}{\partial x_j} \mathrm{d}\Omega = \int_{\partial\Omega_i^e} n_j N_i \mathrm{d}\Gamma = n_{1j}\frac{1}{3}s_1 + n_{2j}\frac{1}{3}s_2 + n_{3j}\frac{1}{3}s_3 = -\int_{\Gamma_i^e} n_j \mathrm{d}\Gamma, \tag{4.12}$$

where $\partial\Omega_i^e$ remains the boundary of the element and Γ_i^e is the elemental contribution to the FVM control volume. It should be noted that the LT element is orientated such that surface s_4 is opposite vertex i.

4.1.3.2 Bilinear Pentahedral elements

The shape functions associated with both the FVM and the FEM for bilinear pentahedral (BLP) elements are described in Appendix B. The BLP element is described in local coordinates in Figure 4.9b.

The Gauss points for the FEM are described in Figures 4.14 and the integration points for the FVM are described in Figures 4.15. The nine integration points for the FVM are drawn in three planes, Figure 4.15a, Figure 4.15b and Figure 4.15c, where as the six Gauss points are drawn in two planes in Figure 4.14a and Figure 4.14b.

For the FVM the nine integration points coincide with the nine internal faces required to construct the six cubic sub-control volumes associated with a BLP element. The elemental stiffness matrices formed from a BLP element also distinctive for the two methods. Additionally, for the FVM an asymmetric elemental contribution is added to the coefficient matrix for BLP elements when the triangular faces are non-orthogonal or not equilateral,

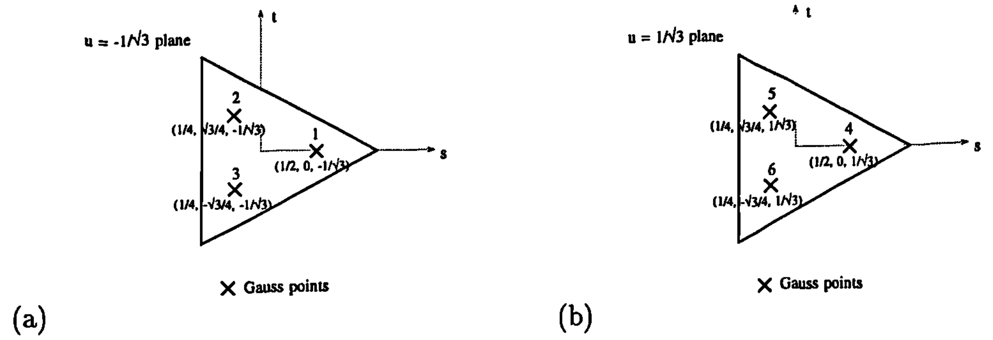

Figure 4.14: BLP Gauss points in local coordinates. (a) $u = -1/\sqrt{3}$ and (b) $u = 1/\sqrt{3}$.

where as for the FEM the contributions are again always symmetric.

The consequence of this asymmetry is analysed and discussed with regard to linear solvers in the following chapters.

4.1.3.3 Trilinear Hexahedral elements

The shape functions associated with both the FVM and the FEM for trilinear hexahedral elements (TLH) are described in Appendix B. The TLH element is described in the local coordinate system in Figure 4.10b.

The twelve integration points for the FVM are drawn in three planes, Figures 4.17a, 4.17b and 4.17c, where as the eight Gauss points are drawn in two planes, Figures 4.16a and 4.16b.

For the FVM the twelve integration points coincide with the twelve internal surfaces required to construct the eight cubic sub-control volumes associated with a TLH element.

The elemental stiffness matrices formed from a TLH element are again different for the two methods. Additionally, for the FVM an asymmetric contribution to the coefficient matrix is provided for non-orthogonal elements, where as for the FEM the contributions are always

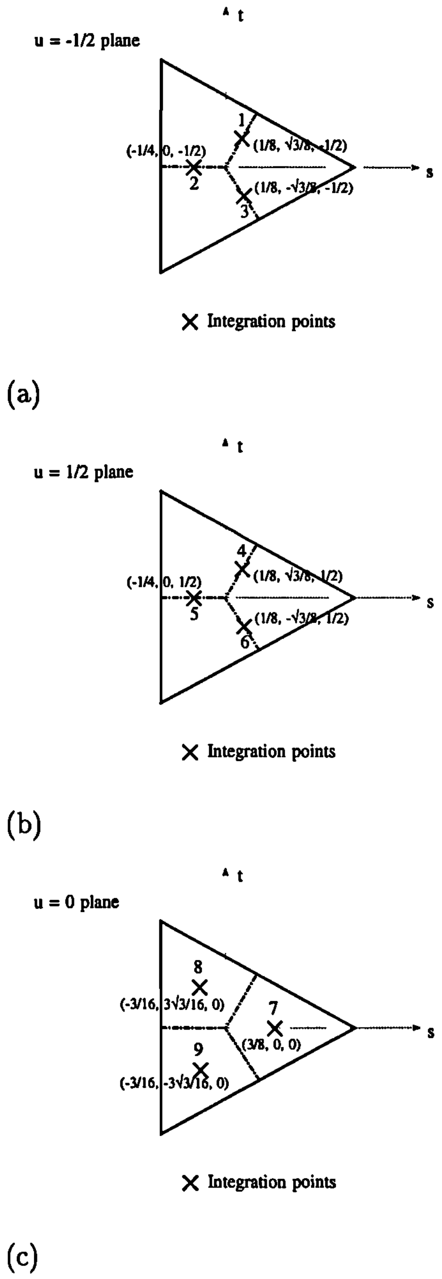

Figure 4.15: BLP FVM integration points in local coordinates. (a) $u = -\frac{1}{2}$, (b) $u = \frac{1}{2}$ and (c) $u = 0$ planes.

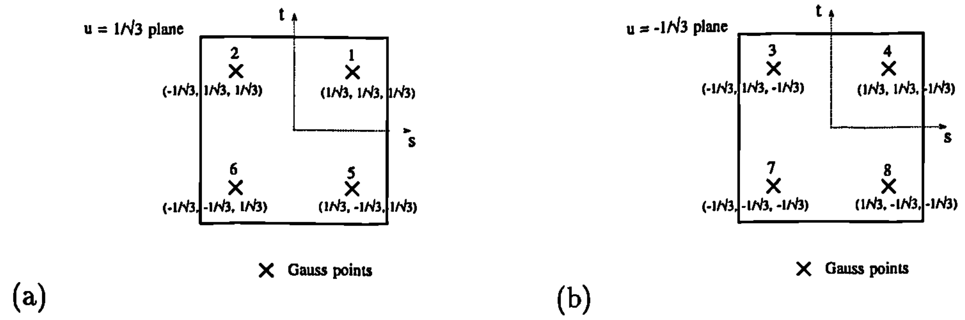

Figure 4.16: TLH Gauss points in local coordinates. (a) $u = 1/\sqrt{3}$ and (b) $u = -1/\sqrt{3}$.

symmetric regardless of the orthogonality of the TLH element.

Again, the consequence of this asymmetry is analysed and discussed with regard to linear solvers in the following chapters.

4.2 Closure

In this chapter, a rudimentary theoretical comparison of the FVM and the FEM, when applied to problems involving material non-linearity, has been given. The direct equivalence of the two methods for the linear family of elements, which includes the one dimensional linear element, the two dimensional CST element and the three dimensional linear tetrahedral element have been illustrated and commented upon. At present, to the best of the authors knowledge, no definitive theoretical comparisons of higher order two or three dimensional elements has been performed, the difficulty being the bilinear and trilinear nature of the higher order elements, which furnishes linear or bilinear variation of the strain and other associated constitutive variables over the element concerned.

In the following chapter the two methods will be compared against a number of verification problems to complete the comparison.

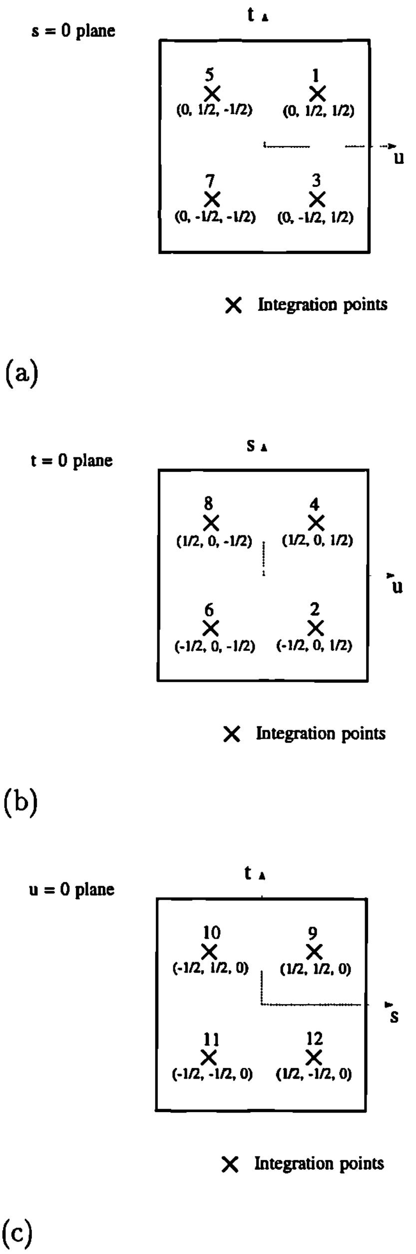

Figure 4.17: TLH FVM integration points in local coordinates. (a) u, (b) s and (c) t planes.

Chapter 5

Mechanical Validation

In this chapter the FV implementation of the segregated and whole displacement field algorithms are applied to a variety of validation problems and compared with a standard FE implementation. The problems comprise of applications where analytical, semi-analytical or experimental reference solutions are available, in order to validate the algorithms employed. It should be noted that due to the non-linear nature of the applications under investigation, purely analytical reference solutions are generally not available.

The algorithms are compared with regard to accuracy and computational cost. They are also analysed for a variety of meshes with varying connectivities and element assemblies. The algorithms are compared for two and three dimensional test cases. Complete descriptions of the validation problems will be presented, and the reference solutions will be fully described when possible.

5.1 Test case 1: Uniaxial tensile piece

The first test case is a uniaxial tensile piece undergoing strain hardening. As the problem is uniaxial, a one dimensional analytical solution is available. The application can be modelled in two and three dimensions. The two dimensional approximation is achieved via a plane stress approximation. Initially, this problem provides a reasonable test case for a variety of elements and element assemblies, orthogonal and non-orthogonal.

For a plane stress approximation the problem is specified in Figure 5.2. In this case, the problem was modelled using a series of orthogonal meshes involving BLQ elements. The mesh was refined in order to investigate the CPU time required for the different algorithmic approaches and associated solvers.

5.1.1 Analytical solution

Assuming a basic one dimensional elasto-visco-plastic model as described in Figure 5.1a, it is possible to derive the following first order ordinary differential equation defining the relationship between a constant applied stress and a time dependent strain under visco-plastic conditions [72]:

$$\gamma\beta\epsilon + \frac{\mathrm{d}\epsilon}{\mathrm{d}t} = \frac{\gamma\beta}{E}\sigma_A + \gamma\left(\sigma_A - Y\right),$$

where σ_A represents the constant applied stress and β is the strain hardening portion of the stress-strain curve after the removal of the elastic strain component, as defined earlier in equation 2.8. The variables γ and Y are the previously defined fluidity and yield stress.

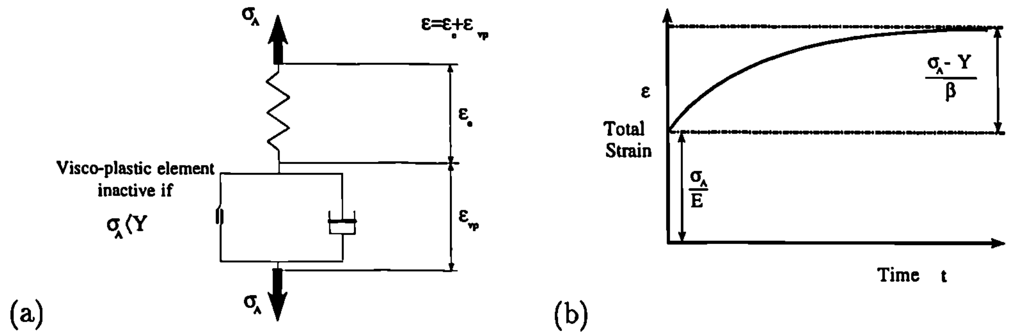

Figure 5.1: One dimensional elasto-visco-plastic (a) model and (b) response.

The solution to the above differential equation is relatively straight forward and is stated here as

$$\epsilon = \frac{\sigma_A}{E} + \frac{(\sigma_A - Y)}{\beta}\left[1 - e^{-\beta\gamma t}\right].$$

Provided that β is non-zero, the form of response is illustrated in Figure 5.1b which represents an initial elastic response followed by a time dependent strain increase which approaches a steady state value in an exponential fashion.

Hence, the total strain is

$$\epsilon = \frac{\sigma_A}{E} + \frac{(\sigma_A - Y)}{\beta} = \epsilon_e + \epsilon_{vp} \tag{5.1}$$

in the limit $t \rightarrow \infty$. It is important to note that the final solution in this limit is independent of the fluidity γ. Hence, the final solution is equivalent to an elasto-plastic analysis. For a time independent solution the time stepping scheme and the fluidity are viewed purely as acceleration parameters in the non-linear solution approach [105].

E	ν	H	Y	γ
$7000\,\text{kgmm}^{-2}$	0.2	$225\,\text{kgmm}^{-2}$	$24.3\,\text{kgmm}^{-2}$	$1.0 \times 10^{-5}\,\text{s}^{-1}$

Table 5.1: Material properties of aluminium alloy 57S.

Considering a tensile piece of aluminium with material properties as described in Table 5.1 and linear strain hardening characteristics as described in section 2.2.3, the strain response to an applied stress σ_A can be obtained from equation 5.1 and is stated in Table 5.2.

σ_A	ϵ	ϵ_{vp}
$27\,\text{kgmm}^{-2}$	1.54714×10^{-2}	1.16143×10^{-2}

Table 5.2: Analytical solution of the strain response to an applied stress.

5.1.2 Numerical solutions

The numerical results for a variety of single elements and simple element assemblies, in two and three dimensions, are described in Tables 5.3 and 5.4. A simple element assembly involving two CST elements is illustrated in Figure 5.2. Equivalent element configurations

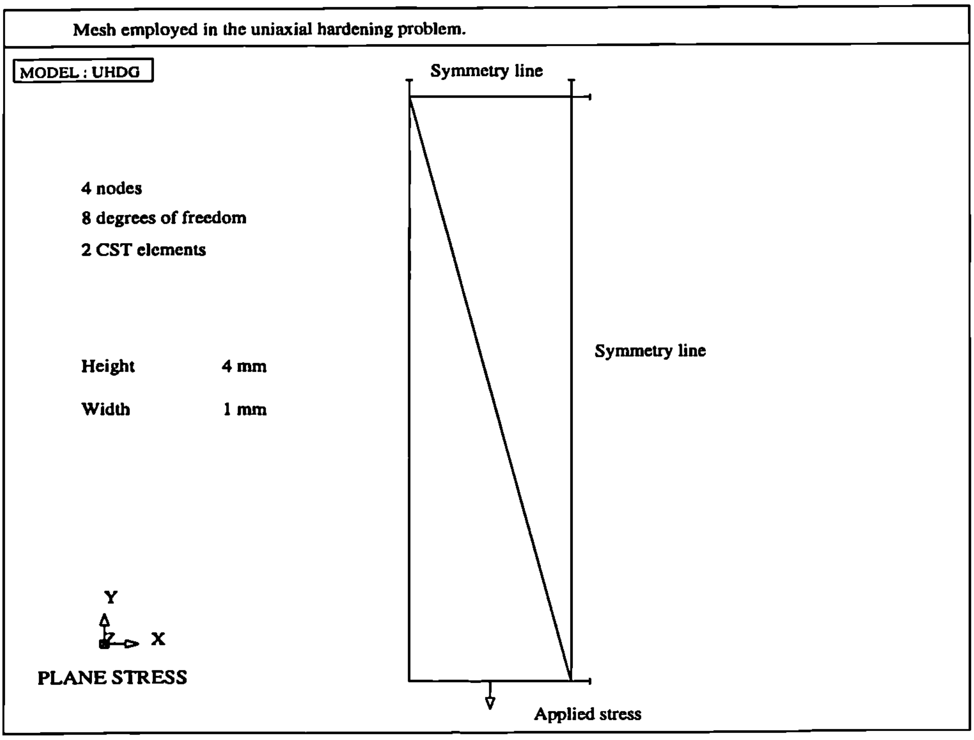

Figure 5.2: Uniaxial hardening problem.

for the FVM and the FEM have been compared. For this validation problem the FVM and the FEM provide complete agreement with regard to the numerical solution, for all elements and element assemblies as described in Tables 5.3 and 5.4. The numerical solution obtained is in good agreement with the analytical solution as stated in Table 5.2.

As described in Tables 5.3 and 5.4 the FEM and the FVM require an equivalent number of time steps to converge. This illustrates the agreement of the two methods with regard to strain response over time.

It should be noted that when the BLQ, TLH or BLP elements are non-orthogonal in the FVM a BiCG (Bi-Conjugate Gradient) solver is employed. The BiCG solver is required as the resultant coefficient matrix is asymmetric. Alternatively, a CGM (Conjugate Gradient Method) solver is always employed in the FEM as the resultant coefficient matrix is always symmetric regardless of the orthogonality of the elements. Additionally, a CGM solver is

	Solver	Time steps	ϵ	ϵ_{vp}
1 BLQ FVM	CGM	232	1.54703×10^{-2}	1.16132×10^{-2}
2 CST FVM	CGM	232	1.54703×10^{-2}	1.16132×10^{-2}
3 BLQ FVM	BiCG	232	1.54703×10^{-2}	1.16132×10^{-2}
1 BLQ FEM	CGM	232	1.54703×10^{-2}	1.16132×10^{-2}
2 CST FEM	CGM	232	1.54703×10^{-2}	1.16132×10^{-2}
3 BLQ FEM	CGM	232	1.54703×10^{-2}	1.16132×10^{-2}

Table 5.3: Numerical results for a plane stress approximation.

	Solver	Time steps	ϵ	ϵ_{vp}
1 TLH FVM	CGM	232	1.54703×10^{-2}	1.16132×10^{-2}
2 BLP FVM	CGM	232	1.54703×10^{-2}	1.16132×10^{-2}
6 LT FVM	CGM	232	1.54703×10^{-2}	1.16132×10^{-2}
3 TLH FVM	BiCG	232	1.54703×10^{-2}	1.16132×10^{-2}
1 TLH FEM	CGM	232	1.54703×10^{-2}	1.16132×10^{-2}
2 BLP FEM	CGM	232	1.54703×10^{-2}	1.16132×10^{-2}
6 LT FVM	CGM	232	1.54703×10^{-2}	1.16132×10^{-2}
3 TLH FEM	CGM	232	1.54703×10^{-2}	1.16132×10^{-2}

Table 5.4: Numerical results for a three dimensional analysis.

employed for both the FEM and the FVM with regard to CST and LT elements. These observations agree with the theoretical discussions of the previous chapter.

This problem furnishes comprehensive patch tests for simple element assemblies and was employed to verify the implementation of the pressure loads with regard to both the FEM and the FVM. This was achieved by applying the pressured load over faces of the element assemblies consisting of non-orthogonal faces. The results were in agreement with those in Table 5.4.

This validation problem is somewhat limited due to the constant values of the stress and strains throughout the tensile piece. Hence, the complete agreement for both methods regardless of element choice. The following mechanical validation problems are more demanding and will provide a more detailed comparison of the two methods.

5.1.3 Algorithm performance

This validation problem was solved using a plane stress approximation with an increasing number of BLQ elements. The FVM using a segregated algorithmic approach and the FVM and the FEM using the standard algorithmic approach, were compared with regard to computational cost. As the BLQ elements can be assembled in an orthogonal fashion for this problem, the CGM solver can be employed for the FVM and the FEM. The CPU time was measured on an Intel 486DX 33MHz processor and the results obtained are plotted in Figure 5.3.

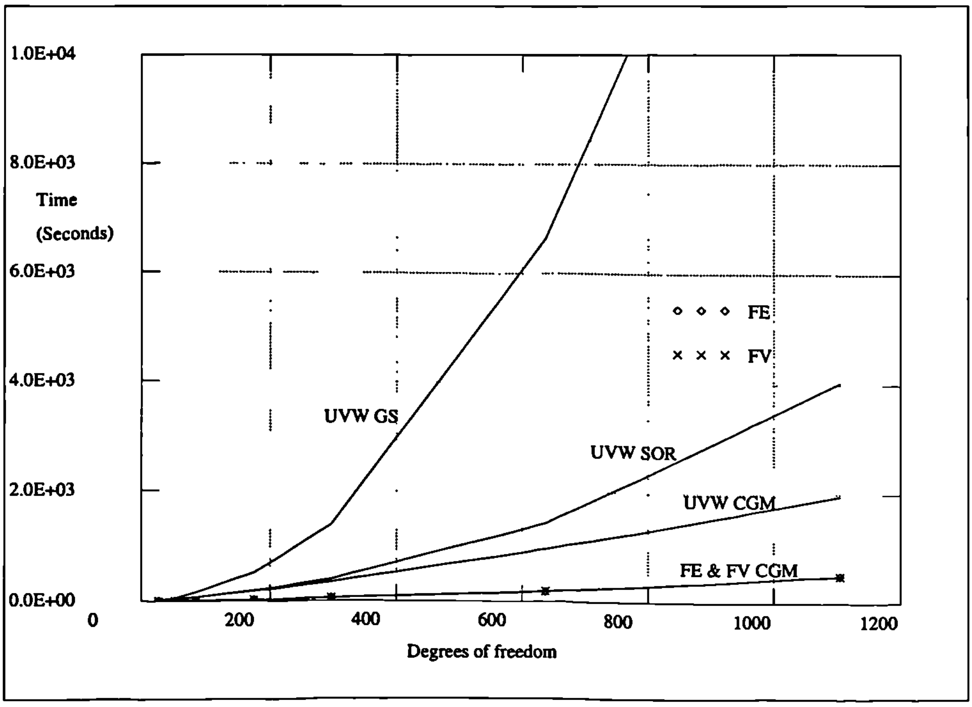

Figure 5.3: CPU times measured on an Intel 486DX 33Mhz processor.

As expected the segregated algorithm (UVW) performs considerably slower than the whole field (FE & FV) algorithms, this is in agreement with the performance of the algorithms when applied to linear elastic problems [43, 42, 4]. The segregated algorithm was studied for a variety of linear solvers. The conjugate gradient solver with Jacobi preconditioning (UVW CGM) performed best, with the SOR solver (UVW SOR) comparing reasonably well on this simple test case with an over-relaxation factor of $\omega = 1.8$. The Gauss-Seidel solver (UVW GS) showed the poorest performance.

5.2 Test case 2: Perforated tensile strip

The perforated tensile strip has been modelled extensively using the traditional FEM [105, 108] and a reference solution based upon experimental data is available [91]. The problem involves an applied stress as described in Figure 5.4, which is increased incrementally, with the initial increment loading the strip to the yield point and the following load increments causing plastic deformation up to the point of plastic flow. The six applied load increments are described in Table 5.5 For the reference solution the material under investigation was the aluminium alloy 57s as described in the previous validation problem, the properties of which are described in Table 5.1.

	I	II	III	IV	V	VI
Increment (kgmm^{-2})	5.59	0.95	1.46	1.73	1.52	1.64
Total (kgmm^{-2})	5.59	6.54	8.00	9.73	11.25	12.89

Table 5.5: Load increments applied to the perforated tensile strip.

5.2.1 Reference solution

The reference solution with regard to the stress distribution is based upon the experimental results for the total strain. The total strain was measured using a birefringent coating technique on the perforated tensile strip [91]. The stresses were obtained by applying the incremental Prandtl-Reuss stress-strain relations [50]. The total strain and stress profiles obtained along the minimum section of the perforated tensile strip, which is the line X-X' in Figure 5.4, are described for all load increments in Figures 5.5.3 and 5.6.3 respectively.

5.2.2 Numerical analysis

The perforated tensile strip can be modelled using a plane stress approximation, as described in Figure 5.4. The geometry of this problem requires a non-orthogonal mesh with regard to BLQ elements as also illustrated in Figure 5.4. The problem can also be modelled in two dimensions using CST elements. The FVM and the FEM are compared for meshes consisting of BLQ and CST elements.

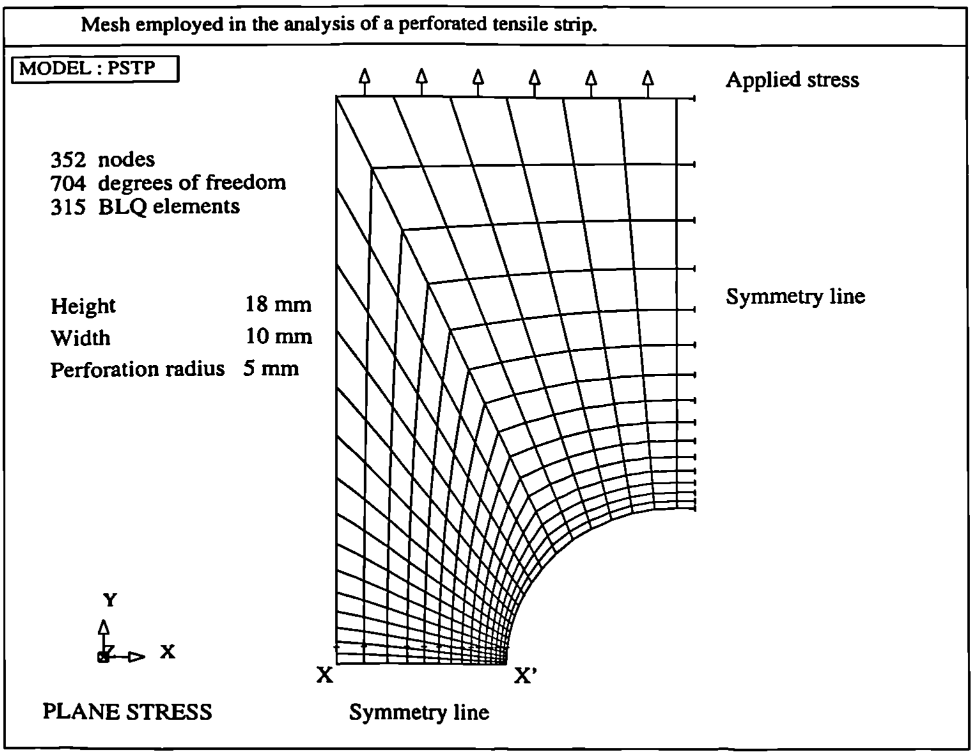

Figure 5.4: Perforated tensile strip

5.2.2.1 Reference numerical analyses

The elasto-visco-plastic solution of this problem is time independent. Hence, the final solution is equivalent to the solution obtained in an elasto-plastic analysis [105]. An elasto-plastic numerical analysis with a Von-Mises yield criterion has been performed using the commercial engineering software ANSYS [88], in order to provide a further reference solution. An identical mesh, using BLQ elements as described in Figure 5.4, was processed in ANSYS. The total strain profile obtained using ANSYS is described in Figure 5.5.4.

Additionally, an explicit elasto-visco-plastic analysis with a Von-Mises yield criterion has been performed using the commercial engineering software MICROFIELD [81]. Unfortunately, the relevant module in MICROFIELD is restricted to higher order BBQ (Bi-Quadratic Quadrilateral) elements. Hence, an equivalently accurate, but coarser mesh, was processed in MICROFIELD. The stress profile obtained using MICROFIELD is described in Figure 5.6.4.

5.2.3 Discussion of numerical results

With regard to the total strain profile, the previous numerical analyses performed using the FEM, have largely over predicted the strain values when compared to the reference solution [105]. The same over prediction occurs in the numerical analyses performed in this research using the FEM and the FVM, as illustrated in Figures 5.5.1 and 5.5.2 respectively. Relatively good agreement between the numerical analyses and the reference solution is obtained with regard to the stress profile, as illustrated in Figure 5.6.

The problem was modelled with a number of meshes consisting of BLQ and CST elements, with varying mesh density. As predicted from the theoretical analysis in the previous chapter, the results for the FVM and the FEM with regard to CST elements are in complete agreement, as illustrated in Figures 5.8 and 5.10. Hence, providing further evidence to establish the direct equivalence of the two methods with regard to CST elements.

For BLQ elements, the two methods are generally in close agreement, but it is interesting to note that the two methods agree more closely when the problem is loaded initially than at the the final load increment VI, as illustrated in Figures 5.7 and 5.9. At the final load increment the tensile piece is undergoing total strains of several percent, and the infinitesimal strain theory is reaching the limit of applicability. At this stage plastic flow is beginning to occur and the material non-linearity would begin to be augmented by geometrical non-linearity. Interestingly, the two methods appear to differ more as the overall non-linearity of the problem increases.

5.2.4 Algorithmic performance

For this validation problem, the non-orthogonality of the mesh with regard to BLQ elements requires a BiCG solver for the asymmetric coefficient matrix assembled by the FVM, where as the symmetric coefficient matrix assembled by the FEM requires a CGM solver.

The computational expense of the BiCG solver with regard to the FVM when compared to the FEM is illustrated in Figure 5.11, where the computational processing time is plotted against mesh density. As expected the FVM is approximately twice as expensive as the FEM, because the BiCG solver is computationally twice as expensive as the CGM solver. In this research the Jacobi pre-conditioner is applied for the BiCG and the CGM solver, though it should be noted that a number of other pre-conditioners could be applied that may reduce the computational cost.

For the previous validation problem an orthogonal mesh was employed for BLQ elements and it was possible to employ a CGM solver for the FVM and the FEM, hence the agreement in computational cost as indicated in Figure 5.3.

For meshes consisting of CST elements the coefficient matrices with regard to the FEM and the FVM are identical, hence the CGM solver can be employed for both methods. The computational cost of the FVM and the FEM are in closer agreement as illustrated in Figure 5.12. The FVM is approximately ten percent slower than the FEM, this is attributable to the larger number of integration points associated with the FVM than with the FEM for CST elements, as described in section 4.1.2.1.

5.2.5 Invariant and integration point scheme

In the FVM and the FEM it is necessary to compute and store the constitutive values, such as stress and strain, for all elements. The values can either be calculated and stored at the element centre and assumed invariant over the element or be calculated and stored at the integration points. The latter technique is obviously more accurate, but also requires more storage.

It should be noted that the scheme adopted is not an issue with regard to linear elements as the constitutive values are invariant over the element. The following comparisons are for a mesh consisting of BLQ elements as illustrated in Figure 5.4.

Comparisons of the stress and strain profiles furnished by the invariant and integration point schemes are illustrated in Figures 5.15 and 5.13 and Figures 5.16 and 5.14, for the FVM and the FEM, respectively. A comparison of the integration point scheme for the FVM and the FEM is illustrated in Figures 5.17 and 5.18. The stress and strain profiles are consistent with the invariant schemes employed in the previous numerical analyses, hence the invariant method provides a reasonable solution approach for this problem with a considerable reduction in memory requirements. This can be very important when considering problems involving complex three dimensional geometries, with many thousands of elements.

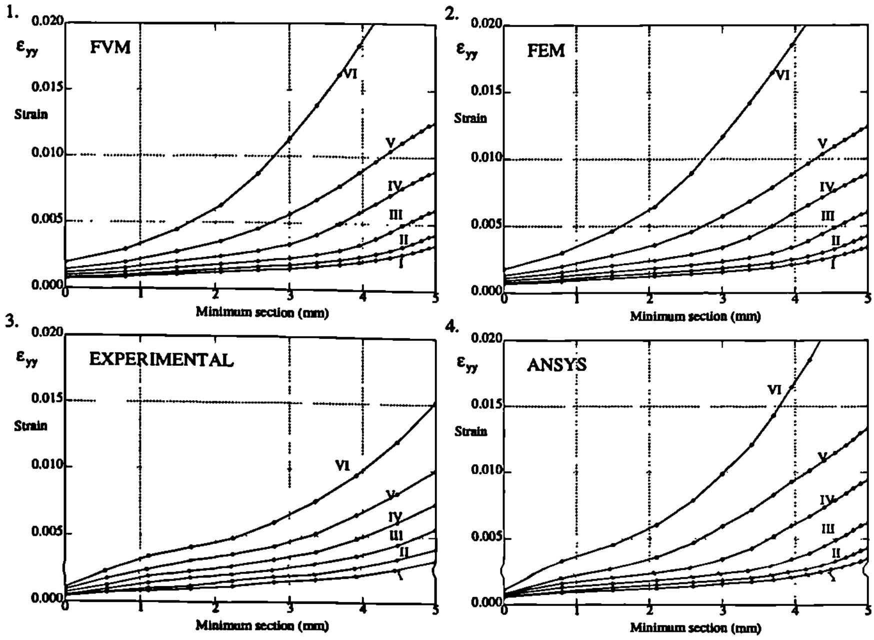

Figure 5.5: Total strain profile of numerical and semi-experimental analyses.

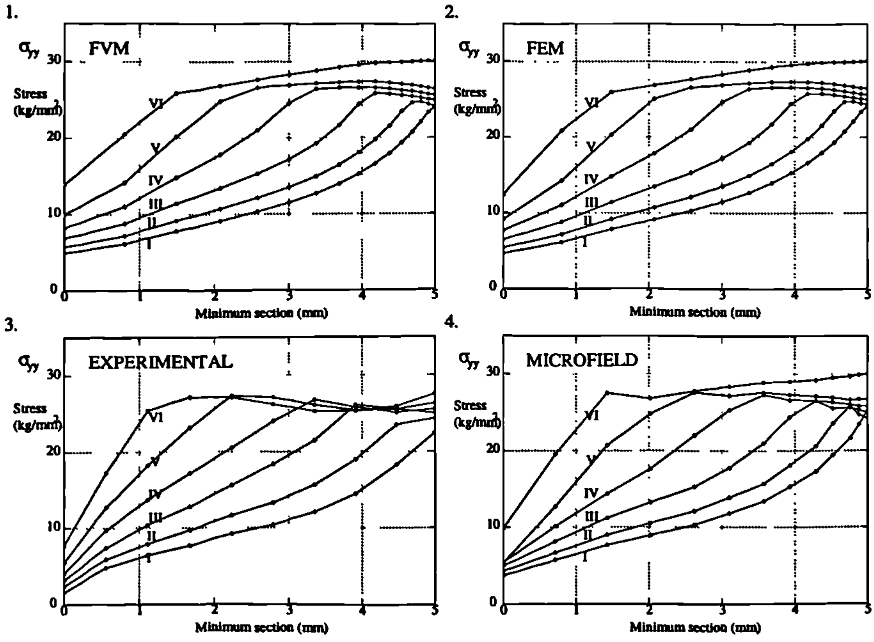

Figure 5.6: Stress profile of numerical and semi-experimental analyses.

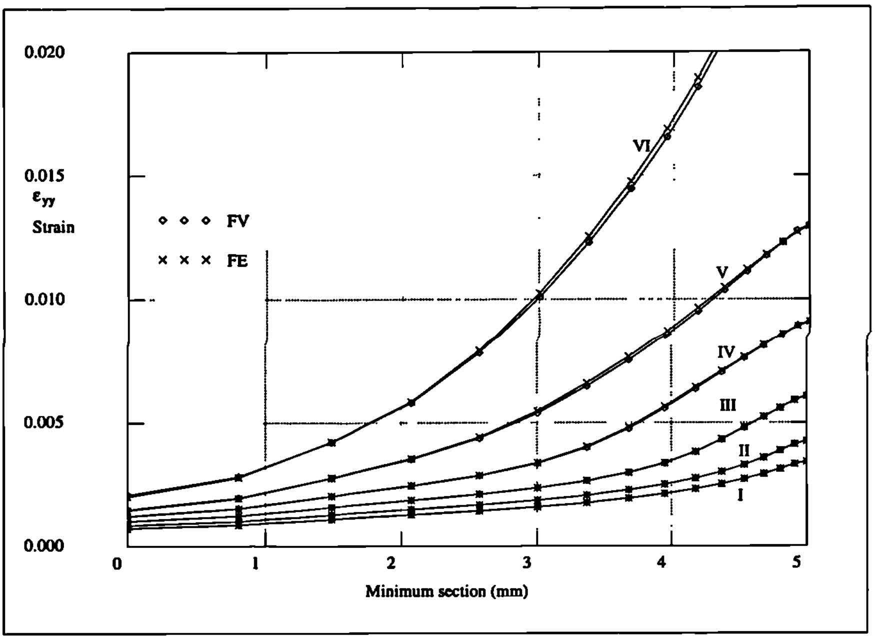

Figure 5.7: Comparison of the total strain for BLQ elements.

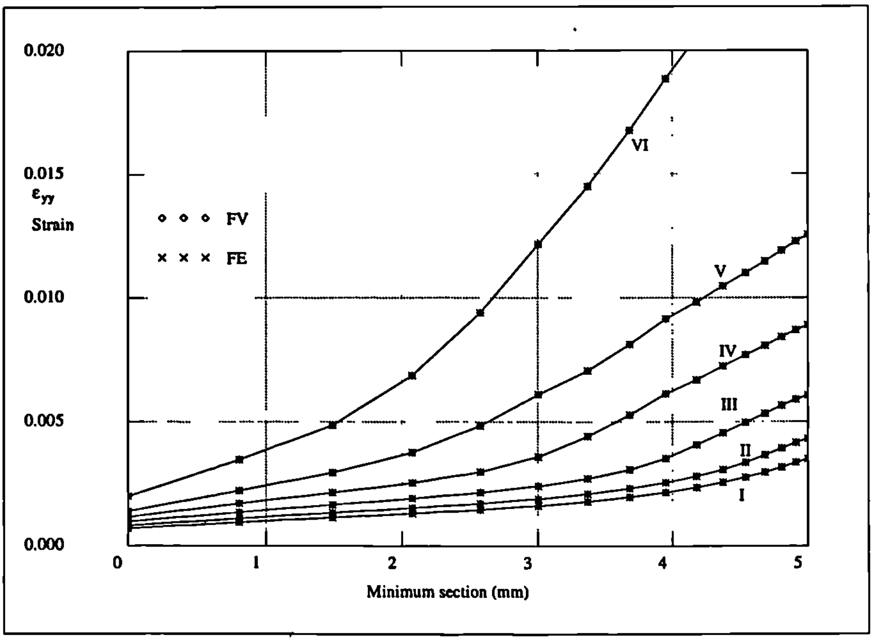

Figure 5.8: Comparison of the total strain for CST elements.

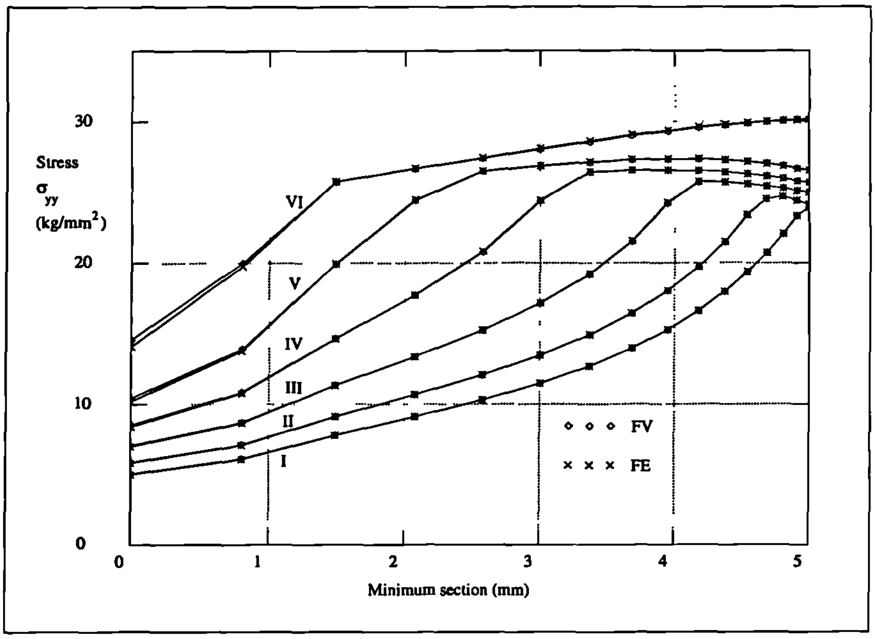

Figure 5.9: Comparison of the stress distribution for BLQ elements.

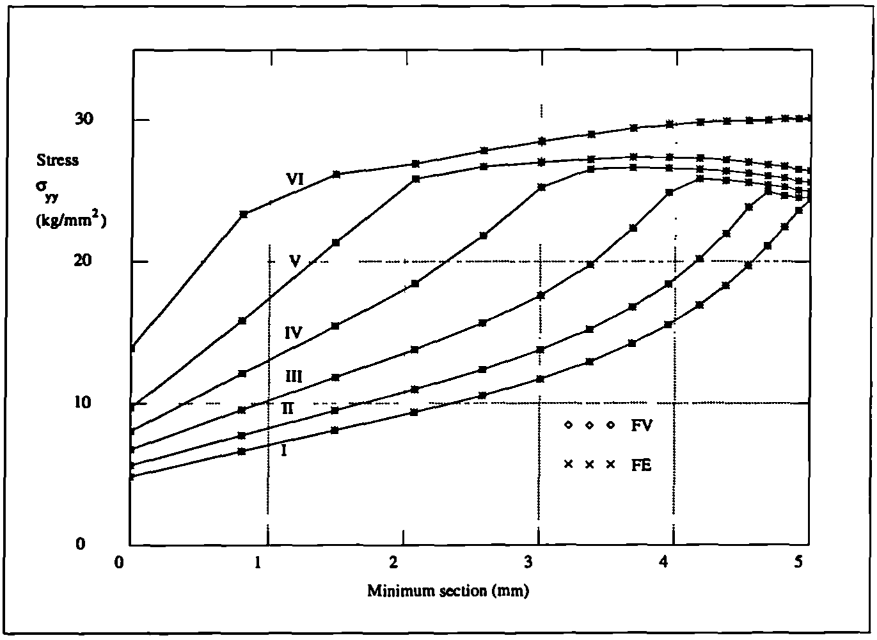

Figure 5.10: Comparison of the stress distribution for CST elements.

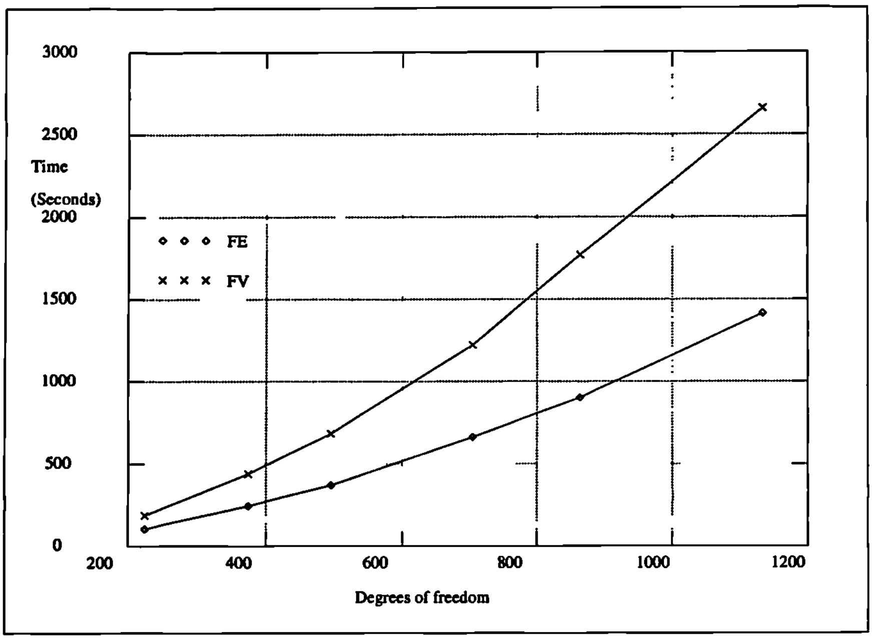

Figure 5.11: CPU times for BLQ elements on a SPARC 4, 110MHz work station.

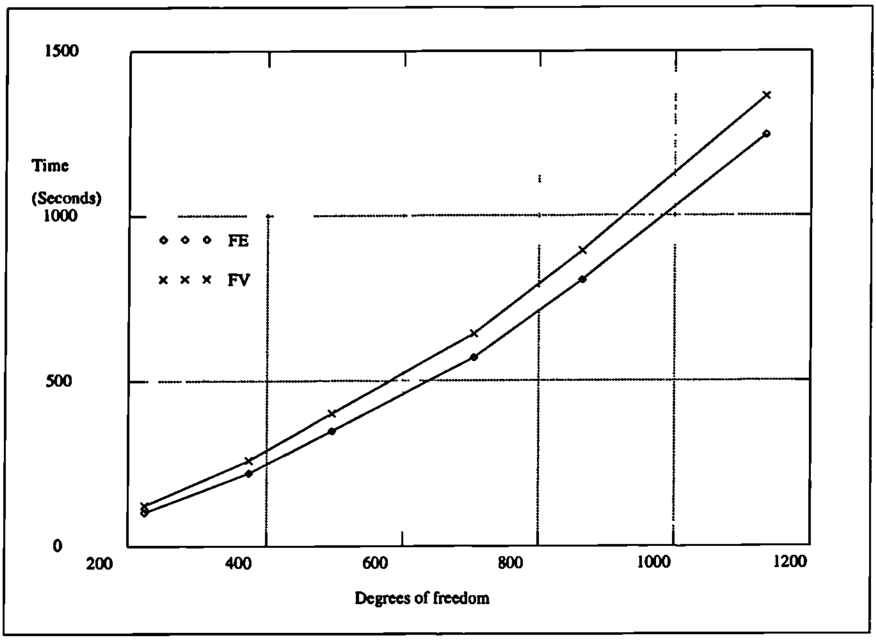

Figure 5.12: CPU times for CST elements on a SPARC 4, 110MHz work station.

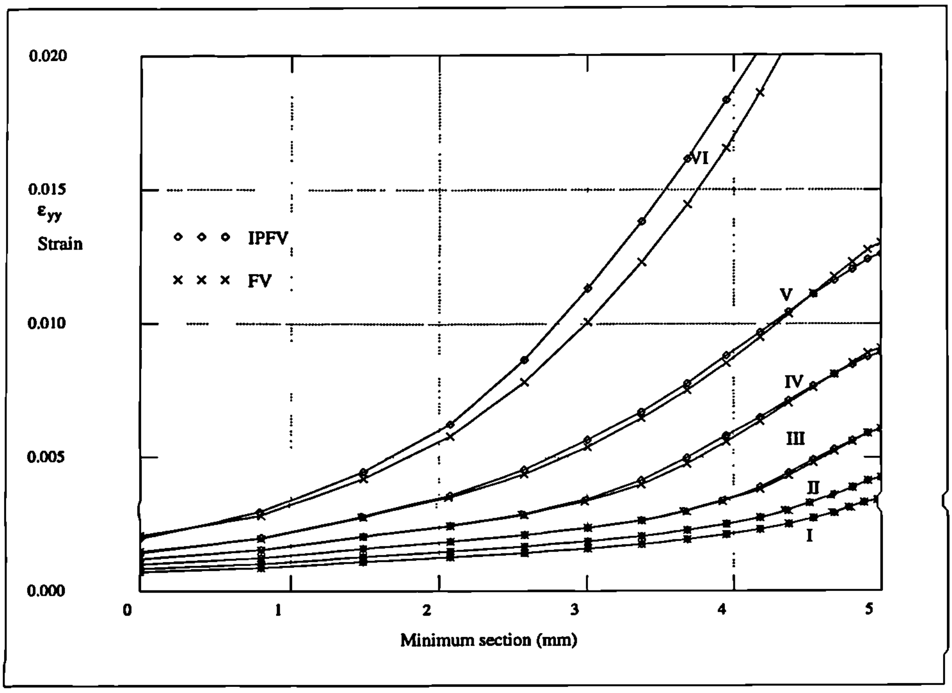

Figure 5.13: Comparison with FV integration point method for strain.

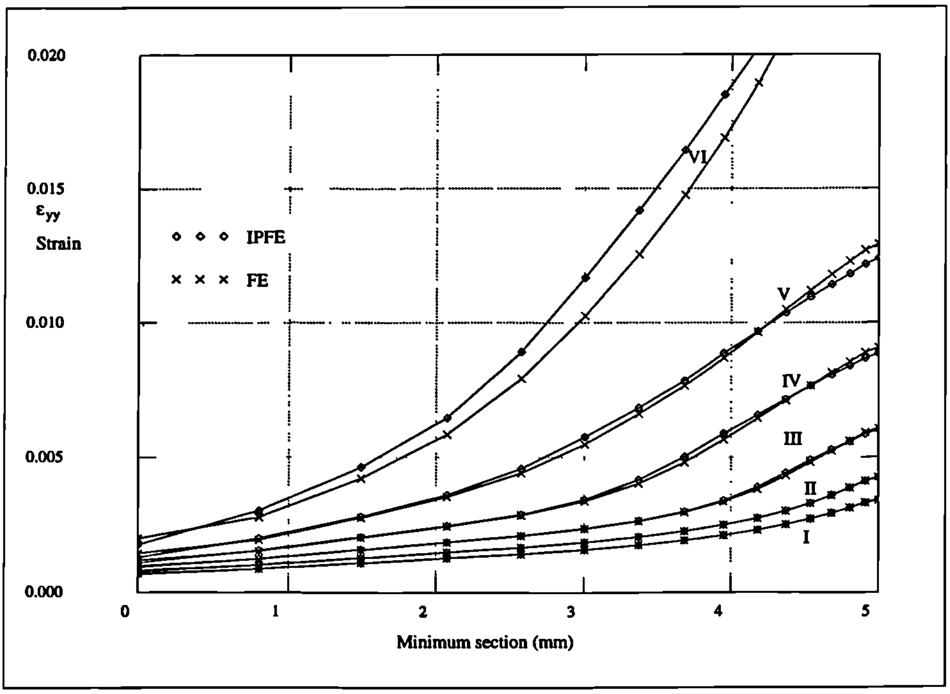

Figure 5.14: Comparison with FE integration point method for strain.

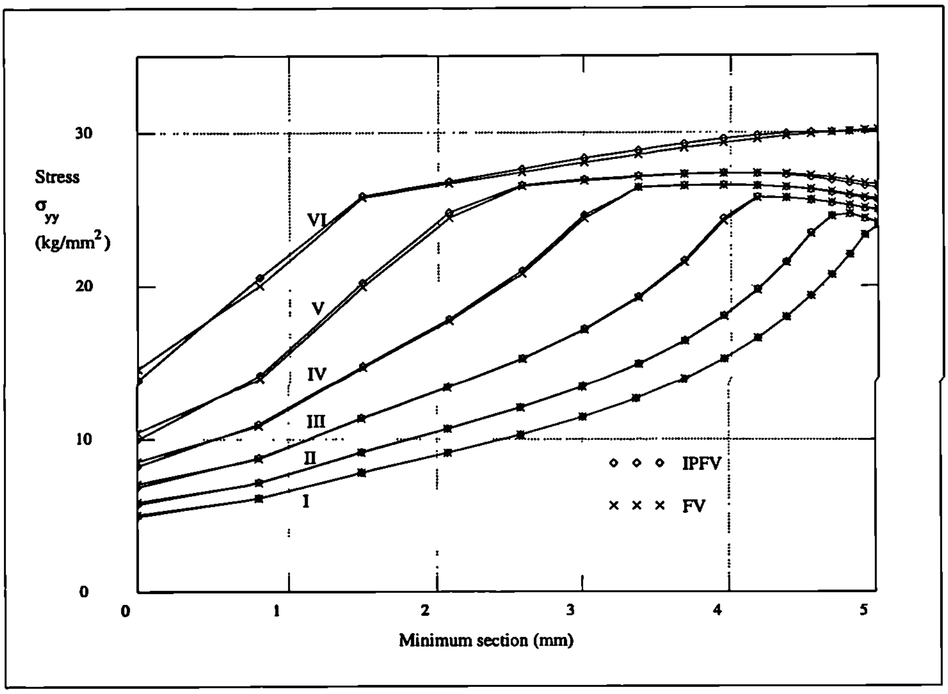

Figure 5.15: Comparison with FV integration point method for stress.

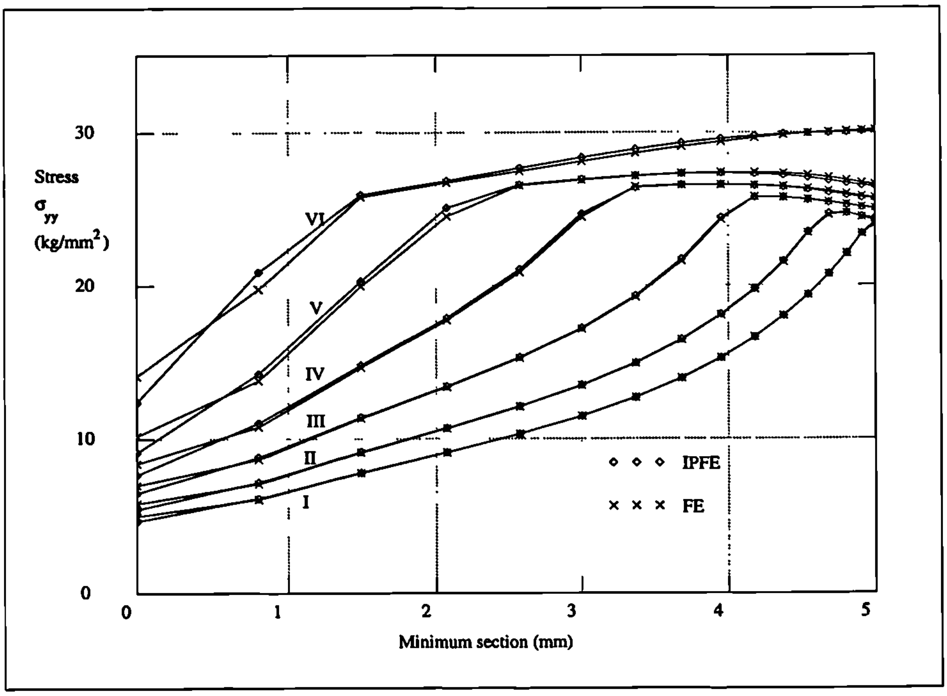

Figure 5.16: Comparison with FE integration point method for stress.

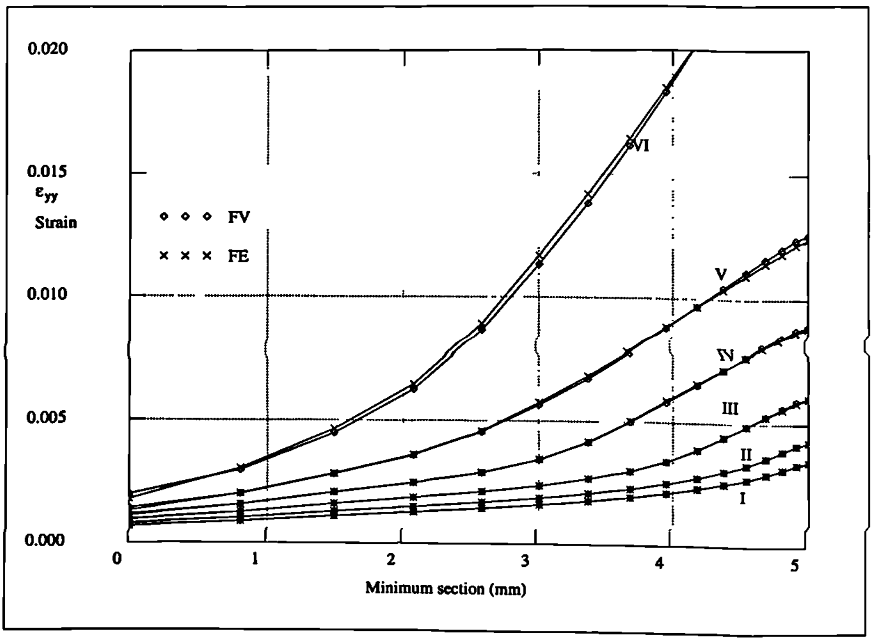

Figure 5.17: Comparison of integration point methods for strain.

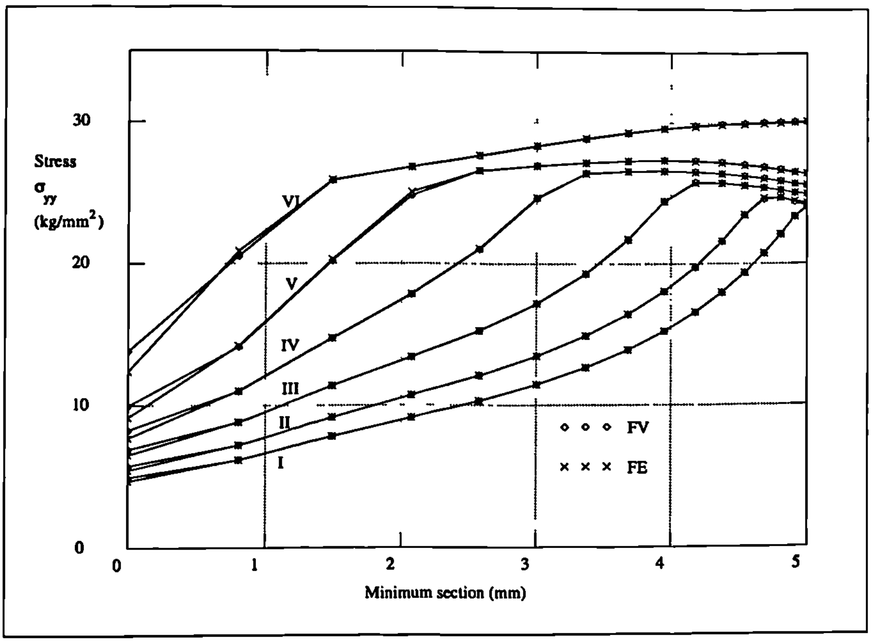

Figure 5.18: Comparison of integration point methods for stress.

5.3 Test case 3: Internally pressurised thick cylinder

For this validation problem a thick walled cylinder consisting of an elastic/perfectly plastic material undergoes an incrementally increasing internal pressure. A Von-Mises yield criterion is associated with the idealized material of the cylinder. The properties of the cylinder material are described in Table 5.6 and the pressure load increments are described in Table 5.7.

E	ν	H	Y	γ
$21000\,\text{dNmm}^{-2}$	0.3	$0\,\text{dNmm}^{-2}$	$24\,\text{dNmm}^{-2}$	$1.0 \times 10^{-5}\,\text{s}^{-1}$

Table 5.6: Material properties of the thick cylinder.

	I	II	III	IV	V	VI	VII
Increment (dNmm^{-2})	8.0	2.0	2.0	2.0	2.0	2.0	2.0
Total (dNmm^{-2})	8.0	10.0	12.0	14.0	16.0	18.0	20.0

Table 5.7: Load increments applied to the pressurized thick cylinder.

5.3.1 Theoretical analysis

As the problem is axisymmetric, a semi-analytical reference solution is available for this validation problem [53]. Due to the non-linear nature of the problem a closed form solution is not available. In the reference solution a hyperbolic system of three quasi-linear first order partial differential equations is obtained, which is then solved numerically after applying a finite difference approximation [53].

5.3.2 Numerical analysis

This problem is also time independent and again the final solution is equivalent to that of an elasto-plastic analysis. An elasto-plastic analysis with a Von-Mises yield criterion has been performed using the commercial engineering software LUSAS [36], in order to provide a reference numerical solution. The mesh consisting of BLQ elements as described in Figure 5.19 was processed in LUSAS. Numerically the problem can be modelled using a plane strain approximation [72]. The BLQ mesh employed in the numerical analyses performed in this research is also illustrated in Figure 5.19. A mesh consisting of CST elements is also considered.

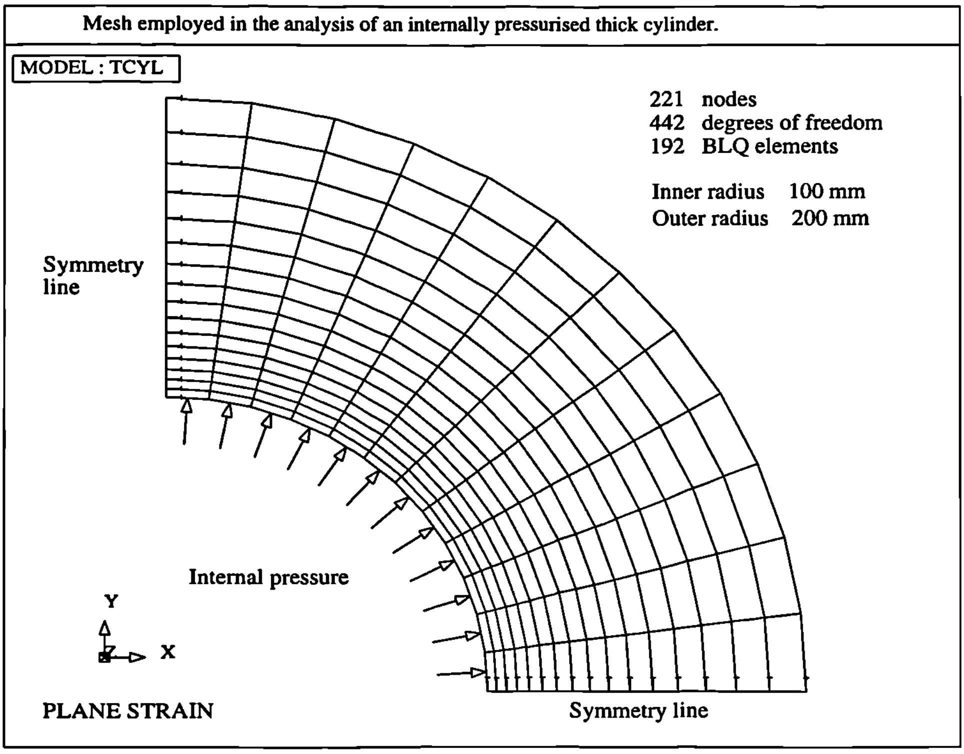

Figure 5.19: Internally pressurized thick cylinder.

5.3.3 Discussion of numerical results

For this problem the FEM and the FVM are in very close agreement for both BLQ and CST elements, as indicated by Figures 5.20 and 5.21 respectively. Though it is possible to observe a slight difference between the FVM and the FEM with regard to BLQ elements as the amount of plastic straining increases. Where as for CST elements the two methods are in complete agreement as expected. This is illustrated in Figures 5.22 and 5.23, where the hoop stresses along the radial axes are compared for the load increment VI, involving an internal pressure of 18dNmm^{-2}.

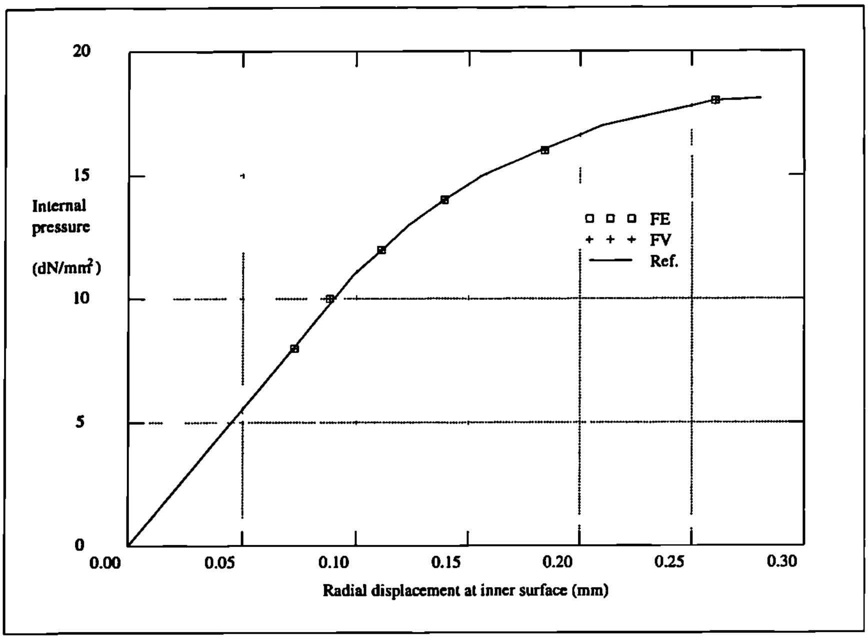

Figure 5.20: Mesh consisting of BLQ elements.

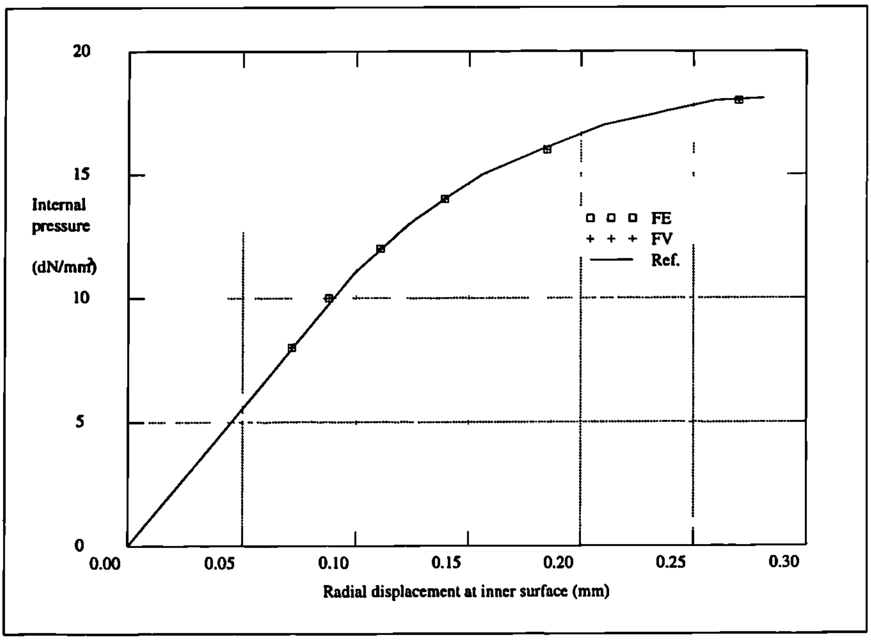

Figure 5.21: Mesh consisting of CST elements.

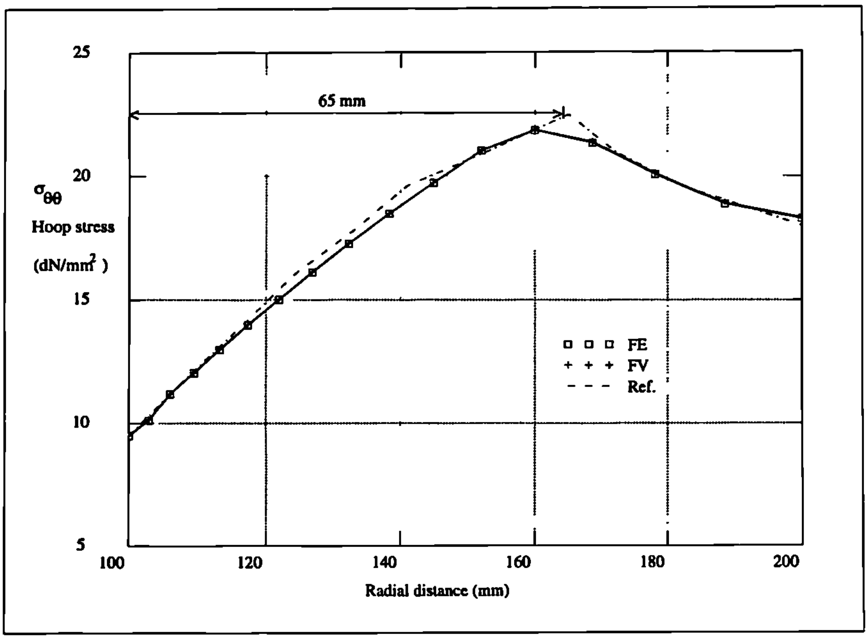

Figure 5.22: Mesh consisting of BLQ elements.

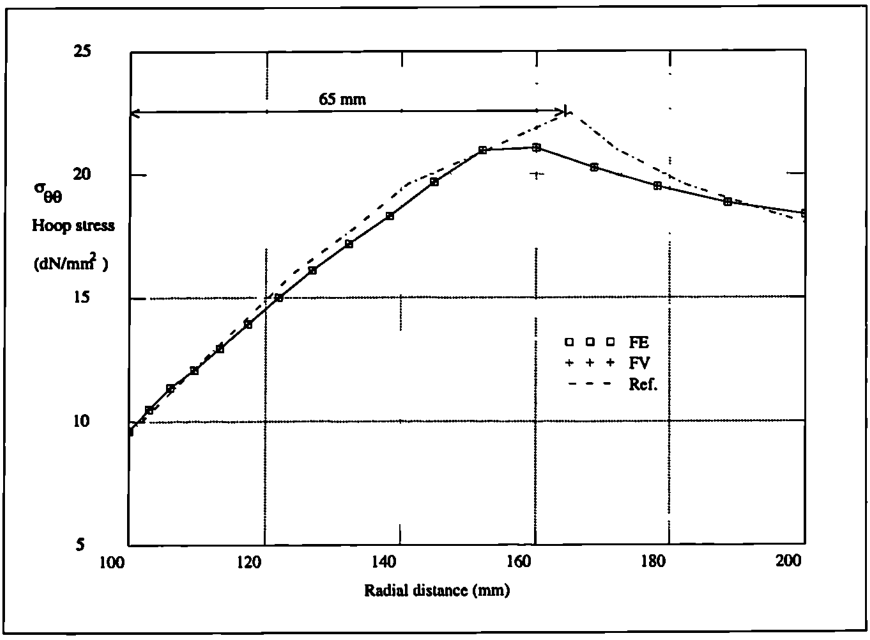

Figure 5.23: Mesh consisting of CST elements.

5.4 Test case 4: Internally pressurised spherical vessel

For this validation problem a thick walled spherical vessel, consisting of an elastic/perfectly plastic material, undergoes an instantaneously applied internal pressure load. A Von-Mises yield criterion is associated with the idealized material of the spherical vessel. The properties of the spherical vessel are equivalent to those of the previous validation problem, which are described in Table 5.6, and the instantaneously applied pressure load is 30dNmm^{-2}.

5.4.1 Theoretical analysis

As the problem is spherical and the pressure load is applied instantaneously, a closed form solution is available [50]. The analytically derived equations will be stated here for completeness. Considering a cross-section through the central point of a hollow sphere, with internal radius a and external radius b, as illustrated in Figure 5.24, then the radius of the plastic region c, as a result of the uniformly distributed pressure load p, can be obtained

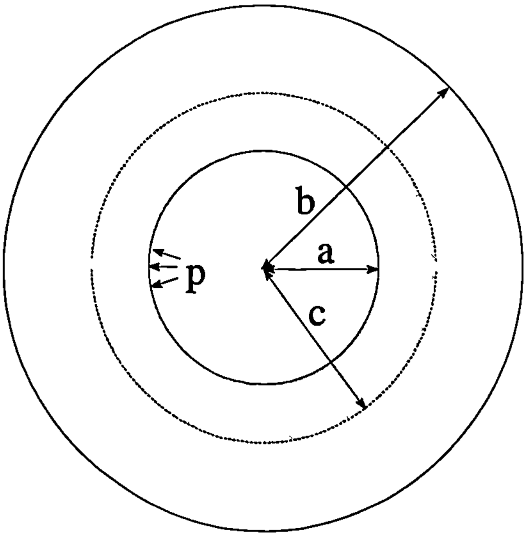

Figure 5.24: Plastic region round a spherical cavity, expanded by a uniformly distributed pressure.

from solution of

$$\frac{2Y}{3}\left(1-\frac{c^3}{b^3}\right)+2Y\log\left(\frac{c}{a}\right)-p=0, \tag{5.2}$$

where Y is the uniaxial yield stress [50]. Equation 5.2 was solved using MATHEMATICA, for a uniformly distributed pressure load of 30 dNmm^{-2}, and the radius of the plastic region was found to be 157.562 mm.

It is possible to derive the following equations [50]:

$$\sigma_{\theta\theta} = Y-\frac{2Y}{3}\left(1-\frac{c^3}{b^3}\right)-2Y\log\left(\frac{c}{r}\right) \qquad \text{for } a \leq r \leq c, \tag{5.3}$$

$$\sigma_{\theta\theta} = \frac{2Yc^3}{3b^3}\left(1+\frac{b^3}{2r^3}\right) \qquad \text{for } c \leq r \leq b, \tag{5.4}$$

which describe the normal hoop stress $\sigma_{\theta\theta}$ as a function of the radius r.

The profile of the hoop stress can then be obtained from equations 5.3 and 5.4, where equation 5.3 describes the profile of the hoop stress in the plastic region and equation 5.4 describes the profile of the hoop stress in the elastic region.

5.4.2 Numerical analysis

This problem is also time independent and again the final solution is equivalent to that of an elasto-plastic analysis. Numerically the problem can be modelled in three dimensions, with the respective displacements fixed to zero in the respective symmetry planes. The spherical vessel is then reduced to an octant as illustrated in Figure 5.25(1). A number of meshes, of varying element density and type, were employed in the numerical analysis. Examples of meshes consisting of LT, BLP and TLH elements are illustrated in Figures 5.25(2), 5.25(3) and 5.25(4), respectively. The geometry of this problem requires a non-orthogonal mesh with regard to BLP and TLH elements as illustrated in Figures 5.25(3) and 5.25(4), respectively.

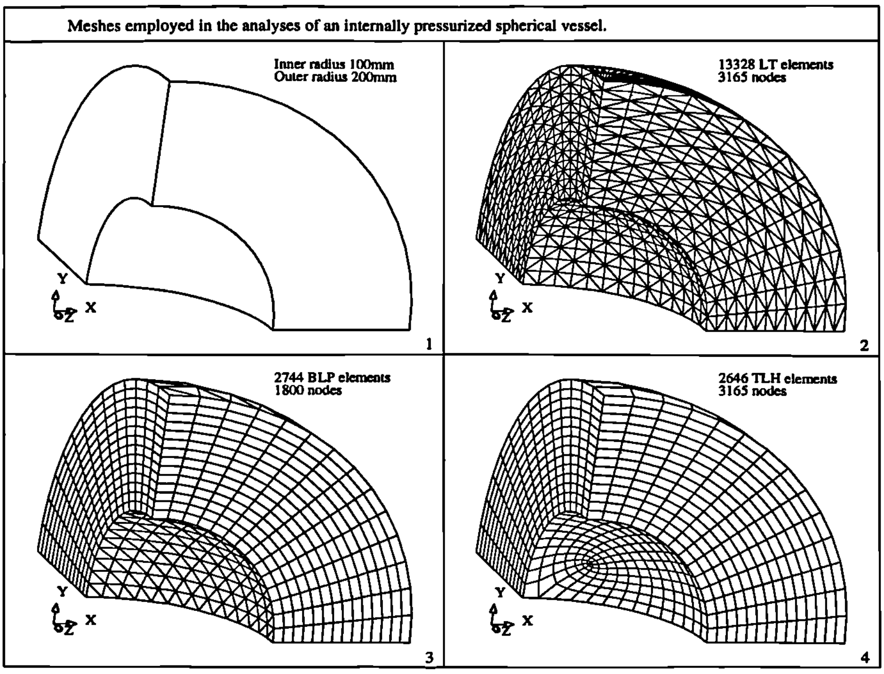

Figure 5.25: Meshes employed in the analyses of an internally pressurized spherical vessel.

5.4.3 Discussion of numerical results

Firstly, the problem was analysed with a series of meshes consisting of TLH elements. The meshes were continually refined. The hoop stress profiles, along the radii, as obtained from two of the numerical analyses are plotted and compared against the reference solution in Figures 5.26 and 5.27. In Figure 5.26 the results from one of the coarser meshes employed, consisting of 1,221 nodes and 950 TLH elements, are presented. Additionally, in Figure 5.27 the results from the finest mesh employed, consisting of 3,165 nodes and 2,646 TLH elements, are presented.

The close agreement of the FEM and the FVM is illustrated in both cases. However, it is important to note the closer agreement between the reference solution and the FVM in both cases. With regard to the FEM, the disagreement with the reference solution is worse for the coarser mesh.

These observations may be associated with the higher order, trilinear nature of the elements employed in the three dimensional analysis at this stage. With regard to the FVM, the implementation of surface tractions will involve bilinear face elements for TLH elements. Hence, when considering the application of surface tractions for the FEM and the FVM as described in equations 3.20 and 3.23, respectively, the contributions are different for the FVM and the FEM as a result of the different weighting techniques associated with each method.

Extending this point further, the weighting technique employed for the FVM may be more complementary, when applied generally, as all the terms are integrated conservatively at a local level. Conversely, for the FEM the weighting is not locally conservative which may introduce errors when surface tractions are employed. These conclusions are tentative and rely heavily on the authors own interpretation of the present observations, but they strongly suggest further possible avenues of research for the FVM, particularly with regard to surface tractions when associated with contact analysis.

It is important to note that the FVM employing the segregated displacement field approach (UVW) does not provide as favourable a comparison with regard to the reference solution. This can be attributed to the decoupling of the displacement components which is a direct consequence of the method. The decoupling will have greater effect when the problems are truly two or three dimensional and is also the case for elastic problems, as described in two dimensions by Fryer et al [43, 42].

Secondly, the problem was analysed with a series of meshes consisting of BLP elements. Again, the meshes were continually refined and the hoop stress profiles plotted in Figures 5.28 and 5.29.

There is much closer agreement between the FVM and the FEM for both the coarse mesh described in Figure 5.28 and the fine mesh described in Figure 5.29. This is attributable to the lower order, bilinear nature of the element concerned and the linear nature of the triangular faces over which the surface tractions are applied. As illustrated in Figure 5.25(3) the BLP elements are orientated so the pressure load (surface traction) is prescribed over a triangular face. This was a fortuitous outcome of the automatic mesh generator employed [37] and it is obviously possible to further study the element when surface tractions are applied to the bilinear, quadrilateral faces, though it was not studied in this research.

Thirdly, the problem was analysed with a series of meshes consisting of LT elements. Again, the meshes were continually refined and the hoop stress profiles plotted in Figures 5.30 and 5.31.

As predicted in the previous Chapter, there is complete agreement between the FVM and the FEM with regard to LT elements. This is a consequence of the linear nature of both the element concerned and the triangular faces over which the surface traction is applied.

5.4.4 Algorithmic performance

As described in the previous section, this validation problem was solved in three dimensions with meshes consisting of a variety of element types and in each case an increasing number of elements.

Considering TLH elements, the FVM, employing a segregated algorithmic approach, and the FVM and the FEM, employing a standard algorithmic approach, were compared with regard to computational cost. The geometrical nature of this validation problem prohibits an orthogonally assembled mesh. Hence, for the standard FVM a BiCG solver is required due to the asymmetric nature of the coefficient matrix obtained. Conversely, for the standard FEM a CGM solver is sufficient as the coefficient matrix obtained is symmetric. These requirements agree with the conclusions of the previous Chapter. Additionally, for the segregated version of the FVM a GS (Gauss-Seidel) solver is applicable due to the diagonally dominant nature of the coefficient matrices obtained.

As illustrated in Figure 5.32, the segregated version of the FVM, employing the GS solver (UVW GS), requires considerably more CPU time than either the standard FVM (FVM BiCG) or the standard FEM (FEM CGM). As illustrated in Figure 5.33, the standard FVM, employing the BiCG solver (FVM BiCG) requires approximately twice the CPU time as the FEM, employing the CGM solver (FEM CGM). This observation is expected due to the computational requirements of the two different linear solvers employed. Also with regard to TLH elements, the FVM visits twelve integration points per element, while the FEM visits eight Gauss points per element. Hence, any improvement in accuracy obtained by the FVM must be offset against the extra computational cost.

Considering BLP elements, the FEM (FEM CGM) and the FVM (FVM BiCG), employing the standard algorithmic approach, were compared with regard to computational cost, as illustrated in Figure 5.34. Again, the geometrical nature of the validation problem furnishes an asymmetric coefficient matrix with regard to the FVM and a symmetric coefficient matrix with regard to the FEM. Additionally, the FVM visits nine integration points per element, while the FEM visits six Gauss points per element.

Hence, the relative performances of the FVM and the FEM with regard to BLP elements are equivalent to those for TLH elements, as illustrated in Figures 5.34 and 5.33, respectively.

Considering TL elements, the FEM (FEM CGM) and the FVM (FVM CGM), employing the standard algorithmic approach, were compared with regard to computational cost, as illustrated in Figure 5.35. In this case the FVM and the FEM furnish identical, symmetric, coefficient matrices regardless of the problem geometry. However, the FVM visits six integration points, while the FEM visits a single Gauss point.

Hence, the FVM still incurs a greater computational cost, even when the same linear solver is employed, as illustrated in Figure 5.35.

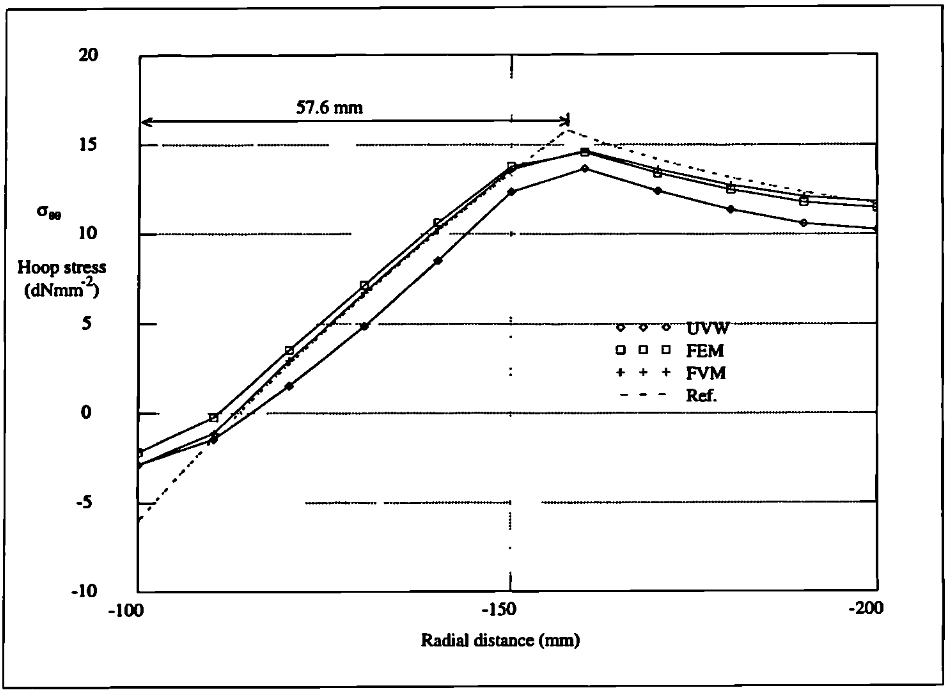

Figure 5.26: Mesh consisting of 1,221 nodes and 950 TLH elements.

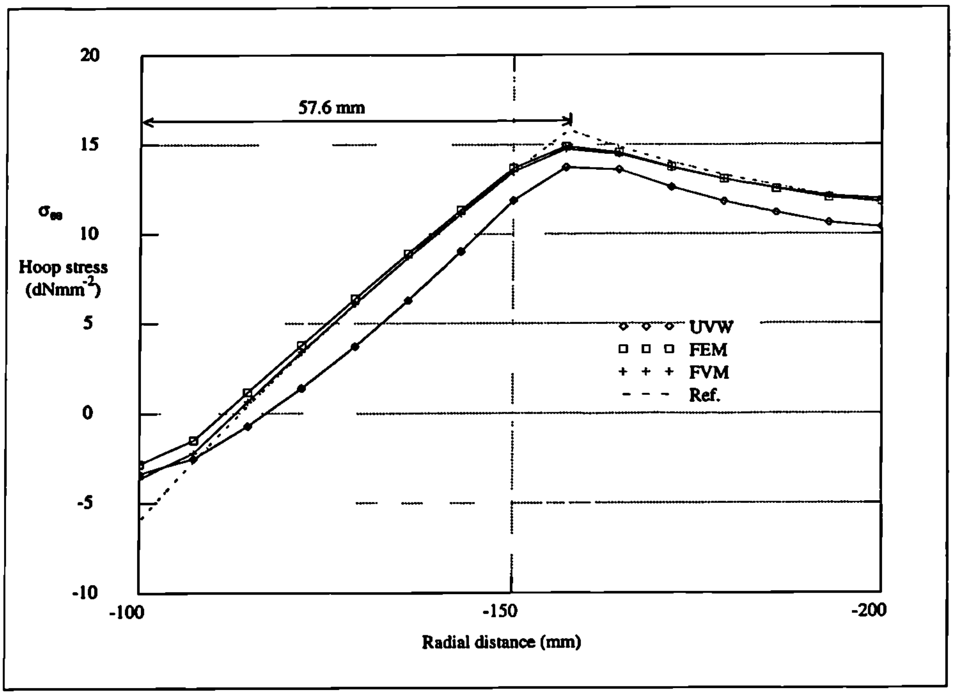

Figure 5.27: Mesh consisting of 3,165 nodes and 2,646 TLH elements.

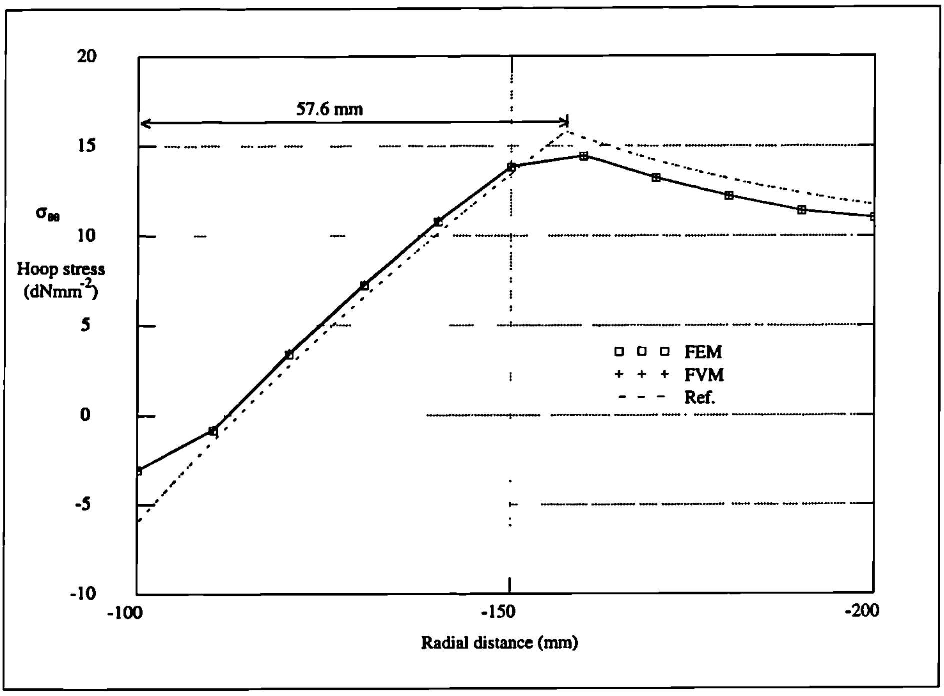

Figure 5.28: Mesh consisting of 726 nodes and 1,000 BLP elements.

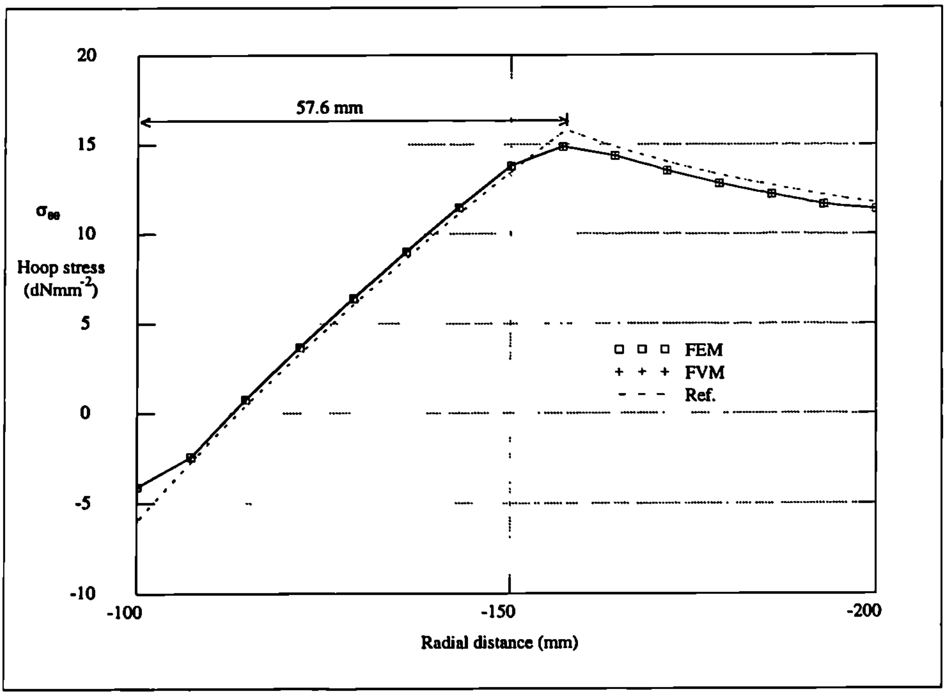

Figure 5.29: Mesh consisting of 1,800 nodes and 2,744 BLP elements.

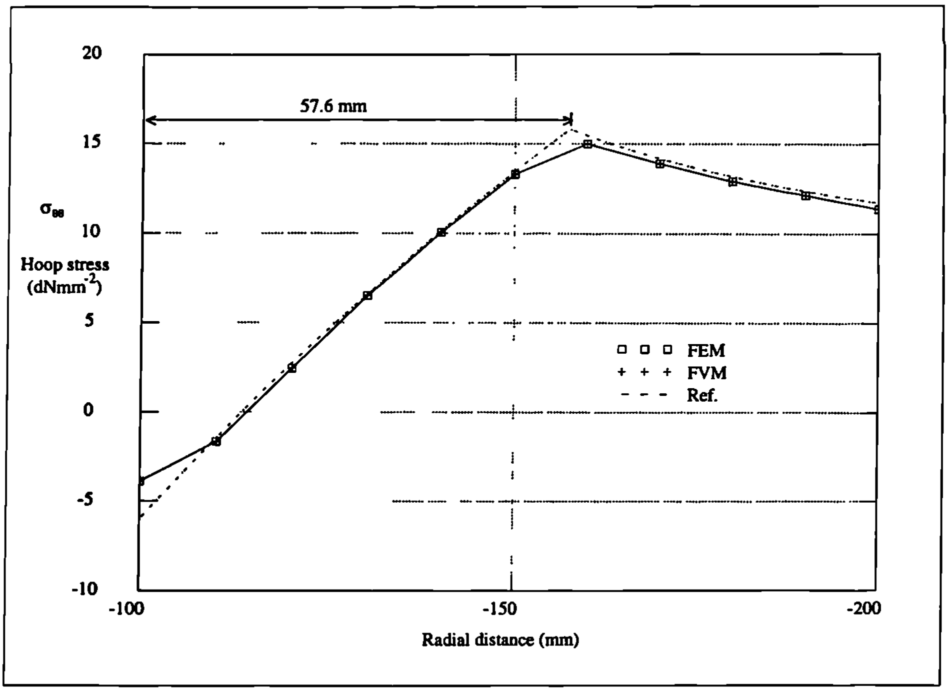

Figure 5.30: Mesh consisting of 1,221 nodes and 4,800 LT elements.

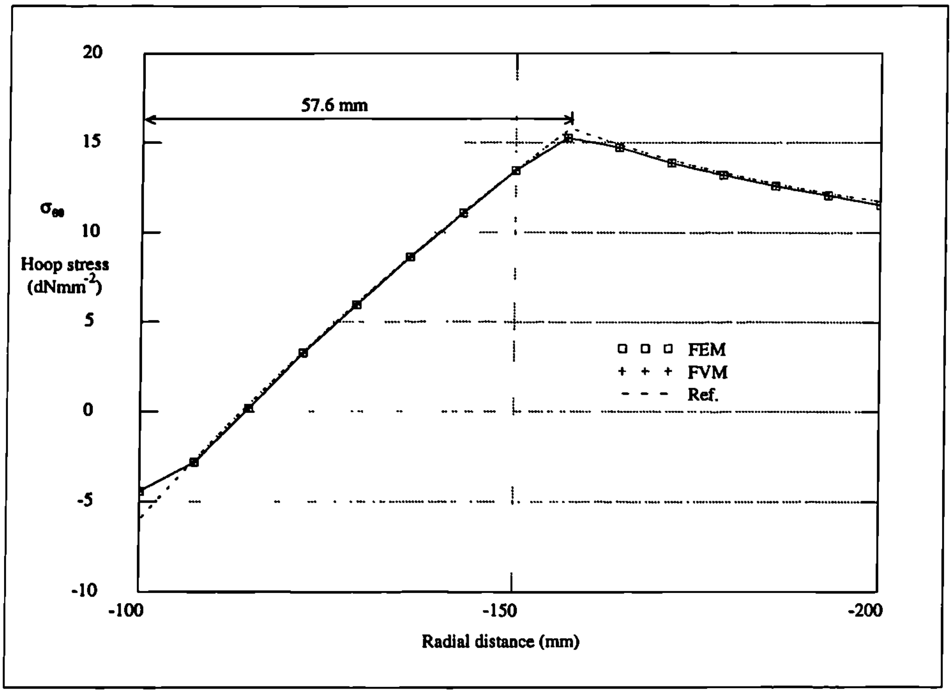

Figure 5.31: Mesh consisting of 3,165 nodes and 13,328 LT elements.

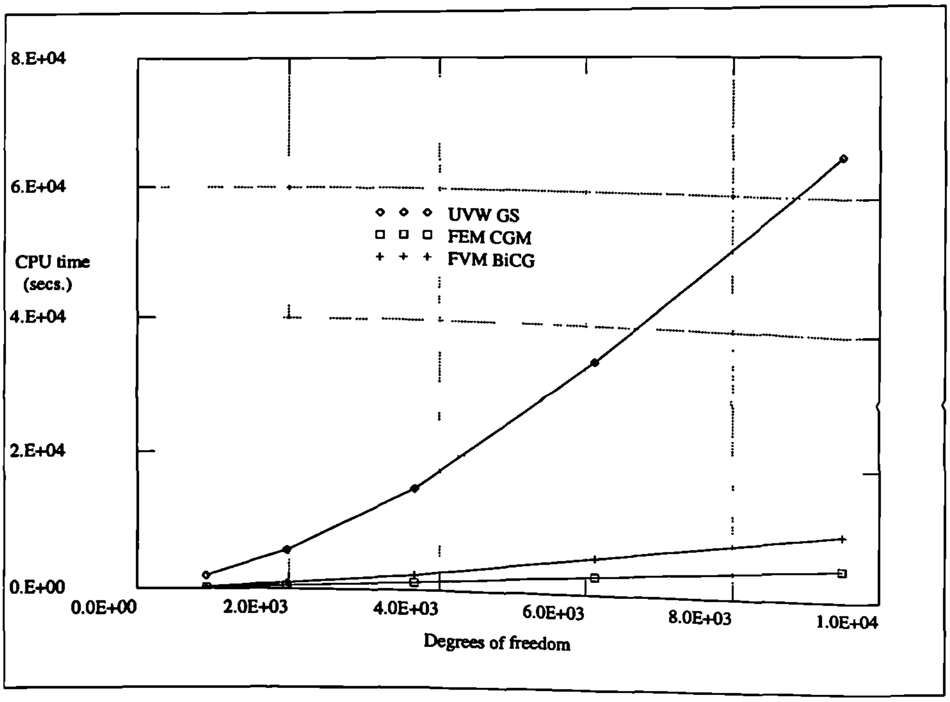

Figure 5.32: CPU times for TLH elements on a SPARC 4, 110MHz.

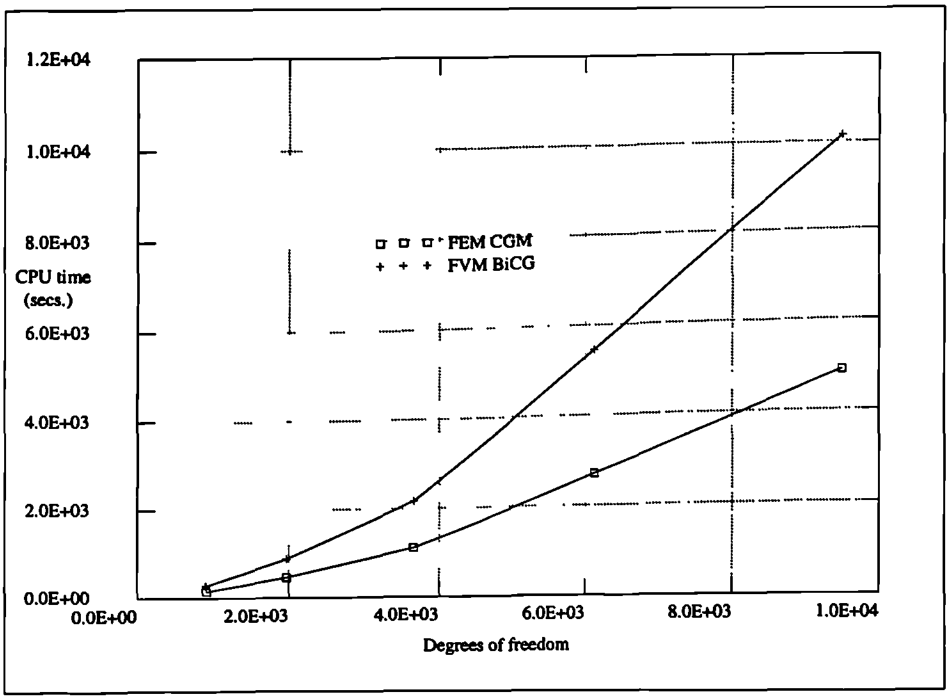

Figure 5.33: FE and FV CPU times for TLH elements on a SPARC 4, 110MHz.

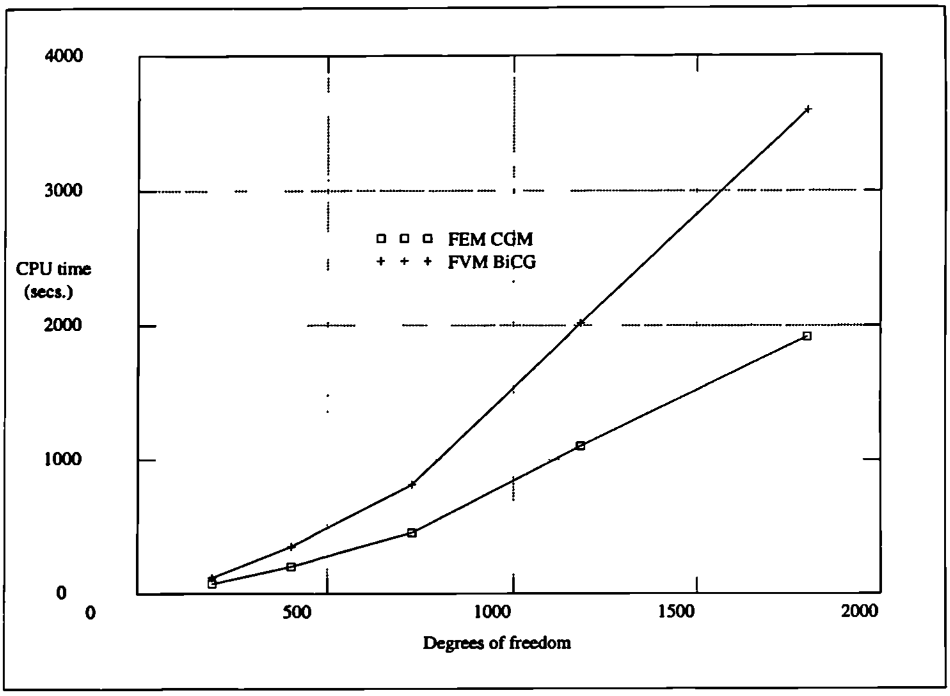

Figure 5.34: CPU times for BLP elements on a SPARC 4, 110MHz.

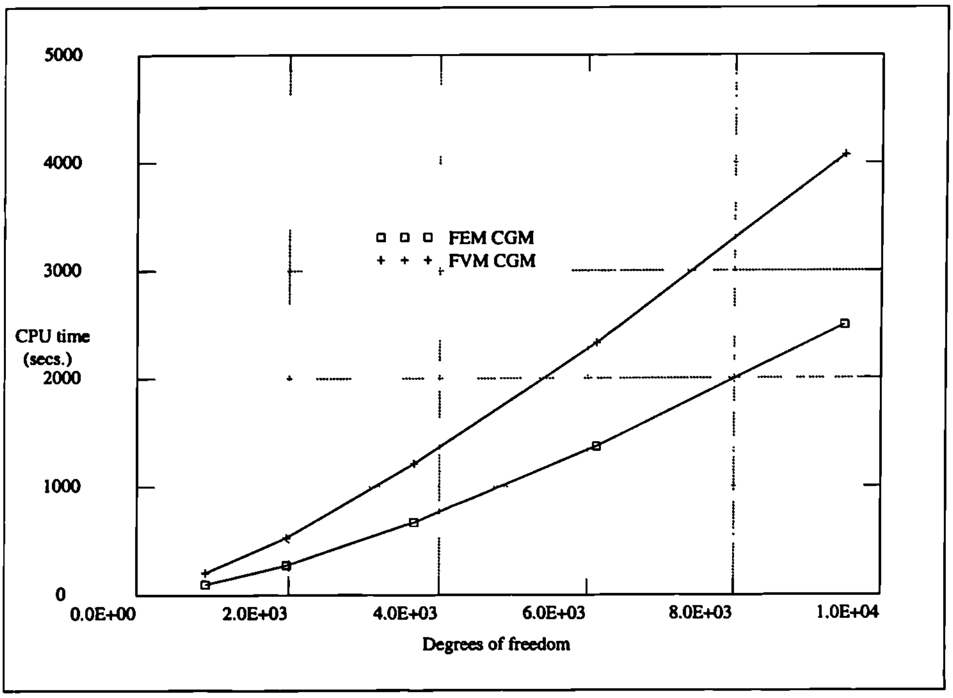

Figure 5.35: CPU times for LT elements on a SPARC 4, 110MHz.

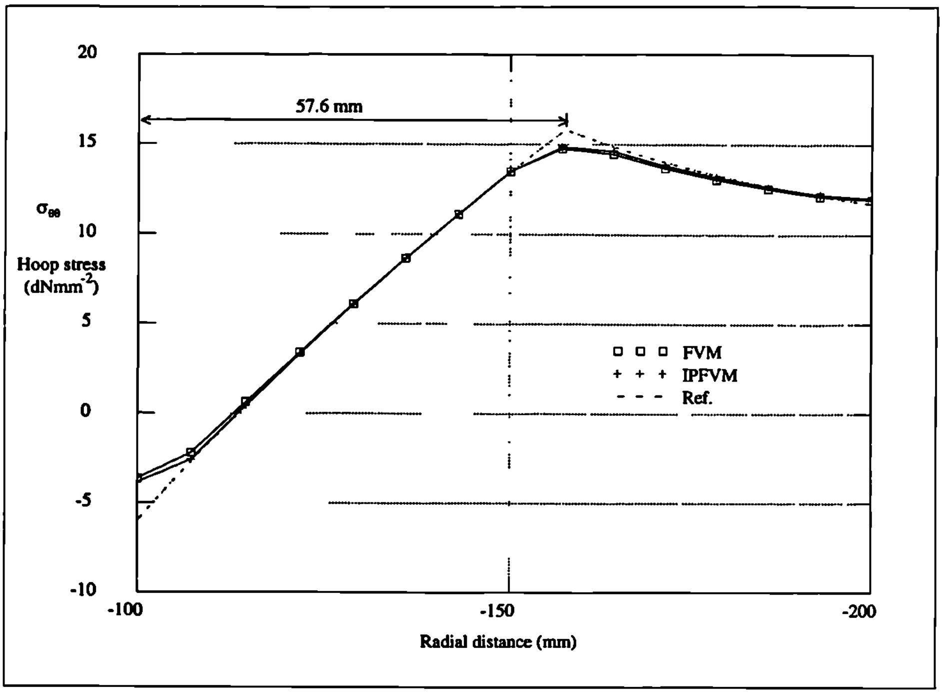

Figure 5.36: Comparison for FVM with TLH elements.

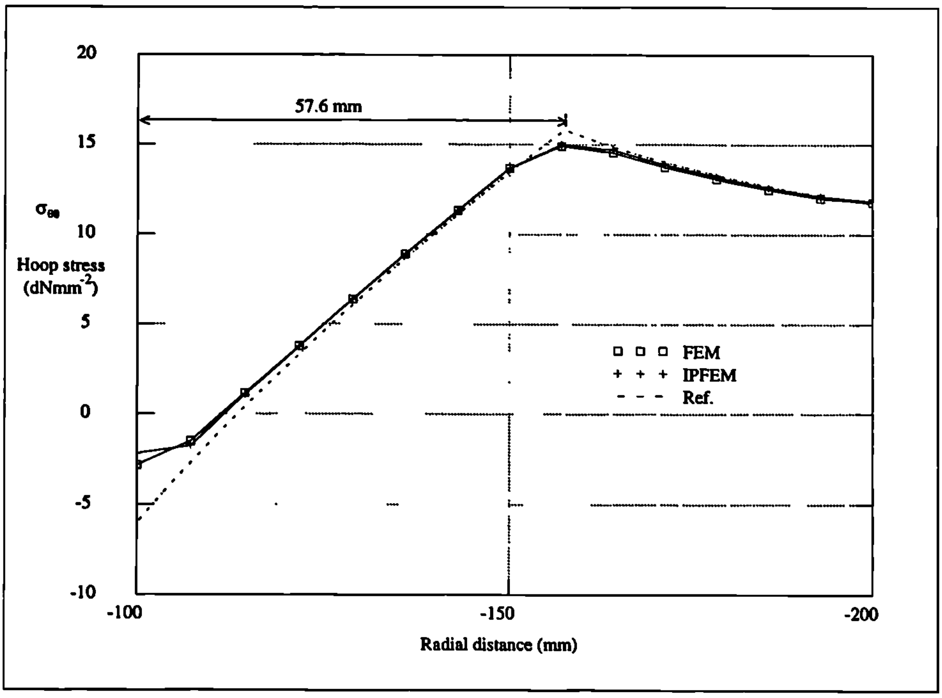

Figure 5.37: Comparison for FEM with TLH elements.

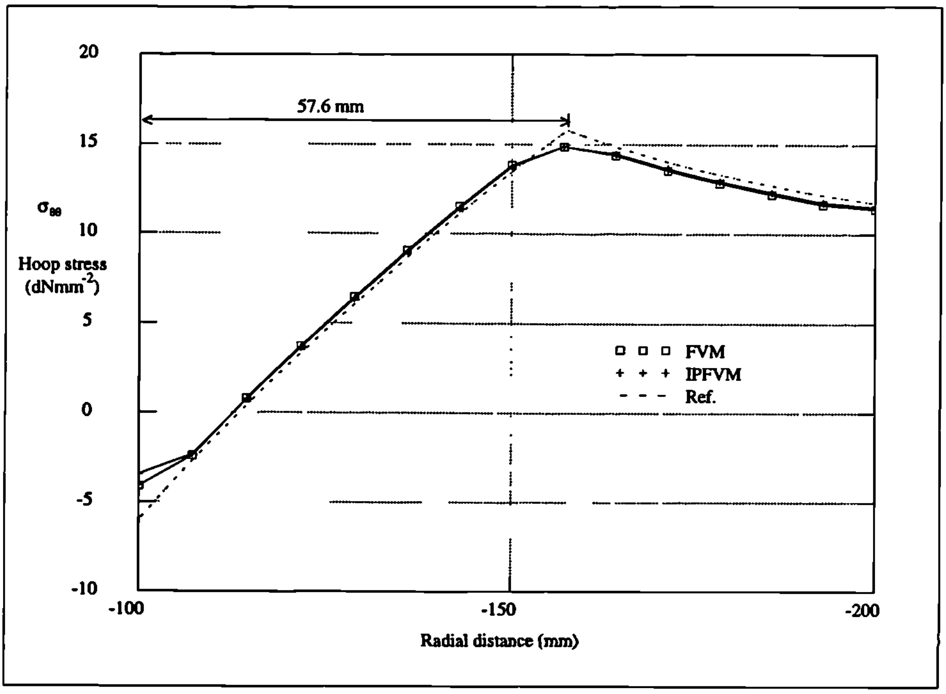

Figure 5.38: Comparison for FVM with BLP elements.

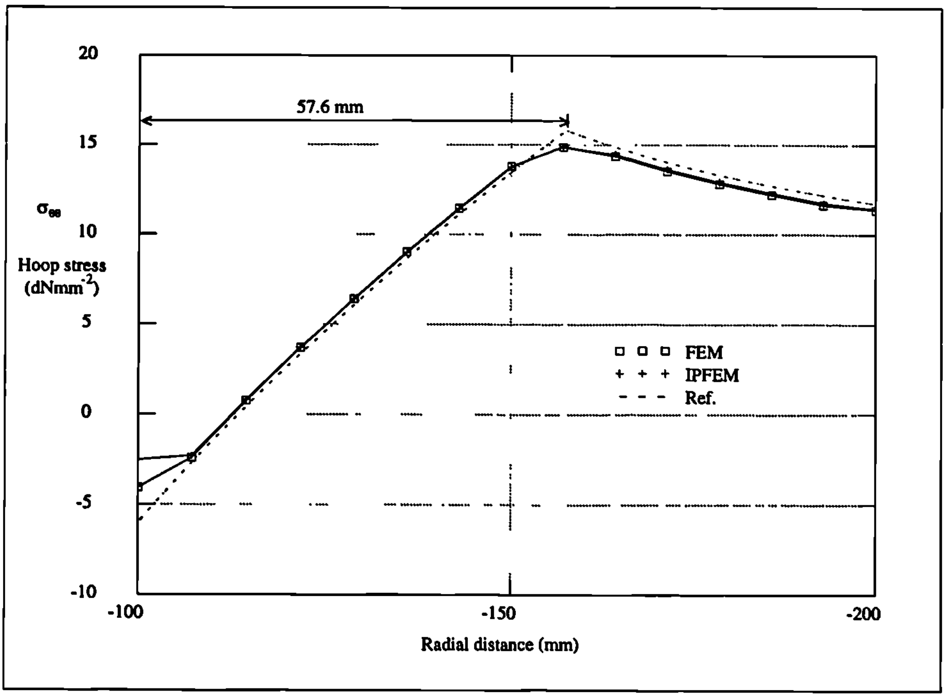

Figure 5.39: Comparison for FEM with BLP elements.

5.5 Closure

In this Chapter the FVM and the FEM have been compared against reference solutions for a variety of mechanical problems.

With regard to the linear elements in two and three dimensions the FVM and the FEM employed in this research are in complete agreement with respect to the numerical solution. The FVM requires slightly more computational effort as it visits more integration points than the FEM for an equivalent element.

It is important to note the potential superiority with regard to accuracy of the FVM when compared to the FEM with regard to the internally pressurised spherical vessel, when TLH elements are employed. However, it should also be noted that the resultant coefficient matrix associated with the FVM is asymmetric and requires approximately twice the computational effort to solve.

Chapter 6

Thermo-mechanical Validation

The further aim of this research is to include material non-linearity within a FV framework, enabling the simulation of complex industrial processes involving not only solid mechanical behaviour, but also other complex physical behaviour such as heat transfer, solidification and fluid dynamics. A case in point is the casting of metals, which involves a wide variety of physical behaviour including that previously described.

The original FV framework upon which this research is based was restricted to two dimensional analyses and was developed as the engineering software UIFS (Unstructured Integrated Fluids and Solids) at the University of Greenwich [42, 20, 22, 26, 25]. The inclusion of material non-linearity within this framework to improve the simulation of a metal casting process is described by Taylor et al [89].

The FV framework has now been extended to the three dimensional engineering software framework PHYSICA [24], also developed at the University of Greenwich. The inclusion of material non-linearity within this framework will be described in this Chapter as it also applies generally to the two dimensional case.

The implementation and the methods employed in the heat transfer, solidification and fluid flow algorithms are those developed at the University of Greenwich by Chow et al [20, 25]. They will not be described in detail in this thesis as they are the results of prior research.

Though it is important to note that for heat transfer, solidification and fluid flow algorithms that exist within PHYSICA at present, a cell-centred FVM as discussed in Chapter 1 is employed.

6.1 Conservation equations

The additional equilibrium equations governing the conservation of heat transfer and fluid flow in three dimensions are described as follows:

For momentum

$$\begin{aligned}\frac{\partial \rho U}{\partial t} + \nabla(\rho \mathbf{V} U) &= \nabla.(\mu \nabla U) - \frac{\partial p}{\partial x} + S_U, \\ \frac{\partial \rho V}{\partial t} + \nabla(\rho \mathbf{V} V) &= \nabla.(\mu \nabla V) - \frac{\partial p}{\partial y} + S_V, \\ \frac{\partial \rho W}{\partial t} + \nabla(\rho \mathbf{V} W) &= \nabla.(\mu \nabla W) - \frac{\partial p}{\partial z} + S_W, \end{aligned} \tag{6.1}$$

for continuity

$$\frac{\partial \rho}{\partial t} + \nabla.(\rho \mathbf{V}) = 0, \tag{6.2}$$

and for energy

$$\frac{\partial \rho h}{\partial t} + \nabla(\rho \mathbf{V} h) = \nabla.\left(\frac{k}{c} \nabla h\right) + S_h. \tag{6.3}$$

Where $\mathbf{V} = (U, V, W)$ is the fluid velocity vector, p is the pressure, h is the enthalpy and ρ, μ, c and k are the material density, viscosity, specific heat and thermal conductivity, respectively.

The source terms S_U, S_V, S_W and S_h contain the additional source terms necessary for the modelling of the solidification process.

For momentum these sources are; buoyancy, to characterize the natural convection of the molten material as it cools and Darcy, to terminate the velocity components as the material solidifies. For the energy equation the latent heat source, S_T, depicts the energy release during the phase change. If the specific heat c is constant, the relationship between enthalpy h and temperature T simplifies to

$$h = cT$$

which upon substitution in equation 6.3 provides

$$\frac{\partial \rho T}{\partial t} + \nabla(\rho \mathbf{V} T) = \nabla . \left(\frac{k}{c} \nabla T\right) + \frac{S_h}{c}. \tag{6.4}$$

In this manner, temperature is chosen as the dependent variable of the energy equation to emphasise the thermo-mechanical coupling via the temperature field.

6.2 Thermo-mechanical coupling

The coupling between the thermal and the mechanical analysis is mainly unidirectional via the temperature field. The coupling can occur at an incremental or iterative level, for strongly coupled systems iterative coupling is a necessity. For thermo-mechanical problems involving large plastic strains considerable heat loss can occur as described in section 2.1.1.2, the coupling is then bidirectional and can be performed at an iterative level [99]. Only small strain problems are considered in this research and the heat loss due to plastic straining can be neglected without any reasonable loss of accuracy. For small strain thermo-mechanical problems which have relatively weak coupling, incremental coupling is possible. At an incremental level the thermal analysis is performed over a suitable number of time steps and then the mechanical analysis is performed, this staggered approach is then continually repeated for the complete analysis.

It is important to note that the application of the thermal load in an incremental fashion is essential to capture the path dependent non-linear material behaviour. The geometry may or may not be updated with regard to the thermal analysis, for some problems involving small strains little accuracy is lost by not updating the geometry. Hence, in some cases the thermal and mechanical analysis can be performed separately. For complex applications, such as the die casting of metals, the geometry must be updated with regard to the thermal analysis in order to model the forming of gaps between the cast and mould as deformation

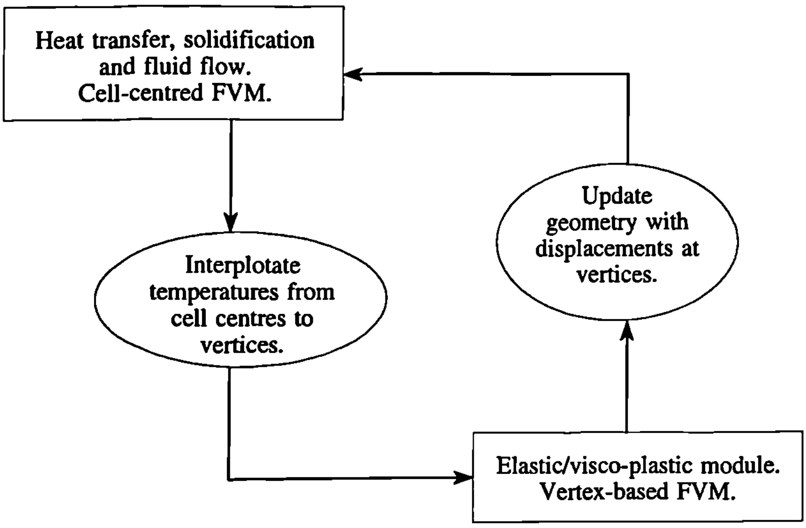

Figure 6.1: Incremental thermo-mechanical coupling within the FV framework.

occurs [12, 67, 42, 68, 63]. The coupling is now bidirectional and for this reason a complete thermo-mechanical coupling of the temperature field and geometry as illustrated in Figure 6.1 is provided within the FV framework PHYSICA [24]. This is equivalent to the original coupling method as employed by Cross et al [26] in the engineering software UIFS.

6.2.1 Test case 1: Quenching of a steel slab

This test case involves the quenching of a large steel plate and the consequential residual stress. If interest is restricted to the regions away from the edges of the plate, a plate of infinite extent can be assumed. For a plate of infinite extent, the heat conduction analysis associated with a convective cooling boundary condition at the surfaces is one dimensional and a thermal gradient exists in one direction only, through the thickness of the plate.

The heat flux due to the convective cooling is

$$q = h_c(T - T_A),$$

where h_c is the heat transfer coefficient and T_A is the ambient temperature of the surrounding fluid. The material properties associated with the thermal analysis are described in Table 6.1.

ρ	k	c	h_c	T_A
7832 kgm^{-3}	58.8 W/(mK)	600 J/(kgK)	193.1 $\text{W/(m}^2\text{K)}$	70 °C

Table 6.1: Material properties associated with the thermal analysis.

The plate consists of an elastic/perfectly plastic material with a temperature dependent yield stress, as described in Table 6.2. It should be noted that the time dependent stresses are large enough to cause plastic deformation and hence residual stresses will remain after the plate has cooled. The remaining material properties associated with the mechanical analysis are described in Table 6.3. The plate is initially at a very high uniform temperature $T_i = 1038°\text{C}$, close to the melting point of the material. The plate then cools to the ambient temperature associated with the convective boundary condition.

Temperature (°C)	70.0	121.0	1121.0
Yield stress (MPa)	248.2	248.2	24.82

Table 6.2: Temperature dependent yield stress.

6.2.1.1 Reference solution

The reference solution is obtained from a semi-analytical method, where an elasto-plastic behaviour with a Von-Mises yield criterion is assumed for the mechanical analysis [62]. The governing differential equations are manipulated in such a way that a numerical step-by-

E	ν	α	γ	H
2.068×10^5 MPa	0.3	1.35×10^{-5} /K	1.0×10^{-4} /s	0 MPa

Table 6.3: Material properties associated with the mechanical analysis.

step procedure can be performed with regard to time, where the temperature, stress and location of the plastic regions at time $t+\Delta t$ are computed from values at time t. An explicit finite difference technique is employed with regard to temperature, but an implicit finite difference technique is employed with regard to the solid mechanics [62].

6.2.1.2 Numerical analysis

The numerical analysis is performed in three dimensions using the engineering software PHYSICA [24]. One of the meshes employed in the analysis is illustrated in Figure 6.2 and consists of 40 TLH elements. With regard to the mechanical and thermal analysis within the FV framework, it is important to note that mesh elements are conceptually different at present. With regard to the thermal analysis the cell-centred FVM employed allows an arbitrary polygon to be employed as an element in the mesh, thus any element selected for a mechanical analysis is compatible with the thermal analysis [24, 20]. Thus allowing the

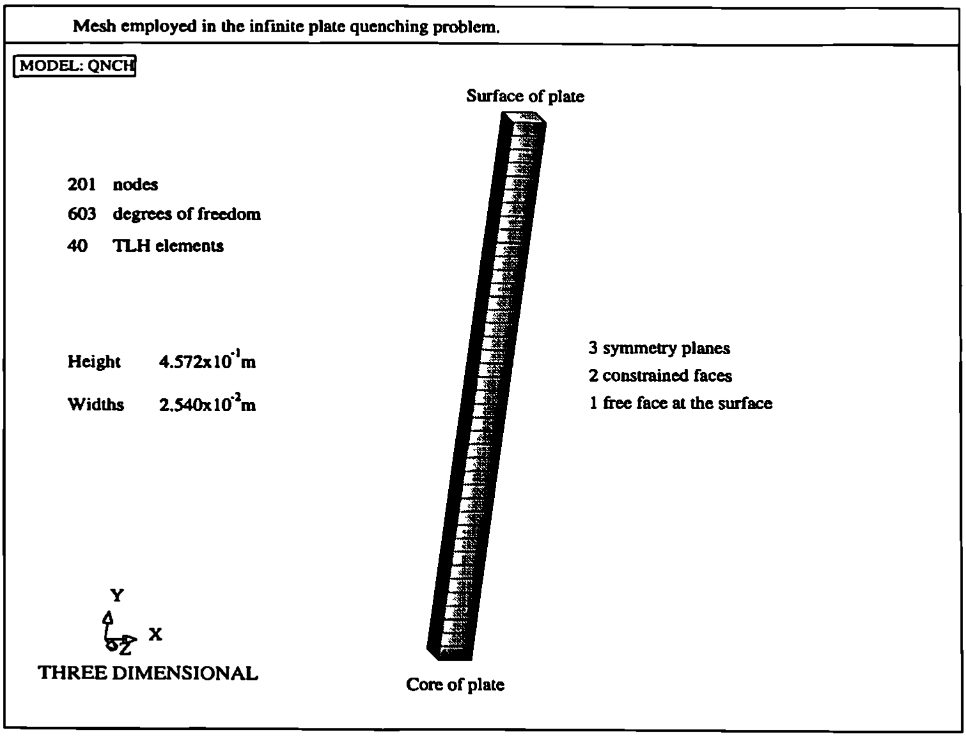

Figure 6.2: Quenching of an infinite steel plate.

simulation of complex geometries with irregular meshes. Though it is important to note that any non-orthogonality and non-conjuctionality present can introduce mesh effects into the thermal analysis [24]. Methods have been developed to overcome these difficulties [24, 20]. Such problems involving complex geometries will be modelled in the following chapter.

For the mechanical analysis a state of generalized plane strain is assumed [58], such that

$$\sigma_{xy} = \sigma_{yz} = \sigma_{zx} = 0,$$

$$\sigma_{xx} = \sigma_{zz},$$

$$\sigma_{yy} = 0.$$

This is achieved using constraint equations as described in Appendix E. The nodes on the free faces in the x and z planes, as illustrated in Figure 6.2, are constrained to translate with the same displacement in the x and z directions, respectively. This is achieved by assigning a master degree of freedom to slave degrees of freedom on the relevant faces. The transient thermal analysis is performed with a gradually increasing time step. The mechanical analysis is performed at every ten time steps of the thermal analysis and in this way the thermal load is applied in an incremental fashion, which captures the path dependent mechanical behaviour. It is important to note that the elasto-visco-plastic analysis converges to a steady state solution during each mechanical analysis and is equivalent to an inviscid elasto-plastic solution [105].

Additionally, a numerical reference solution is available using the FE engineering software LUSAS [36]. This problem is described in the LUSAS verification manual [36] and is available as an example case. In LUSAS the numerical analysis is performed using a two dimensional axisymmetric approximation and the mesh consists of ten bi-quadratic quadrilateral elements [36]. The results obtained using LUSAS are illustrated in Figure 6.6.

6.2.1.3 Discussion of numerical results

The transient behaviour of the mechanical analysis is illustrated in Figure 6.3. The transient stress and plastic strain behaviour at the core, mid-point and surface of the plate are illustrated in Figures 6.3.1 and 6.3.3.

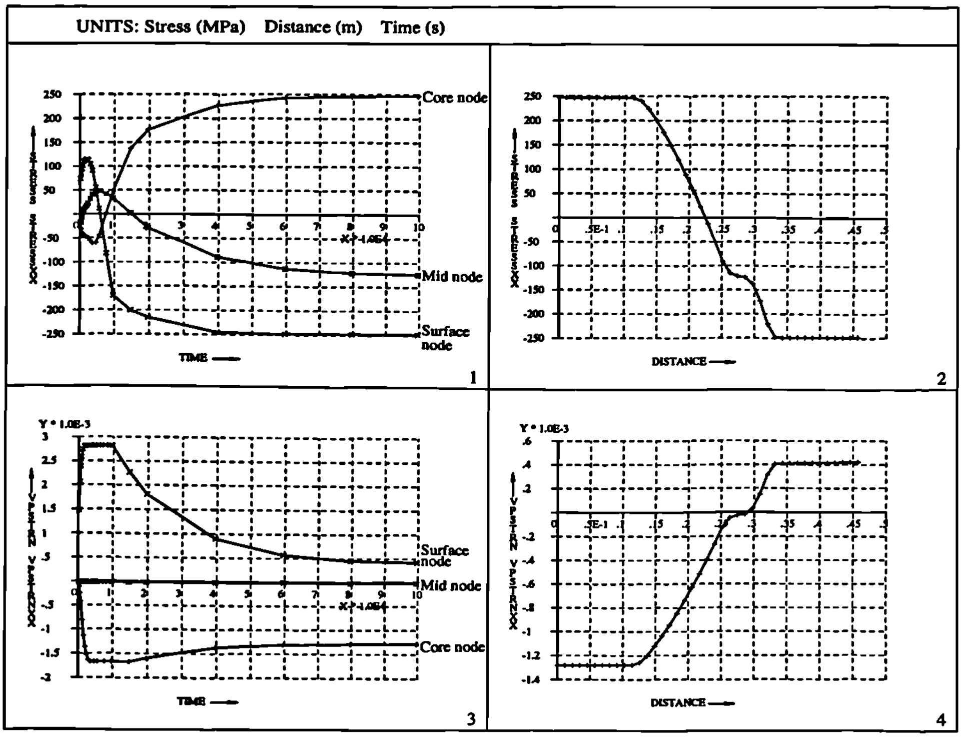

Figure 6.3: Transient behaviour of stress and plastic strain during quenching.

From the stress behaviour it is possible to observe the stress reversal phenomenon associated with the quenching problem. Initially the stress at the surface is tensile, but at the end of the analysis the residual stress is compressive, the opposite is true for the core. From the plastic strain behaviour it is possible to observe a mid-point region which is permanently elastic and does not undergo any plastic straining during the quenching. The residual stresses are illustrated in Figure 6.3.2 and the associated plastic strains are illustrated in Figure 6.3.4.

The numerical analysis was performed with PHYSICA using a fine mesh involving 40 TLH elements as illustrated in Figure 6.2 and a coarser mesh involving 9 TLH elements. The results from the coarse mesh are illustrated in Figure 6.4 and compare well with the reference solution and the numerical analysis performed in LUSAS, which is illustrated in Figure 6.6.

Though it is important to note, that to capture the purely elastic behaviour in the mid-point region a finer mesh is required. This is illustrated in Figure 6.5, where the residual

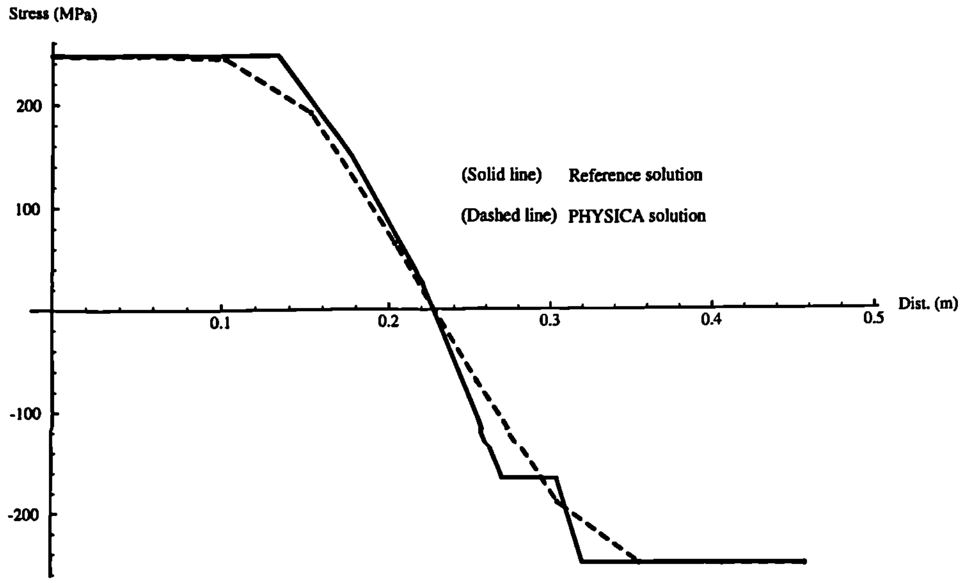

Figure 6.4: Residual stress after quenching (coarse mesh).

stresses are much closer to those of the reference solution.

In closure, it should be noted that for this problem the heat transfer coefficient h_c associated with the convective boundary condition is constant and was selected to resemble quenching in air. Further research has been performed on quenching in liquids such as water and temperature dependent heat transfer coefficients have been employed [58]. Also the Leidenfrost phenomenon can be included, which accounts for the formation of vapour blankets around the quenched component, severely effecting the cooling rate [40, 39]. Finally, for metals such as steels, crystal transformations can occur during the quenching process which will then contribute to the total strains. Such phenomena has been studied elsewhere, extensively, and is noted in this research as a point of interest [1].

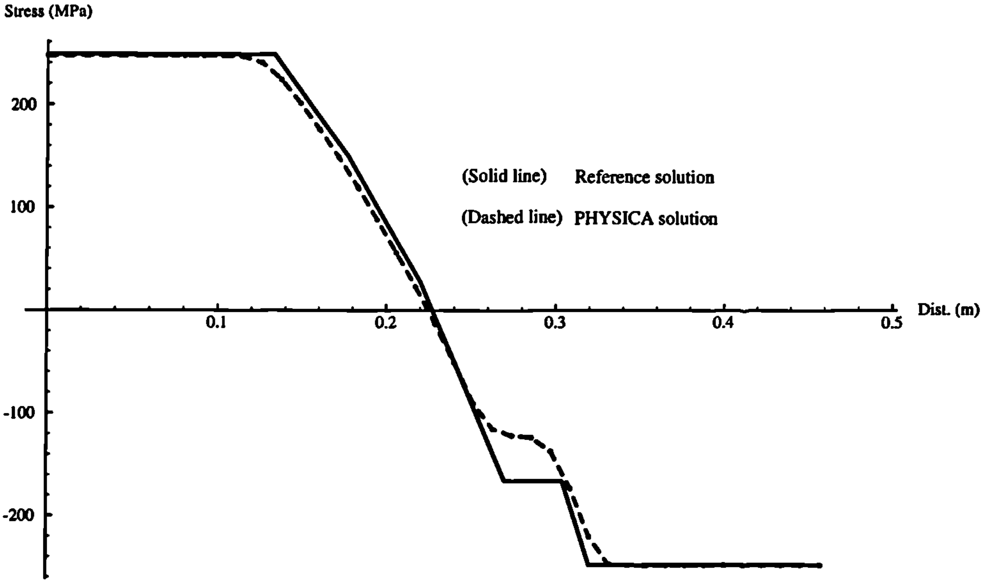

Figure 6.5: Residual stress after quenching (fine mesh).

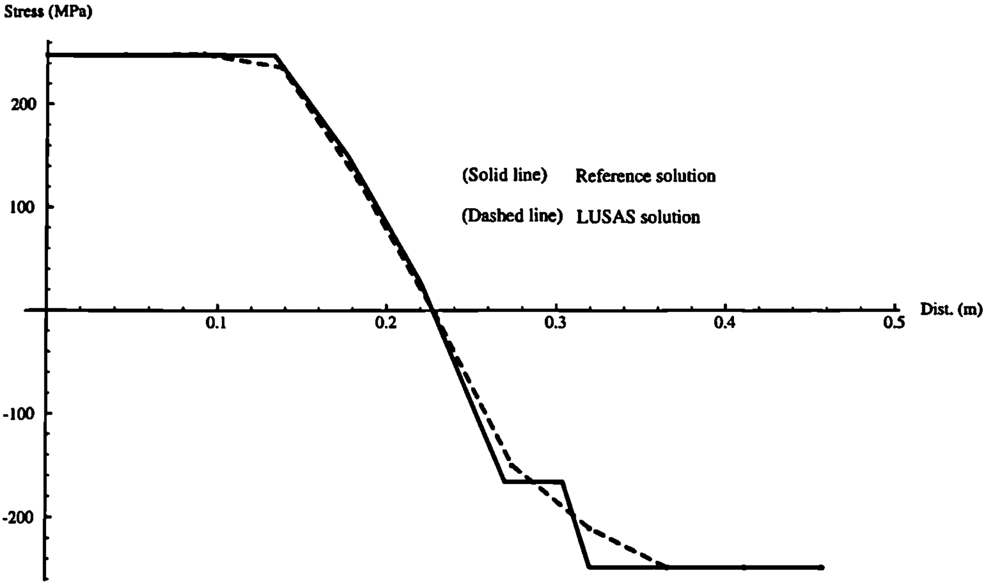

Figure 6.6: Residual stress after quenching.

6.2.2 Test case 2: Solidification of a steel slab

This validation problem is an extension of the previous problem. In this case the slab is initially liquid and is assumed to solidify by heat conduction only. The heat conduction analysis is simplified by assuming a fixed temperature at the surface. This validation problem has been studied by a number of researchers employing a variety of commercial FE software [95, 60].

The geometrical approximation of an infinite slab as described in Figure 6.2 can also be assumed in the modelling of the continuous casting of steel [60]. Where the geometry represents a slice of the cross-section of a casting strand. In this case the dimensions of the problem are length, *8mm and widths, 1mm and the mesh consists of 40 TLH elements. The* thermal boundary conditions and material properties can be modified to represent different types of steel under various cooling conditions [60].

6.2.2.1 Analytical solution

A commonly referenced analytical solution is available for this problem [98]. The analytically derived equations will be stated here for completeness. With regard to the one dimensional thermal analysis the position of the solidification front at any time t is

$$x_s = 2\lambda\sqrt{\frac{kt}{\rho c}}, \tag{6.5}$$

where the constant λ is the solution of the following equation:

$$\frac{1}{e^{\lambda^2}\,\mathrm{Erf}(\lambda)} - \frac{T_l - T_s}{e^{\lambda^2}\,T_s\,(1-\mathrm{Erf}(\lambda))} = \frac{h\,\lambda\,\sqrt{\pi}}{c\,T_o} \tag{6.6}$$

and the temperatures T_s, T_l and T_o denote the solidus, liquidus and initial temperature drop at the surface, respectively [17]. The error function $\mathrm{Erf}(\lambda)$ is defined in Appendix A and h is the latent heat per unit mass. Initially at time $t = 0$, the slab is at the liquidus temperature and the temperature at the surface is dropped to $T_s = 1300$°C and kept constant thereafter. Using the material properties as described in Table 6.4, equation 6.6 can be solved for λ, in this case using the commercial software MATHEMATICA [102].

T_s	T_l	T_o	h	c
1468 °C	1525 °C	168 °C	2.72×10^5 J/Kg	700 J/(KgK)

Table 6.4: Material properties associated with the solidification analysis.

With regard to the theoretical mechanical analysis an assumption of similarity is employed [98], which assumes that the stress solution and hence ratio of the elastic and plastic regions is independent of time. This coincides with temperature distribution which is also independent of time when the equations are cast in a normalized fashion [98].

From the theoretical analysis the following simultaneous equations with respect to s and t are obtained:

$$\begin{aligned}\frac{2\,(1-m)\,s}{e^{s^2}} &= \frac{-\frac{1-m}{e^{s^2}} - \left(1+e^{-\lambda^2}\right) m + \frac{1+m}{e^{t^2}}}{s-t},\\ \frac{2\,(1-m)\,s}{e^{s^2}\sqrt{\pi}} &= \frac{2\,m\,\mathrm{Erf}(\lambda) + (1-m)\,\mathrm{Erf}(s) - (1+m)\,\mathrm{Erf}(t)}{\log(\frac{s}{t})}.\end{aligned}$$

Where

$$m = \frac{(1-\nu)Y_o}{\alpha E T_o}$$

and the ratio of the elastic and plastic regions are defined by the variables s and t. It is important to note that the yield stress is assumed to vary linearly, decreasing from Y_o at the surface temperature to zero at the solidus temperature.

ν	Y_o	α	E
0.35	20 MPa	2.0×10^{-5} /K	4.0×10^4 MPa

Table 6.5: Material properties associated with the mechanical analysis.

Substituting the material properties as described in Table 6.5 into the above simultaneous equations and solving for s and t using MATHEMATICA [102], the following values can be obtained:

$$s = 0.218068, \qquad t = 0.0830676.$$

The stress distribution is described by the following three equations [98]:

$$\sigma(x) = m\left(1 - \frac{\mathrm{Erf}(\lambda\,x)}{\mathrm{Erf}(\lambda)}\right) \qquad \text{for} \quad s' < x < 1, \qquad (6.7)$$

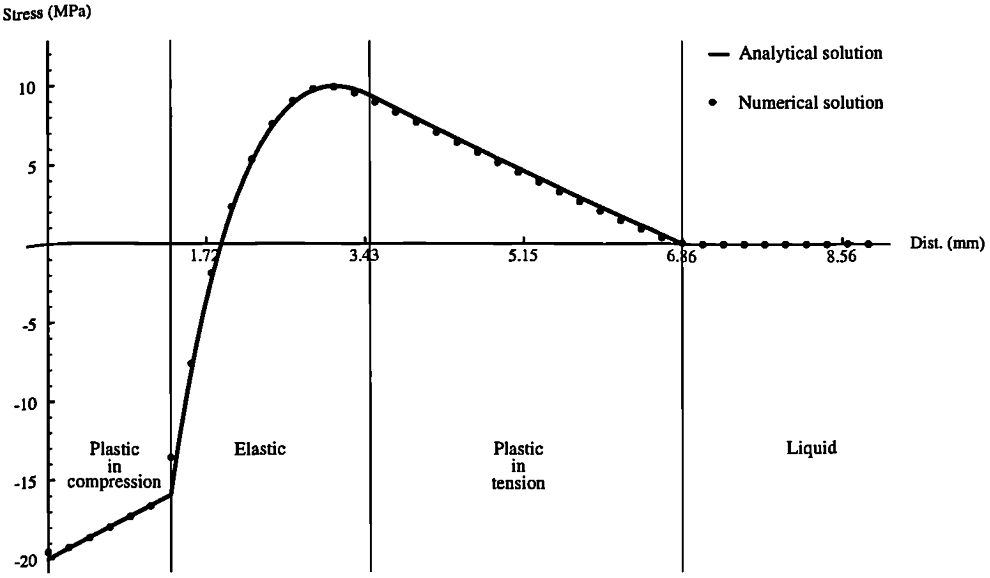

Figure 6.7: Stress distribution after 10s of solidification.

$$\begin{aligned} \sigma(x) &= m\left(1-\frac{\operatorname{Erf}(s)}{\operatorname{Erf}(\lambda)}\right)+\frac{\operatorname{Erf}(s)-\operatorname{Erf}(\lambda\, x)}{\operatorname{Erf}(\lambda)}- \\ &\quad \frac{2\,(1-m)\; s\,\log(\frac{s}{\lambda x})}{e^{s^2}\sqrt{\pi}\operatorname{Erf}(\lambda)} \qquad \text{for} \quad t'<x<s', \qquad (6.8) \\ \sigma(x) &= m\left(\frac{\operatorname{Erf}(\lambda\, x)}{\operatorname{Erf}(\lambda)}-1\right) \qquad \text{for} \quad 0<x<t'. \qquad (6.9) \end{aligned}$$

Where $s' = \lambda s$ and $t' = \lambda t$. Equations 6.7, 6.8 and 6.9 represent the normalised stress distribution, such that the solidification front is at $x = 1$ and the surface is at $x = 0$. The non-normalized stress distribution can be obtained and is employed as the reference solution in Figure 6.7. Equation 6.7 describes the stress distribution in the compressive plastic range, equation 6.8 describes the stress distribution in the elastic range and equation 6.9 describes the stress distribution in the tensile plastic range [98]. In the theoretical analysis, only the stresses in the growing elastic/perfectly plastic solidified portion of the slab are considered. The stresses in the liquid region are considered zero.

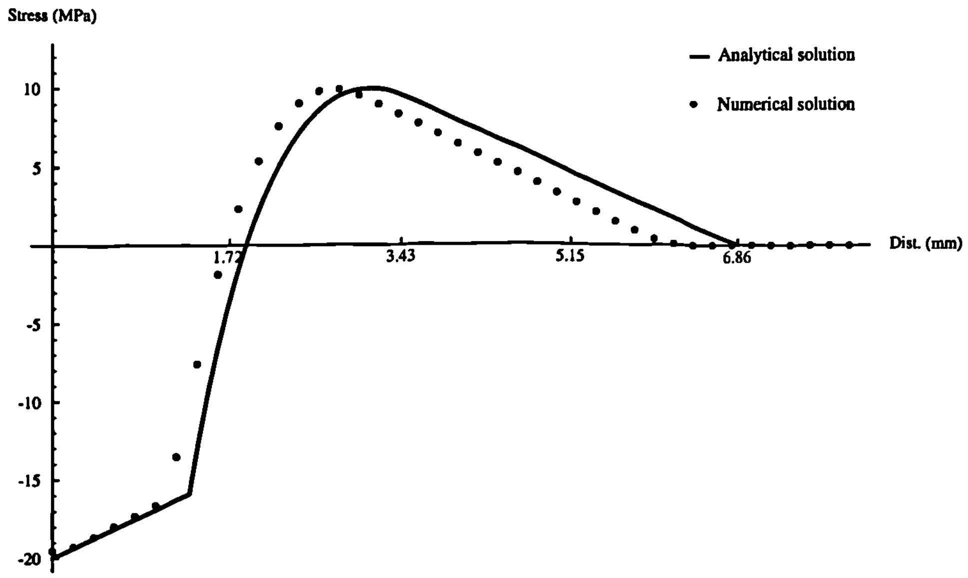

Figure 6.8: Comparison of stress distributions with regard to solidification fronts.

6.2.2.2 Numerical procedure for solidification

The solidification is assumed to occur by heat conduction only. The problem is then simplified considerably, which allowed a theoretical analysis to be performed. With regard to the numerical analysis performed using PHYSICA, a number of correction methods for the liquid fraction update are available [22]. For this problem the default method of Voller and Prakash is employed [79]. This technique is a source based method with regard to solidification. Which casts the problem in a non-linear form, but furnishes a more robust algorithmic approach [97].

6.2.2.3 Numerical procedure for liquid regions

In order to consider the deformation of both liquid and solid regions in the mechanical analysis, a special procedure is required for liquid regions. The procedure adopted for this validation problem is that described by Tszeng and Kobayashi [95]. Other procedures exist, such as that described by Kristiansson [60], but these methods involve prescribing zero displacements to nodes that exist within liquid regions and can fail to account for hydrostatic pressure acting along the solidification front [95].

In the procedure adopted here, at temperatures greater than the coherence temperature (which is assumed to be equal to the liquidus temperature in this case), a Poisson's ratio very close to 0.5 is artificially assigned. Hence, making the liquid phase close to incompressible for mechanical loads. In order to avoid singularity occurring in the coefficient matrix, a value close to zero is assigned to the Young's modulus. This is equivalent to assigning zero stiffness to liquid regions. In this fashion, values of Poisson's ratio and Young's modulus can be chosen to suppress the deviatoric stress component, whilst allowing a volumetric (or metallostatic) component to exist [95].

6.2.2.4 Numerical analysis

The numerical analysis was performed using PHYSICA and the stress distribution after 10s is illustrated in Figures 6.7 and 6.8. The stress distribution of the theoretical solution is matched to that of the numerical solution with regard to the solidification front in Figure 6.7. In Figure 6.8 the position of the solidification front is calculated using equation 6.5, which assumes a semi-infinite body with regard to the thermal analysis. For the numerical analysis a symmetry condition is assumed at the core of the body with regard to the thermal analysis, this will effect the temperature distribution and hence the prediction of the solidification front in the body, causing disagreement between the theoretical and numerical solution. This is clearly illustrated in Figure 6.8.

In this validation problem the hydrostatic pressure is negligible and the stresses in the liquid region are zero as illustrated in Figures 6.7 and 6.8.

6.3 Closure

In this Chapter, the procedures employed to obtain numerical solutions for non-linear, thermo-mechanical problems have been described. The procedures have been validated against a number of test cases involving simple geometries and unidirectional coupling with regard to the thermo-mechanical analysis. In the following Chapter, the procedures will be validated and verified against a number of test cases involving more complex geometry and complete coupling with regard to the thermo-mechanical analysis.

Chapter 7

Applications

In this chapter the previously described finite volume framework, in the form of the three dimensional engineering software PHYSICA [24], is employed in the simulation of the shape casting of metals, which involves complex thermo-mechanical behaviour.

This is an extension to the research performed using UIFS, where a linear elastic material behaviour was also assumed [42] and further research where an elasto-visco-plastic material behaviour was assumed [89].

Initially, PHYSICA is employed to simulate the gravity die casting of a hollow aluminium cylinder and, finally, the sand casting of an aluminium test bar.

7.1 Shape casting of metals

In basic terms, a shape casting process is one in which a supply of liquid metal, of appropriate composition, is prepared, poured into a mould and then allowed to solidify [27, 15]. Heat transfer occurs from the molten metal alloy to the mould and in most cases from the mould to the environment.

A number of shape casting processes are generally described in this manner, each with their own particular advantages and disadvantages. The foundry engineer can select a suitable casting process for a component, by offsetting geometrical accuracy and/or structural soundness required for the component against the relative cost of a particular casting process. Until recently the foundry engineer relied heavily upon personal expertise and accepted working practices. In the advent of the cheaper and more powerful desktop computer, the possibility of realistic simulation software for casting processes as an aid to the foundry engineer is now becoming feasible.

7.1.1 Shape casting processes

The shape casting processes that have been studied and modelled in this thesis are those typically associated with foundries and can be briefly described as follows.

7.1.1.1 Die casting

Die or permanent mould casting involves a reusable mould, consisting of a highly conducting metal, typically tool steel [27, 15]. As the mould is highly conducting, the process furnishes castings which have undergone particularly rapid freezing, and consequently exhibit particularly fine microstructures [27]. With regard to mould filling two methods are generally employed in die casting, pressure die casting [15] and gravity die casting [82, 15]. The former involves the pressurized injection of the molten metal into the mould and is not simulated in this research, while the latter simply involves the pouring of the molten metal alloy into the mould under the action of gravity and is simulated in this thesis, as experimental data is available for the cooling, solidification and deformation [82]. Additionally, the mould is not gas permeable and for this reason the process can be more prone to porosity formation, unless precautions are taken such as performing the filling process in a vacuum [15].

7.1.1.2 Sand casting

Sand casting involves a non-reusable sand mould, which is generally chemically bonded or clay bonded (Green Sand Casting) [15]. The mould is particularly deformable and is a very poor conductor [15]. The rigidity of the sand based mould is dependent upon the bonding of the sand, for clay bonded sand the moulds are less rigid, while for chemically bonded sand the moulds are more rigid [15]. The process furnishes castings which have undergone prolonged freezing and consequently exhibit coarser microstructures [27]. Additionally the mould is gas permeable, which can reduce the amount of porosity formation in the cast [27, 15].

7.1.1.3 Investment casting

Though the process is not modelled in this research, higher precision castings can generally be achieved using the investment casting process, where particularly rigid and precise ceramic moulds are utilised [27, 15]. A wax pattern is shaped for the mould using extremely accurate and reusable metal dies and then a ceramic mould is produced from the wax pattern [15, 27].

7.1.2 Simulation of shape casting processes

Over the last 10 to 15 years a large amount of research effort has been employed in the development of physically accurate software tools for the complete simulation of the metals casting process [25, 92], with the ultimate aim being a useful computational tool for the foundry engineer. To be of major use to the foundry engineer, the simulation software must be tolerably accurate, within a reasonable computational time. This generally requires a flexible software framework which can be extended in a modular fashion depending upon the physical nature of the particular casting simulation required [25, 3].

A number of casting simulation software tools have been developed from the previously mentioned research. ProCAST [96], MAGMAsoft [64] and THERCAST3 [12, 67] to name but a few, though at present the simulation packages available are generally of limited scope with regard to their overall modelling capability of the complete casting process.

The MAGMAsoft software [64] is a consequence of the research performed by Hattel and Hansen [48, 47, 46] as previously discussed in section 1.2.1. The software offers the simulation of mould filling and solidification by heat conduction only, in conjunction with a three dimensional finite difference analysis of the thermo-elastic equations using a staggered grid, which can be interpreted as applying a cell-centred FVM on a structured mesh as indicated in section 1.2.1. Though as yet, the solid mechanics is not fully integrated into the software MAGMAsoft [47].

The ProCAST software [96] is a well established commercial package that offers a wide range of functionality, including the simulation of mould filling, solidification by heat conduction and radiative heat transfer, in conjunction with the three dimensional mechanical analysis of non-linear material behaviour in a loosely coupled fashion [96]. The software has been developed in a FE framework [96].

The THERCAST3 software is a consequence of the research performed by Bellet et al [12, 67, 13]. At present the software offers the simulation of solidification by heat conduction only, in conjunction with a three dimensional analysis of the non-linear material behaviour in a loosely coupled fashion [12, 67, 13]. Again, the software has been developed in a FE framework [12, 67, 13].

7.1.3 Dual thermo-mechanical coupling

During the shape casting process coupled thermo-mechanical behaviour occurs. The molten metal is initially in contact with the mould and a thermal resistance can be associated with the casting/mould interface, at this stage of the process, due to the rugosity of the mould surface [29]. As the casting solidifies, due to heat transfer to the mould, gap formation can occur at the casting-mould interface and the thermal resistance will increase as a function of the gap. In this manner the thermo-mechanical process exhibits dual coupling.

7.1.3.1 Casting/mould gap formation

The variation of the heat transfer coefficient associated with the casting/mould interface during the casting process has been commented upon by a number of researchers [42, 67, 12, 27]. With regard to die casting the thermal resistance due to the gap formation is highly effective due to the high conductivity of the metallic moulds employed [82], alternatively the gap formation is often assumed to be less effective in the cases of sand and investment casting due to the poor conductivity of the sand or ceramic moulds employed [27].

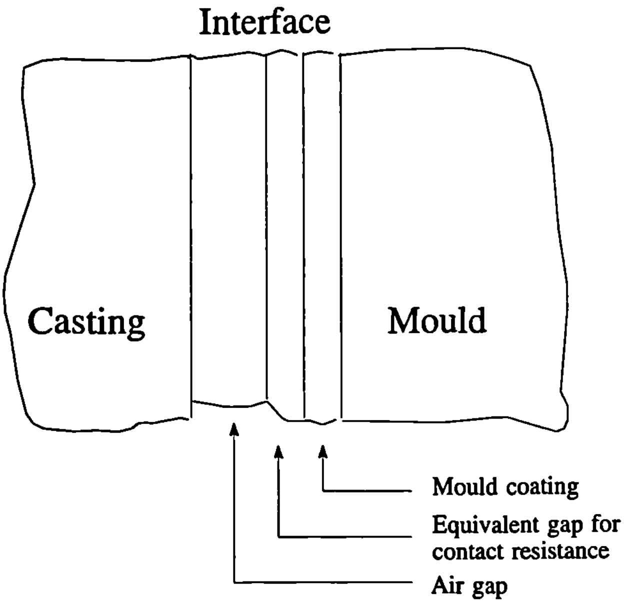

Figure 7.1: The die casting/mould interface.

Considering die casting, the heat transfer coefficient is often assumed to consist of a number of different layers, this leads to a series of thermal resistances as illustrated in Figure 7.1 [82]. In this research the coating layer of the mould is included in the contact resistance and the heat transfer coefficient across the interface h_{if} can be expressed as [82]

$$\frac{1}{h_{if}} = \frac{1}{h_{cr}} + \frac{1}{h_{ag}}, \tag{7.1}$$

where h_{cr} is the heat transfer coefficient of the contact resistance and h_{ag} is the heat transfer coefficient of the air gap.

The thermal contact resistance $\frac{1}{h_{cr}}$ is caused by the rugosity of the mould, which can cause a non-uniform thermal contact between the melt and the mould [82, 29]. In PHYSICA the die casting/mould interface can be implemented by defining the lower limit of the heat transfer coefficient across the casting/mould interface to be equal to h_{cr}. Consequently, if no air gap exists this value will be assigned to the heat transfer coefficient.

The gap formation in PHYSICA is achieved via coincident nodes at the casting/mould interface, consequently the cell faces at the casting/mould interface are initially coincident [42]. The heat transfer flux is calculated at the respective centres of the initially coincident cell faces and as the gap develops it is computed as the distance between the associated face centres. This is a reasonable method for problems involving small strains as the face associations of the original geometry are not drastically altered due to the mechanical deformation.

As described in Figure 7.1 an equivalent gap Δ_{eq} can be associated with the thermal contact resistance [82]

$$\frac{1}{h_{cr}} = \frac{\Delta_{eq}}{k_{cr}}, \tag{7.2}$$

where k_{cr} is the thermal conductivity associated with the die casting/mould interface, initially.

The complete behaviour of the die casting/mould interface can be implemented using a convective heat transfer flux [63]

$$\frac{\partial T}{\partial n} = h_{eff}\left(T_{casting} - T_{mould}\right), \tag{7.3}$$

where the effective heat transfer coefficient at the casting/mould interface is a function of the effective air gap Δ_{ag} and can be calculated as follows [82, 68];

$$h_{eff} = \begin{cases} h_{cr}, & \text{when } \Delta_{ag} \leq \Delta_{eq} \\ \frac{k_{ag}}{\Delta_{ag}}, & \text{when } \Delta_{ag} > \Delta_{eq} \end{cases}, \tag{7.4}$$

where k_{ag} is the conductivity associated with the air gap.

It is important to note that the gap may not be purely air, a mixture of gases could be possible. Additionally, the heat transfer across the casting/mould interface is not necessarily a solely conductive process. Consequently, an effective conductivity associated with air gap can be utilised to facilitate this behaviour. This requires accurate experimental measurement of the heat transfer coefficient as a function of the gap at the casting/mould interface [82, 12].

7.2 Gravity die casting of a hollow aluminium cylinder

The experimental results, against which the numerical analyses of the die casting of a hollow aluminium cylinder are compared, were originally obtained by Schmidt and Svensson [82]. They experimentally studied the heat transfer and air gap formation associated with the die casting of aluminium alloys. A large number of experiments were performed, under a variety of casting conditions and with a selection of aluminium alloys.

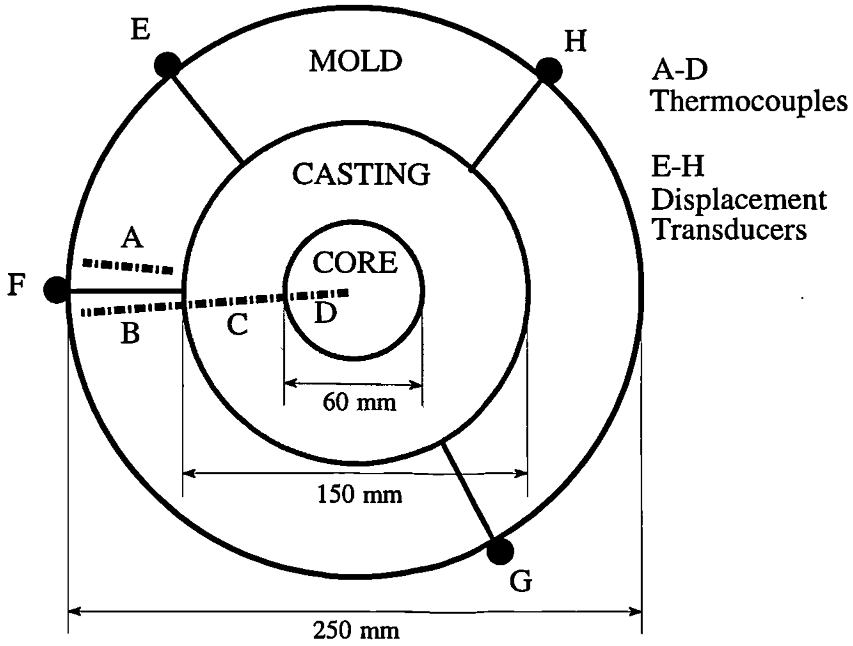

Figure 7.2: Experimental design: Top view.

The particular experimental design, with regard to geometry, thermocouples and displacement transducers, that was employed to obtain the experimental data utilised in this re-

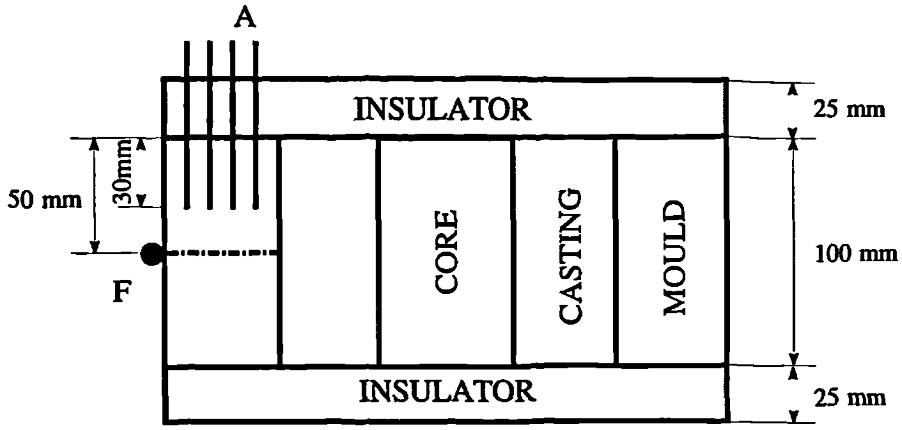

A Thermocouples

F Displacement transducers

Figure 7.3: Experimental design: Side view.

search, is illustrated in Figures 7.2 and 7.3.

It is important to note the positioning of, both, the thermocouples and the displacement transducers. The thermocouples are arranged along the radius of the die casting design, as illustrated in Figure 7.2, to enable inverse heat transfer analyses to be performed at a variety of time intervals. Additionally, a number of displacement transducers are located at mid-height with regard to the aluminium casting, as illustrated in Figure 7.3. Which furnishes an average measurement of the gap formation at the mid-height point over time.

The cylindrical mould and core are made of steel (Fe–0.14%C–0.35%Si–1.2%Mn) and the cylindrical casting consists of the aluminium alloy (Al–7%Si–0.3%Mg). The associated material properties are described in Tables 7.3 and 7.2, respectively. As illustrated in Figures 7.2 and 7.3 the experimental design is axisymmetric and, after the filling of the mould, the top and bottom of the mould are insulated. In this manner, the majority of the heat transfer associated with the cooling and subsequent solidification of the casting is confined to the radial direction.

Heat transfer coefficient (W/(m^{2}K))	400	20.0
Gap distance (mm)	0	0.5

Table 7.1: Relationship between heat transfer coefficient and gap distance.

From the experimental results and the, consequential, inverse heat transfer analyses, it is possible to obtain a relationship between the heat transfer coefficient at the gap and the gap size [82]. In this research the experimentally obtained relationship was suitably approximated by a linear relationship as described in Table 7.1. The values associated with the heat transfer coefficient are particularly low in this experimental case due to the extra thermal resistance of the coating layer. Indeed, for experimental the cases not involving a coating layer the heat transfer coefficient values are an order of magnitude greater [82].

7.2.1 Numerical analysis

The die casting experiment described here, has been previously modelled in three dimensions, by Bellet et al [12, 67, 13], utilising the FEM. As a complex, three dimensional, fully coupled, thermo-mechanical numerical analysis, the experimental casting provides a comprehensive validation test with regard to the FV software framework PHYSICA.

With regard to the thermal analysis the following assumptions were made. After pouring the liquid aluminium alloy is assumed to be static and residual convection is neglected. The liquid alloy is assumed to be at an initial, uniform, temperature of 800°C, the mould, core and insulation are at a, pre-heated, uniform temperature of 200°C and the insulators are at an initial, uniform, temperature of 20°C. These initial temperatures are consistent with the experimental analysis [82].

For the solidification, the latent heat of fusion is assumed to be constant during the solidification phase, hence simplifying the solidification analysis. The numerical methods employed in the thermo-mechanical test case involving solidification, which was described in the previous Chapter, are employed again. It should be noted that it is possible to model the solidification phase with greater accuracy, by accounting for the eutectic behaviour associated with a binary alloy [12, 82]. This method involves the latent heat of fusion as a function of temperature, but as yet this facility is not implemented within PHYSICA. Fortunately, this loss of accuracy is acceptable with regard to the modelling of the gap formation at the casting/mould interface and associated heat transfer. The material properties associated with the thermal analysis are described in Tables 7.2, 7.3 and 7.4, the additional material properties required for the solidification analysis of the aluminium alloy are highlighted in Table 7.2.

T_L	Liquidus temperature	618.8°C	
T_S	Solidus temperature	566.4°C	
h	Latent heat of fusion	440 kJ/kg	
k	Thermal conductivity	150 W/(mK)	
ρ	Density	2,710 kg/m^3	
c	Specific heat capacity	1160 J/(kgK)	
α	Coefficient of thermal expansion	5×10^{-5} /K	
ν	Poisson's ratio	0.33	
E	Young's modulus	60,000MPa	20°C
		34,000MPa	450°C
		1×10^{-2}MPa	566.4°C
Y	Yield stress	500MPa	20°C
		1×10^{-4}MPa	566.4°C

Table 7.2: Material properties of the aluminium casting alloy.

With regard to the boundary conditions at the external faces of the mould and insulators, as illustrated in Figures 7.4(2) and (4), a convective cooling condition is assumed, with a heat transfer coefficient of 20W/(m^{2}K) and an ambient temperature of 20°C, between these faces and the surrounding air. At the internal faces, when the casting is in contact with the mould, a heat transfer coefficient of 400W/(m^{2}K) is assigned. When a gap occurs between the casting and the mould, the experimentally obtained relationship between the gap distance and the heat transfer coefficient is employed. Additionally, symmetry planes are assigned with regard to the heat transfer in the x and z directions, as illustrated in Figures 7.4(1), (2), (3) and (4).

With regard to the mechanical analysis the following assumptions were made. The mould, core and insulators as described in Figures 7.2 and 7.3 are assumed to be rigid and their

k	Thermal conductivity	33 W/(mK)
ρ	Density	7,880 kg/m^3
c	Specific heat capacity	600 J/(kgK)

Table 7.3: Material properties of the mould and core steel.

k	Thermal conductivity	0.1 W/(mK)
ρ	Density	1,000 kg/m^3
c	Specific heat capacity	1,760 J/(kgK)

Table 7.4: Material properties of the insulation.

dilation due to heating is neglected.

The contact between the casting and the core, insulators and mould is accounted for by applying fixed displacements of zero to the casting a priori. The simple geometry of the casting allows this approach to be performed easily. As the casting cools and solidifies it will contract around the, assumed rigid, core. Hence, the x and z displacements are fixed to zero at the nodes on the inner face of the casting, as illustrated in Figures 7.4(2) and (3). Additionally, due to gravity the base of the casting will rest on the, assumed rigid, base insulator. Hence, the y displacement components are fixed to zero at the nodes on the base of the casting as illustrated in Figures 7.4(3) and (4). The x and z displacement components are set to zero at the nodes on the respective symmetry planes as illustrated in Figures 7.4(1) and (3). The material properties associated with the mechanical analysis are highlighted in Table 7.2. Obviously, no mechanical material properties are required for the mould, core and insulation as they are assumed to be rigid.

The thermal and mechanical material properties, as described in Tables 7.2, 7.3 and 7.4, were obtained from a number of sources, including the original experimental analysis [82, 12, 67, 87]. The thermal expansion coefficient has been suitably modified to account for shrinkage during the phase change.

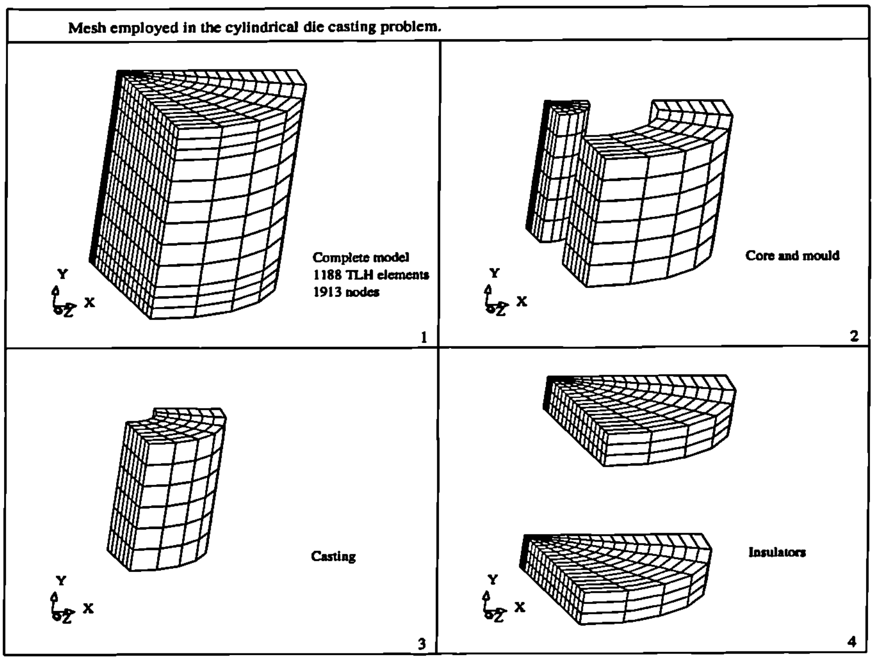

Figure 7.4: Mesh employed in the analysis of gravity die casting.

7.2.2 Discussion of numerical results

The die casting problem described here, was originally proposed by Bellet et al [13, 67, 12] as evidence for the necessity of a coupled thermo-mechanical treatment in the modelling of the die casting process.

This was achieved by first performing a purely thermal analysis and neglecting the mechanical analysis. In this manner, the heat transfer coefficient is initially assumed constant at the casting/mould interface. Secondly, a thermo-mechanical analysis is performed and the heat transfer coefficients at the casting/mould interface can vary as a function of the gap formed there. These analyses were performed in the FV framework PHYSICA and the results are illustrated in Figures 7.5, 7.7, 7.12 and 7.13. The contraction of the cylindrical casting and the resultant gap formation over time is illustrated in Figure 7.7. The radial stresses, hoop stresses and hoop visco-plastic strains associated with the temperature fields at 500 and 900 seconds, are illustrated in Figures 7.12 and 7.13, respectively.

The temperature profiles over time are plotted at points approximately 5mm from the casting/mould interface, with regard to both the casting and the mould. The temperature profile in the casting is initially at 800°C, when the casting is completely liquid. The casting then cools to the liquidus temperature in a linear fashion, at which time solidification begins. The casting then cools again in a linear fashion until the solidus temperature is reached. During these initial stages of cooling the thermal and thermo-mechanical analyses are in agreement. It is at solidus and sub-solidus temperature that the cooling rates vary and it is during this stage that the thermo-mechanical analysis is closer to the experimental results. Indeed, at 900 seconds the thermal analysis differs by approximately −50°C with regard to the thermo-mechanical and experimental results.

Similar, but not as drastic behaviour is also illustrated by the temperature profile in the mould, which heats quickly from the initial temperature of 200°C before solidification begins and then levels out. The gap formation at the casting/mould interface is illustrated in Figure 7.6 and is in good qualitative agreement with the experimental results. The gap prediction could be quantitatively improved if, either a more accurate solidification analysis

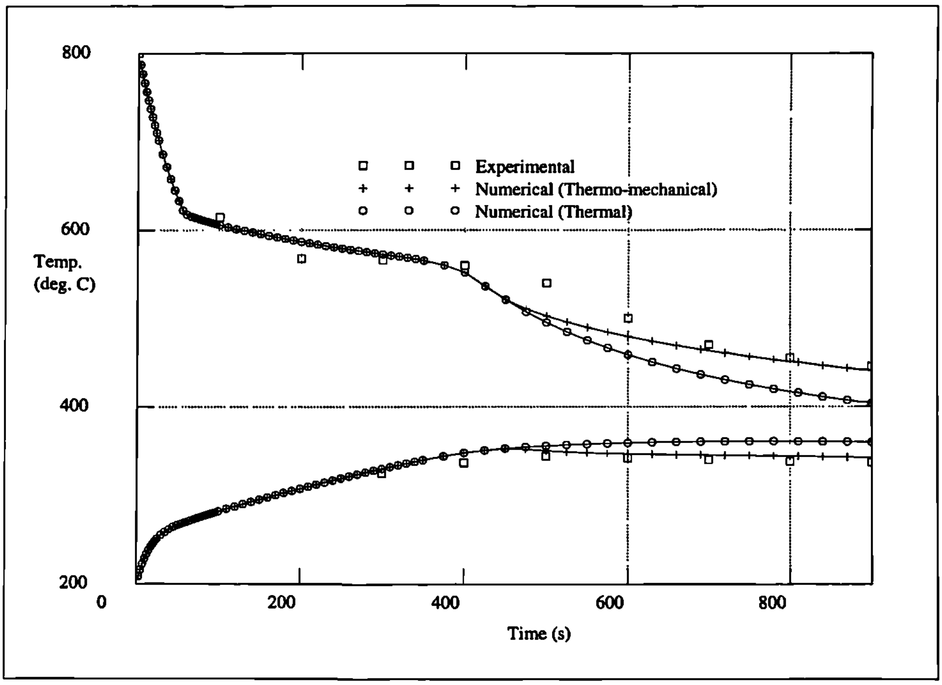

Figure 7.5: Temperature profiles in mould and casting.

was performed, as discussed in the previous section, which would furnish a longer freezing range [82] and hence later gap formation, or the mould and core dilation was included in the mechanical analysis which could enlarge the gap size.

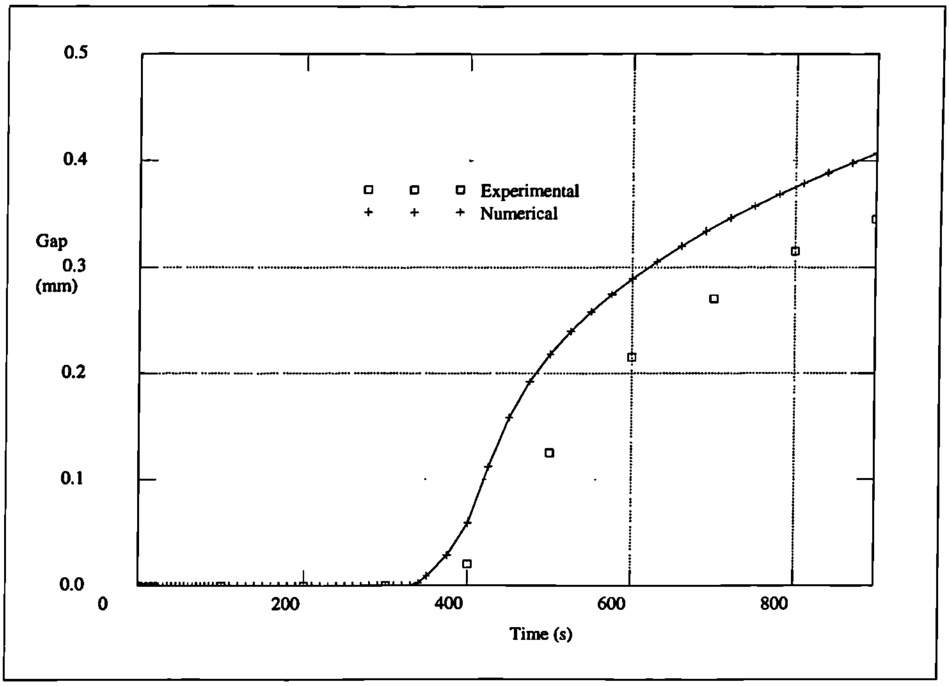

Figure 7.6: Gap formation at mould/cast interface.

Initially, the analysis was performed assuming rate independent elasto-plastic behaviour and the results were illustrated in Figures 7.5 and 7.6. Secondly, the analysis was performed assuming rate dependent elasto-visco-plastic behaviour. This was achieved by employing the additional material properties as described in Table 7.5 [13, 67, 12], and in this analysis the time interval associated with the mechanical analysis must not exceed that employed during the thermal analysis. The results are compared against those of the rate independent

		20°C	566.4°C
γ	Fluidity (/s)	1.0×10^6	3.7×10^3
m	Rate sensitivity	0.02	0.2

Table 7.5: Rate dependent material properties.

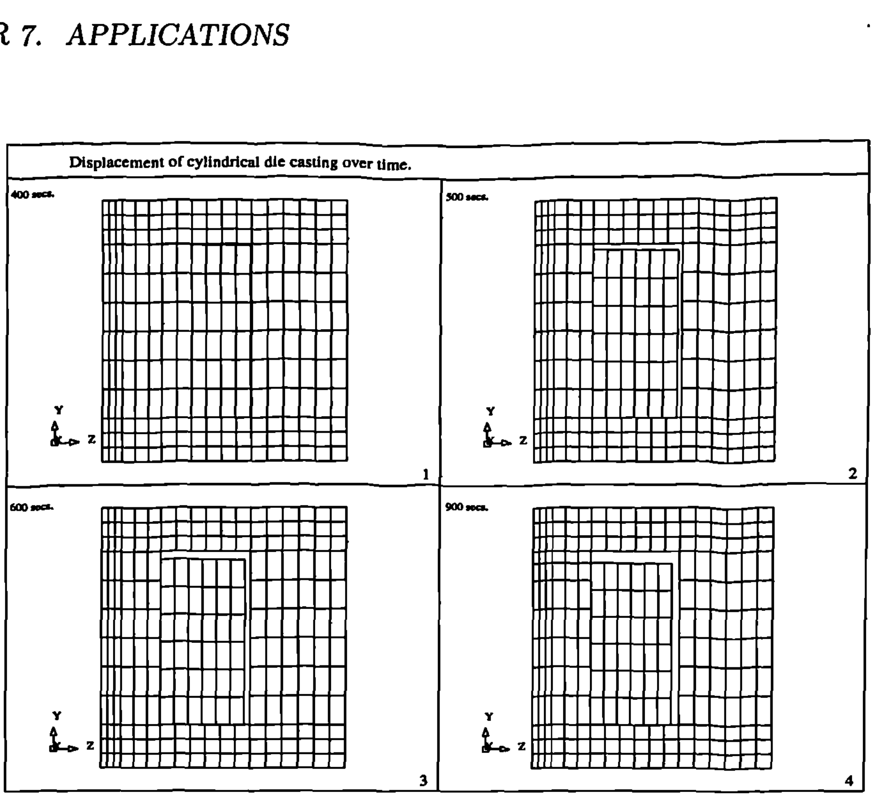

Figure 7.7: Casting shrinkage and gap formation over time (Mg. ×10).

analysis in Figures 7.8 and 7.9. Surprisingly, the two analyses are in remarkably close agreement. This may be attributable to the insensitivity of the algorithmic approach, as described in this research, to rate dependent material non-linearity over the sub-solidus temperature range or to the possibility that viscous effects are negligible when the cooling rates are are extreme, such as those exhibited in die casting. The latter hypothesis is reinforced by the negligible viscous effects exhibited in quenching problems as discussed in the previous chapter. These points are of considerable interest and may well point to further avenues of research.

When considering the possibility of residual convection of the liquid metal in the casting after pouring, it is informative to study the temperature profiles at the inner and outer surfaces of the cylindrical casting and, additionally, at a point in the centre of the casting. These profiles are illustrated in Figure 7.10. Obviously, with regard to the liquid phase, negligible thermal gradients exist and hence no buoyancy driven recirculation will occur. The slight thermal gradients appearing during the solidification phase will be ineffective due to the permeability coefficient appearing in the momentum equations when solidification is

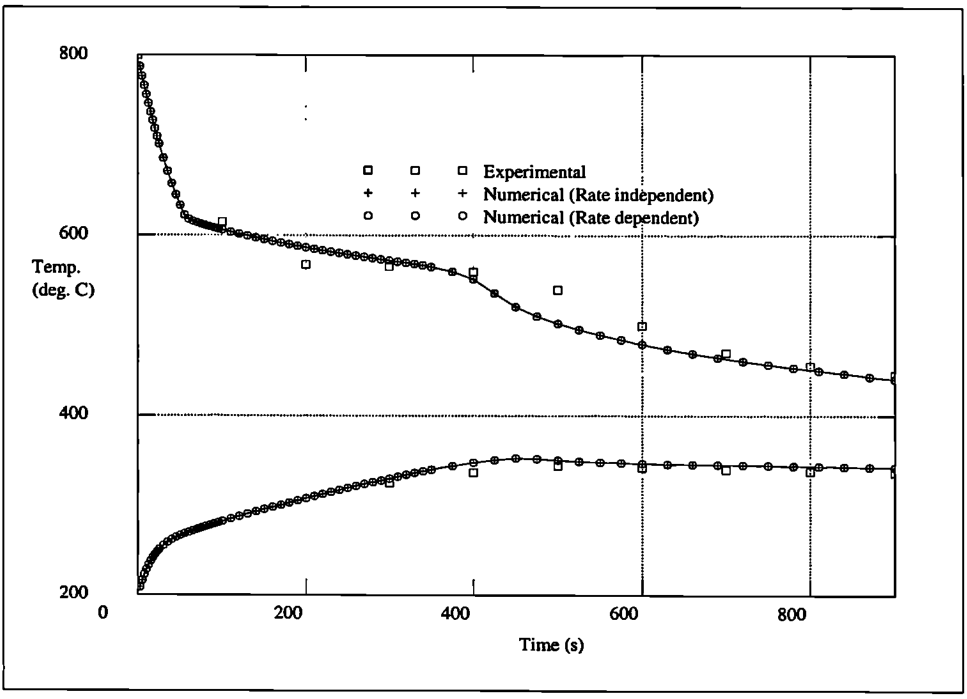

Figure 7.8: Temperature profiles in mould and casting.

occurring.

At present further contributions to residual convection due to the material dilation during phase changes and porosity formation are not available within the PHYSICA framework. Though it should be noted that research is underway to extend the two dimensional treatment of Fryer et al [42, 3] for inclusion within the PHYSICA framework. The heat transfer problem involving solidification as associated with the die casting problem described here, was simulated with and without the inclusion of convection. With regard to the analysis including convection a constant viscosity was employed $\mu = 2.0 \times 10^{-3}\mathrm{Ns/m^2}$. Wall boundary conditions were applied at the casting/mould and casting/insulator interface, which furnished the required momentum boundary conditions.

As illustrated in Figure 7.11 the inclusion of convection due to buoyancy driven recirculation has no observable effect on the heat transfer. Indeed, this is consistent with the design of the experimental analysis which is intended to restrict heat transfer to conduction only.

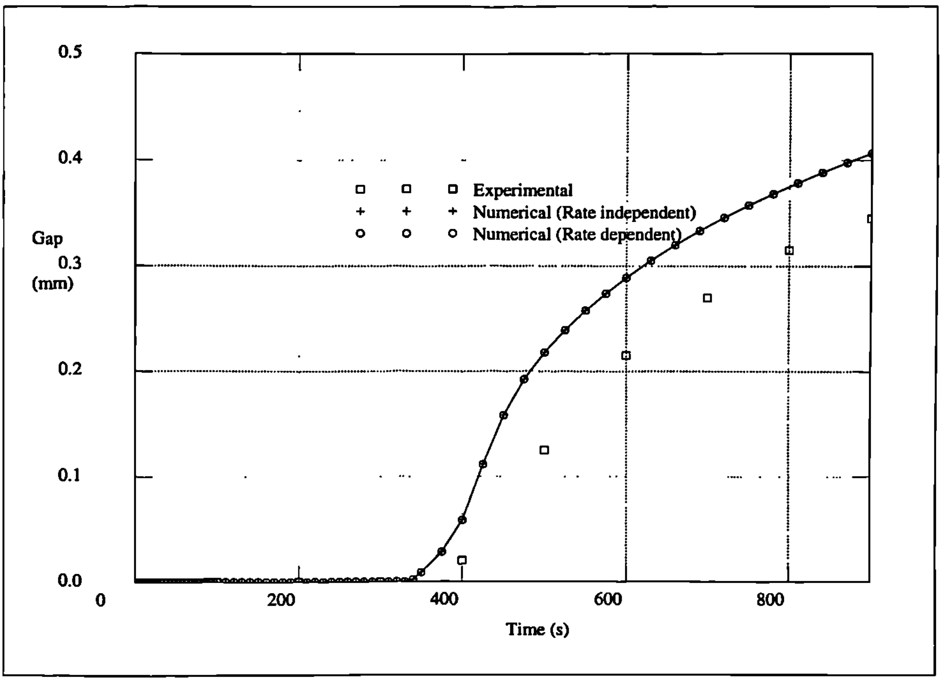

Figure 7.9: Gap formation at mould/cast interface.

In order to assess the accuracy and stability of the thermo-mechanical coupling technique employed in this research, a number of analyses were performed with different time intervals relating to the thermal and mechanical staggering. The results obtained are illustrated in Figures 7.14 and 7.15. With regard to scheme 1 an increasing time interval was employed, which ranged from a value of 2.5 to 30 seconds, this scheme is the most accurate and was employed generally. With regard to schemes 2 and 3 a fixed time interval of 30 and 60 seconds was employed, respectively. It should be noted that employing a greater time interval reduces the accuracy of the solidification analysis, and the outcome can be misleading as the resultant cooling rate and gap formation appear closer to the experimental results.

Additionally, in order to investigate mesh dependency, the mesh was refined by increasing the number of divisions in the radial direction. Initially, a fine mesh consisting of 2,112 elements and 3,201 nodes and finally a coarser mesh consisting of 1,118 elements and 1913 nodes was employed. As illustrated by Figures 7.16 and 7.17 the results are reasonably mesh independent.

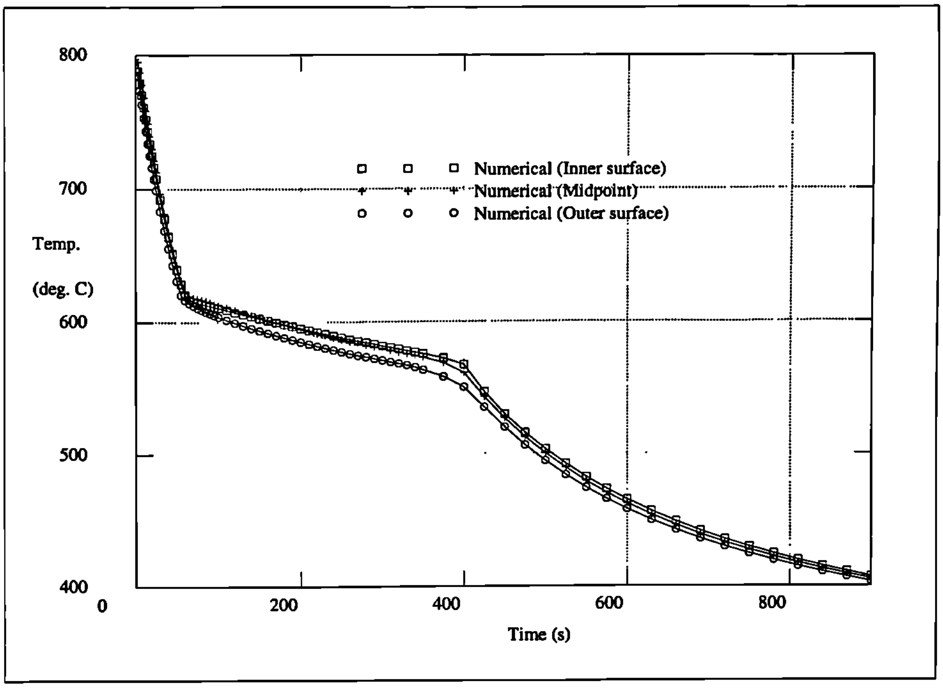

Figure 7.10: Temperature profiles in the casting.

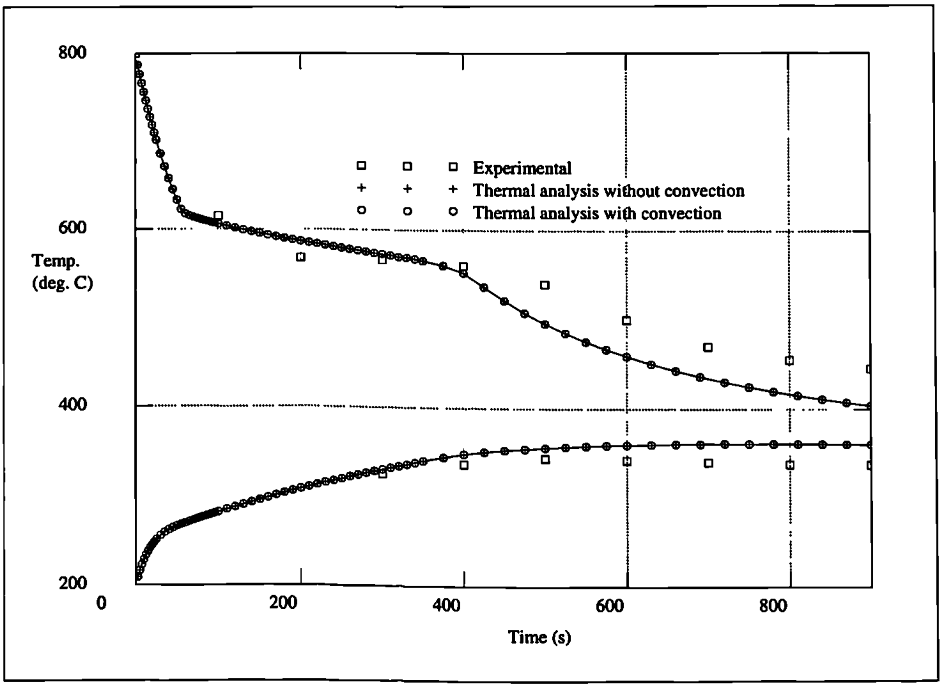

Figure 7.11: Temperature profiles in mould and casting .

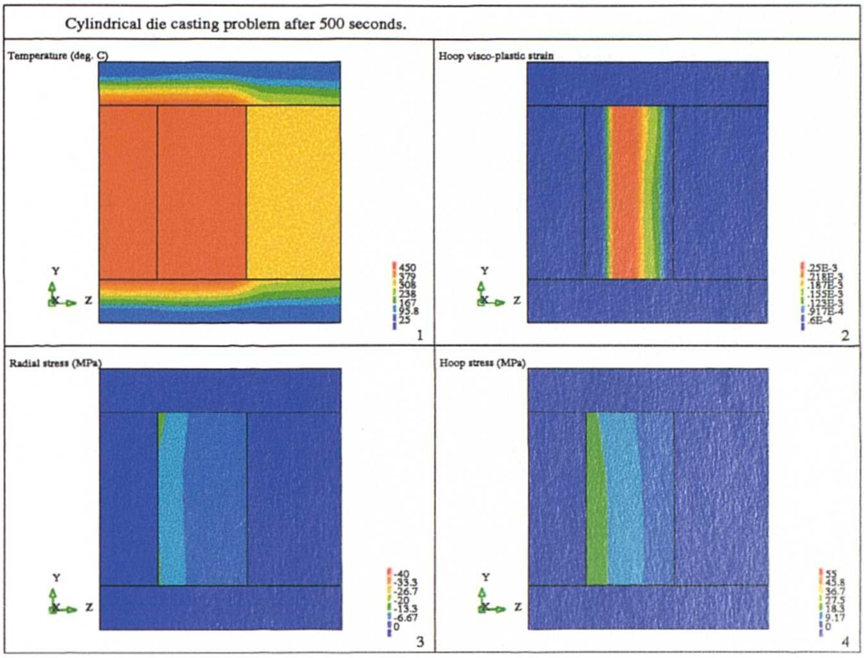

Figure 7.12: Stress and visco-plastic strain at 500 seconds.

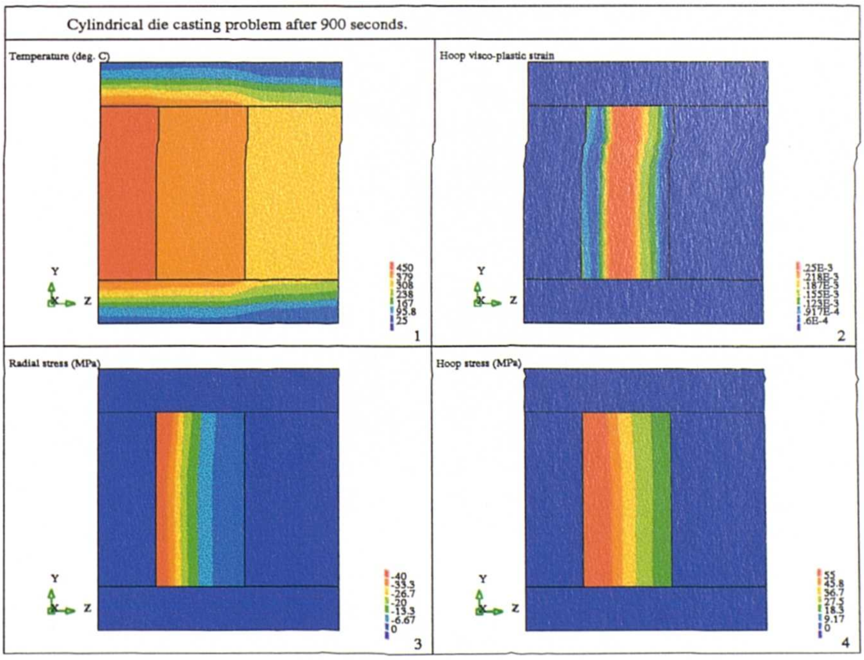

Figure 7.13: Stress and visco-plastic strain at 900 seconds.

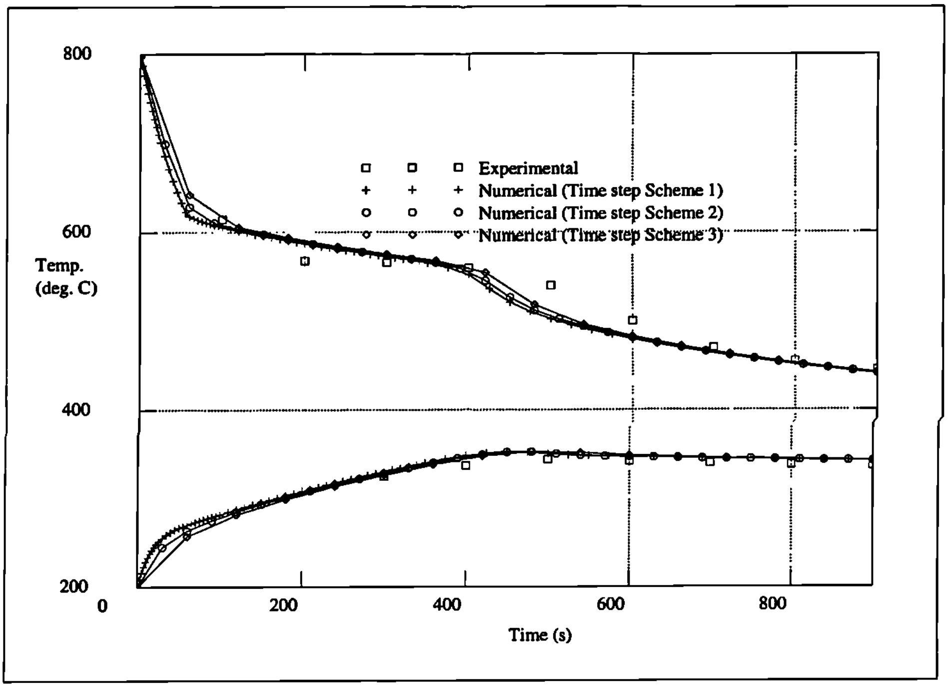

Figure 7.14: Temperature profiles in mould and casting .

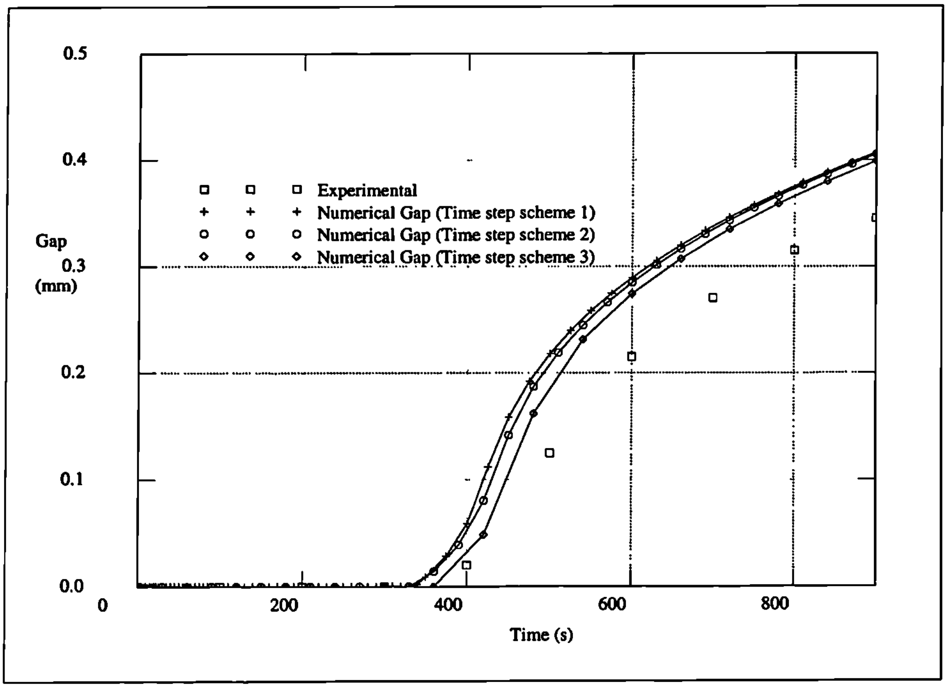

Figure 7.15: Gap formation.

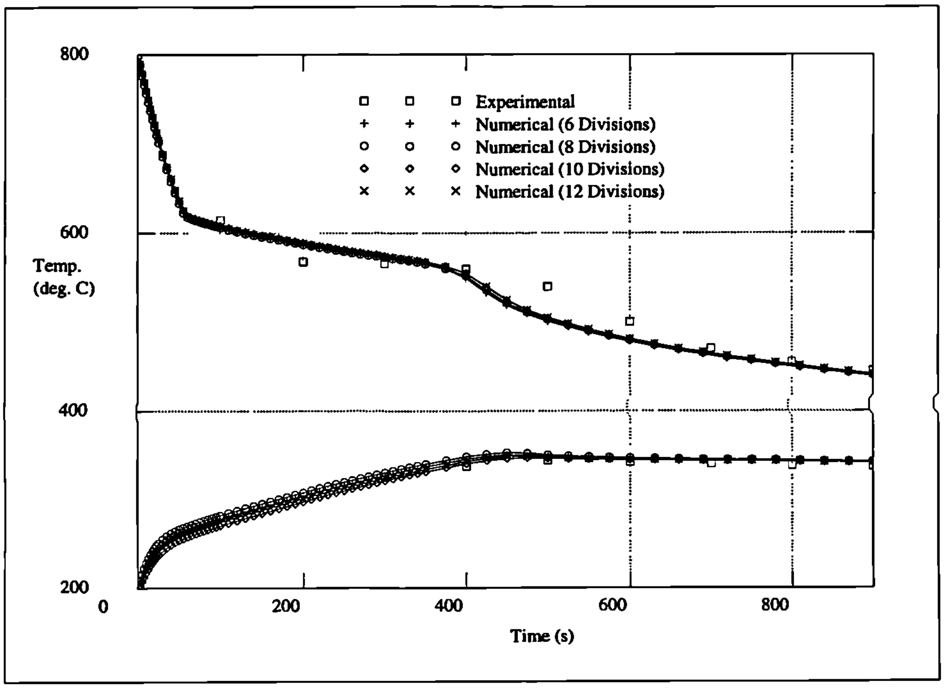

Figure 7.16: Temperature profiles in mould and casting .

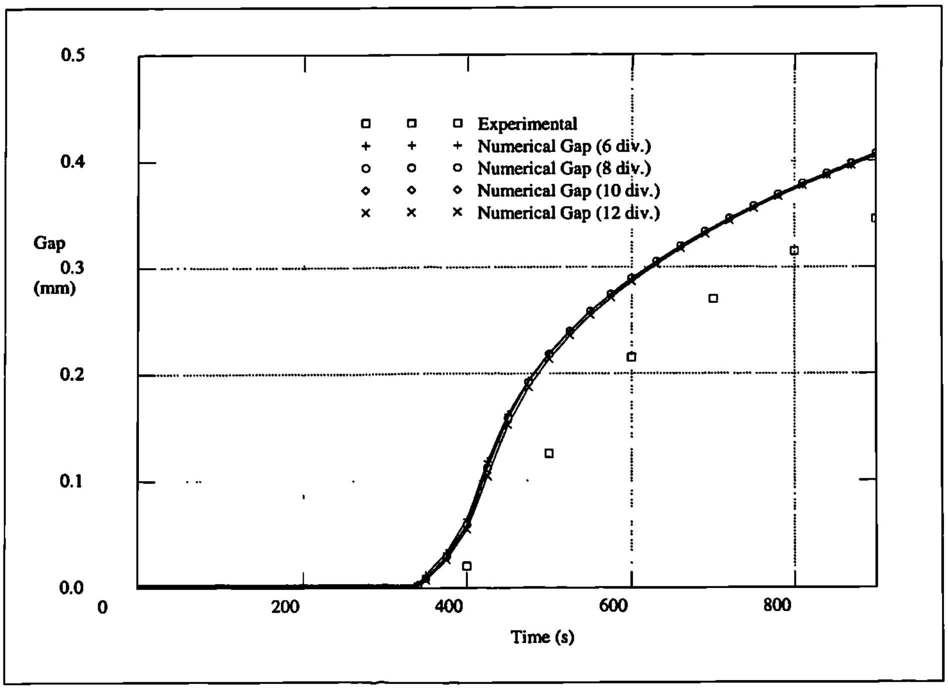

Figure 7.17: Gap formation.

7.3 Sand casting of an aluminium test bar

The experimental analyses of the sand casting of aluminium test bars were originally performed by Castings Technology International (CTI) and modelled by Chow et al [21] with material property data originally provided by the National Physics Laboratory [21].

The objective of these experimental investigations was to observe porosity formation as associated with shrinkage defects [21]. Unfortunately, to the best of the authors knowledge, no thermal or mechanical results were recorded during these experiments. However, with regard to the simulation of the shape casting of metals, the test bar problem as illustrated in Figures 7.18, 7.19, 7.20 and 7.21 provides a suitable academic illustration of the present capabilities and future requirements of the engineering software PHYSICA.

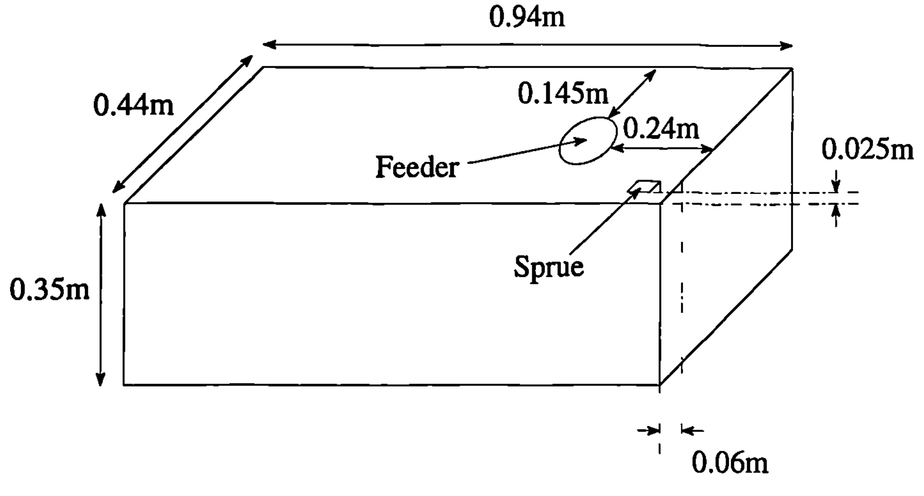

Figure 7.18: Geometry of the sand mould.

In these experiments a 10mm thick insulation sleeve was placed around the feeder, as illustrated in Figure 7.22(4), and the moulds consisted of chemically bonded sand.

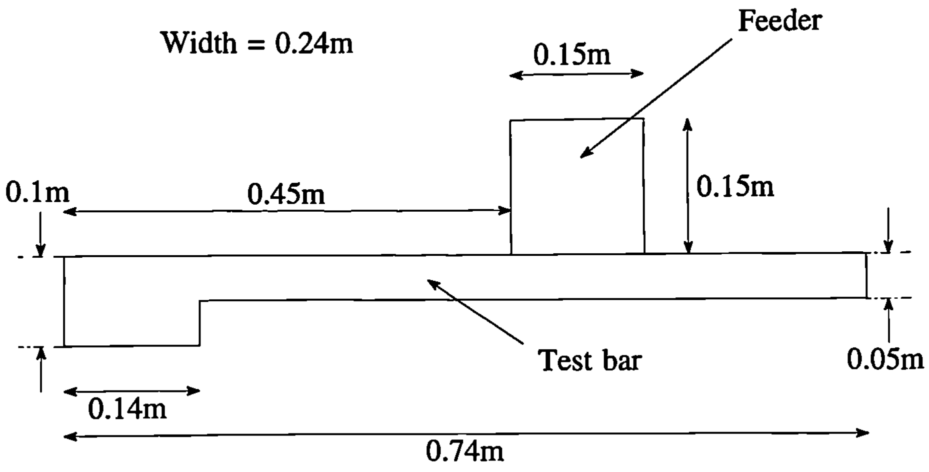

Figure 7.19: Geometry of aluminium test bar (without sprue).

7.3.1 Numerical analysis

With regard to the thermal analysis the liquid metal alloy is assumed to be static initially and at a uniform temperature of 714°C, alternatively the mould and insulation sleeve are at a uniform temperature of 25°C. These initial temperatures are consistent with experimental analysis [21].

The chemically bonded sand and the insulation sleeve have thermal conductivities of 0.8 W/(mK) and 0.39 W/(mK), respectively. The heat transfer coefficient applied at the casting/mould interface when the mould and cast are in thermal contact is 1500 W/(m^2K). This value is higher than that employed in the die casting problem, where a coating layer applied at the casting/mould interface increased the thermal resistance. Additionally, the heat transfer coefficient at the casting/mould interface is assumed to vary linearly with the gap formation, the conductivity of the gap is equivalent to that described for the die casting problem in Table 7.1. The aluminium alloy employed in the sand castings is assumed

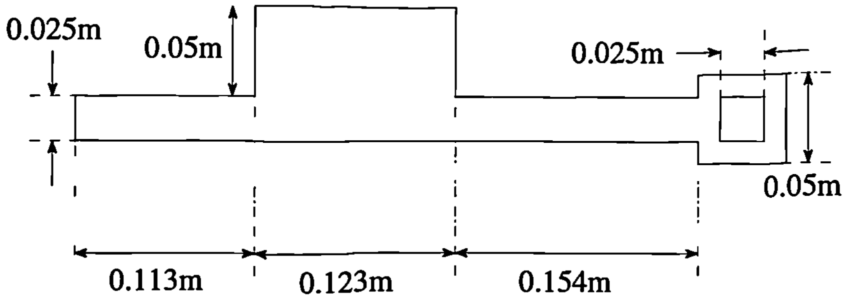

Figure 7.20: Geometry of sprue (top view).

equivalent to that of the previous die casting problem and the material properties are those described in Tables 7.2 and 7.5.

Considering the solidification, the same assumptions were applied as in the die casting problem. With regard to the thermal boundary conditions, a convective cooling condition with a heat transfer coefficient of 1000 W/(m^2K) and an ambient temperature of 25°C is applied at all the external surfaces except the feeder surface which is assumed to be adiabatic. Hence, it is ensured that the alloy remains liquid in the feeder longer than anywhere else in the test bar.

With regard to the mechanical analysis the following assumptions were made. The thermal contraction of the test bar is constrained by the mould geometry and gravitational effects. As in the die casting problem, the mould is assumed to be rigid and the contact constraints are applied a priori. Unfortunately, as illustrated by the geometry of the casting in Figure 7.22(3), it is no longer immediately obvious where the mechanical constraints should be applied a priori. In this case a number of mechanical constraints have been applied, which

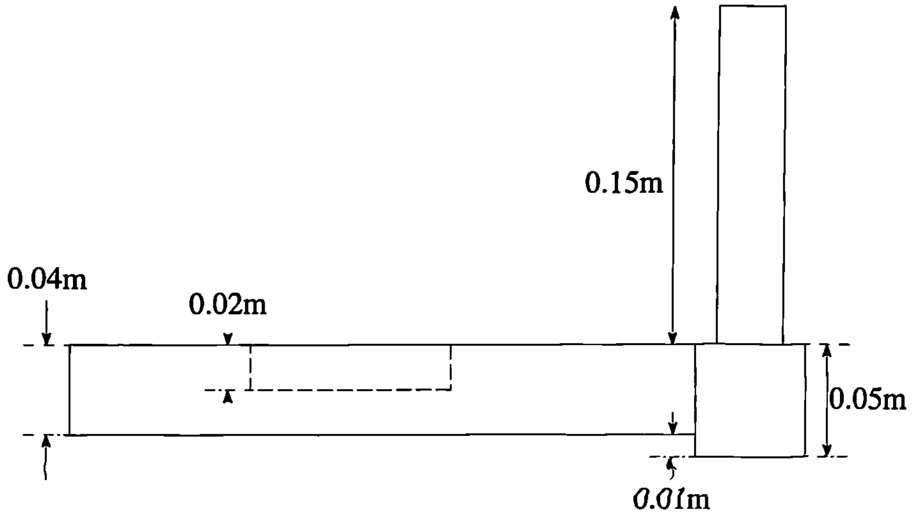

Figure 7.21: Geometry of sprue (side view).

can be assumed to satisfy contact conditions between the mould and casting. However, it is important to note that even for such a simple geometry as this test bar, once the sprue and feeder are included, as illustrated in Figure 7.22(3), a more physically accurate contact algorithm is preferable. Indeed, present research is underway to include a completely coupled deformable-deformable FV contact algorithm within the PHYSICA framework.

7.3.2 Natural convection

Considering the heat transfer associated with this problem it is appropriate to investigate the effects of buoyancy driven recirculation. This is attributable to the problem geometry, which furnishes the necessary thermal gradients during the cooling of the liquid alloy.

However, for this problem it is interesting to compare heat transfer by conduction and convection with heat transfer by conduction only. It should be noted that any natural convection which occurs can contribute to the heat transfer and will modify the thermo-

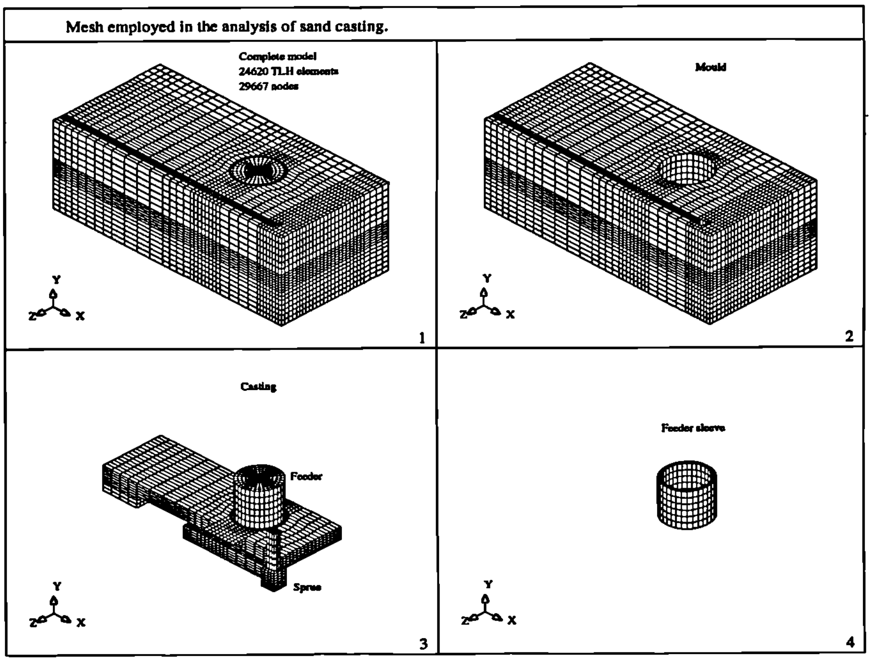

Figure 7.22: Mesh employed in the analyses of the CTI test bar.

mechanical behaviour of the casting and mould. Additionally, the quality and soundness of the casting can be affected by other resulting transport phenomena, such as the convection of solute produced by alloy segregation, which can significantly affect the solidification of the alloy [16]. At present this capability is not available within the PHYSICA framework, but current research is underway to facilitate this capability also.

The buoyancy driven recirculation is furnished by employing the Boussinesq approximation. Where the viscosity is assumed to have a constant value of 1.3×10^{-3}Pas, the flow is assumed to be laminar and wall friction boundary conditions are applied at the casting/mould interface.

7.3.3 Discussion of numerical numerical results

In this section the numerical results of the sand casting problem will be discussed. Initially, the results of the thermal analyses that were performed will be discussed and finally the results of the thermo-mechanical analyses that were performed will be discussed.

7.3.3.1 Thermal analyses

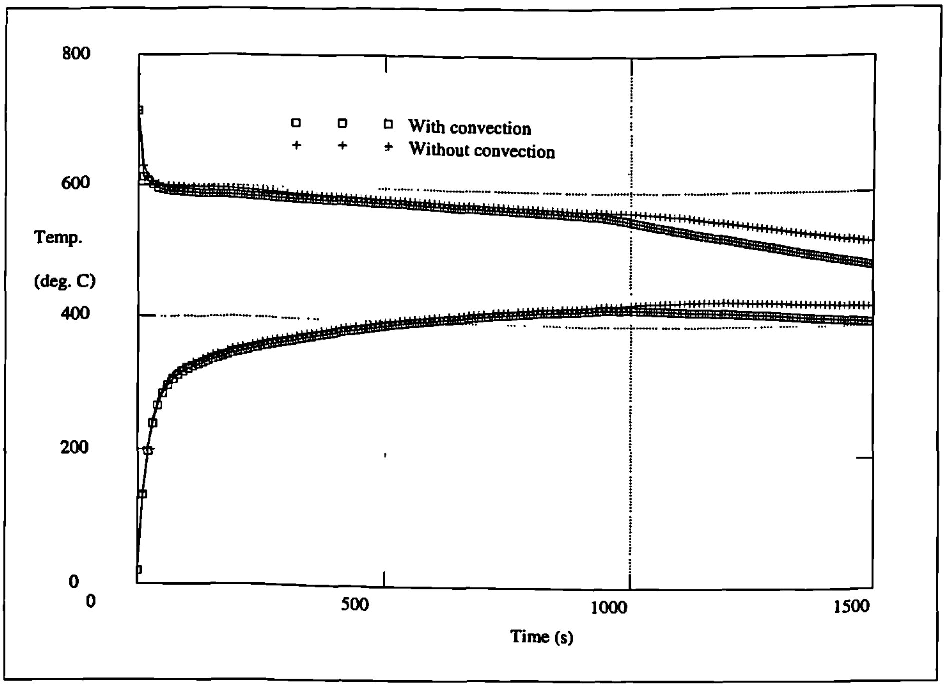

Figure 7.23: Cooling rates in the test bar and sand mould.

Initially, several thermal analyses of the sand casting problem were performed and the associated mechanical behaviour was neglected. In the thermal analyses the casting was considered for problems with and without convection. In this manner, it was possible to investigate the effects of the inclusion of natural convection in the sand casting simulation.

In both cases the thermal analyses were simulated for 1500 seconds, at which time the test bar had completely solidified. With regard to the computational effort, the analyses required 15 to 20 hours CPU time on a SPARC 20 100 MHz work station with 320 Mbytes of main memory. The thermal analysis including natural convection required approximately 25% additional CPU time.

The cooling rates at points 5cm either side of the centre of the base of the casting/mould interface are illustrated in Figure 7.23. Additionally, the cooling rates at several positions

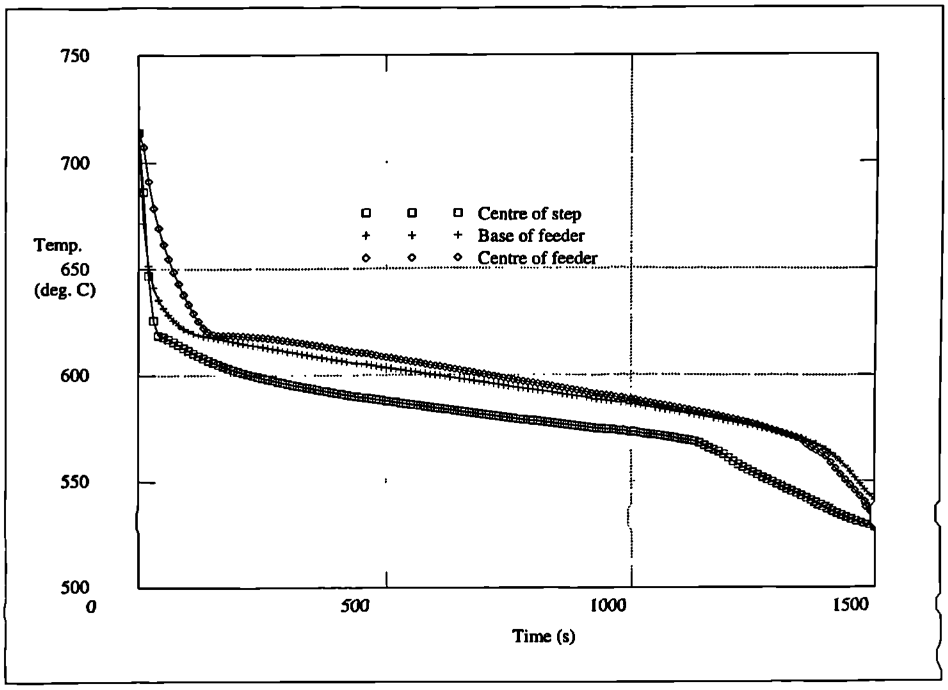

Figure 7.24: Cooling rates for heat transfer without convection (1500 secs.).

within the test bar are illustrated in Figures 7.24 and 7.25 for the thermal analyses, with and without natural convection respectively.

With regard to the simulation that included natural convection it should be noted that the temperatures are approximately 20°C to 30°C cooler in the casting and the mould after 1500 seconds. This can be attributed to the mixing effect of the natural convection, which will redistribute the temperatures in the casting more evenly. Hence, providing greater temperature differences at the casting mould interface which in turn can lead to greater heat transfer at the interface. This phenomenon is more clearly illustrated by considering figures 7.31, 7.32, 7.33 and 7.34.

Considering in more detail the thermal analysis with natural convection included, the re-circulations associated with natural convection are clearly illustrated after 20 seconds in Figure 7.35. It should be noted that the present analysis assumes initial uniform temperatures throughout the casting and mould and that the liquid alloy is initially static. This neglects any heat transfer that can occur during the filling of the sand mould and any

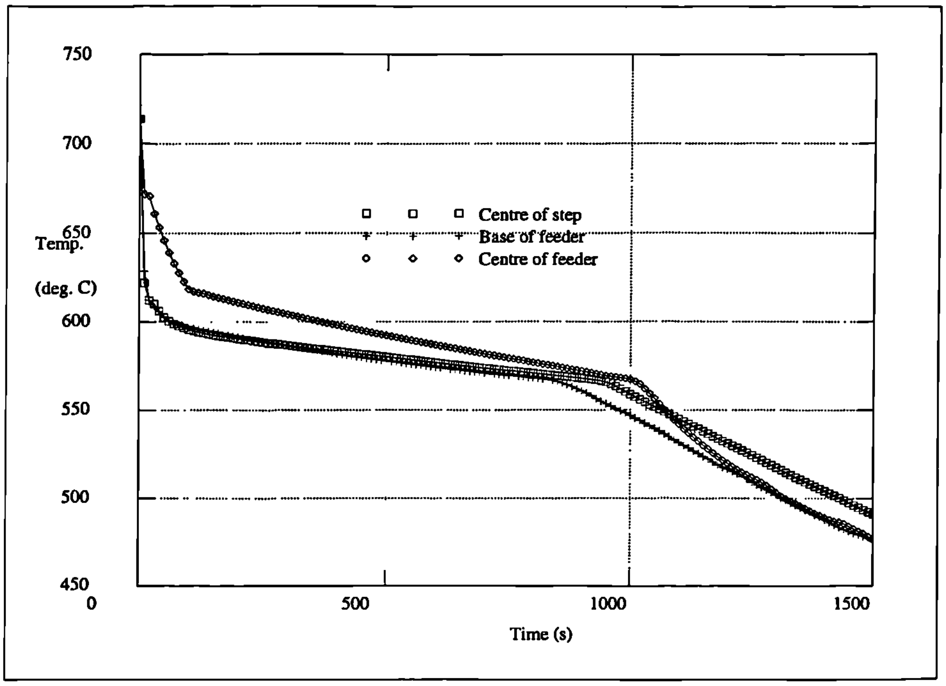

Figure 7.25: Cooling rates for heat transfer with convection (1500 secs.).

residual flow in the liquid alloy after the filling. Present research is underway to include a filling capability coupled with heat transfer within the PHYSICA framework.

For these reasons the initial flow patterns change quite dramatically and it is interesting to note that a sharp transition occurs in the cooling rate in the feeder during the liquid phase. This phenomenon can be observed in Figure 7.25 and more clearly in Figures 7.27 and 7.28. The phenomenon is obviously not occurring in the thermal analysis without convection as illustrated in Figures 7.24 and 7.26. This phenomenon is attributable to the transition between the reasonably active natural convection which occurs originally and the more sedate natural convection occurring later in the analysis. This is more clearly illustrated by the variation of the velocity and temperature profiles over time, as plotted across the diameter of the feeder in Figures 7.29 and 7.30, respectively. The velocity and temperature profiles are typical of those associated with recirculatory flows and as can be observed the flows subside significantly as the temperature is redistributed more evenly and the heat transfer at the casting/mould interface reduces. Obviously if the mould were pre-heated the effect would be less significant.

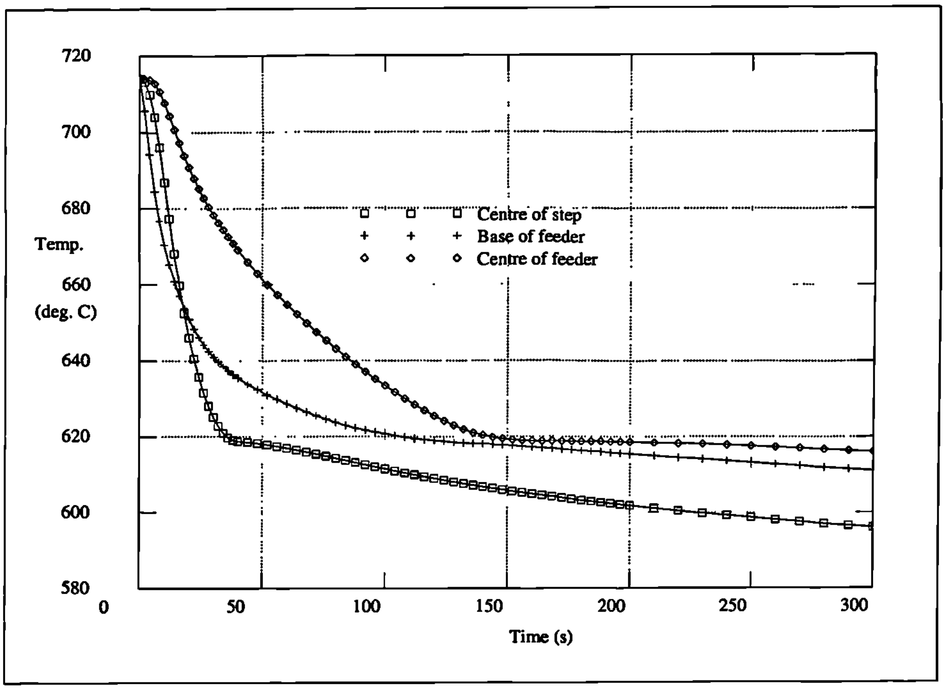

Figure 7.26: Cooling rates for heat transfer without convection (300 secs.).

Finally, it should be noted that a finer mesh than that illustrated in Figure 7.22 would improve the accuracy of the thermal analysis when including natural convection. Unfortunately, a finer mesh would be prohibitive for a thermo-mechanical analysis with regard to memory requirements and computational effort. For these reasons the mesh described in Figure 7.22 was employed in all the analyses of the sand casting problem.

It should be noted that the inclusion of natural convection in the casting simulation and the consequential effect upon the cooling rates requires further validation and is included in this research as an additional feature presently available within the PHYSICA framework.

7.3.3.2 Thermo-mechanical analyses

Several thermo-mechanical analyses were performed with regard to the sand casting problem. Initially, the thermo-mechanical analysis was investigated with and without the inclusion of natural convection and finally the thermo-mechanical analysis was investigated with

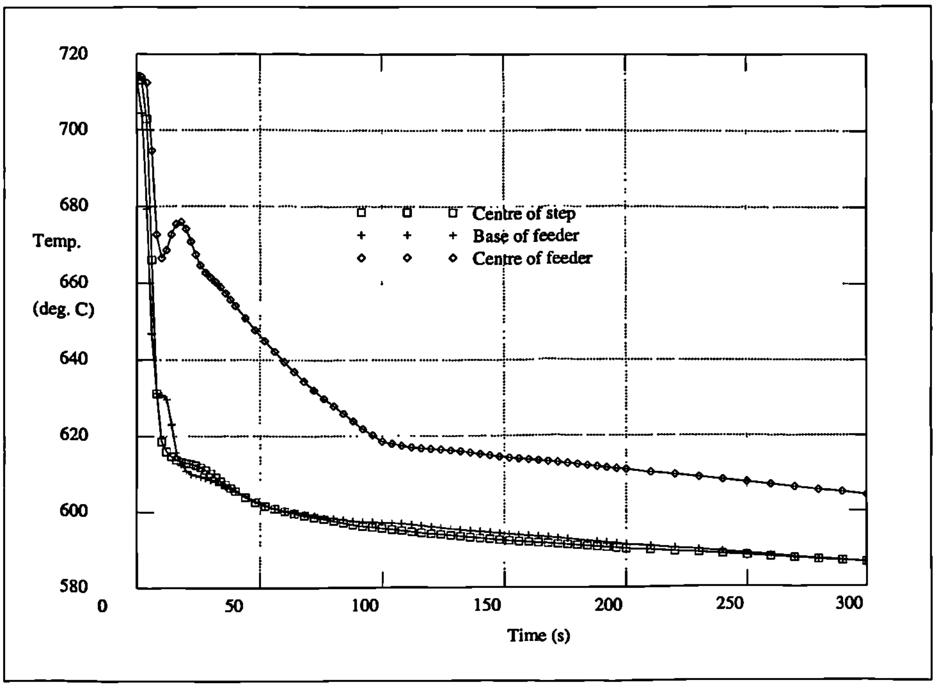

Figure 7.27: Cooling rates for heat transfer with convection (300 secs.).

regard to rate dependent material behavior.

The thermo-mechanical analyses were somewhat limited by memory requirements, which increased by a factor of three for the thermo-mechanical analysis including convection and a factor of five for the thermo-mechanical analysis without. More significantly, the thermo-mechanical analyses were severely limited by the computational effort required. A simulation of 300 seconds required 50 to 60 hours CPU time on a SPARC 20 100 MHz processor with 320 Mbytes main memory.

The deformation of the test bar after 300 seconds is illustrated in Figure 7.36. The deformation has been magnified by a factor of ten and it is obvious that the contact constraints with regard to the mould have been satisfied so far.

The thermo-mechanical analyses with and without natural convection are illustrated in Figures 7.37, 7.38, 7.39 and 7.40. After 100 seconds no mechanical effects are observable in either case as expected. After 300 seconds considerable stress effects are observable in

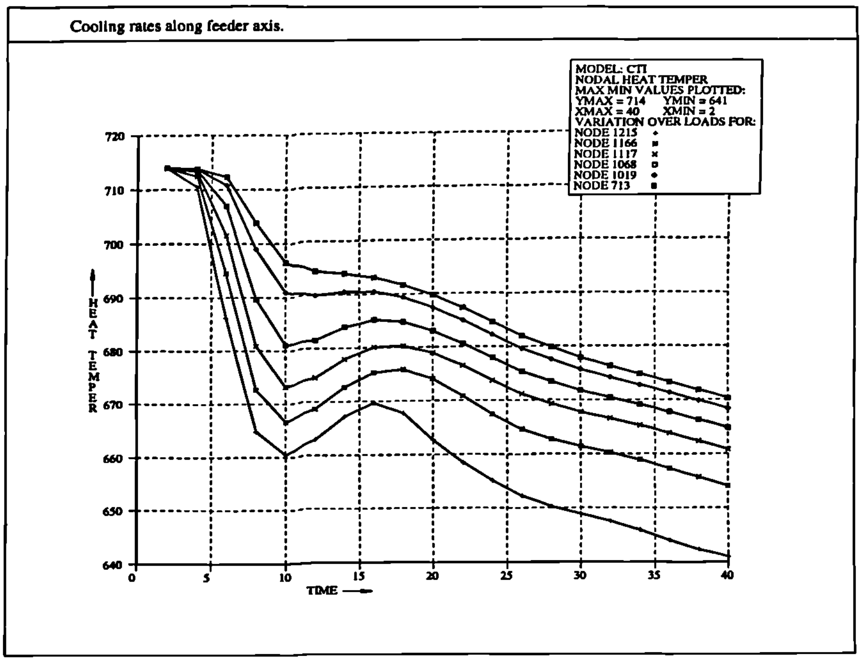

Figure 7.28: Cooling rates at various nodal points on the feeder axis.

the thermo-mechanical analysis without natural convection, but no observable stress effects are occurring in the thermo-mechanical analysis with natural convection included. This is attributable to the different cooling rates of the sprue and test bar that can be observed between the two analyses. It can be assumed that similar stress effects will occur in the latter thermo-mechanical analysis at a later stage in the analysis. Indeed, though not observable in Figure 7.39, small initial stress effects are present.

The stresses and inelastic strains agree physically with the deformation illustrated in Figure 7.36, where the casting is free to contract no stresses will occur, but where the casting is constrained by the mould stresses and inelastic strains will occur as illustrated in Figures 7.40 and 7.42.

With regard to gap formation at the casting/mould interface, the cooling rates are affected in both the thermo-mechanical analyses as illustrated by comparing Figures 7.33 and 7.34 with Figures 7.39(1) and 7.40(1), respectively. Though it should be noted that the effect of gap formation on the cooling rate requires further validation against experimental results with regard to sand casting.

Finally, it was interesting to compare a rate dependent and rate independent analysis. The results are illustrated for thermo-mechanical analyses without natural convection in Figures 7.38, 7.40, 7.41 and 7.42. The stresses in the rate dependent analysis are much higher and the associated visco-plastic strains are much lower. This agrees physically with rate dependent phenomena as the associated stresses are allowed to exist above the yield stress and the visco-plastic strain is limited by the time interval associated with the mechanical analysis.

It is interesting to note the occurrence of rate dependent effects in the sand casting problem and not in the previous die casting problem, this can be attributed to the different cooling rates associated with both problems. The die casting cools relatively quickly and in a uniform manner, whereas the sand casting cools slowly and in a non-uniform manner. The initial conclusions with regard to the occurrence of rate dependent material behaviour exhibited in the casting of metals are tentative and further research combined with experimental validation must be performed to reinforce these conclusions further.

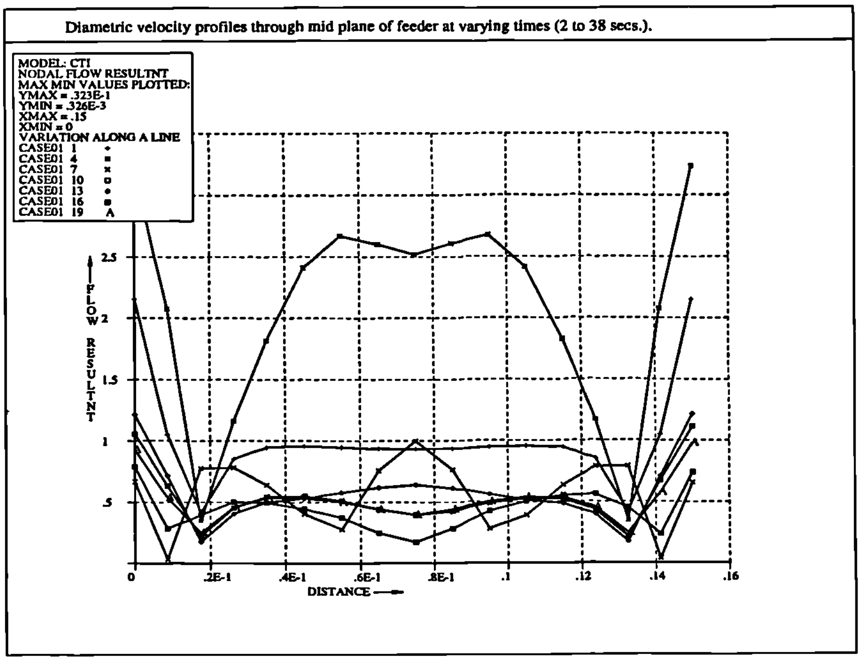

Figure 7.29: Velocity profiles along the diameter of the mid plane of the feeder.

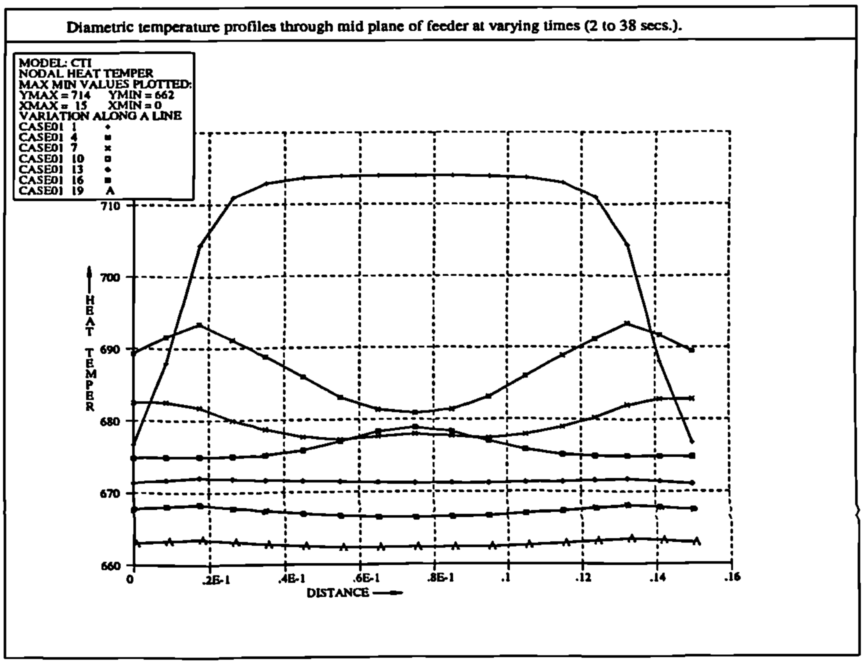

Figure 7.30: Temperature profiles along the diameter of the mid plane of the feeder.

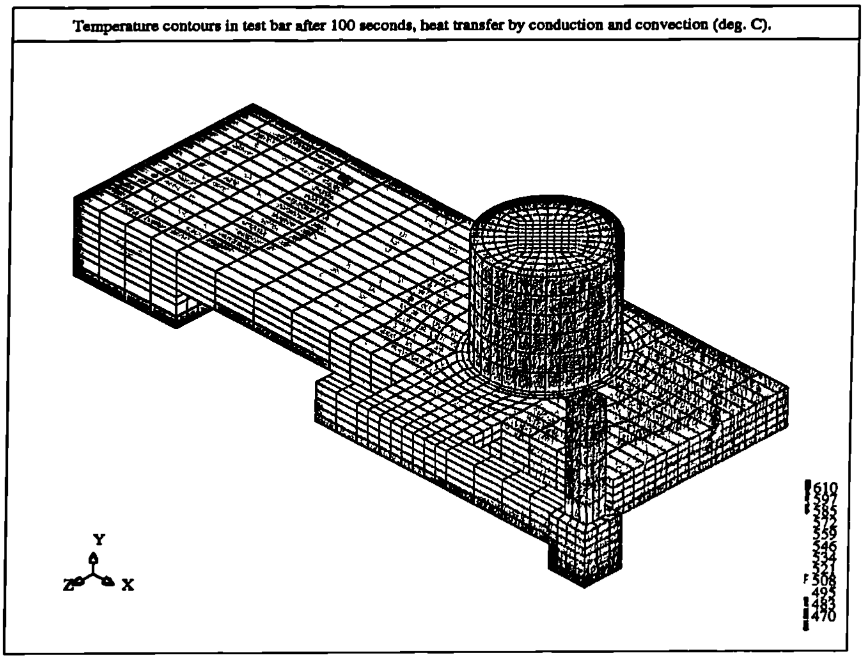

Figure 7.31: Heat transfer by conduction and convection after 100 seconds.

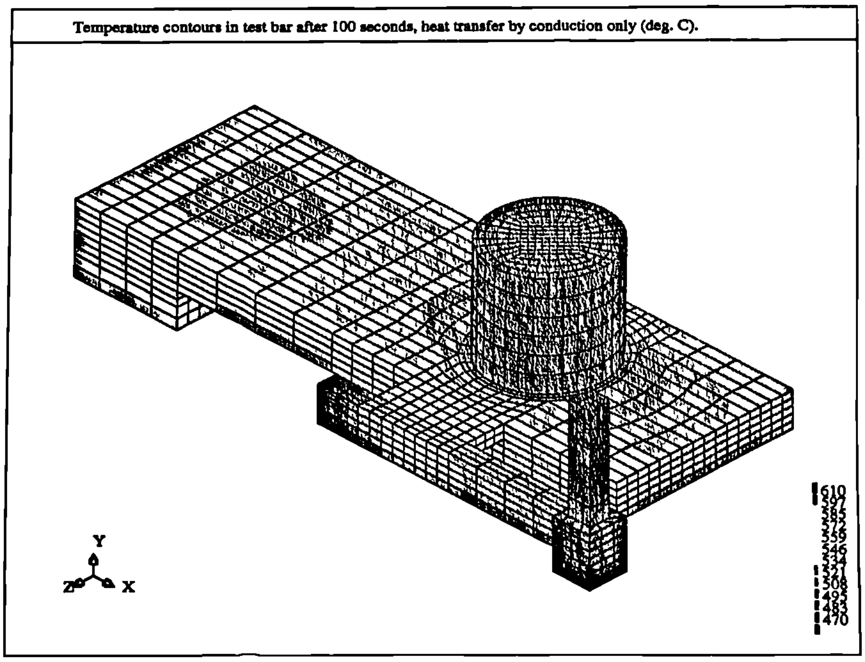

Figure 7.32: Heat transfer by conduction only after 100 seconds.

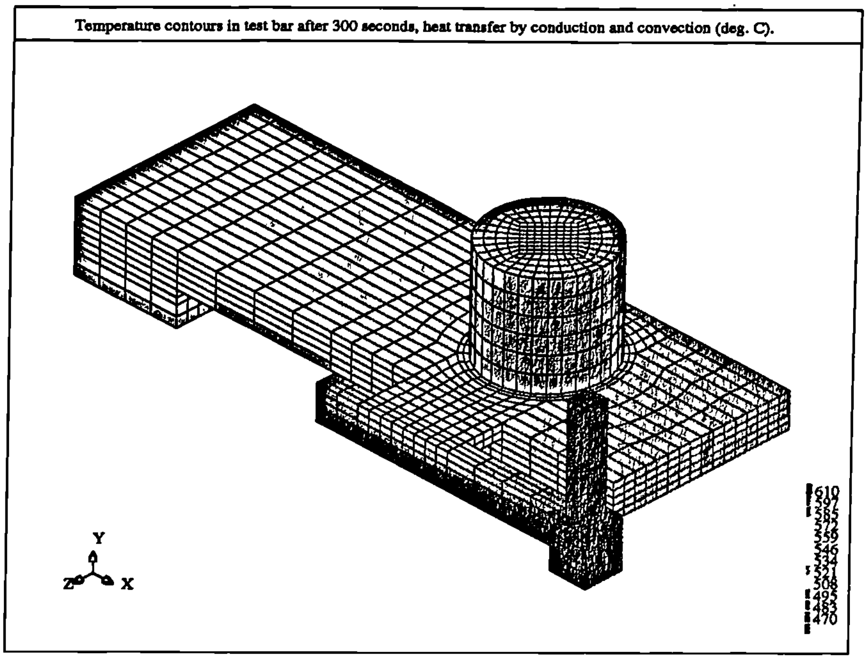

Figure 7.33: Heat transfer by conduction and convection after 300 seconds.

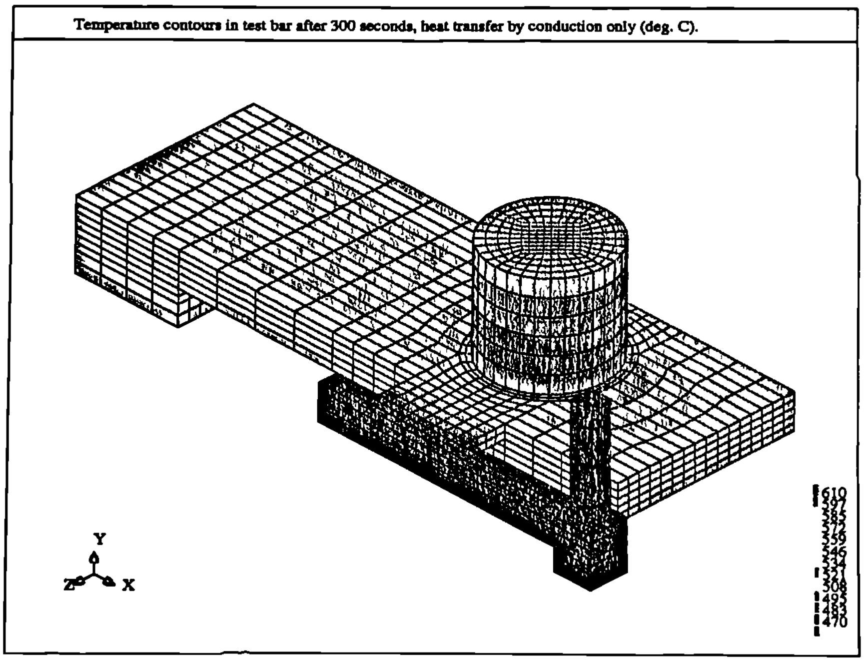

Figure 7.34: Heat transfer by conduction only after 300 seconds.

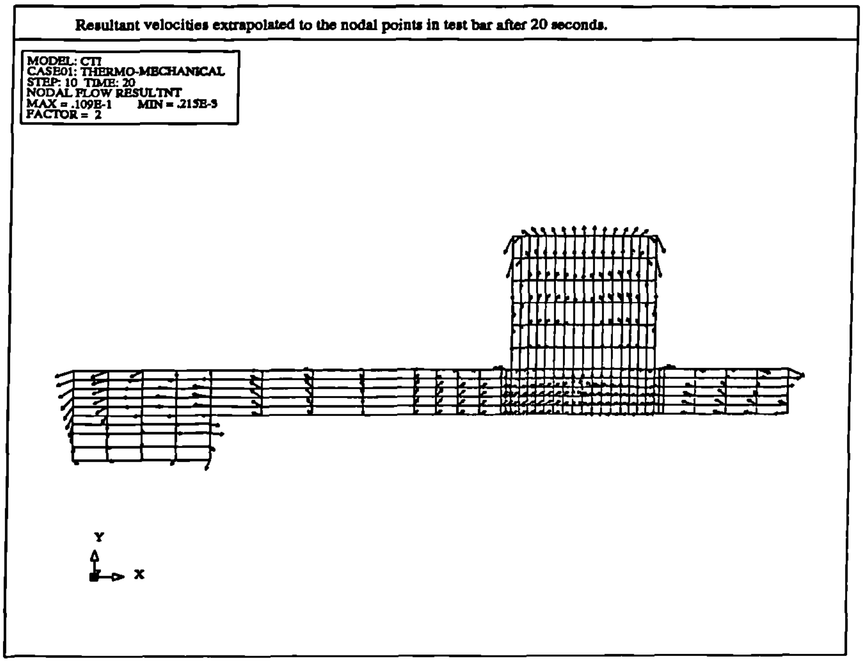

Figure 7.35: Resultant liquid velocity through a cross section at 20 seconds.

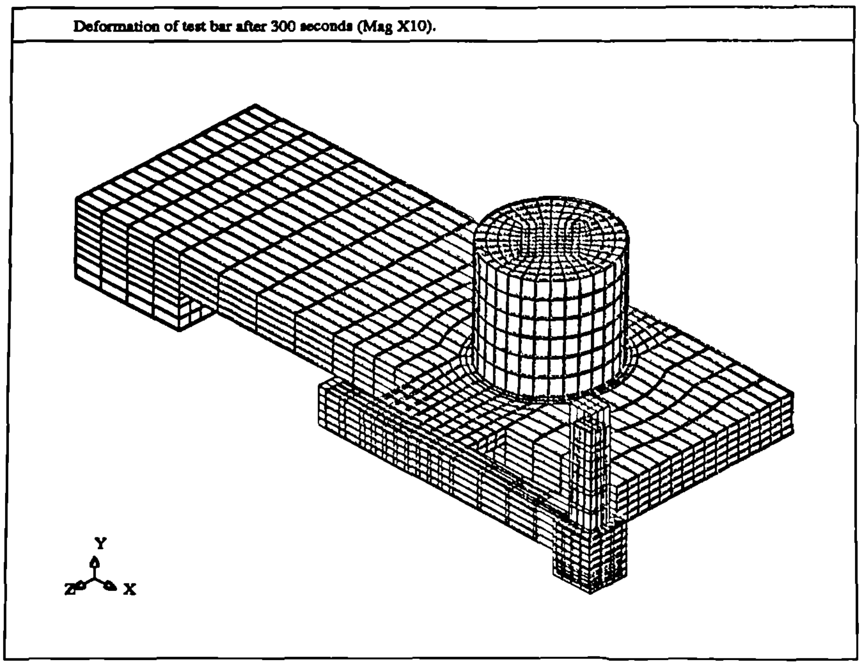

Figure 7.36: Deformation of the test bar after 300 seconds.

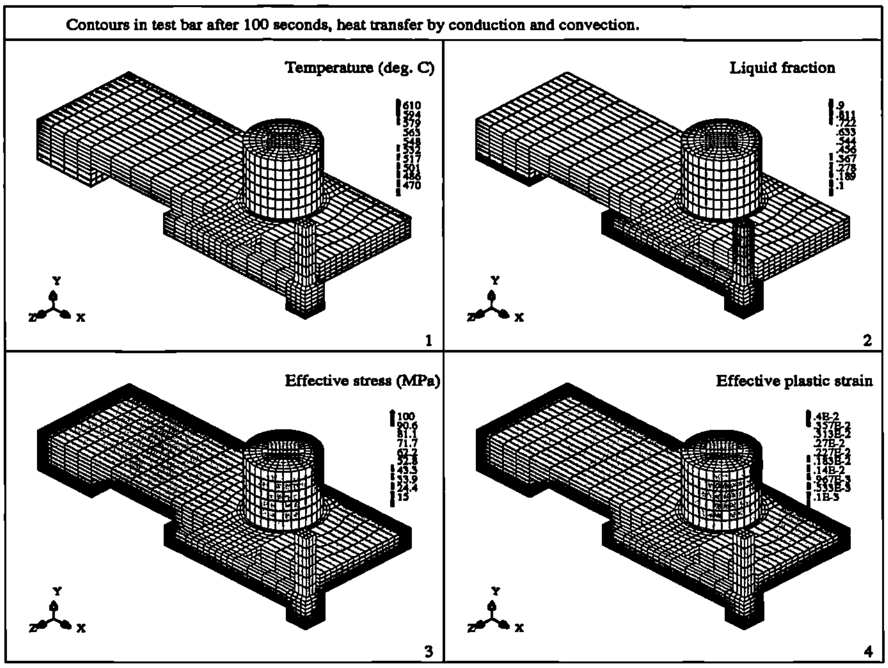

Figure 7.37: Thermo-mechanical behaviour after 100 seconds, heat transfer with convection.

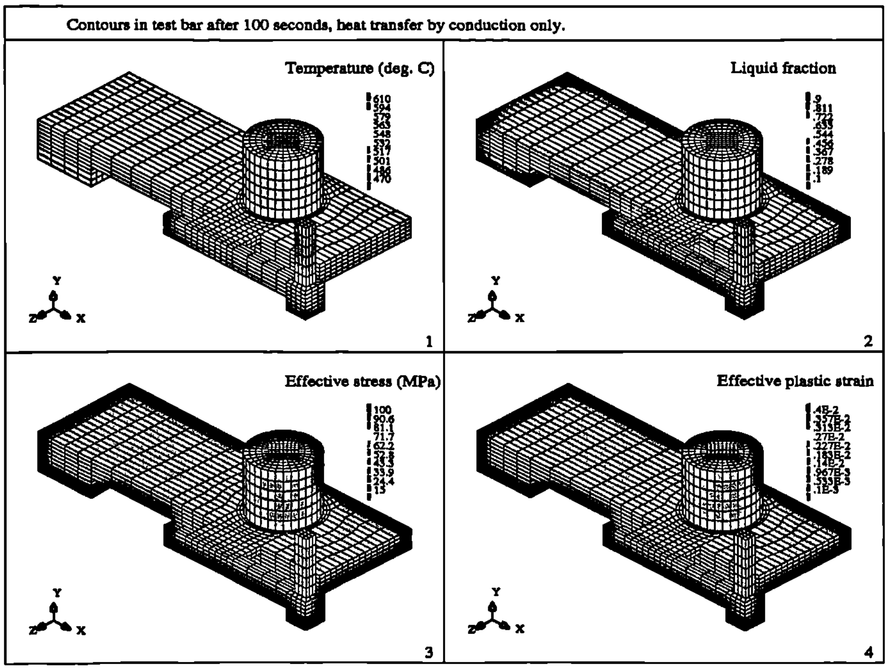

Figure 7.38: Thermo-mechanical behaviour after 100 seconds, heat transfer without convection.

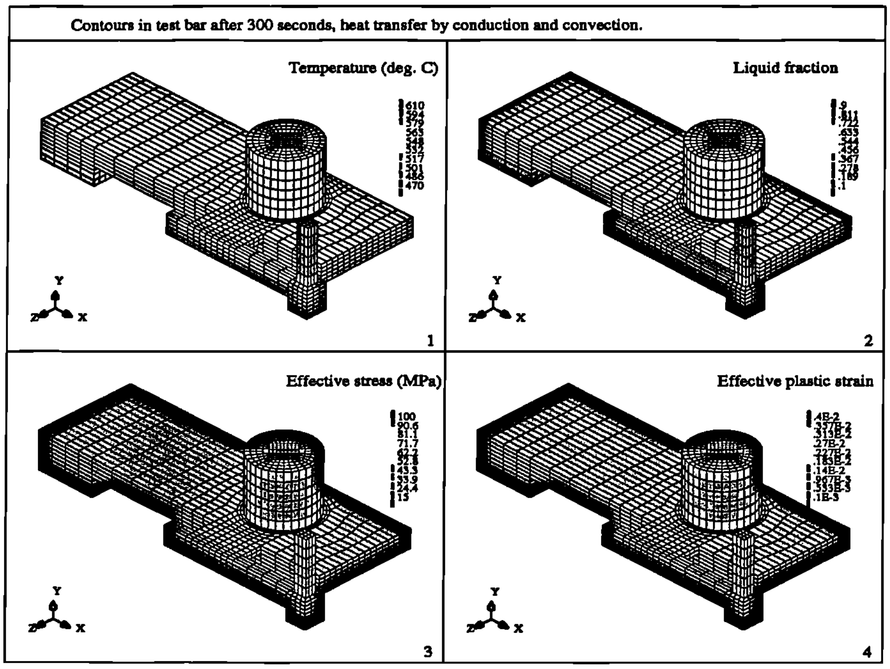

Figure 7.39: Thermo-mechanical behaviour after 300 seconds, heat transfer with convection.

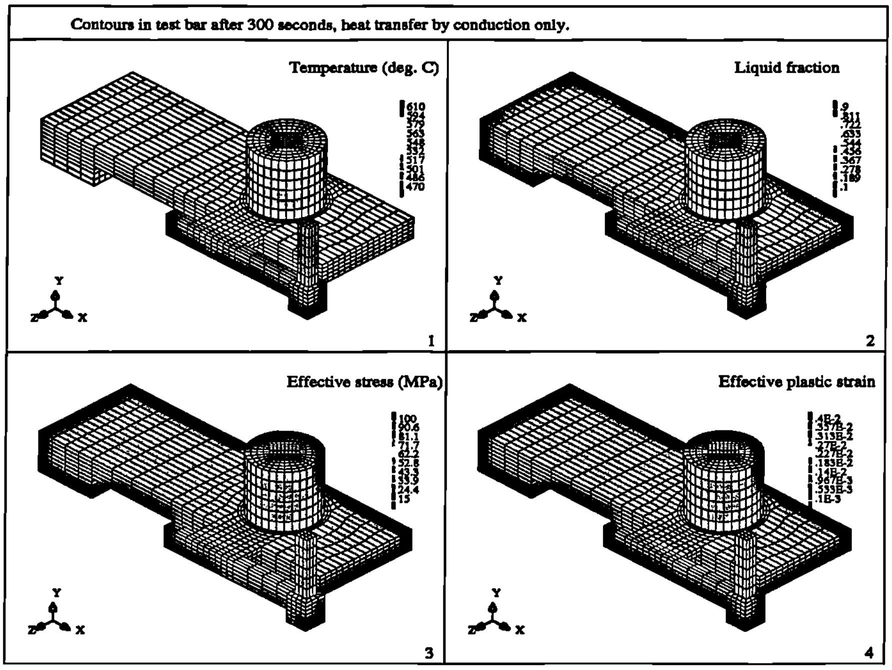

Figure 7.40: Thermo-mechanical behaviour after 300 seconds, heat transfer without convection.

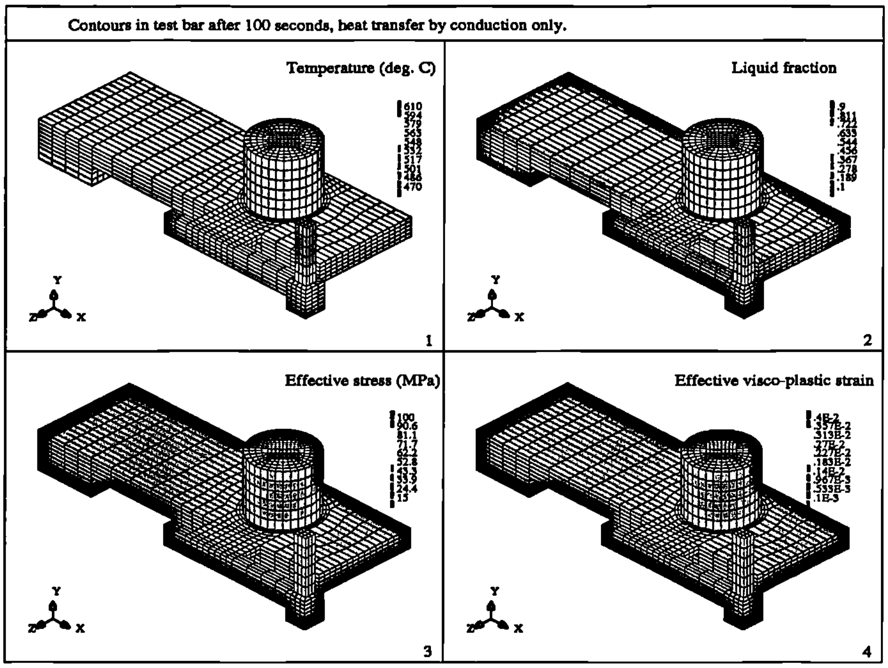

Figure 7.41: Rate dependent thermo-mechanical behaviour after 100 seconds.

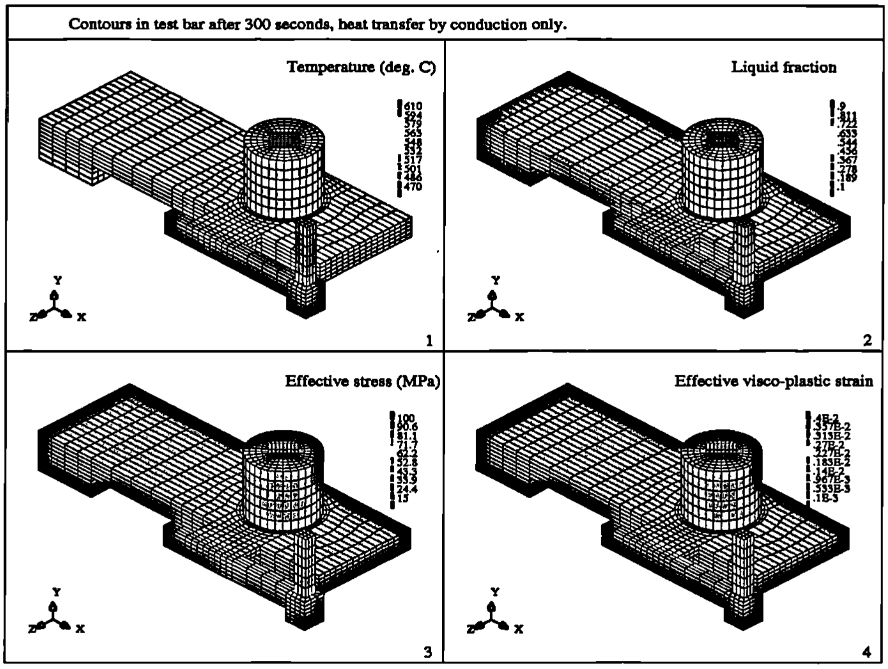

Figure 7.42: Rate dependent thermo-mechanical behaviour after 300 seconds.

7.4 Closure

In this chapter the capability of the FV framework PHYSICA to simulate the shape casting of metals has been illustrated and the importance of a fully coupled thermo-mechanical analysis has been demonstrated.

Initially, the die casting of an aluminium cylinder was simulated as a validation problem and the consequential results compared well against those of the experimental analysis. The comparison can be improved immediately by extending the PHYSICA framework to include a latent heat to solid fraction relationship suitable for binary alloys and a deformable-deformable contact algorithm to furnish mould dilation.

Finally, the sand casting of an aluminium test bar was simulated as an academic problem and the consequential results provided an illustration of both the full capability and present limitations of the PHYSICA framework with regard to the shape casting of metals. The sand casting problem illustrates interesting results from the inclusion of natural convection and rate dependent material behaviour in the thermo-mechanical analysis. Additionally, the problem illustrated the necessity for a robust contact algorithm and for the optimisation of the CSM algorithms with regard to computational effort.

Chapter 8

Closure

Initially in this chapter, the conclusions drawn from the research described in this thesis will be presented and finally the potential avenues of further research will be discussed.

8.1 Conclusions

In this section, the major conclusions of the thesis will be presented. A number of the conclusions have been drawn earlier in the thesis as the theoretical and numerical analyses were performed but they are represented here in summation.

8.1.1 Elemental comparisons

With specific regard to mechanical problems exhibiting elasto-visco-plastic material behaviour, it has been illustrated that for the Constant Strain Triangular (CST) and Linear Tetrahedral (LT) elements, the FVM and the FEM as described in this thesis are directly equivalent. This equivalence was first proven theoretically in Chapter 4 and then illustrated numerically in Chapter 5.

From these conclusions it can be postulated that the direct equivalence of the two methods with regard to the linear elements will apply generally for all solid mechanics problems involving material non-linearity. Thus strengthening the position of the FVM as an alternative to the FEM for problems involving non-linear material behaviour. The close agreement of the two dimensional Bi-Linear Quadrilateral (BLQ) and three dimensional Bi-Linear Pentahedral (BLP) and Tri-Linear Hexahedral (TLH) elements also illustrates the effectiveness of the FVM for the said problems. A tentative conclusion can be drawn after close inspection of the results for the higher order elements as employed in the solid mechanical validation problems of Chapter 5. There is discernible evidence that the FVM appears marginally closer to the numerical reference solutions of non-linear problems when the plastic or visco-plastic strains are large and the non-linearity is greatest.

8.1.2 Surface tractions

When surface tractions or pressure loads are applied over a higher order face element, as in the case of TLH elements employed in the spherical vessel problem of Chapter 5, the FVM appears superior with regard to accuracy on a coarse mesh. As the mesh is refined both methods approach the reference solution and the superiority of the FVM with regard to accuracy is less significant. This superiority is also true for linear elastic problems and has been commented upon by Wheel [100], who considered plane elasto-static problems involving non-uniform stress and strain distribution. It can be argued that the superiority is associated with the discretisation and the definition of the control volumes employed in the FVM. In the FVM the constitutive variables, such as stress and visco-plastic strain, are equivalent at control volume boundaries. This is a direct result of the conservative approach to the control volume definition. This is not the case in the FEM, where the weighting functions employed do not ensure that the constitutive variables are equal at the control volume boundaries [43, 42, 4, 100, 31, 48].

The FVM appears to be closer to the reference solution in these cases, but these cases are limited and further numerical and theoretical analysis must be performed before any definitive conclusions can be drawn. It is also important to note that any improvement in accuracy furnished by the FVM appears to be offset against a considerable increase in computational cost when compared to the FEM, as again illustrated in Chapter 5.

8.1.3 Thermo-mechanical problems

With regard to the coupling of mechanical analyses involving non-linear materials, specifically those that behave elasto-visco-plastically, and thermal analyses involving such phenomena as fluid flow, heat transfer and solidification, the suitability of the three dimensional FV framework PHYSICA as a realistic option for this purpose has been further illustrated. The validity of the thermo-mechanical coupling technique employed within this framework is indicated by the results of the standard benchmark problems as described in Chapters 6 and 7. It should be noted that the staggered coupling technique described and employed in this research, though widely used in many applications, is not suitable for all thermo-mechanical problems, particularly those involving large deformations.

These achievements and conclusions lend weight to the selection of a FV framework for the numerical analyses of complex industrial processes involving a variety of complex physical behaviour. This point is reinforced by the potential of PHYSICA to comprehensively simulate the shape casting of metals as presented in Chapter 7.

8.1.4 Finite volume discretisation

At present within the PHYSICA framework the heat transfer employs a cell-centred FVM and the CSM employs a vertex-based FVM. For this reason the accuracy of the thermo-mechanical coupling is somewhat dependent upon the extrapolation technique employed to obtain the temperature field at the vertices from that at the cell centres. This can introduce inaccuracies in the vertex-based temperature field when the mesh is unstructured, fortunately the inaccuracies diminish as the mesh is refined.

8.2 Further research

The potential avenues for further research have been highlighted as they arose throughout the thesis. In this section a summary of the potential further research will be given.

8.2.1 Contact analysis

At present the solid mechanics facilities within PHYSICA are limited to small strain, quasi-static, non-linear material problems. Further research which has already been undertaken, is the inclusion of contact analysis within a FV framework. This is required for the complete simulation of the shape casting of metals and requires the coupling of elasto-visco-plastic material behaviour with regard to the casting and deformable/rigid or deformable/deformable contact between casting and mould, depending upon the material properties of the mould involved in that particular shape casting process.

A number of researchers have already included contact analysis when applying the FEM to shape casting problems [67, 12], but this is not the case with regard to the FVM and it is possible that subtle differences may occur, again depending on the nature of the problem and the order of the elements employed. On the other hand, as has often been the case when comparing the FVM and the FEM, the two different approaches may actually achieve the same goal.

8.2.2 Optimisation

Further research is required to optimise the non-linear solution approach with regard to the FV formulation of the CSM. This would involve employing implicit integration techniques with regard to time stepping and modified Newton-Raphson methods combined with alternative preconditioners and solvers.

8.2.3 Solid mechanics

A great deal of further research is possible with regard to the CSM. This research includes further comparison and validation of the FVM when compared to the FEM for rate dependent material non-linearity. Comparison of the FVM and the FEM for general two and three dimensional contact analysis. Further research can also include the investigation of the applicability of the FVM to forming problems involving large deformations within a Lagrangian reference frame.

8.2.4 Shape casting of metals

With regard to the solid mechanics, the inclusion of a robust contact algorithm is a priority. This will facilitate deformation of both the casting and mould and provide increased accuracy in the gap formation. Also, gravitational effects have to be included, possibly by including inertial terms in the governing equations.

The PHYSICA framework can be generally extended in a numbers of ways to facilitate the comprehensive simulation of the shape casting of metals. Firstly, the additional modelling of the residual convection after the filling of the mould and the heat transfer associated with the filling. Also, in addition to the effect of buoyancy driven recirculation, the effect of volume change during solidification and the potential porosity formation associated with this phenomenon. Finally, the transient nature of the free surface associated with the liquid phase, with particular regard to feeding mechanisms in complex castings.

Most importantly the PHYSICA framework requires further validation against experimental results. This can include comparisons with the large number of experimental castings performed in the VERICAST project [44] and other benchmark shape casting problems that are now becoming public domain [85]. Additionally, further collaboration with the aerospace and automotive industries is required, particularly with regard to investment casting foundries and precision casting. Indeed, collaboration is currently underway to compare results from the experimental analyses of investment casting with numerical results from PHYSICA.

Appendix A

Standard Formulae

A.1 Divergence Theorem (Gauss' Theorem)

A closed region Ω is bounded by a simple closed surface Γ. If the vector field **F** and its divergence are defined throughout τ, then

$$\oint_{\Gamma} \mathbf{F}.\mathbf{d\Gamma} = \oint_{\Gamma} \mathbf{F}.\mathbf{n}\, d\Gamma = \int_{\Omega} \mathrm{div}\mathbf{F}\, d\Omega. \tag{A.1}$$

where **n** is the outward normal to the surface [14].

A.2 Green's First Theorem

Let the scalar fields ϕ and ψ, together with $\nabla^2\phi$ and $\nabla^2\psi$, be defined throughout a closed region Ω, bounded by a simple closed surface Γ. Then, Green's first theorem is that [14]

$$\oint_{\Gamma} \phi \frac{\partial \psi}{\partial n} d\Gamma = \int_{\Omega} (\phi \nabla^2 \psi + \mathrm{grad}\phi.\mathrm{grad}\psi)\, d\Omega. \tag{A.2}$$

Here, $\partial/\partial n$ denotes the directional derivative along the outward normal to Γ and

$$\frac{\partial \phi}{\partial n} = \mathrm{grad}\, \phi.\mathbf{n}.$$

By defining the vector field $\mathbf{f} = \operatorname{grad}\phi$ such that $\nabla^2\phi = \nabla.\mathbf{f}$, Green's first theorem is redefined as

$$\oint_\Gamma \phi\mathbf{f}.\mathbf{n}\, d\Gamma = \int_\Omega \phi(\nabla.\mathbf{f})\, d\Omega + \int_\Omega \nabla\phi.\mathbf{f}\, d\Omega.$$

A.3 Stokes's Theorem (in the plane)

Let $\phi(x,y)$ and $\psi(x,y)$ be defined and have continuous first derivatives throughout a closed region Ω in the xy-plane. Let Ω be bound by the closed curve Γ described in the anti-clockwise sense. Then Stokes's theorem is that [14]

$$\oint_\Gamma (\phi dx + \psi dy) = \iint_\Omega \left(\frac{\partial\phi}{\partial x} - \frac{\partial\psi}{\partial y}\right) dx\, dy. \qquad \text{(A.3)}$$

A.4 Error Function

- The error function is defined as

$$\operatorname{Erf}(x) = \frac{2}{\sqrt{\pi}} \int_0^x e^{-\xi^2} \mathrm{d}\xi$$

and has the properties $\operatorname{Erf}(0) = 0$ and $\operatorname{Erf}(\infty) = 1$ [17].

A.5 Kronecker delta

The Kronecker delta is defined by [14]

$$\delta_{ij} = \begin{cases} 0 & \text{when } i \neq j \\ 1 & \text{when } i = j \end{cases} .$$

Appendix B

Shape Functions

The following shape or basis functions and their associated derivatives are defined in the local coordinates s, t and u.

B.1 Constant Strain Triangular Elements

Shape functions,

$$\begin{aligned} N_1(s,t) &= \tfrac{1+2s}{3}, \\ N_2(s,t) &= \tfrac{1-s+\sqrt{3}t}{3}, \\ N_3(s,t) &= \tfrac{1-s-\sqrt{3}t}{3}. \end{aligned} \tag{B.1}$$

Local derivatives,

$$\begin{aligned} \tfrac{\partial N_1}{\partial s} &= \tfrac{2}{3}, & \tfrac{\partial N_1}{\partial t} &= 0, \\ \tfrac{\partial N_2}{\partial s} &= -\tfrac{1}{3}, & \tfrac{\partial N_2}{\partial t} &= \tfrac{1}{\sqrt{3}}, \\ \tfrac{\partial N_3}{\partial s} &= -\tfrac{1}{3}, & \tfrac{\partial N_3}{\partial t} &= -\tfrac{1}{\sqrt{3}}. \end{aligned} \tag{B.2}$$

B.2 Bilinear Quadrilateral Elements

Shape functions,

$$\begin{aligned} N_1(s,t) &= \tfrac{1}{4}(1+s)(1+t), & N_2(s,t) &= \tfrac{1}{4}(1-s)(1+t), \\ N_3(s,t) &= \tfrac{1}{4}(1-s)(1-t), & N_4(s,t) &= \tfrac{1}{4}(1+s)(1-t). \end{aligned} \tag{B.3}$$

Local derivatives,

$$\begin{array}{rclrcl}
\frac{\partial N_1}{\partial s} & = & \frac{1}{4}(1+t), & \frac{\partial N_1}{\partial t} & = & \frac{1}{4}(1+s), \\
\frac{\partial N_2}{\partial s} & = & -\frac{1}{4}(1+t), & \frac{\partial N_2}{\partial t} & = & \frac{1}{4}(1-s), \\
\frac{\partial N_3}{\partial s} & = & -\frac{1}{4}(1-t), & \frac{\partial N_3}{\partial t} & = & -\frac{1}{4}(1-s), \\
\frac{\partial N_4}{\partial s} & = & \frac{1}{4}(1-t), & \frac{\partial N_4}{\partial t} & = & -\frac{1}{4}(1+s).
\end{array} \tag{B.4}$$

B.3 Linear Tetrahedral Elements

Shape functions,

$$\begin{array}{rclrcl}
N_1(s,t,u) & = & \frac{1}{4}+\frac{2}{3}s-\frac{1}{3\sqrt{2}}u, & N_2(s,t,u) & = & \frac{1}{4}-\frac{1}{3}s+\frac{2\sqrt{3}}{6}t-\frac{1}{3\sqrt{2}}u, \\
N_3(s,t,u) & = & \frac{1}{4}-\frac{1}{3}s-\frac{2\sqrt{3}}{6}t-\frac{1}{3\sqrt{2}}u, & N_4(s,t,u) & = & \frac{1}{4}+\frac{1}{\sqrt{2}}u.
\end{array} \tag{B.5}$$

Local derivatives,

$$\begin{array}{rclrclrcl}
\frac{\partial N_1}{\partial s} & = & \frac{2}{3}, & \frac{\partial N_1}{\partial t} & = & 0, & \frac{\partial N_1}{\partial u} & = & -\frac{1}{3\sqrt{2}}, \\
\frac{\partial N_2}{\partial s} & = & -\frac{1}{3}, & \frac{\partial N_2}{\partial t} & = & \frac{2\sqrt{3}}{6}, & \frac{\partial N_2}{\partial u} & = & -\frac{1}{3\sqrt{2}}, \\
\frac{\partial N_3}{\partial s} & = & -\frac{1}{3}, & \frac{\partial N_3}{\partial t} & = & -\frac{2\sqrt{3}}{6}, & \frac{\partial N_3}{\partial u} & = & -\frac{1}{3\sqrt{2}}, \\
\frac{\partial N_4}{\partial s} & = & 0, & \frac{\partial N_4}{\partial t} & = & 0, & \frac{\partial N_4}{\partial u} & = & \frac{1}{\sqrt{2}}.
\end{array} \tag{B.6}$$

B.4 Bilinear Pentahedral Elements

Shape functions,

$$\begin{array}{rclrcl}
N_1(s,t,u) & = & \frac{1}{6}(1+2s)(1-u), & N_2(s,t,u) & = & \frac{1}{6}(1-s+\sqrt{3}t)(1-u), \\
N_3(s,t,u) & = & \frac{1}{6}(1-s-\sqrt{3}t)(1-u), & N_4(s,t,u) & = & \frac{1}{6}(1+2s)(1+u), \\
N_5(s,t,u) & = & \frac{1}{6}(1-s+\sqrt{3}t)(1+u), & N_6(s,t,u) & = & \frac{1}{6}(1-s-\sqrt{3}t)(1+u).
\end{array} \tag{B.7}$$

Local derivatives,

$$\begin{array}{rclrclrcl}
\frac{\partial N_1}{\partial s} & = & \frac{1}{3}(1-u), & \frac{\partial N_1}{\partial t} & = & 0, & \frac{\partial N_1}{\partial u} & = & -\frac{1}{6}(1+2s), \\
\frac{\partial N_2}{\partial s} & = & -\frac{1}{6}(1-u), & \frac{\partial N_2}{\partial t} & = & \frac{\sqrt{3}}{6}(1-u), & \frac{\partial N_2}{\partial u} & = & -\frac{1}{6}(1-s+\sqrt{3}t), \\
\frac{\partial N_3}{\partial s} & = & -\frac{1}{6}(1-u), & \frac{\partial N_3}{\partial t} & = & -\frac{\sqrt{3}}{6}(1-u), & \frac{\partial N_3}{\partial u} & = & -\frac{1}{6}(1-s-\sqrt{3}t), \\
\frac{\partial N_4}{\partial s} & = & \frac{1}{3}(1+u), & \frac{\partial N_4}{\partial t} & = & 0, & \frac{\partial N_4}{\partial u} & = & \frac{1}{6}(1+2s), \\
\frac{\partial N_5}{\partial s} & = & -\frac{1}{6}(1+u), & \frac{\partial N_5}{\partial t} & = & \frac{\sqrt{3}}{6}(1+u), & \frac{\partial N_5}{\partial u} & = & \frac{1}{6}(1-s+\sqrt{3}t), \\
\frac{\partial N_6}{\partial s} & = & -\frac{1}{6}(1+u), & \frac{\partial N_6}{\partial t} & = & -\frac{\sqrt{3}}{6}(1+u), & \frac{\partial N_6}{\partial u} & = & \frac{1}{6}(1-s-\sqrt{3}t),
\end{array} \tag{B.8}$$

B.5 Trilinear Hexahedral Elements

Shape functions,

$$\begin{array}{rclrcl}
N_1(s,t,u) & = & \frac{1}{8}(1+s)(1+t)(1+u), & N_2(s,t,u) & = & \frac{1}{8}(1-s)(1+t)(1+u), \\
N_3(s,t,u) & = & \frac{1}{8}(1-s)(1-t)(1+u), & N_4(s,t,u) & = & \frac{1}{8}(1+s)(1-t)(1+u), \\
N_5(s,t,u) & = & \frac{1}{8}(1+s)(1+t)(1-u), & N_6(s,t,u) & = & \frac{1}{8}(1-s)(1+t)(1-u), \\
N_7(s,t,u) & = & \frac{1}{8}(1-s)(1-t)(1-u), & N_8(s,t,u) & = & \frac{1}{8}(1+s)(1-t)(1-u).
\end{array} \tag{B.9}$$

Local derivatives,

$$\begin{array}{rclrcl}
\frac{\partial N_1}{\partial s} & = & \frac{1}{8}(1+t)(1+u), & \frac{\partial N_1}{\partial t} & = & \frac{1}{8}(1+s)(1+u), \\
\frac{\partial N_2}{\partial s} & = & -\frac{1}{8}(1+t)(1+u), & \frac{\partial N_2}{\partial t} & = & \frac{1}{8}(1-s)(1+u), \\
\frac{\partial N_3}{\partial s} & = & -\frac{1}{8}(1-t)(1+u), & \frac{\partial N_3}{\partial t} & = & -\frac{1}{8}(1-s)(1+u), \\
\frac{\partial N_4}{\partial s} & = & \frac{1}{8}(1-t)(1+u), & \frac{\partial N_4}{\partial t} & = & -\frac{1}{8}(1+s)(1+u), \\
\frac{\partial N_5}{\partial s} & = & \frac{1}{8}(1+t)(1-u), & \frac{\partial N_5}{\partial t} & = & \frac{1}{8}(1+s)(1-u), \\
\frac{\partial N_6}{\partial s} & = & -\frac{1}{8}(1+t)(1-u), & \frac{\partial N_6}{\partial t} & = & \frac{1}{8}(1-s)(1-u), \\
\frac{\partial N_7}{\partial s} & = & -\frac{1}{8}(1-t)(1-u), & \frac{\partial N_7}{\partial t} & = & -\frac{1}{8}(1-s)(1-u), \\
\frac{\partial N_8}{\partial s} & = & \frac{1}{8}(1-t)(1-u), & \frac{\partial N_8}{\partial t} & = & -\frac{1}{8}(1+s)(1-u),
\end{array}$$

$$\begin{array}{rcl}
\frac{\partial N_1}{\partial u} & = & \frac{1}{8}(1+s)(1+t), \\
\frac{\partial N_2}{\partial u} & = & \frac{1}{8}(1-s)(1+t), \\
\frac{\partial N_3}{\partial u} & = & \frac{1}{8}(1-s)(1-t), \\
\frac{\partial N_4}{\partial u} & = & \frac{1}{8}(1+s)(1-t), \\
\frac{\partial N_5}{\partial u} & = & -\frac{1}{8}(1+s)(1+t), \\
\frac{\partial N_6}{\partial u} & = & -\frac{1}{8}(1-s)(1+t), \\
\frac{\partial N_7}{\partial u} & = & -\frac{1}{8}(1-s)(1-t), \\
\frac{\partial N_8}{\partial u} & = & -\frac{1}{8}(1+s)(1-t).
\end{array} \tag{B.10}$$

Appendix C

Local-global transformation

Assuming that x_i, y_i and z_i are the global coordinates at a local node i defined in the local (s,t,u) coordinate system, the coordinate transformation is simply described by

$$\begin{aligned} x(s,t,u) &= \sum_{i=1}^{n} N_i(s,t,u)x_i, \\ y(s,t,u) &= \sum_{i=1}^{n} N_i(s,t,u)y_i, \\ z(s,t,u) &= \sum_{i=1}^{n} N_i(s,t,u)z_i. \end{aligned}$$

Where n is the number of nodes associated with the element under consideration. Obviously in the two dimensional instance the z and u coordinates are neglected.

Similarly for any variable ϕ_i described at the nodes, the variation within the element can be described by the same shape functions employed above when the element is isoparametric.

$$\phi(s,t,u) = \sum_{i=1}^{n} N_i\phi_i.$$

Additionally, the partial derivatives of the variable with respect to the local coordinates can be represented as follows:

$$\frac{\partial\phi(s,t,u)}{\partial s}=\sum_{i=1}^{n}\frac{\partial N_i(s,t,u)}{\partial s}\phi_i,$$
$$\frac{\partial\phi(s,t,u)}{\partial t}=\sum_{i=1}^{n}\frac{\partial N_i(s,t,u)}{\partial t}\phi_i,$$
$$\frac{\partial\phi(s,t,u)}{\partial u}=\sum_{i=1}^{n}\frac{\partial N_i(s,t,u)}{\partial u}\phi_i.$$

To map the local derivatives to global derivatives the following standard transformation is employed:

$$\begin{bmatrix}\frac{\partial N_i}{\partial x}\\ \frac{\partial N_i}{\partial y}\\ \frac{\partial N_i}{\partial z}\end{bmatrix}=\begin{bmatrix}\frac{\partial x}{\partial s} & \frac{\partial y}{\partial s} & \frac{\partial z}{\partial s}\\ \frac{\partial x}{\partial t} & \frac{\partial y}{\partial t} & \frac{\partial z}{\partial t}\\ \frac{\partial x}{\partial u} & \frac{\partial y}{\partial u} & \frac{\partial z}{\partial u}\end{bmatrix}^{-1}\begin{bmatrix}\frac{\partial N_i}{\partial s}\\ \frac{\partial N_i}{\partial t}\\ \frac{\partial N_i}{\partial u}\end{bmatrix}=\mathbf{J}^{-1}\begin{bmatrix}\frac{\partial N_i}{\partial s}\\ \frac{\partial N_i}{\partial t}\\ \frac{\partial N_i}{\partial u}\end{bmatrix}, \tag{C.1}$$

where $\mathbf{J}^{-1}$ is the inverse of the Jacobian matrix associated with a mesh element. As x, y and z are explicitly given by the relations C.1, the Jacobian can be written explicitly in terms of the local coordinates. Hence, the Jacobian can be defined in terms of the shape functions defining the coordinate transformation as follows:

$$\mathbf{J}=\begin{bmatrix}\sum_{i=1}^{n}\frac{\partial N_i}{\partial s}x_i & \sum_{i=1}^{n}\frac{\partial N_i}{\partial s}y_i & \sum_{i=1}^{n}\frac{\partial N_i}{\partial s}z_i\\ \sum_{i=1}^{n}\frac{\partial N_i}{\partial t}x_i & \sum_{i=1}^{n}\frac{\partial N_i}{\partial t}y_i & \sum_{i=1}^{n}\frac{\partial N_i}{\partial t}z_i\\ \sum_{i=1}^{n}\frac{\partial N_i}{\partial u}x_i & \sum_{i=1}^{n}\frac{\partial N_i}{\partial u}y_i & \sum_{i=1}^{n}\frac{\partial N_i}{\partial u}z_i\end{bmatrix}. \tag{C.2}$$

Additionally in a typical FEM, to transform the variables and the region with respect to which the integration is performed involves the determinant of the Jacobian matrix. Hence, a volume element is transformed as follows:

$$\mathrm{d}x\,\mathrm{d}y\,\mathrm{d}z=\det\mathbf{J}\,\mathrm{d}s\,\mathrm{d}t\,\mathrm{d}u.$$

Appendix D

Two dimensional approximations

In the following sections the elasticity matrices associated with FVM and the FEM for two dimensional approximations are are illustrated, where E is the Young's modulus and ν is the Poisson's ratio. Additionally, the differential and normal operator matrices are stated.

D.1 Plane stress

The augmented elasticity matrix for the plane stress approximation is

$$\mathbf{D} = \frac{E}{1-\nu^2}\begin{bmatrix} 1 & \nu & 0 & 0 \\ \nu & 1 & 0 & 0 \\ 0 & 0 & 0 & 0 \\ 0 & 0 & 0 & \frac{1-\nu}{2} \end{bmatrix}. \tag{D.1}$$

The redundant row and column allows the plane stress and strain elasticity matrices to be treated similarly in computational terms.

D.2 Plane strain and Axisymmetry

The elasticity matrix for the plane strain and axisymmetric approximation is

$$\mathbf{D} = \frac{E}{(1+\nu)(1-2\nu)} \begin{bmatrix} 1-\nu & \nu & \nu & 0 \\ \nu & 1-\nu & \nu & 0 \\ \nu & \nu & 1 & 0 \\ 0 & 0 & 0 & \frac{1-2\nu}{2} \end{bmatrix}. \tag{D.2}$$

D.3 Differential and normal operators

The general differential **L** and normal **R** operators are also augmented, as the out of plane contributions are neglected in the construction of the internal and external force terms. They are defined for the plane stress and strain approximations as follows:

$$\mathbf{R} = \begin{bmatrix} n_x & 0 \\ 0 & n_y \\ 0 & 0 \\ n_y & n_x \end{bmatrix}, \tag{D.3}$$

$$\mathbf{L} = \begin{bmatrix} \frac{\partial}{\partial x} & 0 \\ 0 & \frac{\partial}{\partial y} \\ 0 & 0 \\ \frac{\partial}{\partial y} & \frac{\partial}{\partial x} \end{bmatrix}. \tag{D.4}$$

The differential operator for the axisymmetric approximation is defined as follows:

$$\mathbf{L} = \begin{bmatrix} \frac{\partial}{\partial r} & 0 \\ 0 & \frac{\partial}{\partial z} \\ \frac{1}{r} & 0 \\ \frac{\partial}{\partial z} & \frac{\partial}{\partial r} \end{bmatrix}. \tag{D.5}$$

Appendix E

Constraint equations

The simplest use of constraint equations is the slaves to to master coupling of unknown variables, where n slave unknowns are directly equivalent to a master unknown variable.

Consider the set of linear simultaneous equations in the unknown u_j:

$$\sum_{j=1}^{L} K_{kj} u_j = f_k \qquad (1 \leq k \leq L). \tag{E.1}$$

The slave unknown u_i can be related to the master unknown as follows:

$$u_i - u_m = 0. \tag{E.2}$$

Rearranging equation E.1 as follows:

$$K_{ki} u_i + \sum_{j=1}^{L, j \neq i} K_{kj} u_j = f_k \qquad (1 \leq k \leq L) \tag{E.3}$$

and multiplying equation E.2 by K_{ki}

$$K_{ki} u_i - K_{ki} u_m = 0$$

and subtracting from equation E.3 gives

$$\sum_{j=1}^{L, j \neq i} K_{kj} u_j + K_{ki} u_m = f_k \qquad (1 \leq k \leq L).$$

For the unknown u_i explicitly

$$\sum_{j=1}^{L,j\neq i} K_{ij}u_j + K_{ii}u_m = f_i \qquad (k = i)$$

and adopting the standard Lagrange multiplier technique

$$\sum_{j=1}^{L,j\neq i} K_{kj}u_j + K_{ki}u_m - f_k + \lambda_k \left(\sum_{j=1}^{L,j\neq i} K_{ij}u_j + K_{ii}u_m - f_i \right) = 0 \tag{E.4}$$

for $1 \leq k \leq L$, where the Lagrange multiplier is

$$\lambda_k = \frac{\partial u_i}{\partial u_k}$$

and in this case

$$\begin{aligned} \lambda_k &= 1, & &\text{if } k = m, \\ \lambda_k &= 0, & &\text{if } k \neq m. \end{aligned}$$

Hence, if $k = m$

$$\begin{aligned} \sum_{j=1}^{L,j\neq i} K_{mj}u_j + K_{mi}u_m - f_m + \sum_{j=1}^{L,j\neq i} K_{ij}u_j + K_{mi}u_m - f_i &= 0, \\ \sum_{j=1}^{L,j\neq i} (K_{mj} + K_{ij})\, u_j + (K_{mi} + K_{ii})\, u_m &= f_m + f_i, \end{aligned}$$

which is equivalent to adding the linear equation for the slave unknown to equation for the master unknown and adding the coefficient of the slave unknown to the coefficient of the masterunknown.

If $k \neq m$

$$\sum_{j=1}^{L,j\neq i} K_{kj}u_j + K_{ki}u_m = f_k,$$

which is equivalent to adding the coefficient of the slave unknown to the coefficient of the master unknown.

Essentially, these operations are equaivalent to reducing the linear system of equations by the number of slave unknowns.

Bibliography

[1] F. Abassi and A. J. Fletcher. Effect of transformation plasticity on generation of thermal stress and strain in quenched steel plates. *Materials science and technology*, 1:830–837, 1985.

[2] C. J. Adkins. *Equilibrium Thermodynamics*. Cambridge University Press, Cambridge, UK, 1983.

[3] C. Bailey, P. Chow, M. Cross, Y. Fryer, and K. Pericleous. Multiphysics modelling of the metals casting process. In *Proc. R. Soc. Lond. A*, volume 452, pages 459–486, 1996.

[4] C. Bailey and M. Cross. A finite volume procedure to solve elastic solid mechanics problems in three dimensions on an unstructured mesh. *Int. Journal for Num. Methods in Engg.*, 38:1757–1776, 1995.

[5] B. R. Baliga and S. V. Patankar. Elliptic systems: Finite-element method 2. In W. J. Minkowycz, E. M. Sparrow, G. E. Schneider, and R. H. Pletcher, editors, *Handbook of Numerical Heat Transfer*, chapter 11, pages 379–420. John Wiley and Sons, 1988.

[6] B. R. Baliga and S. V. Patanker. A new finite-element formulation for convection-diffusion problems. *Numerical Heat Transfer*, 3:393–409, 1980.

[7] B. R. Baliga and S. V. Patanker. A control volume finite-element method for two-dimensional fluid flow and heat transfer. *Numerical Heat Transfer*, 6:245–261, 1983.

[8] B. R. Baliga, B. R. Pham, and S. V. Patanker. Solution of some two-dimensional incompressible fluid flow and heat transfer problems, using a control volume finite-element method. *Numerical Heat Transfer*, 6:263–282, 1983.

[9] R. Barrett, M. Berry, and T. Chan et al. *Templates for the solution of linear systems: Building blocks for iterative methods.* SIAM, 1996.

[10] K. J. Bathe and E. L. Wilson. *Numerical Methods in Finite Element Analysis.* Prentice Hall, Inc., New Jersey, USA, 1976.

[11] G. Beer and J. O. Watson. *Introduction to finite and boundary element methods for engineers.* John Wiley and Sons Ltd., Chichester, UK, 1992.

[12] M. Bellet, F. Decultieux, M. Menai, F. Bay, C. Levaillant, J.-L. Chenot, P. Schmidt, and I. L. Svensson. Thermomechanics of the cooling stage in casting processes: Three-dimensional finite element analysis and experimental validation. *Metallurgical and Materials Transactions B*, 27B:81–99, 1996.

[13] M. Bellet, M. Menai, F. Bay, P Schmidt, and I. L. Svensson. Finite element modelling of the cooling phase in casting processes. In T. S. Piwonka, V. Voller, and L. Katgerman, editors, *Modeling of Casting, Welding and Advanced Solidification Processes VI*, pages 561–568, 1993.

[14] D. E. Bourne and P. C. Kendal. *Vector Analysis and Cartesian Tensors.* The Camelot Press Ltd., Southampton, UK, 1980.

[15] J. Campbell, editor. *Castings.* Butterworth-Heinemann Ltd., Oxford, UK, 1991.

[16] J. Campbell. Review of computer simulation versus casting reality. In M. Cross and J. Campbell, editors, *Modelling of Casting, Welding and Advanced Solidification Processes VII*, pages 907–913, 1995.

[17] H. S. Carslaw and J. C. Jaeger. *Conduction of heat in solids.* Oxford University Press, Oxford, UK, 1959.

[18] CFDS AEA Technology, Harwell, Oxon, UK. *FLOW3D.*

[19] CHAM Ltd., Wimbledon, London, UK. *PHOENICS.*

[20] P. Chow. *A Control Volume Unstructured Procedure for Convection-Diffusion Solidification Processes.* PhD thesis, The University of Greenwich, 1993.

[21] P. Chow, C. Bailey, M. Cross, and K. Pericleous. Integrated numerical modelling of the complete casting process. In M. Cross and J. Campbell, editors, *Modeling of Casting, Welding and Advanced Solidification Processes VII*, pages 213–221, 1995.

[22] P. Chow and M. Cross. An enthalpy control volume-unstructured mesh (cv-um) algorithm for solidification by conduction only. *Int. Journal for Num. Methods in Engg.*, 35:1849–1870, 1992.

[23] I. C. Cormeau. Numerical stability in quasi-static elasto/visco-plasticity. *Int. Journal for Num. Methods in Engg.*, 9:109–127, 1975.

[24] N. Croft, K. A. Pericleous, and M. Cross. PHYSICA: A multiphysics environment for complex flow processes. In C. Taylor and P. Durbetaki, editors, *Numerical Methods in Laminar and Turbulent Flow '95*, volume 2, pages 1269–1280, 1995.

[25] M. Cross. Development of novel computational techniques for the next generation of software tools for casting simulation. In T. S. Piwonka, V. Voller, and L. Katgerman, editors, *Modeling of Casting, Welding and Advanced Solidification Processes VI*, pages 115–126, 1993.

[26] M. Cross, C. Bailey, P. Chow, and K. Pericleous. Towards an integrated control volume unstructured mesh code for the simulation of all the macroscopic processes involved in shape casting. In J. L. Chenot, R. D. Wood, and O. C. Zienkiewicz, editors, *Numerical Methods in Industrial Forming Processes IV*, pages 787–792, 1992.

[27] J. A. Dantzig. Thermal stress development in metal casting processes. *Metallurgical Science and Technology*, 7[3]:133–178, 1989.

[28] M. S. Darwish, J. R. Whiteman, and M. J. Bevis. Numerical modelling of viscoelastic liquids using a finite-volume method. *Journal of Non-Newtonian Fluid Mechanics*, 45:311–337, 1992.

[29] K. Davey. An analytical solution for the unidirectional solidification problem. *App. Math. Modelling*, 17(12):658–663, 1993.

[30] A. J. Davies. *The finite element method: A first approach.* Clarendon press, Oxford, UK, 1980.

[31] I. Demirdzic and D. Martinovic. Finite volume method for thermo-elasto-plastic stress analysis. *Computer Methods in Applied Mechanics and Engineering*, 109:331–349, 1992.

[32] I. Demirdzic and S. Muzaferija. Finite volume method for stress analysis in complex domains. *Int. Journal for Num. Methods in Engg.*, 37:3751–3766, 1994.

[33] J. D. Denton. A time marching method for two- and three-dimensional blade to blade flows. Technical Report 3775, Reports and Memoranda, Aeronautical research council, 1974.

[34] G. E. Dieter. *Mechanical Metallurgy.* McGraw Hill, 1988.

[35] N. N. Dioh, A. Ivankovic, P. S. Leevers, and J. G. Williams. Stress wave propagation effects in split hopkinson pressure bar tests. *Proc. R. Soc. Lond. A*, 449:187–204, 1995.

[36] FEA Ltd., Forge House, Kingston-upon-Thames, UK. *LUSAS V11.0.*

[37] Femview Ltd., Leicester, UK. *FEMGEN/FEMVIEW.*

[38] R. T. Fenner. *Engineering elasticity: Applications of Numerical and Analytical Techniques.* Ellis Horwood Ltd., Chichester, UK, 1986.

[39] A. J. Fletcher and W. D. Griffiths. Heat transfer during vapour blanket stage of quench. *Materials science and technology*, 9(11):958–965, 1993.

[40] A. J. Fletcher and W. D. Griffiths. Quenching of steel plates in sodium polyacrylate solutions. *Materials science and technology*, 9(2):176–183, 1993.

[41] Fluent, Inc., Lebanon, NH, USA. *FLUENT.*

[42] Y. D. Fryer. *A Control Volume Unstructured Grid Approach to the Solution of the Elastic Stress-Strain Equations.* PhD thesis, The University of Greenwich, 1993.

[43] Y. D. Fryer, C. Bailey, M. Cross, and C.-H. Lai. A control volume procedure for solving the elastic stress-strain equations on an unstructured mesh. *Appl. Math. Modelling*, 15:639–645, 1991.

[44] N. P. Gray and G. C. Coyle. Verification of defect and temperature predictions for commercial software using a variable geometry t-plate casting. In M. Cross and J. Campbell, editors, *Modelling of Casting, Welding and Advanced Solidification Processes VII*, pages 849–856, 1995.

[45] D. S. Griffin and R. S. Varga. Numerical solution of plane elasticity problems. *J. Soc. Indust. Appl. Math.*, 11(4):1046–1056, 1963.

[46] J. Hattel and P. N. Hansen. Simulating distortion and residual stresses in castings using fdm techniques. In M. Rappaz, M. R. Ozgu, and K. W. Mahin, editors, *Modeling of Casting, Welding and Advanced Solidification Processes V*, pages 253–258, 1991.

[47] J. Hattel and P. N. Hansen. Analysis of thermal induced stresses in die casting using a novel control volume fdm-technique. In T. S. Piwonka, V. Voller, and L. Katgerman, editors, *Modeling of Casting, Welding and Advanced Solidification Processes VI*, pages 585–592, 1993.

[48] J. H. Hattel and P. N. Hansen. A control volume-based finite difference method for solving the equilibrium equations in terms of displacements. *Appl. Math. Modelling*, 19:210–243, 1995.

[49] M. Heinlein, S. Mukherjee, and O. Richmond. A boundary element method analysis of temperature fields and stresses during solidification. *Acta Mechanica*, 59:59–81, 1986.

[50] R. Hill. *The Mathematical Theory of Plasticity.* Clarendon Press, Oxford, UK, 1950.

[51] E. Hinton, editor. *NAFEMS Introduction to Nonlinear Finite Element Analysis.* NAFEMS, East Kilbride, Glasgow, UK, 1992.

[52] C. Hirsch. *Numerical Computation of Internal and External Flows: Fundamentals of Numerical Discretization*, volume 1. John Wiley and Sons, 1988.

[53] P. H. Hodge, G. N. White, and R. I. Providence. A quantitive comparison of flow and deformation theories of plasticity. *J. of Appl. Mech.*, 9:180–184, 1950.

[54] S. R. Idelsohn and E. Onate. Finite volumes and finite elements: Two 'good friends'. *Int. Journal for Num. Methods in Engg.*, 37:3323–3341, 1994.

[55] A. Ivankovic, I. Demirdzic, J. G. Williams, and P. S. Leevers. Application of the finite volume method to the analysis of dynamic fracture problems. *Int. Journal of Fracture*, 66:357–371, 1994.

[56] Jr. J. E. Jackson and M. S. Ramesh. The rigid-plastic finite-element method for simulation of deformation processing. In P. Hartley, I. Pillinger, and C. Sturgess, editors, *Numerical modelling of material deformation processes: Research, Development and Applications*, chapter 7, pages 148–178. Springer-Verlag, 1992.

[57] A. Jameson, W. Schmidt, and E. Turkel. Numerical solutions to the euler equations by finite volume methods using runge-kutta time-marching schemes. *AIAA*, 81:1259, 1981.

[58] P. Jeanmart and J. Bouvaist. Finite element calculation and measurement of thermal stresses in quenched plates of high-strength 7075 aluminium alloy. *Materials science and technology*, 1:765–769, 1985.

[59] W. Johnson and P. B. Mellor. *Engineering Plasticity.* The Camelot Press Ltd., Southampton, UK, 1973.

[60] J. O. Kristiansson. Thermal stresses in the early stage of solidification of steel. *Journal of thermal stresses*, 5:315–330, 1982.

[61] W. M. Lai, D. Rubin, and E. Krempl. *Introduction to Continuum Mechanics.* Pergamon Press Ltd., Oxford, UK, 1978.

[62] H. G. Landau, J. H. Weiner, and E. E. Zwicky. Thermal stress in a viscoelastic-plastic plate with temperature dependent yield stress. *J. of Appl. Mech.*, 27:297–302, 1960.

[63] R. W. Lewis and P. M. Roberts. Finite element simulation of solidification problems. In T. J. Smith, editor, *Modelling of Flow and Solidification of Metals*, pages 61–92, 1987.

[64] MAGMA GmbH, Achen, Germany. *MAGMAsoft.*

[65] P. V. Marcal and I. P. King. Elastic-plastic analysis of two-dimensional stress systems by the finite element method. *Int. J. Mech. Sci.*, 9:143–155, 1967.

[66] P. W. McDonald. The computation of transonic flow through two-dimensional gas turbine cascades. Technical Report 71-GT-89, ASME, 1971.

[67] M. Menai and M. Bellet. Thermomechanical coupling during solidification: a 3d finite element approach. In M. Cross and J. Campbell, editors, *Modeling of Casting, Welding and Advanced Solidification Processes VII*, pages 723–730, 1995.

[68] K. P Michalek, J.E. Kelly, and J.A Dantzig. Modeling of in-mold heat transfer in continuous castin of steel. In S. Kou and R. Mehrabian, editors, *Modeling of Casting, Welding and Advanced Solidification Processes*, pages 497–516, 1986.

[69] K. W. Morton and E. Suli. Finite volume methods and their analysis. *IMA Journal of Numerical Analysis*, 11:241–260, 1991.

[70] G. C. Nayak and O. C. Zienkiewicz. Elasto-plastic stress analysis. a generalization for various constitutive relations including strain softening. *Int. Journal for Num. Methods in Engg.*, 5:113–135, 1972.

[71] E. Onate, M. Cervera, and O. C. Zienkiewicz. A finite volume format for structural mechanics. *Int. Journal for Num. Methods in Engg.*, 37:181–201, 1994.

[72] D. R. J. Owen and E. Hinton. *Finite elements in plasticity: Theory and practice.* Pineridge Press Ltd., Swansea, UK, 1980.

[73] G. N. Pande, D. R. J. Owen, and O. C. Zienkiewicz. Overlay models in time-dependent non-linear material analysis. *Computers and Structures*, 7:435–433, 1975.

[74] S. V. Patanker. *Numerical Heat Transfer and Fluid Flow.* Hemisphere, Washington DC, 1980.

[75] S. V. Patanker and D. B. Spalding. A calculation procedure for heat, mass and momentum transfer in three-dimensional parabolic flows. *Int. J. of Num. Heat and Mass Transfer*, 15:1787–1806, 1972.

[76] P. Perzyna. The constitutive equations for rate sensitive plastic materials. *Quart. Appl. Mech.*, 20:321–332, 1963.

[77] P. Perzyna. Fundamental problems in visco-plasticity. *Advan. Appl. Mech.*, 9:243–377, 1966.

[78] N. Phan-Thien and R. I. Tanner. Boundary element analysis of forming processes. In P. Hartley, I. Pillinger, and C. Sturgess, editors, *Numerical modelling of material deformation processes: Research, Development and Applications*, chapter 6, pages 131–147. Springer-Verlag, 1992.

[79] C. Prakash and V. R. Voller. On the numerical solution of the continuum mixture model equations describing solid-liquid phase change. *Numer. Heat Transfer, Part B*, 15:171–189, 1989.

[80] C. M. Rhie and W. L. Chow. Numerical study of the turbulent flow past an airfoil with trailing edge separation. *AIAA J.*, 21:1525–1532, 1983.

[81] Rockfield Software Ltd., The Innovation Centre, University College of Swansea, UK. *Microfield V2.3.*

[82] P. Schmidt and I. L. Svensson. Heat transfer and air gap formation in permanent mould casting of aluminium alloys. Technical Report TRITA-MAC-0541, Materials research centre, The royal institute of technology, S10044 Stockholm 70, 1994.

[83] G. E. Schneider. Elliptic systems: Finite-element method 1. In W. J. Minkowycz, E. M. Sparrow, G. E. Schneider, and R. H. Pletcher, editors, *Handbook of Numerical Heat Transfer*, chapter 10, pages 379–420. John Wiley and Sons, 1988.

[84] V. Selmin. The node-centred finite volume approach: Bridge between finite differences and finite elements. *Computer Methods in Applied Mechanics and Engineering*, 102:107–138, 1992.

[85] B. Sirrell, M. Holliday, and J. Campbell. The benchmark test 1995. In M. Cross and J. Campbell, editors, *Modelling of Casting, Welding and Advanced Solidification Processes VII*, pages 915–933, 1995.

[86] I. M. Smith and D. V. Griffiths. *Programming the finite element method.* John Wiley and Sons Ltd., 1988.

[87] C. J. Smithells, editor. *Metals reference book.* Butterworth & Co. Ltd., London, UK, 1976.

[88] Swanson Analysis Systems, Inc., Houston, USA. *ANSYS V5.0.*

[89] G. A. Taylor, C. Bailey, and M. Cross. Material non-linearity within a finite volume framework for the simulation of a metal casting process. In D. R. J. Owen, E. Oñate, and E. Hinton, editors, *Fourth international conference on computational plasticity: Fundamentals and Applications: Pt. 2*, pages 1459–1470, 1995.

[90] G. A. Taylor, C. Bailey, and M. Cross. Solution of the elastic/visco-plastic constitutive equations: A finite volume approach. *Appl. Math. Modelling*, 19:746–760, 1995.

[91] P. S. Theocaris and E. Marketos. Elastic-plastic analysis of perforated thin strips of a strain-hardening material. *J. Mech. Phys. Solids*, 12:377–390, 1964.

[92] B. G. Thomas. Stress modelling of casting processes: An overview. In T. S. Piwonka, V. Voller, and L. Katgerman, editors, *Modeling of Casting, Welding and Advanced Solidification Processes VI*, pages 519–534, 1993.

[93] B. G. Thomas, I. V. Samarasekera, and J. K. Brimacombe. Mathematical model of the thermal processing of steel ingots: Part 2: Stress model. *Metallurgical Transactions B*, 18B:131–147, 1987.

[94] S. P. Timoshenko and J. N. Goodier. *Theory of elasticity.* McGraw-Hill, Inc., New York, USA, 1970.

[95] T. C. Tszeng and S. Kobayashi. Stress analysis in solidification processes: Application to continuous casting. *Int. J. Mach. Tools Manufact.*, 29(1):121–140, 1989.

[96] UES, Ohio, USA. *ProCAST.*

[97] V. R. Voller and C. R. Swaminathan. General source-based method for solidification phase change. *Numer. Heat Transfer, Part B*, 19:175–189, 1991.

[98] J. H. Weiner and B. A. Boley. Elasto-plastic thermal stresses in a solidifying body. *J. Mech. Phys. Solids*, 11:145–154, 1963.

[99] J. H. Weiner and B. A. Boley. *Theory of Thermal stresses.* John Wiley and Sons, Inc., New York, US, 1967.

[100] M. A. Wheel. A geometrically versatile finite volume formulation for plane elastostatic stress analysis. *Journal of strain analysis*, 31(2):111–116, 1996.

[101] A. M. Winslow. Numerical solution of quasi-linear poisson equation in a nonuniform triangle mesh. *J. Comput. Phys.*, 1(2):149–172, 1966.

[102] Wolfram Research, Inc., Champaign, Illinois, USA. *Mathematica V2.*

[103] Y. Yamada, N. Yoshimura, and T. Sakurai. Plastic stress-strain matrix and its application for the solution of elastic-plastic problems by the finite element method. *Int. J. Mech. Sci.*, 10:343–354, 1968.

[104] O. C. Zienkiewicz. Origins, milestones and directions of the finite element method - a personal view. In *Archives of Computational Methods in Engineering: State of the art reviews*, volume 2.1, pages 1–48. Int. Center for Num. Methods in Engg., Barcelona, Spain, 1995.

[105] O. C. Zienkiewicz and I. C. Cormeau. Visco-plasticity—plasticity and creep in elastic solids—a unified numerical solution approach. *Int. Journal for Num. Methods in Engg.*, 8:821–845, 1974.

[106] O. C. Zienkiewicz and E. Onate. Finite volumes vs finite elements. is there really a choice? In P. Wriggers and W. Wagner, editors, *Nonlinear computational mechanics*, chapter 4, pages 240–254. Springer-Verlag, 1991.

[107] O. C. Zienkiewicz and R. L. Taylor. *The finite element method: Volume 1: Basic formulation and linear problems.* Magraw-Hill, Maidenhead, Berkshire, UK, 1989.

[108] O. C. Zienkiewicz and R. L. Taylor. *The finite element method: Volume 2: Solid and fluid mechanics, dynamics and non-linearity.* Magraw-Hill, Maidenhead, Berkshire, UK, 1991.

[109] O. C. Zienkiewicz, S. Valliappan, and I. P. King. Elasto-plastic solutions of engineering problems 'initial stress', finite element approach. *Int. Journal for Num. Methods in Engg.*, 1:75–100, 1969.